UNIVERSITY OF LEEDS

Zinc oxides for nanopigmented coatings for electroactive anti-corrosion protection of C-steel structures

Raisah Ahmed Saleh AlShehri

Submitted in accordance with the requirements for the degree of PhD Degree

The University of Leeds
School of Chemistry

June 2023

Acknowledgements

First and foremost, all praise Allah for giving me patience and strength throughout this trying time. Words cannot express my gratitude to my supervisor Professor Long Lin for his invaluable patience, assistance, cooperation and encouragement. Also, I could not have undertaken this journey without my co-supervisor Dr Kelvin Tapley, who very kindly shared with me his knowledge, expertise and feedback. Additionally, this research would not have been possible without generous support from the Chemistry Department of King Saud University's and funding from the Saudi Royal Embassy of Saudi Arabia in London.

I am also grateful to the School of Chemistry's faculty members, Drs Alexander Kulak, Algy Kazlauciunas, Christopher Pask, Mohammed Asaf and Andrew Hobson from the School of Earth and Environment and Richard Barker from the Mechanical Engineering School for doing their best to be cooperative and supportive.

I would like to thank my parents, Ahmed and Sharifah (may God rest their souls in peace), who encouraged me to follow my dreams and raised me well. My thanks also go out to my husband Nasser for his unyielding support. I am grateful to my beautiful children, Mohammad (child with disabilities), Fahad, Abdul Mosin and my little angel Jouri, who have always filled me with happiness. I would also like to express my gratitude to my brothers Ajlan and Saleh and sisters Afiah, Salhah and Lamia. Furthermore, I would be remiss not to mention my mother-in-law Norah and father-in-law Awadh for their patience and support. I would also like to thank Mohammad's childminder for her patience and cooperation and for all those who supported me with their words or prayers. I appreciate and thank you all.

Abstract

Zinc oxide particles (ZnO) were studied by investigating factors such as the effects of synthesis by precipitation, reflux and hydrothermal methods, the use of sodium hydroxide (NaOH) concentrations as participant agents with zinc acetate dihydrate, and the use of zinc resources such as zinc acetate dihydrate and zinc nitrate hexahydrate ($Zn(NO_3)_2 \cdot 6H_2O$). The effect of addition time on zinc oxide morphology using zinc nitrate hexahydrate and ammonium carbonate ($(NH_4)_2CO_3$) was also studied. The current study highlights the effects of different addition types (DATs) using zinc acetate dihydrate and zinc nitrate hexahydrate as zinc sources and sodium hydroxide and ammonium carbonate as precipitation agents through precipitation and reflux methods. The effects of adding sodium dodecyl sulphate (SDS) were investigated, and it was found that adding SDS as a surfactant to zinc acetate dihydrate and sodium hydroxide resulted in a highly regular particle arrangement.

All zinc oxide particles were calcinated at 550°C for 4 hours and investigated using scanning electron microscopy (SEM), x-ray diffraction (XRD), Fourier transform infrared (FTIR) and Raman spectroscopy.

The results showed different zinc oxide morphologies, such as a flower shape consisting of rod or platelet morphologies, in the synthesis of zinc acetate and NaOH in the reflux method. The flower shape consisting of porosity sheet shapes was obtained using zinc nitrate hexahydrate and ammonium carbonate in the reflux method. These porosity sheet shapes seem to be new shapes that can be created without adding any chemical compounds or organic substances as surfactants. The rod and porosity shapes of steel coated with epoxy resin were applied to study the effect of corrosion resistance. Corrosion resistance was more efficient in zinc oxide with porosity-shaped morphology than in zinc oxide with rod-shaped morphology.

Contents

Acknowledgements iii

Abstract iv

List of figures ix

List of tables xvi

Preface xvii

Introduction 1

1.1 Nanomaterial science 1

1.2 Types of nanomaterials 5

1.2.1 Carbon nanotubes 5

1.2.2 Fullerenes 5

1.2.3 Carbon black 6

1.2.4 Nano-carbides 7

1.2.5 Metal oxide nanoparticles 7

1.3 Applications of ZnO 14

1.4 Introduction of Miller–Bravais indices for a hexagonal crystal 16

1.4.1 Miller–Bravais indices of directions 17

1.5 Morphology of ZnO 20

1.6 Factors affecting zinc oxide morphology 29

1.6.1 Ostwald ripening process 29

1.6.2 Oriented attachment 29

1.6.3 Nucleation 30

1.6.4 Growth process 30

1.7 Zinc oxide crystals 31

1.8 Effects of synthesis parameters on the morphology of ZnO nanoparticles 36

1.9 Synthesis of ZnO nanostructures 40

1.9.1 Sol–gel method 41

1.9.2 Hydrothermal methods 42

1.9.3 Direct precipitation method 44

1.9.4 Sonochemical methods 46

1.10 Epoxy-based composites in coating 49

1.11 Nanoparticles – polymer interfacial interaction 54

1.12 Anti-corrosion protection 56

1.13 Electrochemical impedance spectroscopy.....62

1.13.1 Capacitance 63

1.13.2 Inductance.....64

1.13.3 Impedance plots.....65

1.13.4 EIS application 65

1.14 Electrochemical behaviour of semiconductors' electrodes in solution.....66

Aim of the research 70

Experimental methods.....73

2.1 Synthesis of zinc oxide nanoparticles 73

2.1.1 Materials.....73

2.2 Synthesis of zinc oxideusing zinc acetate dihydrate Zn $(CH_3CO_2)_2.2H_2O$ and sodium hydroxide NaOH by precipitation method 76

2.3 Synthesis of zinc oxide using zinc acetate dihydrate and sodium hydroxide NaOH by reflux method 77

2.4 Synthesis of zinc oxide using zinc acetate dihydrate and sodium hydroxide by the hydrothermal method 78

2.5 Synthesis of zinc oxide using zinc nitrate hexahydrate Zn $(NO_3)_2.$ $6H_2O$ and sodium hydroxide by precipitation method.....78

2.6 Synthesis of zinc oxide using zinc nitrate hexahydrate and sodium hydroxide by reflux method.....79

2.7 Synthesis of zinc oxide using zinc nitrate hexahydrate and sodium hydroxide by hydrothermal method 79

2.8 Synthesis of zinc oxide using zinc nitrate hexahydrate and ammonium carbonate by precipitation method 80

2.9 Synthesis of zinc oxide using zinc nitrate hexahydrate and ammonium carbonate by reflux method 80

2.10 Synthesis of zinc oxide using zinc nitrate hexahydrate $Zn(NO_3)_2{\cdot}6H_2O$ and ammonium carbonate $(NH_4)_2CO_3$ by hydrothermal method 81

2.11 Effect of addition time on zinc oxide morphology using zinc nitrate hexahydrate and ammonium carbonate with reflux method.....81

2.12 Electrochemical method 90

2.12.1 Materials 90

2.13 Suggestion of electrochemical cell design 91

Results and discussion 93

3.1 Field emission scanning electron microscopy (FE-SEM) and scanning electron microscopy characterisation of ZnO NPs 93

3.1.1 Zinc oxide using zinc acetate dihydrate $Zn(CH_3CO_2)_2 \cdot 2H_2O$ and sodium hydroxide NaOH by precipitation, reflux and hydrothermal method 94

3.1.2 Zinc oxide using Zinc nitrate hexahydrate and sodium hydroxide by precipitation, reflux and hydrothermal method 102

3.1.3 Zinc oxide using zinc nitrate hexahydrate and ammonium carbonate by precipitation method 104

3.1.4 Effect of time on ZnO using ammonium carbonate and zinc nitrate hexahydrate by reflux method 110

3.1.5 Suggested growth mechanism of flower shape 118

3.1.6 Suggested morphology of platelet shape.....123

3.1.7 Zinc acetate dihydrate and sodium hydroxide using sodium dodecyl sulphate 126

3.1.8 Mechanism of bifrustum morphology using zinc nitrate hexahydrate and ammonium carbonate 128

3.1.8.1 Another perspective explanation for porous morphology: 132

3.1.9 Effect of the addition time using ammonium carbonate and zinc nitrate hexahydrate in the reflux method.....134

3.1.10 Effect of pH 141

3.1.11 Effect of calcination 143

3.2 Morphology of zinc oxide nanoparticles studied via X-ray diffraction analyses.....146

3.2.1 Effect of different concentrations of sodium hydroxide (NaOH) when using 0.03 M of zinc acetate dihydrate (Zn $(CH_3CO_2)_2.2H_2O$) in a precipitation method.....147

3.2.2 Effect of precipitation method on zinc oxide morphology 148

3.2.3 Effect of the reflux method on zinc oxide crystallinity.....152

3.2.4 The effect of different addition time in reflux method when using 1 M of ammonium carbonate $CO_3(NH_4)_2$ and 1 M of zinc nitrate hexahydrate Zn $(NO_3)_2 \cdot 6H_2O$.....156

3.2.5 Effect of the hydrothermal method on zinc oxide crystallinity.....158

3.3 Morphology of zinc oxide nanoparticles studied via FTIR spectroscopic studies 162

3.3.1 Effect of a precipitation method on zinc oxide particles studied 162

3.3.2 Effect of reflux method on zinc oxide particles studied.....166

3.3.3 Effect of different adding time in reflux method when using 1 M of ammonium carbonate $CO_3(NH_4)_2$ and 1 M of zinc nitrate hexahydrate Zn $(NO_3)_2 \cdot 6H_2O$.....170

3.3.4 Effect of the hydrothermal method on zinc oxide particles studied .171

3.4 Raman spectroscopy measurements 173

3.4.1 Effect of different concentrations of sodium hydroxide when using 0.05 M of zinc acetate dihydrate in precipitation method 174

3.4.2 Effect of precipitation method on zinc oxide particles studied 174

3.4.3 Effect of reflux method on zinc oxide particles studied 177

3.4.4 Effect of different adding time in reflux method when using 1 M of ammonium carbonate $CO_3(NH_4)_2$ and 1 M of zinc nitrate hexahydrate Zn $(NO_3)_2 \cdot 6H_2O$ 180

3.4.5 Effect of hydrothermal method on zinc oxide particles studied 181

3.5 Electrochemical method 185

3.5.1 Impedance spectroscopy measurements 200

3.5.2 Mechanism of the corrosion process 206

Conclusion 213

Future work 216

List of abbreviation 217

Appendix A 221

Producing zinc oxide by zinc acetate dihydrate Zn $(CH_3CO_2)_2 \cdot 2H_2O$ and different concentrations of sodium hydroxide NaOH 221

A1 Keyence VHX-2000 digital microscope analysis 222

Appendix B 226

Preparing zinc oxide by zinc acetate dihydrate Zn (CH3CO2)2·2H2O sodium hydroxide NaOH after 7 days 226

Appendix C 232

Preparing zinc oxide using zinc nitrate hexahydrate Zn $(NO_3)_2 \cdot 6H_2O$ and potassium hydroxide KOH 232

Appendix D 233

Preparing zinc oxide using zinc nitrate hexahydrate Zn $(NO_3)_2 \cdot 6H_2O$ and ammonium carbonate $(NH_4)_2CO_3$ 233

Appendix E 234

Preparing zinc oxide using ammonium carbonate $(NH_4)_2CO_3$ and zinc nitrate hexahydrate Zn $(NO_3)_2 \cdot 6H_2O$ (adding different type) 234

Appendix F 235

Preparing zinc oxide using zinc acetate dihydrate Zn $(CH_3CO_2)_2 \cdot 2H_2O$ sodium hydroxide NaOH using reflux method 235

Appendix G 237

Preparing zinc oxide using Zinc acetate dihydrate Zn $(CH_3CO_2)_2 \cdot 2H_2O$ sodium hydroxide NaOH, by reflux method using polyvinyl pyrrolidone PVP 237

References 238

List of figures

Figure 1. Carbon nanotubes. 5

Figure 2. Fullerenes, C60 [15]. 6

Figure 3. Carbon black structure with diverse levels: a) illustration of TEM image of N660 carbon black, b) a primary simple particle consisting of stacks of layers of graphene sheet and c) description of different groups in carbon black structures that contain defects [16]. 7

Figure 4. Zinc oxide components in nature with illustrations of the geometrical structures in a) cubic shape rock-salt, b) wurtzite hexagonal and c) wurtzite lattice constants orthogonal a and c [27]. 13

Figure 5. Estimated chart illustrating ZnO nanoparticle application demands on the market. 15

Figure 9. Hexagonal unit cell of polar; c-plane (0001), semi-polar; m-plane (10**1**1) and nonpolar; a-plane (**1**010). 16

Figure 10. Simple example for planes and directions to clarify Miller–Bravais indices [34]. 18

Figure 6. SEM of ZnO NP flower-like morphology, consisting of a) flake shapes, b) cluster shapes, c) rod shapes and d) needle shapes [38]. 21

Figure 7. Effect of SDS, Tween 80 and Triton X-100 on ZnO nanoparticles [28]. . 24

Figure 8. Anionic surfactants [28]. 25

Figure 11. Effect of Ostwald ripening [53]. 29

Figure 12. Schematic of the effect of oriented aggregation. Initial particles (I) were randomly distributed according to the effect of Brownian motion (II) to obtain crystallographic alignment (III) and ongoing crystal formation (IV) [55]. 30

Figure 13. Morphologies, according to their transformation from the polar facet ratio to the nonpolar facet ratio, when increasing the ratio [70]. 31

Figure 14. Diagram illustrating that 1D, 2D and 3D could be obtained from a hexagonal shape [76]. 33

Figure 15. ZnO type structures: (a) rock salt structure, (b) zincblende type and (c) hexagonal wurtzite [46, 77]. 34

Figure 16. Relationship between Phillip's ionicity (ESF) in common semiconducting materials (group II-Oxide) II–O and II–VI materials as a function of the c/a ratio of the crystals [78] [79]. 35

Figure 17. Scheme illustrating the effect of the aspect ratio of OLA to zinc acetate on the final diameter and morphology of zinc oxide nanostructures [84]. 38

Figure 18. Illustration of the thermal decomposition of changing morphology and the formation of nonporous ZnO nanoparticles and porous micronised particles [39]. 44

Figure 19. Graphic diagram illustrating the synthesis of ZnO nanoparticles [96].... 45

Figure 20. Presence of defects under a coating..... 67

Figure 21. Electrical equivalent circuits when an organic coating was used: (a) ideal conditions for coating, (b) real coating but absence of corrosion, (c) observing coating with the presence of corrosion in holes, (d) coating in the case of disbonding, (e) coating with small Rsi value disbonding. 68

Figure 22. Steps in the precipitation method to produce zinc oxide, ZnO. 75

Figure 23. Steps in the reflux method for producing zinc oxide, ZnO. 75

Figure 24. Steps in the hydrothermal method for producing zinc oxide, ZnO. 76

Figure 25. Zinc oxide-epoxy composite coatings on steel panel (working electrode).91

Figure 26. Suggested design for the electrochemical cell..... 91

Figure 27. Applying the electrochemical cell coating in the lab. 92

Figure 28. Zinc oxide produced from the calcination of zinc acetate dihydrate for 12 hours at 400 °C. 94

Figure 29. SEM images illustrating the effect of various NaOH concentrations on ZnO morphologies using zinc acetate dihydrate as zinc source: (a, b, c) 0.25 M of NaOH at 10,000×, 25,000× and 50,000× magnifications, respectively; (d, e, f) 0.5 M of NaOH at 25,000×, 50,000× and 100,000× magnifications, respectively; (g, h, i) 0.75 M of NaOH at 5,000×, 10,000× and 25,000×, respectively; (j, k, I) represented 1 M NaOH at 50,000×, 100,000× and 100,000× magnifications, respectively; (m, n, o) SEM of different additive types of 1 M of sodium hydroxide and zinc acetate dihydrate at 10,000×, 25,000× and 50,000× magnifications, respectively. 95

Figure 30. Zinc oxide particles prepared by reflux methods using (0.3 M zinc acetate dihydrate and 3 M of sodium hydroxide) at (a) 10,000×, (b) 25,000× and (c, d) 50,000× magnifications. 96

Figure 31. Zinc oxide reflux method with different additives (0.3 M zinc acetate dihydrate on 3M of sodium hydroxide). Different magnifications demonstrated flower shape particles consisting of needles at (a) 1,000×, (b) 5,000×, (c) 10,000×, (d) 20,000×, (e) 25000× and (f) 250,000× magnifications..... 97

Figure 32. SEM images of zinc oxide prepared with sodium dodecyl sulphate SDS used as a surfactant in reflux method with 0.3 M of zinc acetate dihydrate and 3 M of sodium hydroxide at (a) 25,000×, (b) 50,000× and (c) 100,000× magnifications. 97

Figure 33. SEM images of zinc oxide prepared by (0.3 M of zinc acetate dihydrate with 3 M sodium hydroxide) via hydrothermal method at (a) 10,000×, (b) 25000× and (c) 50,000× magnifications. 98

Figure 34. SEM images of ZnO NPs prepared by (0.5 M of zinc nitrate hexahydrate and 1 M of sodium hydroxide) (Experiment 11) at (a) 5,000×, (b) 10,000× and (C) 25,000× magnifications. Zinc oxide morphology by applying different addition types in precipitation method (Experiment 12) at (d) 5,000×, (e) 10,000× and (f) 250,000× magnifications. Experiment 11: Refluxing methods as shown in (g) 25,000×, (h) 50,000× and (i) 65,000× magnifications. Applying different additive types (added NaOH on Zn $(NO_3)_2 \cdot 6H_2O$, then added Zn $(NO_3)_2 \cdot 6H_2O$ on NaOH in the reflux method at different magnifications and (j, k, l) zinc oxide using Zn $(NO_3)_2 \cdot 6H_2O$ and NaOH by the hydrothermal method at (j) 25000x, (k) 25,000x, (l) 50,000x magnifications (Experiment 15)..... 102

Figure 35. SEM images of ZnO NPs prepared by (1 M of zinc nitrate hexahydrate and 1 M of ammonium carbonate) at (a) 25,000×, (b) 50,000× and (c) 500,000× magnifications. Applying different additive types at (d) 5000×, (e) 10,000× and (f) 25,000× magnifications. 104

Figure 36. SEM images of zinc oxide prepared by (1 M of zinc nitrate hexahydrate and 1 M of ammonium carbonate calcinated at 250 ℃ for 4 hours at (a) 10000× (b) 25000× (c) 50000× (d) 200000× magnifications by reflux method. 105

Figure 37. SEM images of zinc oxide prepared by (1 M of zinc nitrate hexahydrate and 1 M of ammonium carbonate calcinated at 550 ℃ for 4 hours) at (a) 10000× (b) 25000× (c) 50000× (d) 100000× magnifications by reflux method. 106

Figure 38. SEM images of zinc oxide prepared by (1 M of zinc nitrate hexahydrate and 1 M of ammonium carbonate) at (a) 5000x, (b) 10000x and (c) 25000x different magnifications by hydrothermal method. 106

Figure 39. Effect of the reaction time, (5 minutes), on the zinc oxide particles produced in the reflux method when using 1 M of zinc nitrate hexahydrate and 1M of ammonium carbonate at (a) 5,000×, (b) 10,000×, (c) 25,000× and (d) 50,000× magnifications..... 110

Figure 40 Effect of the reaction time (10 minutes) on zinc oxide particles in the reflux method using 1 M of zinc nitrate hexahydrate and 1 M of ammonium carbonate at (a) 1,000×, (b) 10,000×, (c) 5,000× and (d) 20,000× magnifications..... 111

Figure 41. Effect of the reaction time (15 minutes) on zinc oxide particles in reflux method using 1 M of zinc nitrate hexahydrate and 1 M of ammonium carbonate at (a) 5,000×, (b) 6,500×, (c) 15,000× and (d) 25,000× magnifications..... 112

Figure 42. Effect of the reaction time (20 minutes) on zinc oxide particles in refluxing method using 1 M of zinc nitrate hexahydrate and 1 M of ammonium carbonate at (a) 1200×, (b) 5000×, (c) 10000× and (d) 15,000× magnifications..... 113

Figure 43. Effect of the reaction time (30 minutes) on zinc oxide particles in the reflux method using 1 M of zinc nitrate hexahydrate and 1 M of ammonium carbonate at (a) 5,000×, (b) 10,000×, (c) 20,000× and (d) 25,000×. 114

Figure 44. Effect of the reaction time (50 minutes) on zinc oxide particles in refluxing method using 1 M of zinc nitrate hexahydrate and 1 M of ammonium carbonate at (a) 1,000×, (b) 5,000×, (c) 10,000× and (d) 20,000× magnifications..... 115

Figure 45. Effect of the reaction time (70 minutes) on zinc oxide particles in the reflux method using 1 M of zinc nitrate hexahydrate and 1 M of ammonium carbonate at (a) 1,000×, (b) 5,000×, (c) 10,000× and (d) 20,000× magnifications..... 116

Figure 46. Mechanism of rod and flower shape formation. 121

Figure 47. Growth of some well-known morphologies for plane (0001) along the c-axis [3]. 122

Figure 48. Mechanism of zinc oxide particles' platelet shape. 124

Figure 49. Differences in growth in axial and equatorial growth. 125

Figure 50. Effect of ion-to-ion self-assembly to form a sheet shape for ZnO in the128

Figure 51. Suggested mechanism of zinc oxide bifrustum formation. 130

Figure 52. Mechanism of spherical nanoparticle formation (Experiment 27) [45]. 140

Figure 53. Scheme of ZnO particles under the effect of (a) Ostwald ripening and (b) oriented attachment [238]. 145

Figure 54. XRD results for zinc oxide synthesised using 0.3 M zinc acetate dihydrate with different sodium hydroxide concentrations. 147

Figure 55. XRD results for zinc oxide samples, compared to a commercial ZnO, using a precipitation method. 148

Figure 56. XRD of zinc oxide when using 0.3 zinc acetate dihydrate with 3 M of sodium hydroxide in a participation method, a) adding zinc acetate dehydrate on NaOH, b) adding NaOH on zinc acetate dihydrate (different addition type, DAT). 149

Figure 57. XRD results of zinc oxide when using 0.5 M of zinc nitrate hexahydrate with 1M of sodium hydroxide in a participation method, a) adding zinc nitrate hexahydrate on NaOH, b) adding NaOH on zinc nitrate hexahydrate (different addition type, DAT). 150

Figure 58. XRD results of zinc oxide, using 1 M of zinc nitrate hexahydrate with 1 M of ammonium carbonate as the precipitant in a participation method a) adding ammonium carbonate on zinc nitrate hexahydrate, (b adding zinc nitrate hexahydrate on ammonium carbonate (different addition type, DAT). 151

Figure 59. XRD results of zinc oxide compared to commercial ZnO when using a reflux method. 152

Figure 60. XRD for zinc oxide when using the reflux method with 0.3 M of zinc acetate dihydrate with 3 M of sodium hydroxide as the precipitant and with different addition types. 153

Figure 61. XRD results of zinc oxide when using a reflux method with 0.5 M of zinc nitrate hexahydrate and 1 M of sodium hydroxide as the precipitant: (a) adding zinc nitrate hexahydrate on sodium hydroxide, (b) adding NaOH on zinc nitrate hexahydrate (different addition type, DAT). 154

Figure 62. XRD for zinc oxide when using the reflux method with 0.3 M of zinc acetate dihydrate and 3 M of sodium hydroxide as a precipitant with sodium dodecyl sulphate (SDS). 155

Figure 63 XRD results of zinc oxide when using1 M of zinc nitrate hexahydrate with 1 M of ammonium carbonate in a reflux method with different addition time. 156

Figure 64 XRD results of zinc oxide compared to commercial ZnO when using a hydrothermal method. 158

Figure 65 Zinc oxide crystallite size when using the hydrothermal method. 160

Figure 66 FT-IR spectra for zinc oxide samples, compared to commercial ZnO, when using the precipitation method. 162

Figure 67 FT-IR spectroscopy for zinc oxide when using a) 3 M of sodium hydroxide on 0.3 zinc acetate dihydrate and b) 0.3 zinc acetate dihydrate on 2 M of sodium hydroxide (different addition types, DAT) in the precipitation method. 163

Figure 68 FT-IR spectroscopy for zinc oxide when using 1M of sodium hydroxide on 0.5 M of zinc nitrate hexahydrate and b) 0.5 M of zinc nitrate hexahydrate on 1M on NaOH in (different addition type, DAT) by precipitation method. 164

Figure 69 FT-IR spectroscopy for zinc oxide when using a) 1 M of ammonium carbonate on 1 M of zinc nitrate hexahydrate and b)1 M of zinc nitrate hexahydrate on 1M of ammonium carbonate (different addition types, DAT) by the precipitation method. 165

Figure 70. FT-IR spectroscopy for zinc oxide, compared to commercial ZnO, when using the reflux method. 166

Figure 71 FT-IR spectroscopy for zinc oxide when using a) 3 M of sodium hydroxide on 0.3 zinc acetate dihydrate and b) 0.3 zinc acetate dihydrate on 3 M of sodium hydroxide (different addition type, DAT) by reflux method. 167

Figure 72 FT-IR spectroscopy for zinc oxide when using the reflux method with zinc acetate dihydrate with NaOH as the precipitant and when using SDS. 167

Figure 73 FT-IR spectroscopy for zinc oxide when using a) 1 M of sodium hydroxide on 0.5 M of zinc nitrate hexahydrate, b) 0.5 M of zinc nitrate hexahydrate on 1 M of sodium hydroxide (different addition type, DAT) by reflux method. 168

Figure 74 FT-IR spectroscopy for zinc oxide when using zinc nitrate hexahydrate and ammonium carbonate in the reflux method after different reflux times. 170

Figure 75. FT-IR spectroscopy results for zinc oxide compared to commercial ZnO when using the hydrothermal method. 171

Figure 76 Raman spectrum for commercial ZnO 173

Figure 77 Raman spectra for zinc oxide using 0.05 M of zinc acetate dihydrate with different concentrations of NaOH when using the precipitation method. 174

Figure 78 Raman spectra for zinc oxide when using the precipitation method. 174

Figure 79 Raman spectra for zinc oxide when using (a 0.3 zinc acetate dihydrate on 3M of sodium hydroxide (different addition types, DAT) and b) 3M of sodium hydroxide on 3M of sodium hydroxide in the precipitation method. 175

Figure 80 Raman spectra for zinc oxide when using, a) 1 M of sodium hydroxide on 0.5 M of zinc nitrate hexahydrate (different addition type, DAT) and b) 0.5 M of zinc nitrate hexahydrate on 1 M of sodium hydroxide by precipitation method... 176

Figure 81 Raman spectra for zinc oxide when using, a) 1 M of zinc nitrate hexahydrate on 1 M of ammonium carbonate and b) 1M of ammonium carbonate on zinc nitrate hexahydrate (different addition type, DAT) by precipitation method. 177

Figure 82 Raman spectra for zinc oxide in reflux method. 177

Figure 83 Raman spectra for zinc oxide when using, a) 0.3 M of zinc acetate dihydrate on 3 M of sodium hydroxide (different addition type, DAT) and b) 3 M of sodium hydroxide on 0.3 M of zinc acetate dihydrate by reflux method. 178

Figure 84 Raman spectrum for zinc oxide when using, (a 0.5 M of zinc nitrate hexahydrate on 1 M of sodium hydroxide and b) 1 M of sodium hydroxide on 0.5 M of zinc nitrate hexahydrate (different addition type, DAT) by the reflux method. 179

Figure 85 Raman spectra for zinc oxide when using zinc nitrate hexahydrate with ammonium carbonate when using the reflux method for different times. 180

Figure 86 Raman spectra for zinc oxide when using the hydrothermal method. ... 181

Figure 87 The electrochemical coating cell contained three electrodes. 187

Figure 88 Blank steel, Epoxy/steel coating and ZnO/epoxy steel coating after exposure to 3.5% NaCl solution for 10 days. 187

Figure 89 SEM images of blank steel surface a) before at 120 x magnification and blank steel after exposure to NaCl solution after 10 days at different magnifications b) 120 x, c) 1200 x, and d) 1500 x magnification. 188

Figure 90 corrosion types in metals and alloys [271]. 189

Figure 91 EDX data for blank steel before exposure to NaCl solution for 10 days. 189

Figure 92 EDX result for blank steel after exposure to NaCl solution for 10 days. 190

Figure 93 SEM images of epoxy-steel surface before exposure to NaCl solution a) 120 x, b) 1200 x and c) 1500 x magnification. 191

Figure 94 EDX data for epoxy steel before the corrosion test. 191

Figure 95 SEM images of epoxy-steel surface after exposure to NaCl solution at 10 days immersion time at a) 500 x, b) 1000 x, c) 5000 x magnification. 192

Figure 96. EDX data for epoxy steel after exposure to NaCl solution for 10 days. 192

Figure 97 SEM images of the ZnO-epoxy steel 1 surface before exposure to NaCl solution a) 120 x, b) 1200 x and c) 1500 x magnification. 193

Figure 98 EDX data for ZnO-epoxy steel 1 before exposure to NaCl solution for 10 days. 194

Figure 99 SEM images of ZnO-epoxy steel 1 surface after exposure to NaCl solution a) 120 x, b) 1200 x and c) 1500 x at different magnifications. 194

Figure 100. EDX data of ZnO-epoxy steel 1 coated result after exposure to NaCl solution for 10 days 195

Figure 101. SEM images of ZnO-epoxy steel 2 surfaces before exposure to NaCl solution a) 120 x, b) 1200 x and c) 1500 x at different magnifications. 195

Figure 102. EDX data for ZnO-epoxy steel 2 before exposure to NaCl solution for 10 days. 196

Figure 103. SEM images ZnO-epoxy steel 2 surface before exposure to NaCl solution a) 120 x, b) 1200 x and c) 1500 x at different magnifications. 196

Figure 104. EDX data for ZnO-epoxy steel 2 after exposure to NaCl solution for 10 days. 197

Figure 105. Nyquist plots for all samples after 8 days. 200

Figure 106. Nyquist plots for all samples after 9 days. 200

Figure 107. Nyquist plots for all samples after 10 days. 201

Figure 108. Bode plots with |Z| modules and phase angle for all samples in 3.5% NaCl solution after 10 days of immersion. 201

Figure 109. Equivalent electrochemical circuit model a) for blank steel, b) for ZnO-epoxy steel 1 and epoxy steel coating [128]. 204

Figure 110. ZnO-epoxy steel coating mechanism. 205

Figure 111. Electrochemical double-layer diagram with an illustration of the potential distribution that occurs at the interface of the working electrode and the electrolyte solution. 206

Figure 1. ZnO after calcination. 221

Figure 2. Zinc acetate dihydrate Zn $(CH_3CO_2)_2 \cdot 2H_2O$ with 1 M of sodium hydroxide NaOH (a and b) before and (c and d) after calcination at 250 °C for 3h. 222

Figure 3. Zinc acetate dihydrate Zn $(CH_3CO_2)_2 \cdot 2H_2O$ with 0.75 M of sodium hydroxide NaOH (a and b) before and (c and d) after calcination at 250 °C for 3 hours.223

Figure 4. Zinc acetate dihydrate Zn $(CH_3CO_2)_2 \cdot 2H_2O$ with 0.2 M of sodium hydroxide NaOH (a and b) before and (c and d) after calcination at 250 °C for 3 hours.223

Figure 5. Zinc acetate dihydrate Zn $(CH_3CO_2)_2 \cdot 2H_2O$ with 0.1 M of sodium hydroxide NaOH (a and b) before and (c and d) after calcination at 250 °C for 3 hours.224

Figure 6 zinc acetate dihydrate Zn $(CH_3CO_2)_2 \cdot 2H_2O$ with 0.1 M of sodium hydroxide NaOH after calcination at 250 °C for 5 hours 224

Figure 7. zinc acetate dihydrate Zn $(CH_3CO_2)_2 \cdot 2H_2O$ with 0.1 M of sodium hydroxide NaOH after calcination at 250 °C for 7 hours 225

Figure 8 zinc acetate dihydrate Zn $(CH_3CO_2)_2 \cdot 2H_2O$ with 0.1 M of sodium hydroxide NaOH after calcination at 250 °C for 10 hours 225

Figure 9 illustration scheme of the process of ZnO particles using zinc acetate and NaOH when ethanol is the solvent. 227

Figure 10. Centrifuge machine. 227

Figure 11. Keyence microscope illustrated zinc acetate dihydrate Zn $(CH_3CO_2)_2 \cdot 2H_2O$ with (a, b) 1 gm, (c, d) 2 gm and (e, f) 4 gm of sodium hydroxide NaOH with after 7 days. 228

Figure 12. SEM results for zinc acetate dihydrate Zn $(CH_3CO_2)_2 \cdot 2H_2O$ with 1gm of NaOH, reaction took place in the in darkness for 7 days at room temperature at different magnification, a) 10000x, b) 25000x, c) 50000x, d) 100000x..... 229

Figure 13. SEM results for zinc acetate dihydrate Zn $(CH_3CO_2)_2 \cdot 2H_2O$ with 2gm of NaOH, reaction took place in the in darkness for 7 days at room temperature at different magnification, a) 10000x, b) 25000x, c) 50000x, d) 65000x..... 230

Figure 14. SEM results for zinc acetate dihydrate Zn $(CH_3CO_2)_2 \cdot 2H_2O$ with 4gm of NaOH, reaction took place in the in darkness for 7 days at room temperature at different magnification, a) 10000x, b) 25000x, c) 50000x, d) 100000x..... 231

Figure 15. KM for ZnO by zinc oxide using zinc nitrate hexahydrate Zn $(NO_3)_2 \cdot 6H_2O$ and potassium hydroxide KOH..... 232

Figure 16. KM results for ZnO particles using zinc nitrate hexahydrate Zn $(NO_3)_2 \cdot 6H_2O$ and ammonium carbonate $(NH_4)_2CO_3$. 233

Figure 17. KM results for ZnO particles by solution process at low temperature of zinc acetate dihydrate Zn $(CH_3CO_2)_2 \cdot 2H_2O$ with sodium hydroxide NaOH. 235

Figure 18. SEM results for ZnO particles by solution process at low temperature of zinc acetate dihydrate Zn $(CH_3CO_2)_2 \cdot 2H_2O$ with sodium hydroxide NaOH after grinded a) 10000x, b) 250000x, c) 50000 and d) 100000x..... 236

Figure 19. Zinc acetate dihydrate Zn $(CH_3CO_2)_2 \cdot 2H_2O$ with sodium hydroxide NaOH adding PVP by reflux method at different magnification, a) 25000x and d) 50000x. 237

List of tables

Table 1. The abbreviations of Roman letters. 16

Table 2. Illustration of values for certain equivalent indices as Miller and Miller-Bravais formula units [35]. 19

Table 3. The effect of molar ratios on zinc oxide morphologies. 37

Table 4. The synthesis methods of ZnO nanoparticles. 47

Table 5. some essential elements in impedance measurements. 64

Table 6. A brief description of methods for zinc oxide synthesis in the lab..... 83

Table 7. pH values and the obtained morphology. 142

Table 8. Crystallite size in experiments 7, 13 and 27 when using the hydrothermal method. 160

Table 9. Samples used in electrochemical corrosion test 185

Table 10. EDX analysis data (Weight %) for corrosion samples tested before and after exposure to NaCl solution for 10 days..... 197

Preface

This PhD thesis covers the results of a project undertaken at the School of Chemistry at the University of Leeds in the United Kingdom. This research was realised within the framework of a programme carried out by King Saud University and funded by the Royal Embassy of Saudi Arabia Cultural Bureau. My thanks and appreciation go to those who supported and cooperated with me throughout this process. I could not have finished my work without your help.

This PhD was a big challenge. Before embarking on my PhD journey, I had to face my phobia of planes as I was an international student. I had to come up with a serious solution to this problem, because I knew that the shortest flight from my country to the UK was at least six hours long. I started with a short flight that lasted only two hours. I followed this up with longer flight until I successfully overcame this problem. During my PhD studies, I experienced several ups and downs. As a mother of four children, I dealt with many difficult days, but I was lucky to be surrounded by excellent supervisors and my family and friends, who always supported me and lifted my spirit.

For the last chapter in this study, I had visualised an electrochemical cell design. This idea took time to develop, and I had to attend specific courses in this research area. I also contacted some schools, such as the Mechanical Engineering School and the Chemical and Process School at the University of Leeds, to help me apply my electrochemical designs. I found what I was looking for after I acquired assistance from my supervisor Prof Long Lin and Dr Richard Parker from the Mechanical Engineering School. I would like to give them special thanks for their cooperation and help.

My PhD journey has taught me how to encourage myself to be open to choosing new experiences and making decisions in life without hesitation. I have also learned that it is okay to make mistakes, as we are human beings; each mistake is an opportunity that guides me to the true path. It is important to be aware of the tiny details that could lead a researcher to new ideas, so focusing and concentrating on goals and discipline was a vital process in my PhD journey.

When I began writing, I felt that I would soon be able to embark on a new beginning and experience new things in life. I now know my own power, and I trust that I have the ability to shape my world and experiences and clarify my thinking, as I am perfectly equipped to do so.

Chapter 1

Introduction

1.1 Nanomaterial science

Nanotechnology is one of the fastest-growing areas of science and technology. The National Nanotechnology Initiative (NNI) has stated that any size of technology/material less than 100 nanometres with attractive properties is considered a nanotechnology [1]. Nanotechnology is the study of materials or nanoparticles with one or more dimensions of the order of 100 nm or lower [2]. The origin of the word 'nano' is a Greek term (*νάνος*) meaning dwarf ('nanos'). A nanometre is a unit of measurement (length, width or thickness) equal to one-billionth of a metre (m x 10^{-9}). A nanometre's size can also be compared to the length of a few atoms of hydrogen.

Nanoparticles are between 1 and 100 nm in size. This small size bridges the gap between the small size of atoms and molecules and the larger size of 'bulk material', which leads to new properties and characterisations in the substance of a material, which cannot be found in bulk materials. The current state of this technology is at the forefront of numerous research fields, including materials, physics, biotechnology, chemistry, biology, biochemistry, medicine, biomedical engineering, optoelectronics, electronics, spintronics, mechatronics, energy production, agriculture, interdisciplinary fields and environmental protection [3].

This technology makes it possible to test, control, regulate, modify, process, produce and use structures with at least one dimension under 100 nm. The characteristics of materials at the nanoscale often significantly differ from those of identical materials at the micro-scale.

Moreover, opportunities are multiplied in nanotechnology according to new structures and functions. Nanoparticles can produce significant materials and have a long-term duration. This offers a broad range of potential applications of nanoparticles, especially in the following industries – textiles, healthcare, food agriculture, electronics, environment, transportation, environmental engineering, biology, physics and materials processing. The success of nanotechnology can be attributed to its promising outcomes, lack of pollutant emission, energy efficiency and low space needs. In addition to these elements, nanotechnology has demonstrated a wide range of applications for risk evaluation in the domains of food, agriculture and the environment [1, 2, 4].

It has become possible to generate and fabricate the functional properties of nanoparticles to be more appropriate and compatible with the requirements of the modern era. Generally, due to the similarity in size between nanoparticles and materials, such as chemical species and biological analytes, nanotechnology appears to have a promising future. One of the features of nanoparticles is their ability to play different vital roles, even if they are similar to each other or from other kinds that change their roles in an electrochemical system, such as in the human body concerning DNA sensors, enzyme sensors and immune sensors.

In addition, nanotechnology has recently contributed to the protection of human life. For example, the spread of COVID-19 is responsible for the ongoing pandemic; the virus can result in severe respiratory issues, pneumonia and human contamination, which puts people's lives in jeopardy. COVID-19 has been deemed a global health emergency by the World Health Organisation due to the alarmingly high number of cases occurring worldwide. Nearly 80 million individuals have been impacted by the pandemic, which resulted in over 1.7 million fatalities globally in 2020 [4]. The virus exhibits novel traits for viruses of its kind.

The pandemic will benefit from cooperative research utilising nanofibre-based facial breathing masks and anticipation methods that are profoundly appealing antibacterial [5].

The primary personal defence against COVID-19 has been antiviral disinfectants, which indicates that nanotechnology can stop the spread of infection. Additionally, extensive research is being done to develop a COVID-19 vaccine based on different nanomaterials. During diagnosis with the virus, nanotechnology has shown a strong guarantee in structuring sensors to increase rapid reactions in COVID-19 testing [4, 5].

In the solid state, the arrangement of atoms and the sizes of molecules or atoms are in one, two or three dimensions. Any change to one or more of these considerations of solid microstructures will lead to a change in the properties of a solid. One of the most well-known intrinsic examples that illustrates the relationship between the atomic structural arrangement and the bulk material properties is the huge alteration of the hardness of the material formed when the atoms are arranged in the changing process from diamond to graphite [6].

In addition, because of the high surface area and tiny size of nanoparticles, they have a unique structure and can be used to develop sensing devices and biosensors [1, 6–9]. In recent decades, nanotechnology has been in high demand due to its vital role in accelerating the improvement of techniques, devices and synthesis of materials at the nanoscale. The nano-size of metal nanoparticles is a fitting aspect to utilise in catalysis according to the distinct properties of catalysts, which include an active surface that allows the reaction to take place. To obtain an active surface, when a catalyst is active, its nanoscale ratio of surface to size becomes larger.

This means that large active catalyst surfaces have the greatest reaction efficiency. Using transition metal oxides as catalyst nanoparticles is useful in oxidation reactions due to the ability of these kinds of catalysts to change from one oxidation state to another oxidation state [9, 10].

In recent years, nanomaterial science has been the focus of attention, especially in technology and industry. Nanotechnology has also spurred a wealth of knowledge in environmental fields [9, 11]. Nanotechnology is classified into four categories. First, in physics, this includes the

use of active, tiny cells in devices, components and integrated automated systems to allow for improvements in the ability to measure, establish and manipulate substances at the nanoscale. Second, in chemistry, a wide variety of nanoparticle uses have prospered to provide the mechanical and chemical properties of coating technology. Third, in biology, the size of the living cell unit is limited to arranging microns and nanometres. Nanostructures allow a superior opportunity to create devices that can control multiple characterisations, such as with diseases, cancer cells and surgery [1].

Fourth, in material science, according to several criteria, such as atomic structure and the nature of bonds between atoms and molecules, scientists have classified materials into three groups:

- Metals and alloys, such as steel and brass, depending on metallic bonding.
- Organic polymers, such as thermoplastic and organic fibres. The bonding types in this type of material are covalent bonding, hydrogen bonding, ionic bonding and van der Waals force [12].
- Ceramics, such as mineral glasses and silicon carbide (SiC), show distinct covalent and ionic bonds.

The three kinds of materials can form possible combinations of composite materials that consist of two or more materials that combine with each other to form specific properties. For example, epoxy resin with glass fibres is lightweight in form but has strong mechanical properties [13]. Metal nanoparticles act as excellent electronic wires to reinforce the process of transferring electrons between oxidation centres in proteins with outer electrode layers due to their catalytic properties and coefficient conductivity. Furthermore, metal nanoparticles play an important role as catalysts, especially in raising electrochemical reactions. On the other hand, oxide nanoparticles have many applications owing to their ability to immobilise biomolecules. Moreover, semiconductor NPs, such as zinc oxide, titanium oxide and aluminium oxide, have significant uses for electrochemical purposes as tracers [1, 13].

1.2 Types of nanomaterials

1.2.1 Carbon nanotubes

Carbon nanotubes (see Figure 1) are allotropes of carbon that are made up of many layers of graphene sheets wrapped in one of two ways. First, multi-walled tubes range in size from 2 to 100 nm. Second, the single-walled variety has a diameter ranging from 0.4 to 1.5 nm. The morphology of a carbon nanotube is a cylindrical structure with a micron as a measurement of length [9].

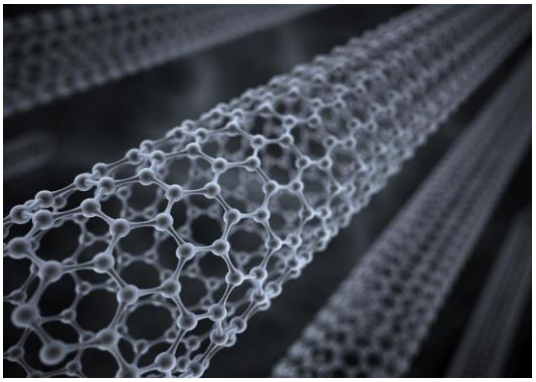

Figure 1. Carbon nanotubes.

The bonding type between carbon atoms in carbon nanotubes is sp2 hybridised. Due to a circular curve and concentric tubes, the σ-π rehybridisation form then leads to three kinds of σ bonds that will be out of plane. To decrease the resultant curvature, the p orbitals are delocalised out of the tube, which evolves into an abundance of π-electron conjugation.

1.2.2 Fullerenes

Fullerenes are a type of allotrope carbon atom, as seen in Figure 2. The morphology of these particles is spherical and ellipsoidal in shape. One kind of fullerene is C60, which looks hollow from the inside and similar to a soccer ball. It consists of two structures – 20 hexagons and 12 pentagons. Fullerenes have a great influence due to the composition of the structure, which is

a sphere in which the strength of the bonding comes from interactions. The above reasons make fullerenes have numerous applications, especially in industry [14].

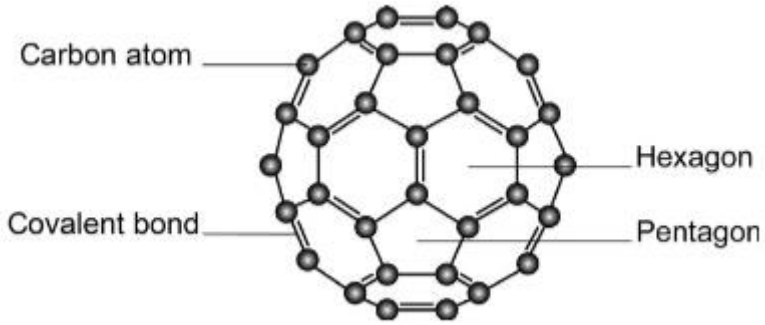

Figure 2. Fullerenes, C60 [15].

1.2.3 Carbon black

As shown in Figure 1, the structure of black carbon is quite complex. Crystalline and semicrystalline varieties look like graphite structures and can mix with amorphous carbon. The bonds of the graphene structure are formed by the reaction between carbon atoms and aromatic radicals. The feature of electrical conductivity relies on the crystalline graphene structure [9].

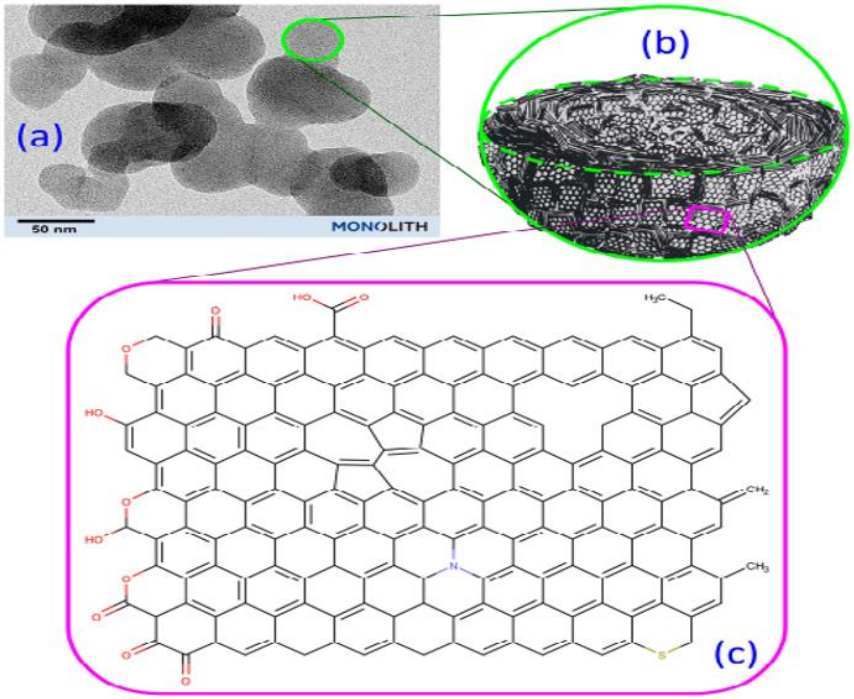

Figure 3. Carbon black structure with diverse levels: a) illustration of TEM image of N660 carbon black, b) a primary simple particle consisting of stacks of layers of graphene sheet and c) description of different groups in carbon black structures that contain defects [16].

1.2.4 Nano-carbides

Carbides are strong and hard materials that consist of carbon atoms with metals or semi-metals that form crystalline configurations. Due to their hardness, carbides are utilised either as refractories as a result of their high melting points or as abrasives. The crystalline structures of SiC and boron carbide (B_4C) are considered to have the highest hardness, similar to diamonds. The SiC nanometric powder is widely used to reinforce polymer resistance. B_4C plays a vital role in nuclear applications and can be used as a bulk material.

1.2.5 Metal oxide nanoparticles

Metal oxide nanoparticles have attracted researchers' attention because they have significant mechanical, chemical, magnetic and electronic properties and have numerous applications in physics, medicine, chemistry, and agriculture, etc [17]. Basically, metal oxide is distinguished

by its band-gap energy, which improves the properties of tolerance to high voltage. In addition, they are chemically stable, so they are preferred for use in manufacturing methods, such as pressure manufacturing, due to the chemical state (oxidised metal), keeping electrical functions properties without loss [18].

One of the metal oxides is titanium dioxide (TiO_2) Np, which has been studied in recent decades, but anatase has 3.2 eV band gaps at 387 nm and rutile has 3 eV band gaps at about 413 nm. These values limit some properties, such as the working photocatalytic effect and activity against UV radiation [19].

TiO_2, ZnO and WO_3 are considered a great opportunity for wastewater treatment using UV and visible light due to their stability, easy synthesis, non-toxicity, suitable band edge position and ability to generate active oxygen atoms in aqueous solution.

Doping with impurities, deposition of noble metals, sensitization with other materials (polymers, dyes, inorganic complexes, normal chelating ligands and inorganic compounds), hydrogenation methods, electronic incorporation of semiconductors, modification with carbon nanostructures and design with exposed facets compatible with the morphology hierarchy are all examples of calibrated and reliable methods for modifying surface electronic structure using metal oxides, such as TiO_2, ZnO and WO_3.

While numerous methods for embedding TiO_2 in photocatalysts have been thoroughly explored, a proportional study on the use of WO_3 and ZnO-based material in nanoparticles is still far-sighted in terms of highlighting their advantages and conferred properties. It is clear from the literature that a similar strategy does not necessarily lead to mirror image results in the photocatalytic effect, free radical generation, and charge carrier processes of these oxides [20].

Phothisarattana and Harnkarnsujarit studied the thermal stability, distilled water behaviour and migration of TiO_2 and zinc oxide as nanofillers and their effect on thermoplastic starch. They

found that the molecular weight of TiO_2 and zinc oxide are similar to each other 80, 81 gm/mol and TiO_2, respectively, has a small size that can be dispersed in the polymer chains, and the presence of two oxygen atoms increases the chance of forming more hydrogen bonds compared to zinc oxide, which makes the TiO_2 absorb more water and have a stronger effect on water plasticization. TiO_2 showed a higher percentage of aggregation than zinc oxide, which led to a decrease in the barrier and mechanical priorities of the film [21].

The titanium dioxide has a higher aggregation ability than zinc oxide, even though it has a smaller atomic size (47.9 A°) compared to zinc (65.4 A°), which is due to the presence of two oxygen atoms in titanium dioxide, which serve as motivation for the active seat in the molecular bond, which increases the aggregation of nanoparticles. It is important to note that the driving force in a nanofiller creates reduced surface energy, which reduces the contact between the polymer and the nanofiller, which is thermodynamically more stable. The addition of ZnO and TiO_2 increases the deflection of the starch particles and improved the amorphous starch structure.

In addition, the X-ray results showed high aggregation of the particles when TiO_2 was used compared to zinc oxide.

In addition, iron oxide (Fe_2O_3) and zinc oxide can effectively act as decontaminants in water due to their ability to extract trace or heavy elements by photocatalysis and adsorption. In all studies, it is important to control and investigate the effect of exposure time. pH could optimise the efficiency of adsorbents. Bharti et al. found that zinc oxides and iron oxide nanoparticles are the best choice for adsorbents and photocatalysts due to their large surface area and easy synthesis [22].

Metal oxide particles, such as alumina (Al_2O_3), titania (TiO_2) and zinc oxide (ZnO), are the most common nano-oxides used in polymers. Several methods can be utilised to produce nanoparticle oxides, such as sol–gel and precipitation.

One issue related to nanometric oxides during synthesis is aggregation. For example, in the case of the preparation of fumed silica, the functional groups on the surface of the nanometric oxide contain silanol groups produced by the reaction of water as a solvent and siloxanes. Silanol molecules contain OH^- functional groups, which lead to the formation of hydrogen bonds between every nearest particle, which ultimately leads to aggregation. When adding these nanoparticles to a polymer matrix to form a polymer nanocomposite, the interparticle forces become stronger when compared with interfacial interaction nanoparticles and polymer chains. Accordingly, the expected dispersion cannot be active.

To overcome the problem related to the huge surfaces of nanoparticles and to improve the chemical properties of nano-oxide particles, thermal treatment or modification of the chemical properties must take place. Hydroxyl groups exposed to high temperatures could lead to a decrease or removal of OH^- ions. The second possibility is to exchange OH^- groups with others during the chemical reactions, such as phenyl, methyl and ethoxy, to change the hydrophilic molecule inside the nanoparticles to be hydrophobic. Therefore, the interparticle forces become less effective than before. Kołodziejczak et al. mentioned that using starch molecules to reduce the agglomeration of ZnO nanoparticles due to the presence of hydroxide functional groups could reduce the surface area of ZnO NPs. Furthermore, adding a thin layer of silica film as a cover on the zinc oxide surface enhances the efficiency of dispersion, which reduces the agglomeration of nanoparticles. Furthermore, minimising the crystalline structure of ZnO by the heterogeneous azeotrope of the produced zinc could avoid a huge area of aggregation and reduce the particle size [8].

Numerous studies have been published in the field of metal oxides. However, to gain profound significance, metal oxides such as ZnO, TiO_2 and WO_3 need to be compared more on their respective morphologies, including synthesis, type of reactions and modification, to learn more important details, such as the photocatalytic effect in optical fields. Furthermore, there is a lack

of a basic understanding of the mechanism [20]. Moreover, the abundance of processes that can be used to generate ZnO is still not fully understood [23]. ZnO is a promising metal oxide because it is quite transparent and absorbs UV rays in the visible range [24]. In addition, zinc oxide can be used in paint rubber and coating [25]. Furthermore, zinc oxide films improve equipment performance and have perfect crystalline particles [26].

In this study, ZnO will be investigated as a nanoparticle for its properties and the influence of geometry using specific sizes and shapes to investigate the interfacial interactions between ZnO nanoparticles and polymer chains.

1.2.5.1 Nano-sized ZnO

Zinc oxide has been known since at least 2000 BC as a basic ingredient in medical creams and ointments for the treatment of carbuncles and boils [23]. Three different crystal forms of ZnO exist – hexagonal wurtzite, cubic rock salt and cubic zinc blende. Figure 4 depicts the various ZnO crystal formations. The rock salt structure is considered a rare crystal form. The hexagonal wurtzite crystal shape occurs more frequently and is stable at room temperature and pressure. ZnO is an octahedral polar crystal. There are two hexagonal unit cell lattices that show constant behaviour in the cases of a and c [27].

ZnO is an n-type semiconductor with distinct properties due to its wide band gap (3.37 eV), high value in binding energy (60 meV), low cost, environmental friendliness and distinct chemical and physical properties, such as thermal stability and chemical absorbency [28].

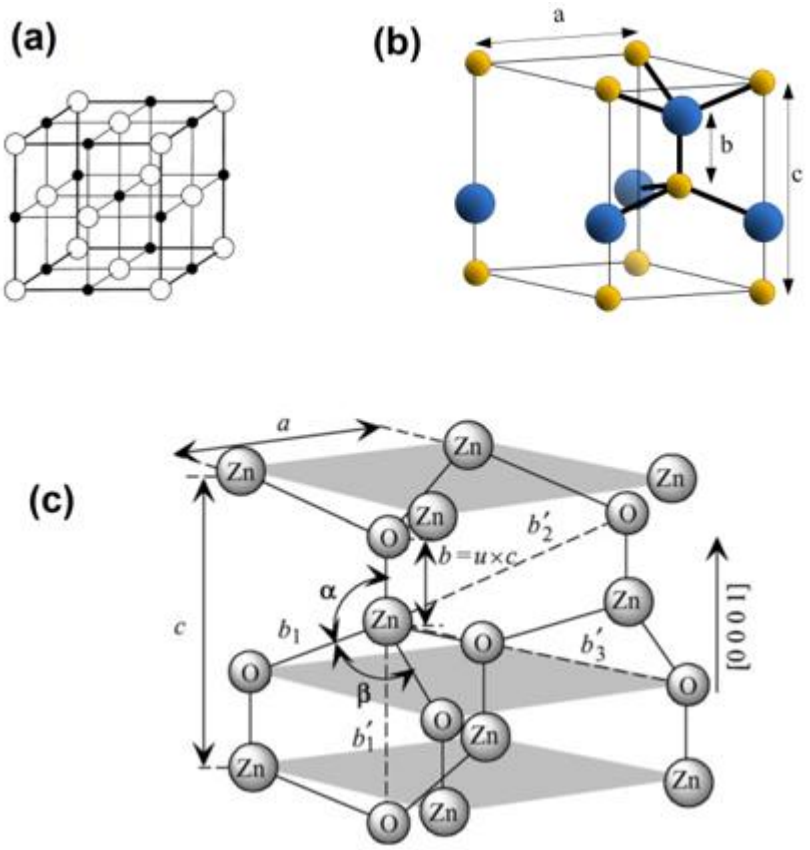

Figure 4. Zinc oxide components in nature with illustrations of the geometrical structures in a) cubic shape rock-salt, b) wurtzite hexagonal and c) wurtzite lattice constants orthogonal a and c [27].

ZnO nanoparticles can be found in hexagonal wurtzite shapes and crystalline structures. Zinc oxide is considered a polar crystal, and oxygen ions O^{2-} are positioned in the hexagonal close-packed organisation with Zn^{2+} ions lying in a specific arrangement in a tetrahedral shape linked with four oxygen ions. These kinds of combinations, and alternatively around the c-axis between zinc and oxygen ions, attain the structures of a polar plane with a positive charge Zn^{2+} and negative polar characteristics rich with O_2. The structure most exhibiting a stable ZnO morphology is the wurtzite crystal structure. This structure consists of polar planes, such as $[000\bar{1}]$ and [0001], and nonpolar planes, such as $[11\bar{2}0]$ and $[10\bar{1}0]$. Polar planes exhibit high surface energy compared to non-polar planes. As a result, the total crystalline structure of the ZnO tent can reduce surface energy by rearranging the organisation of the atoms. ZnO

crystal growth relies on the combination of internal factors, such as dislocations and intermolecular bonding favourites, and external factors, such as the kind of solvent, additives and time [28].

1.3 Applications of ZnO

ZnO is an n-type semiconductor with distinct properties and numerous applications, such as in sensors, catalysts, photoelectrics and electronics. ZnO nanoparticles can be found as hexagonal wurtzite in shape and crystalline in structure at room temperature. Many methods have been produced to synthesise ZnO as nanoparticles, such as hydrothermal, synthesis spray pyrolysis, precipitation, sol–gel and electrochemical methods. All these methods require sequenced steps and specific equipment, such as lasers, microwaves or vacuum chambers. Some agents result in complicated processes due to a need for a high temperature or vacuum environment, such as poor dispersion, impurity and the breakdown of the product in the last step [29, 30].

ZnO is considered to have a promising future as a material, especially in photocatalysis, disinfection catalysis, photoelectrics, electronic functional devices, UV blockers, cosmetics and optical fields. Moreover, ZnO nanoparticles show promising use in semiconductors, gas sensors, paints, solar cells, water purification and solar energy. Scientists attribute this to ZnO's low cost, high degree of photoactivity and environmental friendliness [28, 29]. Today, ZnO is frequently utilised as an ingredient or additive for a variety of purposes, including paints, ceramics, cement, porcelain, plastics, adhesives, sealants and pigments (zinc may be white or green). In addition to altering the colour of paint, ZnO also provides the ability to enhance antifouling and anti-corrosion qualities [3].

The main chemical compound produced from zinc metal is ZnO. A total of 660 thousand tonnes of metal oxide nanoparticles are expected to be produced in 2020, with ZnO NPs accounting for between 45 to 55 thousand or more tonnes, or roughly 7–8% of the usual market needs.

Currently, ZnO NPs are mostly employed to manufacture medicines, paints, cosmetics, a variety of coatings and products that fight bacteria, as well as in various technology and academic research.

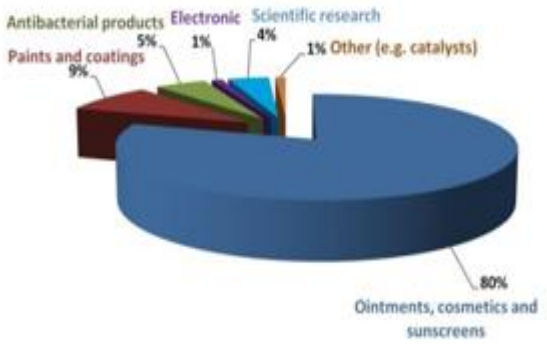

Figure 5. Estimated chart illustrating ZnO nanoparticle application demands on the market.

Samyn et al. used carboxymethyl starch as a means of improving the characterisations of paper coatings by establishing ZnO NPs among paper coatings. These processes enhance the brightness and whiteness of fabricated paper coatings and support stability towards UV radiation. Moreover, the process of dissolving ZnO gradually over time leads to the formation of Zn^{2+}, which can be used to immobilise microbes. In addition to its use in paper coatings, nano ZnO exhibits distinct properties, especially as a UV blocker, and is a long-term additive for paper's life compared with bulk ZnO-coated paper [9].

This study uses several morphologies of ZnO nanoparticles, such as nanoplatelets, nanoplatelets/nanorods and nanospheres to study their influence on thermal stability after adding epoxy resin to produce an epoxy composite. Thermogravimetric analysis demonstrated that nanoplatelets reinforce the thermal stability of a ZnO-epoxy nanocomposite [29].

Solar cell electrodes consisting of ZnO nanoparticles and nanorods with ruthenium as a dye absorber yielded power conversion efficiencies of 0.87% and 1.32% for ZnO nanoparticles and nanorods, respectively. However, ZnO can have a negative effect, particularly in mammal cells. Jeng and Swansing reported that ZnO nanoparticles could be responsible for mammals'

abnormal volumes of neuro-2a cells after exposure to doses greater than 100 mcg/ml. Furthermore, mitochondrial function significantly decreased in mammal cells exposed to ZnO nanoparticles at doses from 50 to $1*10^{*-4}$ mg/ml. However, Agbo et al. reported that ZnO has proven to be efficient in killing cancer cells [30].

1.4 Introduction of Miller–Bravais indices for a hexagonal crystal

The coordinates of polar, semi-polar and nonpolar planes for a hexagonal crystal are shown in Figure 6.

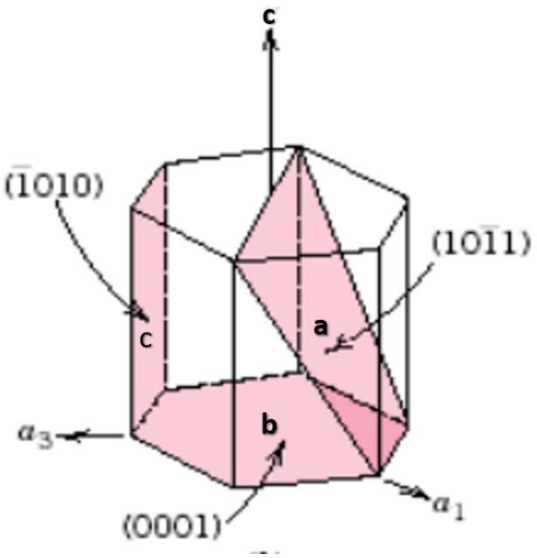

Figure 6. Hexagonal unit cell of polar; c-plane (0001), semi-polar; m-plane (10$\bar{\mathbf{1}}$1) and nonpolar; a-plane ($\bar{\mathbf{1}}$010).

Table 1. Abbreviations of Roman letters.

Abbreviations	Roman letter clarification
(H, K, L)	Quasicrystal Miller indices
(u,v,w)	Lattice node coordinates

[uvw]	Direction symbol
<uvw>	Family of directions
{hkl}	Family of planes
t	Translation vector

For the facets, <101> or $[10\bar{1}0]$ or $[10\bar{1}1]$ belong to the a-axis, and all symmetry belongs to [1000] directions in the hexagonal system = [100], [010], [110], $[\bar{1}00]$, $[1\bar{1}0]$. None of these directions are permutations, and there are three axes in one plane (a1, a2 and a3). The angle between them is 120°, and the fourth axis is the c-axis, which is perpendicular to each of them. This is important in order to understand the Miller–Bravais indices of planes [31].

The family of planes (prismatic planes) is related to $\{1\bar{1}00\}$ = $(10\bar{1}0)$, $(01\bar{1}0)$, $(\bar{1}100)$.

According to the role, (hkl) => (hkil) with i = -(h + k), whereas (hkil) is the Miller–Bravais pattern for planes (see Table 1) [32].

1.4.1 Miller–Bravais indices of directions

In crystallographic Miller indices, the direction as a function can be presented as [*uvw*], such that the translation vector **t** [33] behaves as follows:

$\mathbf{t} = ua_1 + va_2 + wc$, (1)

Considering that the bases' vectors are three (a1, a2, c).

However, when there are four directions (a1, a2, a3, c) (see Figure 7), the **t** value becomes

$\mathbf{t} = Ua_1 + Va_2 + Ta_3 + Wc$, (2)

where $a3 = -(a1 + a2)$

$= Ua_1 + Va_2 + T(-a_1 - a_2) + Wc$ (3)

$= (U - T)\, a_1 + (V - T)\, a2 + Wc$ (4)

[uvw] as a Miller => [UVTW] as a Miller–Bravais index

U - T = u (5)

V - T = v (6)

W = w (7)

This further requires that U + V + T = 0 (8)

U = 1 / 3 (2u - v) (9)

V = 1 / 3(2v - u) (10)

W = w

T = - (u + v) (11)

The T value is not independent and cannot be modified by the user.

X1 : [100] => [2/3 - 1/3 - 1/3 0] ≡ $[2\bar{1}\bar{1}0]$ (12)

X2 : [010] => [- 1/3 2/3 - 1/3 0] ≡ $[\bar{1}2\bar{1}0]$ (13)

X3 : $[\bar{1}\bar{1}0]$ => [- 1/3 11/3 2/3 0] ≡ $[\bar{1}\bar{1}20]$ (14)

So, symmetry related to family <$2\bar{1}\bar{1}0$> is shown in Figure 7. In this case, vertically,

A1 + a2 + a3 = zero (15)

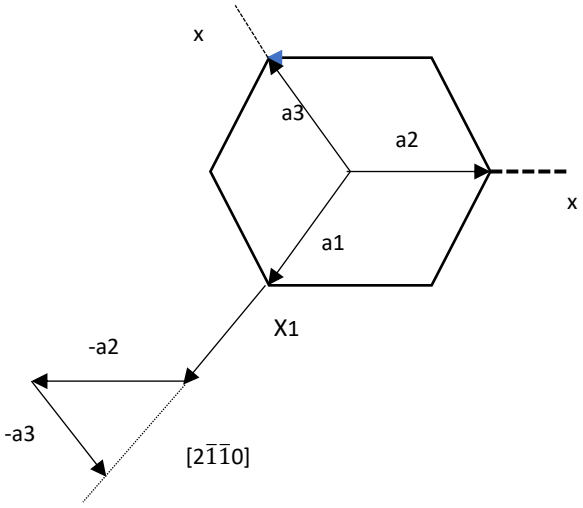

Figure 7. Simple example for planes and directions to clarify Miller–Bravais indices [34].

(002) or [0001] and $[000\bar{1}]$ belong to the c-axis.

A

H, k, i, l

There is 120° between a1, a2 and a3.

Accordingly, a1, a2, a3 and c convert to the unit values as follows:

Intercepts: 1, ∞, -1, 1

Reciprocals: 1, 0, -1, 1

Miller Indices: $(10\bar{1}1)$

B

Intercepts: ∞, ∞, ∞, 1

Reciprocals: 0, 0, 0, 1

Indices: (0001)

C

Intercepts: 1, ∞, -1, ∞

Reciprocals or inverses: 1, 0, -1, 0

Indices: $(10\bar{1}0)$.

Table 2 shows more Miller and Miller–Bravais values.

Table 2. Illustration of values for certain equivalent indices as Miller and Miller–Bravais formula units [35].

Miller	Miller–Bravais	Miller	Miller–Bravais
[100]	$[2\bar{1}\bar{1}0]$	[010]	$[\bar{1}2\bar{1}0]$
[110]	$[11\bar{2}0]$	$[\bar{1}10]$	$[\bar{1}100]$
[001]	[0001]	[101]	$[2\bar{1}\bar{1}3]$
[011]	$[\bar{1}2\bar{1}3]$	[111]	$[11\bar{2}3]$
[210]	$[10\bar{1}0]$	[120]	$[01\bar{1}0]$
[211]	$[10\bar{1}1]$	[112]	$[11\bar{2}6]$

ZnO is known to be non-centrosymmetric in its wurtzite hexagonal structure. Accordingly, it exhibits precise anisotropic growth, as well as a strong ability to aggregate under several factors in a specifically oriented manner [12]. The most well-known orientation occurs along [0001]

and $[000\bar{1}]$ or (0002). In general, polar planes with high energy, which have apposition as the basis and end of a rod structure, are subject to the role [ABAB]—taking into account the exchange of the O^{2-} polar plane and Zn^{2+} ions. In the case of 3D nanoparticle self-organisation, there are three fundamental routes to obtaining mesocrystals:

- Nanoparticle uniformity, under the effect of electrical or magnetic fields or both
- Epitaxial growth, creating mineral tunnels or bridges
- Entropy driven (spatial restrictions) [36]

Fast growth is affected by oriented aggregation. Slow growth decreases defects; in the case of non-classical crystallisation, this leads to the 2D stacking of faults or defects. Thus, the rate of growth could contribute to the rate and type of defect formation [37].

1.5 Morphology of ZnO

Several nanoparticles that are used as nanofillers, such as SiO_2, ZrO_2, carbon nanofiller and titanium oxide, have been found to have their thermal properties improved when combined with polymer to get the perfect composite. However, the ability of these nanoparticles to disperse, as well as their processing difficulties, are considered obstacles to their usage in nanocomposites. This is also true when nanofillers have a high density, such as carbon nanofillers. Recently, limited research has determined that the distinct role of ZnO nanoparticles as nanofillers reinforces the properties of epoxy nanocomposites. The variety of sizes and shapes of ZnO nanofillers have the ability to extend their usage to cover coated composite structures [29].

As previously mentioned, the morphology of ZnO nanoparticles is the richest compared to other metal oxides. There are variations of ZnO nanostructure shapes, such as nanobridges, nanowires, nano-trees, nanotubes, nano-nails, nanoflowers and nanorods. Figure 8 illustrates the types of flower-like shapes of ZnO.

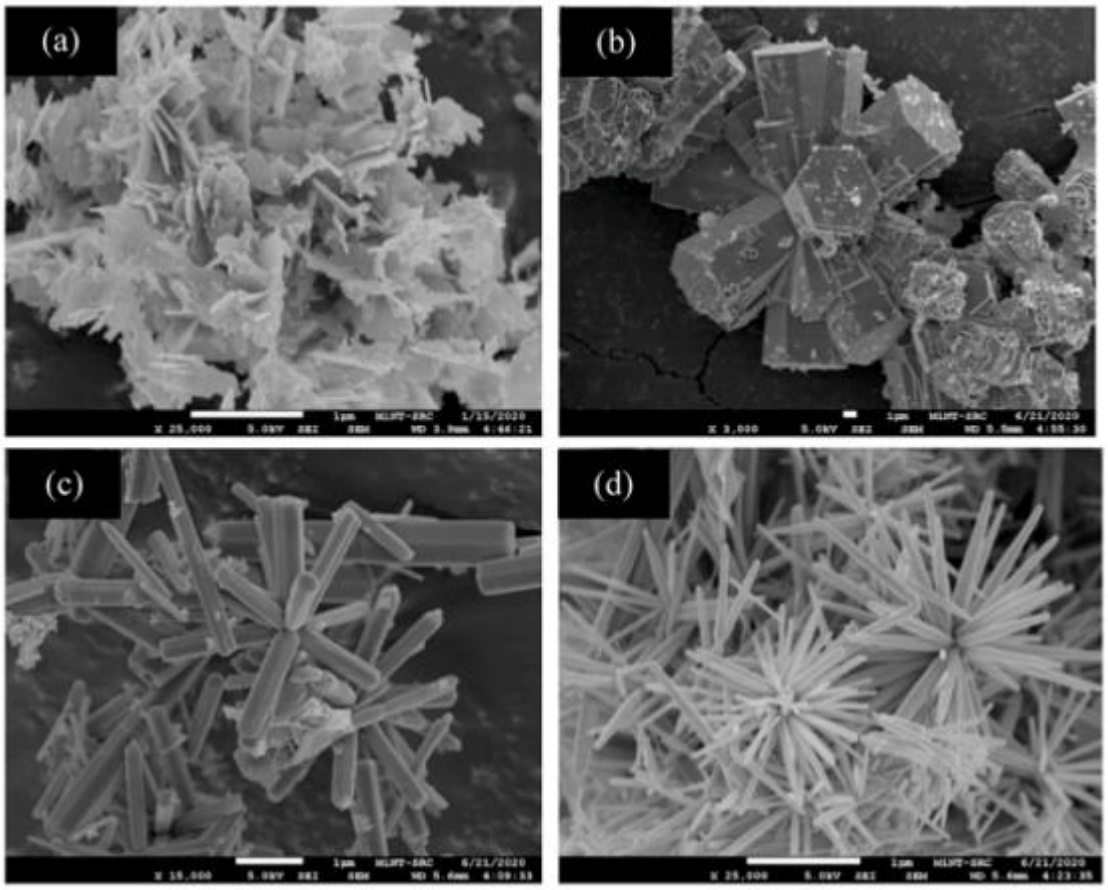

Figure 8. SEM of ZnO NP flower-like morphology, consisting of a) flake shapes, b) cluster shapes, c) rod shapes and d) needle shapes [38].

The decreased surface energy of ZnO nanoparticles, as well as less flexibility and connection with shapes, led to an increase in the fluidity and dispersion process. Moreover, in the case of ZnO NPs with spherical shapes, numerous studies have illustrated the scientific role of these nanoparticles in infrared (IR) spectroscopy analysis. They found that the change in peak values (IR-shielding) could be caused by high packing densities.

Specific sizes with appropriate shape morphologies that consider the degree of crystallinity significantly improve the properties of the ZnO nanoparticles. To reduce the cost of technology processing routes, it is important that scientists develop a process standard for maintaining the multifunctionality of ZnO nanoparticles by focusing on nanoparticles and narrowing the size distribution. The specific size and morphology of nanomaterials is considered a promising

prospect in nanotechnology, especially when looking for high-quality resultant polymer–nanocomposite applications.

In mechanical methods, the required size of ZnO nanocrystal depends on the calcination temperature and milling time; increasing the milling time (2–6 hours) leads to a decreased ZnO nanocrystal. Moreover, the solvents used had a significant effect on the morphology and size of ZnO NPs. For example, using a small amount of water as a solvent catalyses the reaction between 4-picN→O and zinc powder to gain a size ranging from 24–185 nm [8].

Barhoum et al. mentioned that the differences caused by the influence of photocatalyst structures contribute to the effect of the size, the shape and the role of surface area. The smaller it is, the more crystallites it has. Moreover, to gain the specific dimensions of ZnO nanoparticles, there are considerable factors that have to be taken into account, such as reaction temperature, capping agents, concentration and solvents [39].

Furthermore, the potential fabrication of ZnO NPs as nanowires with C-fibres improves hybrid laminates, illustrating the effect of changing and modifying the morphology of ZnO NPs in terms of their ability to enhance inhibition and hardness behaviour by studying the interaction at the interfaces between nanowires and hybrid laminates [40]. In addition, a few studies have revealed the possibilities of ZnO NPs with diverse morphologies for improving mechanical properties, as in the case of studying polymer nanocomposites. Nevertheless, few works have clarified the numerous ZnO NP applications, especially in studying the thermal stability of polymer nanocomposites [29].

Scientists have made efforts to improve a simple method as a solution to produce the morphology of oriented ZnO nanocolumns and nanorods.

As mentioned before, ZnO tends to develop in the [0001] direction or along the c-axis due to the high surface energy of the polar plan (0001) compared to the other planes. However, a variety of morphologies with significant crystal facets can be created by varying the growth

rate in these directions. This demonstrates the enormous diversity of the one-dimension (1D), two-dimension (2D) and three-dimension (3D) ZnO morphological formations. Nanorods, nanowires, nanohelixes, nanotubes, nanorings, nanoneedles and nanobelts are among the most common and substantial types of 1D structures.

One of the most well-known applications for 2D morphology is dye sensitivity in solar cells, such as nanopellets, nanoplates and nanosheets that have larger surface areas. Flowers, snowflakes, coniferous urchins and dandelions are among the 3D formations [27]. In addition, Liu et al. used a seeded growth method to prepare helical ZnO nanocolumns and nanorods. However, due to the limited opportunities to produce needle-like or rod-like ZnO nanostructures in more than one dimension, most of these methods fail to produce the desired morphology. Moreover, some methods that depend on wet chemical treatment were unable to produce the tiny size and narrow shape of ZnO nanowires with a high aspect ratio [27].

On the other hand, ZnO NPs may be used with several syntheses to prepare different morphologies in the case of using (surfactants) sodium dodecyl sulphate (SDS), Triton X-100 and Tween 80, which exhibit active surfaces and illustrate irregular growth mechanisms for several morphologies of ZnO nanostructures. In general, ZnO crystal growth relies on a combination of internal factors, such as dislocations and intermolecular bonding preferences, and external factors, such as the kind of solvents and additives and time. For example, Singh et al. used a surfactant to study the influence of increasing the concentration of active molecules (surfactants) and the effect of temperature on the growth of zinc oxide morphologies. ZnO nanowires are obtained when utilising SDS, while ZnO, with spherical nanoparticles and clusters, is gained in the presence of Tween 80 and Triton X-100 (see Figure 9). In addition, the study uses density functional theory. The binding energy value shows that the hydroxyl functional group OH^- showed physical adsorption on ZnO nanostructure on both surfaces [28].

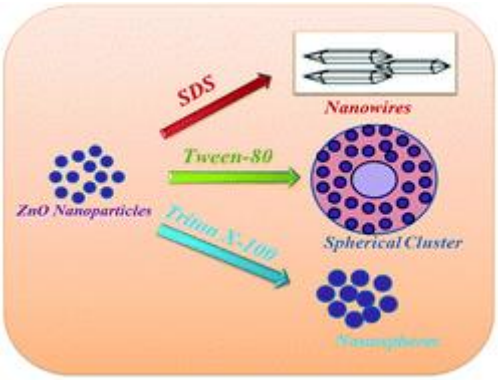

Figure 9. Effect of SDS, Tween 80 and Triton X-100 on ZnO nanoparticles [28].

Sometimes using anionic surfactants (see Figure 10) to modify the surface and as a protected agent in the case of modifying the nature of the surfactant from anionic surfactant SDS to a non-ionic surfactant, Triton X-100 or Tween 80, the role of the functional surfactant is a crucial agent to explain the adsorption mechanism on the surface, taking into account the functional groups, such as $–OCH_2CH_2$, –OH, $–CH_2$, $-CH_3$ and the sulphate group $–SO_4$.

(a) Sodium Dodecyl Sulfate (SDS)

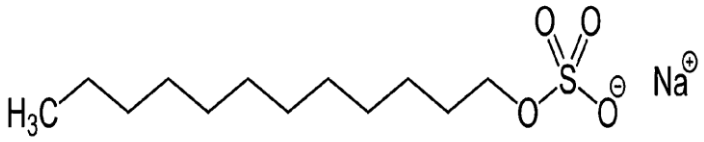

(b) Tween-80

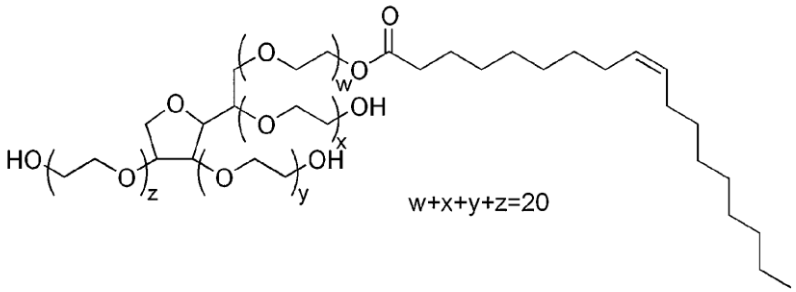

(c) Triton X-100

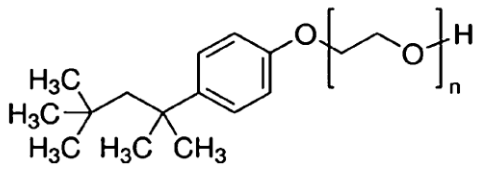

Figure 10. Anionic surfactants [28].

Furthermore, Singh et al.'s study showed that by adding 2 g of polar surfactant SDS at 130 ºC, the average size and diameter obtained were approximately between 40 and 625 nm with a nanorod shape and an aspect ratio of about 13:15. Increasing the concentration of SDS at 130 ºC led to two shapes – morphology nanowires and cemented nanorods. The influence of increasing the temperature to 180 ºC using 2 g of SDS led to coupled nanorods only. On the other hand, adding 2 g from the nonpolar surfactant ZnO-Tween 80 at 130 ºC caused the formation of self-assembling nanoparticles.

Using 4 g of the nonpolar surfactant, TEM revealed the formation of a spherical shape with an average size of 160 nm. Furthermore, the results confirmed the increased crystallinity area with

an increased concentration of Tween 80 at 4 g. A temperature increase from 130° to 180° with the addition of 2 g of Tween 80 led to the creation of a hexagonal structure. Using 2 g of Triton X-100 at 130 ºC led to the aggregation of particles with a spherical shape. In the case of using 4 g at 130 ºC, the agglomerated nanoparticles disappeared with a spherical shape and size of 8 nm. Nevertheless, by increasing the temperature to 180 °C, a huge hexagonal nanostructure was obtained at 40 nm [28].

ZnO is a semiconductor belonging to the II–VI group, which has properties similar to gallium nitride (GaN). ZnO is considered to be at the forefront due to its binding energy, which is greater than that of GaN at ambient temperatures. This gives it an excellent radiative recombination effect for natural emissions, along with

1. A large energy gap (3.37 eV)
2. High ability to create a perfect single crystalline form
3. Production of a high level of diffusion
4. High-quality electrical conductivity [28, 29, 39, 41]

Growth along the c-axis is known to be dominant due to growth stability. However, due to the strong polarisation of the c-axis, electron hole separation to semi- and non-polar faces is known to be a serious problem for the material layer. 1100) is an m-plane, while $\{11\bar{2}0\}$ is a family of planes containing equal numbers of Ga and N; the charge is the natural layer. It is important to note that—according to the presence of adjacent layers—this is caused by an increase in piezoelectric polarisation and, as a result, increasing charge separation. The morphology of ZnO as a wurtzite crystal has a negative plane—due to the presence of O^{2-} ions—and stacked mutually positive panels (Zn^{2+} ions) that are virtually all found along the c-axis (0001) plane. As a result, the (0001) facet is considered a polar plane with the presence of non-polar planes, such as m (for example, plane $(10\bar{1}0)$) and plane $(11\bar{2}0)$, as well as semi-polar planes, such as $(10\bar{1}1)$. It should be taken into account that this kind of structure is a non-inversion symmetry,

causing different equivalents between the two polar planes – the positive direction [0001] and the negative direction [000$\bar{1}$] [42].

In general, ZnO has three well-known shapes – wurtzite, rock salt and ZnO blende. From a thermodynamic view, the wurtzite ZnO shape is more stable than the rock salt and ZnO blend at ambient temperatures. Due to its non-symmetrical structure, ZnO has piezoelectric and pyroelectric properties. Regarding the electrical field of the nanoparticle for ZnO, wurtzite ZnO has an asymmetrical centre because of the presence of the C^4_{6V} or P63ms group [43]. Hexagonal wurtzite has lattice limitation parameter values of c = 0.52065 nm and a = 0.3296 nm. The planes in this structure consist of tetrahedral coordination, whereas Zn^{2+} ions and O^{2-} anions are stacked in an alternating pattern along the polar axis (c-axis). The nature of this structure (tetrahedral coordination) results in pyroelectric and piezoelectric properties due to non-inversion symmetry. In addition, ZnO has a polar surface attributed to (0001) [43]. The polar plane has partially positive terminal zinc and other negative lattice sites. These causes a regular dipole moment, reinforcing the polarisation that occurs spontaneously along the polar c-axis, as well as the distinction observed in the overall surface energy. However—even knowing that polar planes exhibit a massive surface area—the polar surface in the ZnO crystal appears to be flat, steady and stable, with no reconstruction. The nonpolar facets m and a, likewise, have a lower surface energy than the polar facet [8].

ZnO involves numerous morphological structures. These morphologies could be managed by controlling the growth rates for rapid-growing directions: <2$\bar{1}\bar{1}$0> (± [$\bar{1}$2$\bar{1}$0], ± [2$\bar{1}\bar{1}$0], ± [$\bar{1}\bar{1}$20]); <01$\bar{1}$0 > (± [01$\bar{1}$0], ± [10$\bar{1}$0], ± [1$\bar{1}$00]) and ± [0001]. Every crystal plane has a specific kinetic parameter. Thus, after the initial step (nucleation), the process of growth is carried out in three dimensions. For example, a 1D nanowire or rod or nano or polar nanobelt, comprises an atypical common structure, in which the morphology tends to increase the set of planes {2$\bar{1}\bar{1}$0} and {01$\bar{1}$0} due to low energy [32, 41, 44].

In contrast, if the morphology is controlled by a polar surface, the growth structure is ongoing—even with planar defects. These planar defects and twins could appear parallel to the polar planes. Hence, determining dislocation is complex [43, 45–51] [8, 27, 52].

1.6 Factors affecting zinc oxide morphology

Several factors that affected the zinc oxide final morphology, and thus played an essential role in controlling nanocrystal morphology, have been highlighted in this section:

1.6.1 Ostwald ripening process

Ostwald ripening is a phenomenon that occurs in solid or liquid solutions. It relies on the fact that a large crystal is more stable than a smaller one, so the reprecipitation of the dissolved pieces is normal in this effect. The effect of Ostwald ripening on particles is illustrated in Figure 11.

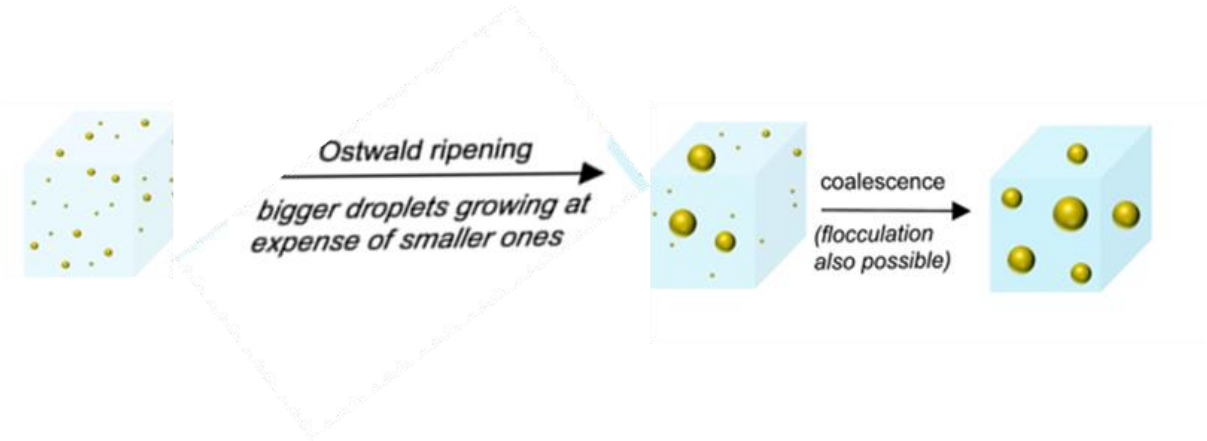

Figure 11. Effect of Ostwald ripening [53].

1.6.2 Oriented attachment

This effect includes the physical process alongside the chemical reactions that occur between ions and nanoparticles [54]. Oriented aggregation could involve oriented attachment and refers to the stage of mediated particle crystal growth in which the primary crystal changes to the secondary crystal via the aggregation process, as shown in Figure 12 [55].

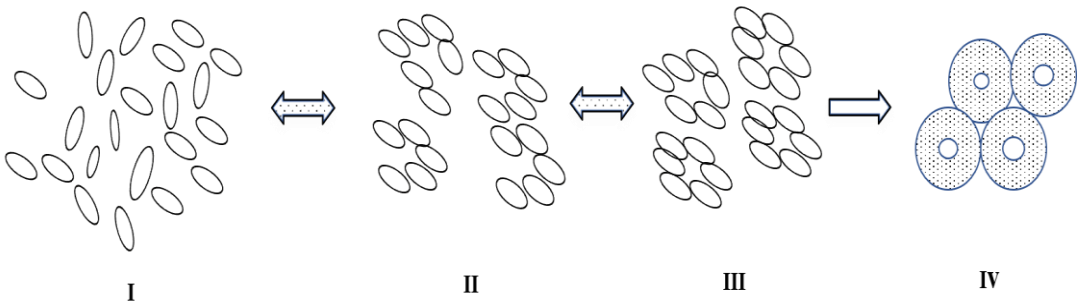

Figure 12. Schematic of the effect of oriented aggregation. Initial particles (I) were randomly distributed according to the effect of Brownian motion (II) to obtain crystallographic alignment (III) and ongoing crystal formation (IV) [55].

1.6.3 Nucleation

During nucleation, sufficient building units were required to arrive at a specific critical supersaturation value, which allowed the nucleation process to start. A short time was initially required to generate a very thin, narrow spread. This step was important—the concentration of supersaturation must be kept below the critical level to avoid extra nucleation.

1.6.4 Growth process

This stage was ongoing until the end of the 'reaction'. By increasing the time and in an equilibrium situation, nanoparticles continually complete their growth due to their high sensitivity. The distribution of the particles had a narrower orientation. Another suggestion was to stay constant during this process. Crystal growth is directed by thermodynamic properties, such as surface energies. The desired equilibrium morphologies were obtained from different facets according to surface energies [56, 57]. As mentioned before, zinc oxide is a non-centrosymmetric wurtzite hexagonal structure. Several factors could affect zinc oxide morphologies, such as the following:

- Internal and external factors, such as pH, solvents, precursors, temperature and time [32, 58–62]

- Interface–solvent interactions [63–65]
- Intrinsic crystal structure of ZnO [56, 66–69].

1.7 Zinc oxide crystals

Zinc oxide crystal formation occurred in an oriented manner, with consistent anisotropic growth. Zinc oxide crystals have a high tendency to aggregate due to the natural structure of the wurtzite hexagonal, which is known as a non-centrosymmetric structure. These results were in an affinity to form this shape, under the effect of orientation attachment along the [0001] and [000$\bar{1}$] or <002> polar direction, which was very active. To understand the nature of this morphology, it was important to know that the [0001] direction referred to polar faces that belong to Zn^{2+} and relied on the structure and electric polarity of ZnO crystals. Moreover, [0001] was considered the highest growth rate (see Figure 13), whereas [000$\bar{1}$] was the lowest growth rate. The other faces—such as ($\bar{1}$100), ($\bar{1}$0$\bar{1}$0), (1$\bar{1}$00) and (10$\bar{1}$0)—lay between these two in terms of growth rate under normal conditions [29].

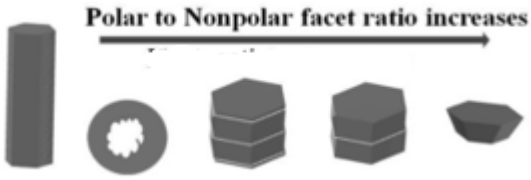

Figure 13. Morphologies, according to their transformation from the polar facet ratio to the nonpolar facet ratio, when increasing the ratio [70].

When the morphology comprised nano or microrods, the polar and high-energy planes followed the role ‘ABAB’ as a chemical structure that relied on changing the planes of the O^{2-} and Zn^{2+} ions [36]. The initial anisotropic structure units underwent an oriented attachment and generated a ZnO × fold (multiple cone superstructure). In the case of a three D-trapezoid shape, twin disc shapes in ZnO NPs were produced due to the effect of exposed polar planes (0001) and (000$\bar{1}$).

The pH and the concentrations of the precursor also played a crucial role in several morphology types, such as doughnuts, hemispheres, twin discs and ring trapezoids [71]. Fast growth is affected by oriented aggregation, whereas slow growth decreases defective spots and, in the case of nonclassical crystallisation, leads to 2D stacking faults or defects. Thus, the growth rate could contribute to the type and rate of defect formation.

Three routes have been suggested to explain the behaviour of nanoparticles as 3D self-organisation into a medium structure or mesocrystal (3D):

- Nanoparticle arrangement, which is subject to the magnetic or electrical field, or both [72–74]

- Epitaxial growth, which could affect the creation of a mineral bridge [75]

- Spatial restriction, known as an entropy driven, and a mineral bridge [36]

The current study highlighted the following to further understand the electrical field of ZnO NPs: due to the C^4_{6V} or P63ms space group (an expression of a symmetry group that shows how the atoms have a repeating pattern in three dimensions), wurtzite ZnO had an asymmetrical centre. The usual hexagonal structure consists of two of the same hexagonal substructures, merged and closely packed, with respect to the three-fold c-axis. The planes were distributed around the c-axis to form a tetrahedral shape. This structure was non-symmetric, so ZnO had piezoelectricity properties [9], [25].

P63mc, as a space group, was the basis of piezoelectricity in some semiconductors, such as zinc oxide. The orientation was aligned towards the c-axis among the layers. Macroscopic polarity was encouraged in cases where there were no affected external fields as a result of strain-reinforced polarity. A strain-reinforced polarity ($\bar{\boldsymbol{P}}$) creates electric fields ($\bar{\boldsymbol{E}}$) or

Shift field vector ($\bar{\boldsymbol{D}}$) that = $k\bar{\boldsymbol{E}}_0 + 4\pi\bar{\boldsymbol{P}}$. (16) [44]

Such that $k = 1 + 4\pi\eta$, η is the capability. (17)

Nevertheless, $\bar{P}$ value = tanh ($\Delta\bar{E}I$ 2k_BT), (18)

$\Delta\bar{E}$ could be presented by $\Delta\bar{E} = g\mu_B\bar{B}$ (19) [44] [36].

Accordingly, all of these factors were important in overcoming the presence of excitation properties in this kind of structure (wurtzite substructure). For zinc oxide, three factors of piezoelectric strain are important:

$d_{15} = -10\times10^{-12}$, $d_{31} = -5\times10^{-12}$ and $d_{33} = 12\times10^{-12}$ (20) [44].

The mesocrystals and complex superstructures that had been formed underwent orientation aggregation from 0D to 1D and from 1D to 3D [44]. All previous morphology was under the aggregation process – dot to rod to cone to multiple cone (Figure 14). The best process for controlling multiple cones is the stirring and sonication step [36].

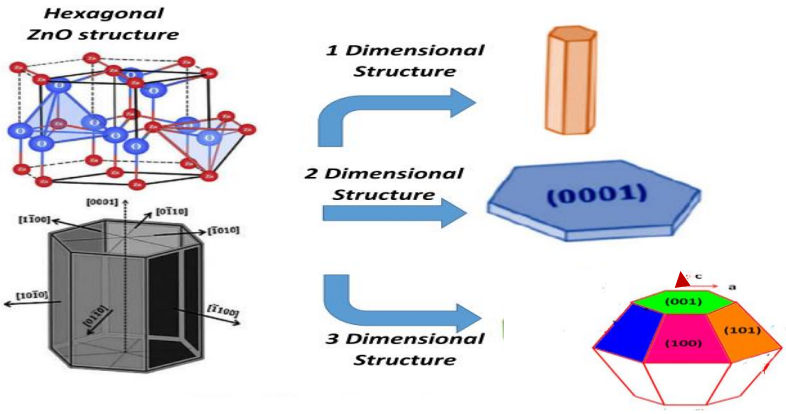

Figure 14. Diagram illustrating that 1D, 2D and 3D could be obtained from a hexagonal shape [76].

Orientation attachment usually occurred in the reaction during the initial stage of the growth process for the crystal—that was, when the parameter for the crystal was between 2–10 nm—taking into account the Brownian motion effect. According to Liu et al. [54], the temperature was important in order to achieve orientation attachment due to the energy that could provide

Brownian motion. In addition, in the initial growth, when a single monocrystalline zinc oxide was formed, the ability for oriented aggregation could occur due to the high surface energy and the high surface-to-volume ratio.

The final result of the crystal's morphology was similar to that of the zinc resource (precursor particles) when oriented attachment occurred [54].

This 3D morphology started in the growth from a 0D (dots) ZnO non-symmetrical structure to a 3D symmetrical structure with another term, mono- to x-fold symmetries (x varying from 2 to 8)—under the effect of the oriented attachment of the initial building block (anisotropic unit).

From a thermodynamic view, the wurtzite ZnO shape was more stable than a rock salt and ZnO blend at ambient temperature (Figure 15).

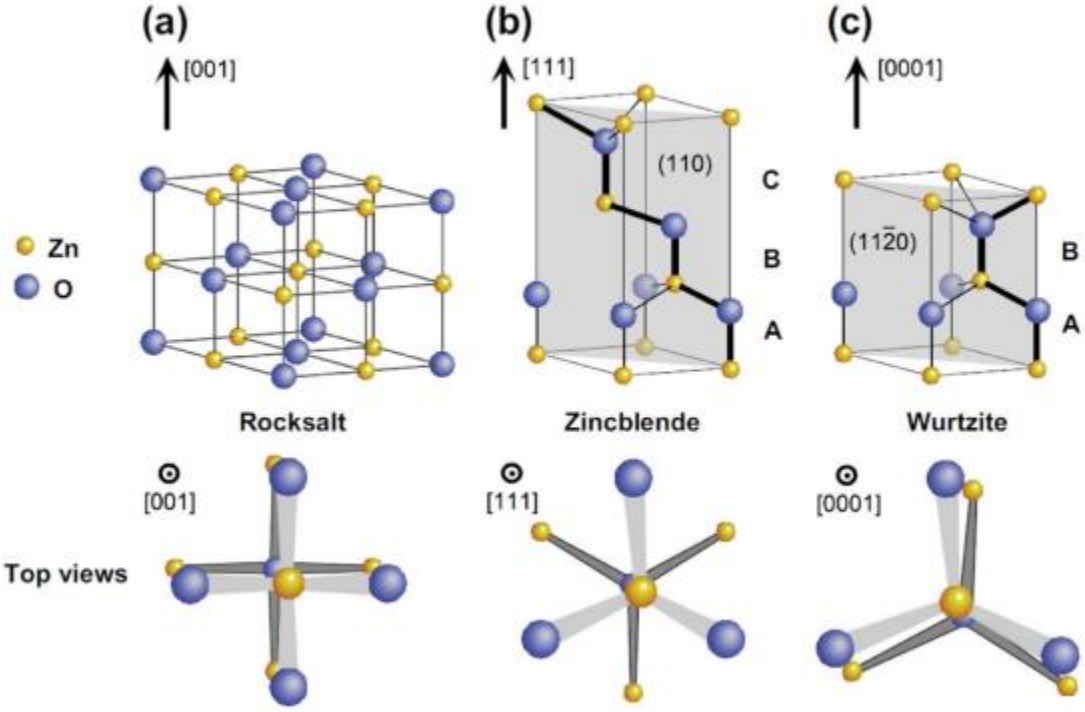

Figure 15. ZnO type structures: (a) rock salt structure, (b) zincblende type and (c) hexagonal wurtzite [46, 77].

This stability was the result of a distinct spatiality, especially towards an ionic curve (Figure 16), which was located between ionic and covalent material as tetragonal coordinated substructure ionic semiconductors. Figure 16 describes the energy of stacking defects or faults and Phillip's ionicity (f_1) as a function of the c/a ratio. These stacking faults were usually a result of tensile strain and compression coming together in parallel with an imbalanced interface between these material systems. As shown in Figure 16, the great value in the c/a ratio led to a decreased value of stacking fault energy (SFE) as well as a lower value with ionicity. In addition, zinc oxide wurtzite hexagonal morphology had an asymmetrical structure due to the presence of a P63mc or C^4_{6V} space group, as mentioned in (1.7 Zinc oxide crystals), which was considered the basis of piezoelectricity in the zinc oxide substructure [78].

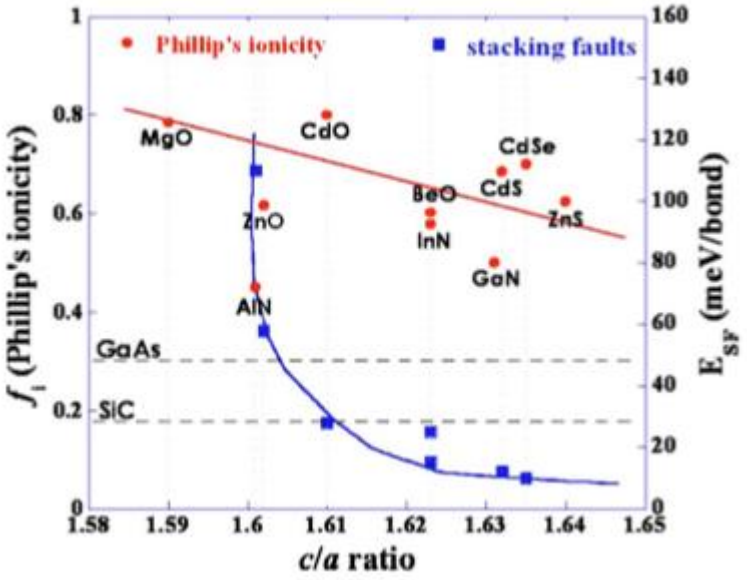

Figure 16. Relationship between Phillip's ionicity (ESF) in common semiconducting materials (group II-Oxide) II–O and II–VI materials as a function of the c/a ratio of the crystals [78] [79].

1.8 Effects of synthesis parameters on the morphology of ZnO nanoparticles

Some studies have found that variations in the parameters of zinc oxide synthesis, such as precursors, temperature, concentrations, surfactants, pH, solvents, reaction times and calcination temperatures, affect the final crystal morphology [80, 81].

In terms of the various zinc sources (zinc nitrate, zinc sulphate and zinc acetate) used for photocatalytic purposes, microsphere morphology was found to be a common structure, with nanosheets covering some species and nanoparticles when applied at 2.45 GHz and 650 W in the microwave method. The zinc salts were zinc sulphate and nitrate. Zinc acetate produced a micro-flower particle and nanosheet structure. Furthermore, the change in morphologies resulted in various effects on the photocatalysts. Zinc oxide produced from zinc nitrate salt showed better photocatalytic degradation with 93% degradation compared to zinc oxide produced from zinc sulphate (64.66%) and acetate (82.35%) [82].

In addition, when zinc acetate dihydrate was used as a precursor, the produced morphology took on a flower-like shape, even when different surfactants, solvents and methods were used [27, 80, 83].

When zinc nitrate was used as a zinc source and hexamethylenetetramine (HMTA), the suggested reactions were as follows:

$Zn(NO)_3 \rightarrow Zn^{2+} + 2NO_3^-$ (1)

$(CH_2)_6N_4 + 6H_2O \rightarrow 6HCHO + NH_3$ (2)

$NH_3 + H_2O \leftrightarrow NH_4^+ + OH^-$ (3)

$Zn^{2+} + 2OH^- \rightarrow ZnO_{(s)} + H_2O$ (4)

During the reaction, HMTA decomposed into ammonia and formaldehyde. Based on Equation 4, the reaction was expected to form intermediate-phase $Zn(OH)_2$; however, according to Guillemin et al. [42], the formation of zinc is still the most dominant view adopted by researchers [42].

HMTA acted as a weak base in the reaction; therefore, an increase in pH led to a decrease in hydrolysis. In addition, HMTA can cap vertically from sidewalls, which involve the m-planes of the zinc oxide nanowire, through the effect of surface adsorption [42]. However, from a thermodynamic view, when the reaction arrives at the equilibrium growth state, the system's energy tends to be minimised. Accordingly, a high-energy surface (polar plane along the c-axis) can possibly form a nanowire top facet, while the surface energy generated from nonpolar (m-planes) could form nanowire sidewalls [42].

Zhang et al. investigated the synthesis of morphology-controlled zinc oxide nanoparticles and produced bullets, nanorods and triangular shapes by controlling the molar ratio of amine to zinc acetate [84].

It is suggested that amine has the ability to act as a mediator when nucleophilic attack steps occur. Amine acts as both a capping agent and an attacking agent. In addition, changing the molar ratio affected the final morphology of ZnO nanocrystals. Nanorods were formed as a result of a molar ratio of 1:2 (amine-to-zinc acetate) and triangular morphology when the ratios were increased by about 4 mmol. Table 3 and Figure 17 illustrate the conditions used to obtain different zinc oxide morphologies according to molar ratios [84].

Table 3. Effect of molar ratios on zinc oxide morphologies.

Amine	Amine-to-zinc acetate ratio	Reaction time (minutes)	T (°C)	Size (nm)	Morphology

OLA	1	20	240	D = 22, L = 500–2000	Nanorods
OLA	2	20	240	D = 51, L = 100–200	Bullet-like crystal
OLA	4	20	240	Dimension was not recorded, L = 85–97	Prisms
DOA	2	20	240	D = 26–30, L = 500–1500	Nanowires

Note: OLA = oleylamine, DOA = dioctylamine.

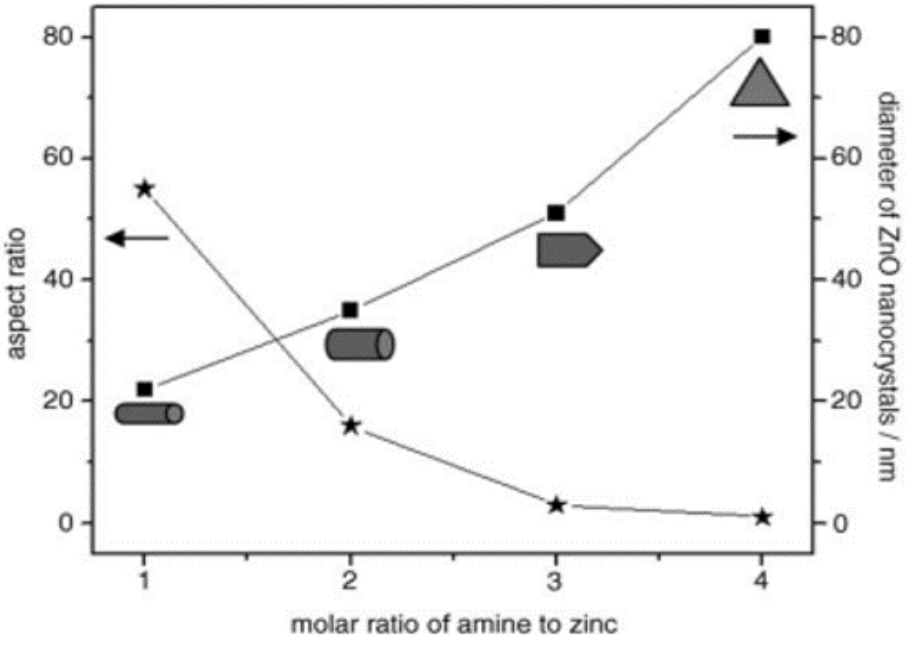

Figure 17. Scheme illustrating the effect of the aspect ratio of OLA to zinc acetate on the final diameter and morphology of zinc oxide nanostructures [84].

Yuan et al. found that increasing the room temperature to 40 °C led to an increase in the particle radius of zinc oxide nanocrystals to approximately 5.23 nm via the Ostwald ripening effect as a result of the increasing presence of thermal energy. In addition, increasing the growth temperature caused an increase in the nanoparticle diameter. As a result, the number of small

particles began to decrease until they eventually disappeared due to the growth process that supplements large particle formation [81].

Nonpolar solvents, such as ethanol and methanol, can also control the mechanism of these reactions. These kinds of solvents could aid researchers in selecting the different faces of zinc oxide crystals during the synthesis process, which can lead to variations in crystal growth [85].

The solvents involved in the use of different carbon chains, from ethanol to hexanol, affect the growth behaviour of zinc oxide particles. A relationship between the molecular weight of solvents and the time of the initial reaction and growth process was observed [27] .

Ludi and Niederberger stated that the efficiency of the interaction between solvents and particles on the surface, which results in an increase in surface energy, could be a reason for the weakness of solvents, which in turn lowers the efficiency of the interaction with surface particles [86]. On the other hand, Amin et al. found that when the pH values ranged from 8 to 12.5, common morphologies included urchin-like and flower-like shapes. In addition, when the pH for the solution was lower than 8 (about 8 to 4.5), the produced morphology was shaped like a rod and gradually reduced to wire-like nanoparticles [87].

Furthermore, different concentrations of the base play vital roles in the final particle structures and the sizes of concentrations of zinc acetate. However, there were conflicting results in many investigations, even when a high molar ratio between zinc acetate and sodium hydroxide was used [86].

1.9 Synthesis of ZnO nanostructures

Barhoum et al. mentioned that in the 19th century, the classification of ZnO nanoparticle synthesis fell into either the American process, called the direct method, or the French process, called the indirect method, in addition to the hydrometallurgical method that was developed to form ZnO particles [39]. Barhoum et al. determined that the calcination of ZnO nanoparticles occurred at 910 ºC during the indirect route in the French process, which led to the agglomeration of the particles. The size of the agglomerated particles was approximately 100 nm and a limited length of micrometres. The French process is usually followed by American and hydrometallurgical processes. Unfortunately, these methods work only in the lab and are not available in the industry [39].

Recently, various efforts have been made to synthesise and prepare ZnO NPs to decrease the cost of nanoparticles and improve the processing approaches by controlling shapes and particle sizes through, for example, the hydrothermal method, solvothermal method, microemulsions, chemical vapour deposition, the direct precipitation method, the electrochemical method, the thermal decomposition method, the laser ablation technique and the sol–gel method. All these methods need to be done in sequenced steps with specific equipment, such as lasers, microwaves or vacuum chambers. Some agents cause complications due to high temperatures or vacuum environments, including poor dispersion, impurity and the breakdown of the product in the last step. Every method allows opportunities to obtain the desired structure [28, 29, 39]. In precipitation methods, there are important parameters, such as precipitation time, pH and temperature. In the case of precipitation in aqueous solutions, controlling the concentration of the reagent, as well as the rate of adding the material, is important [8]. With this method, the calcination temperature has a crucial effect on reducing the band gap of ZnO [88].

1.9.1 Sol–gel method

The most well-known processing route and one largely used by scientists is the sol–gel method due to its reliability, low cost, simplicity, repeatability and environmental friendliness. According to the variation in ZnO morphologies, some scientists state that vital changes had affected the final results because of specific criteria subject to the treatment parameters, such as reaction time, calcination temperature and molar ratio [28].

ZnO nanoparticles were synthesised via the sol–gel method by utilising zinc sulphate hepta hydrate ($ZnSO_4 \cdot 7H_2O$) and sodium hydroxide (NaOH) with ratios of 1:1, 1:2 and 1:3. NaOH was added dropwise to the three solutions with continuous stirring to create varied reaction mixtures. After a creamy white colloid was obtained, gels formed. The next step was the drying process in an oven at about 100 ºC. Agate mortar was used to grind the precursor to fine powder. In the last step, calcination for two hours yielded ZnO nanoparticles [29].

The previous reaction was as follows:

$ZnSO_4 \cdot 7H_2O + 2NaOH + H_2O \rightarrow Zn(OH)_2 + Na_2SO_{4\,(aq)} + 8H_2O$ (5).

$Zn(OH)_2 \rightarrow ZnO + H_2O$ (6) [89].

The methods that have been used to synthesise ZnO nanoparticles consist of four dissimilar phases – hydrolysis, polymerisation, dissolution and conversion into ZnO. Adding ethanol (C_2H_5OH) to zinc acetate dihydrate $Zn(CH_3CO_2)_2.2H_2O$ is an important step in eliminating acetate ions from the colloidal gel solution of the resulting zinc hydroxide ($Zn(OH)_2$). To obtain ZnO nanoparticles, methanol is easily able to form a white, high-molecular polymer to form a gel instead of a sol by rapid polymerisation. $Zn(OH)_2$ divides cation Zn^{2+} and hydroxide as anion OH^-, and after polymerisation, ZnO nanoparticles are obtained. In this method, surface morphology, such as via scanning electron microscopy (SEM), confirms that the shape is spherical nanoparticles with dimensions between approximately 100 and 200 nm [90].

El-Naggar et al. used sodium alginate to avoid agglomeration in the alkali medium by adding sodium hydroxide. The affinity of synthesised SiO_2@ZnO-NPs nanoparticles towards reacting with cotton chains (glyosidic units) is increased due to using amino-propyltriethoxysilan and vinyl triethoxysilan. This method relies on adding distilled water as a solvent to the polymer and then mixing the resultant solution with sodium alginate and Zn $(NO_3)_2.4H_2O$. A zinc alginate complex is produced during the reaction. To avoid precipitation of the complex, it is necessary to activate sodium alginate by adding sodium hydroxide. The last step is slowly adding zinc nitrate to the final solution [91].

Environmentally friendly and green methods have been developed for the synthesis and preparation of nanomaterials. The efforts that have attracted the attention of scientists to manage crystal growth involve using fruit extracts and plants as capping and stabilising factors. Some studies have utilised lemon extraction and sucrose with a sol–gel technique to synthesise ZnO NPs. Lemon juice and sucrose are easily used in laboratories because the precursor is obtainable without the need for expensive equipment or specific treatments [91, 92].

1.9.2 Hydrothermal methods

In hydrothermal methods, there is no requirement to use organic solvents. Dissolving zinc acetate with distilled water and adding sodium hydroxide solution dropwise yielded

$Zn(CH_3COO)_2 + 2NaOH \rightarrow Tempreature \rightarrow ZnO + H_2O + 2(CH_3COONa)$ (1),

which was then stirred gently for 10 minutes at 90 °C. Adding a sodium lauryl sulphate solution as a surfactant to obtain ZnO particles avoids the influence of interaction forces and allows homogeneous dispersion between particles. For hydrothermal treatment, a mixer is placed into an autoclave made of stainless steel, after which deionised water is added to approximately 80% of the autoclave at 120°C for five hours. The next step is to allow a natural cooling process

[93]. With hydrothermal methods, increasing the time in the autoclave increases the size of the ZnO NPs [8].

The thermal decarbonation process of zinc carbonate hydroxide was utilised to synthesise several pure ZnO nanoparticles as photocatalysts. However, the use of ZnO as a photocatalytic faced an obstacle: the band of absorption of ZnO was placed in a UV range, and the amount of emitted solar energy in this range was only 5%. It also faced some problems related to agglomeration.

The nanoparticles were prepared by controlling particle and crystallite sizes as well as morphology. The precursor ZnO photocatalytics had several sizes and shapes between 60 and 100 nm, with a nonporous rhombohedral nanostructure to the value of 5 ± 0.5 ml from porous particles.

The results showed that the porous ZnO nanoparticles were twice as active as photocatalysts when compared to the nonporous ZnO nanostructure when using a methanol solvent as an oxidation agent.

The surface-active spots caused by the decrease in the volume of recomposing particles could be attributed to accelerating the interfacial rate of the nonporous ZnO charge transfer. As a result, among nonporous ZnO nanoparticles, zinc chloride ethanol (Z-EtH), zinc chloride polyacrylic acid salt (Z-PAC) and zinc chloride polyvinyl pyrrolidone (Z-PVP) (see Figure 18) showed the best behaviour as photocatalysts in the case of methanol oxidation. On the other hand, javelin-shaped Z-PACs have a huge surface area and higher photocatalytic activity than the rhombohedral shape of ethanol (Z-Eth) nanoparticles [39].

The challenges in controlling the preferred shape during syntheses are confined. Particle shape is affected by the type of precursor used [43]. Thus, in some cases—especially in the hydrothermal method—using sodium hydroxide and zinc precursors in the presence of organic template agents can play a vital role in changing morphology. For example, during

the synthesis of ZnO, increasing the temperature changes the shape of the particles from rod-like to polyhedral [94, 95].

Controlling the morphologies and crystallisation of ZnO to achieve distinct properties, such as electrical, optical, antimicrobial and photocatalytic properties, is a promising future technology in several fields.

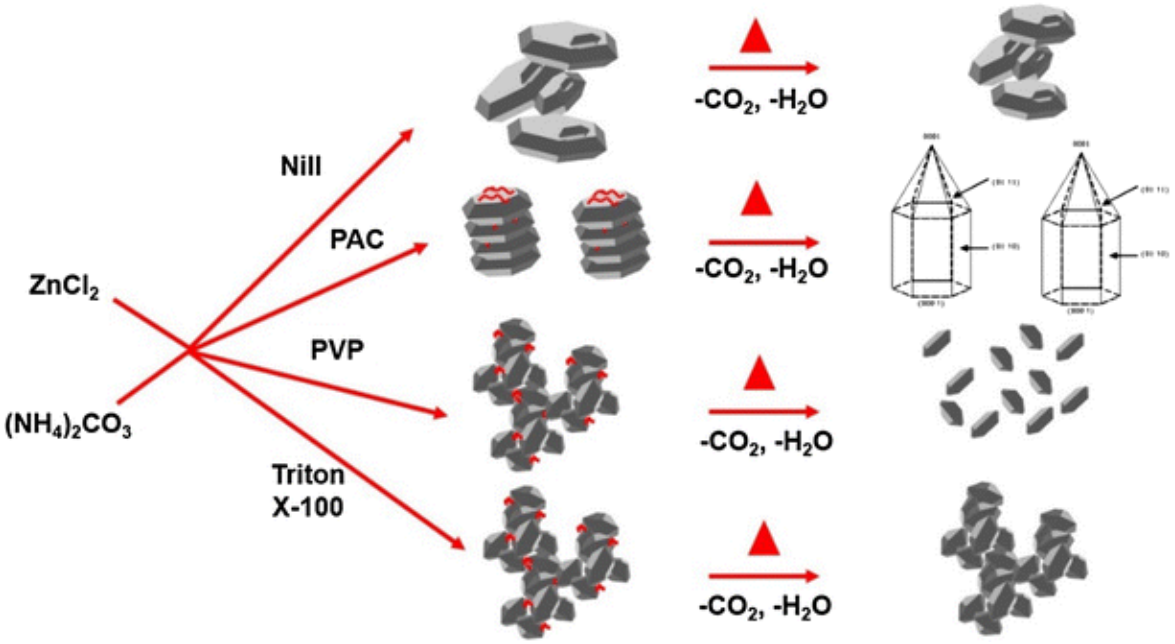

Figure 18. Illustration of the thermal decomposition of changing morphology and the formation of nonporous ZnO nanoparticles and porous micronised particles [39].

1.9.3 Direct precipitation method

ZnO was prepared as nanorods by Mostafaei et al. by dissolving about 14.87 gm of Zn $(NO_3)_2.6H_2O$ with 4 g of NaOH in H_2O to form 100 ml of Zn = 0.5 mol/L and OH^- = 1M of solution [7]. The solution was then heated to 70 ºC, and the next step was stirring at a rate of 500 rpm, adding zinc nitrate dropwise for a half hour. The obvious reaction required about 100 min. At the end, the solution converts to a white precipitate. After washing the precipitate several times with distilled water and ethanol, centrifugation was performed before dehydration in an oven at 100 ºC. This process led to the formation of ZnO nanorods [7].

Moghri et al. determined that the precipitation process to form ZnO NPs from zinc acetate dihydrate in the presence of sodium hydroxide has several advantages due to its low cost, thereby offering a wide range of production, decreasing the temperature needed and requiring few instruments or catalysts to add to the synthesis of ZnO nanoparticles [96].

In this method, ZnO NPs were synthesised using the direct precipitation method at ambient temperatures. This method allows several useful features, such as producing a large number of ZnO NPs that can be obtained simply, at low cost and with precursors of high purity. The previous solution was added to distilled deionised water as a solvent. After obtaining the required concentration of the obvious solution, zinc acetate was slowly added dropwise to the alkali medium sodium hydroxide and stirred at ambient temperature. In this method, the ratios of zinc acetate dehydrate to NaOH were 1:1, 1:2, 1:3 and 1:4. The observed reaction was very slow, and at the end, white precipitates of ZnO particles were obtained. Separation of the composed precipitates by washing with distilled, deionised water and an organic solvent, such as methanol, was the next step. For drying, an electric oven was used for five hours at 100 ºC. Finally, ZnO precursors were calcinated at 250 ºC for about three hours (see Figure 19).

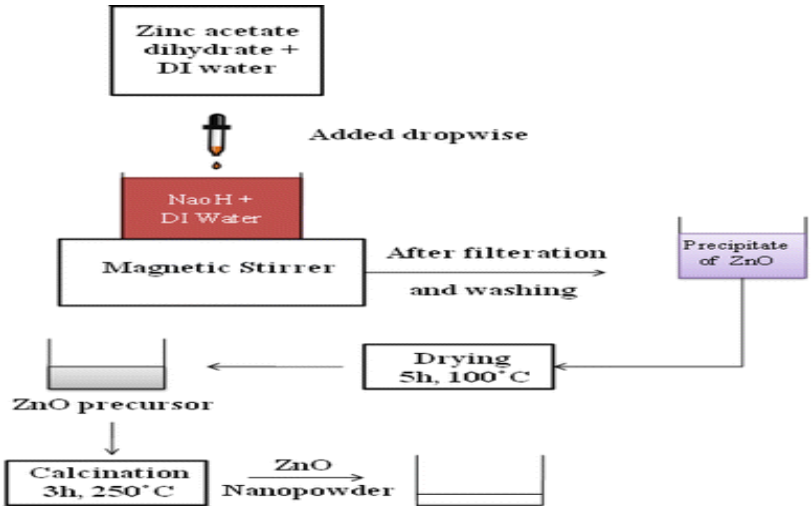

Figure 19. Graphic diagram illustrating the synthesis of ZnO nanoparticles [96].

This study revealed the effect of changing the concentration of the reactant on the morphology of ZnO nanoparticles. In cases for which the concentration ratio was 1:1, the size obtained was

18 nm with a spherical shape. Increasing the concentration ratio from 1:1 to 1:4 led to an increase in the average size of ZnO NPs from 20 to 36 nm. The morphology was also affected by the concentration of the reactant, since SEM revealed that several kinds of shapes can be obtained, such as spherical, irregular clusters and cauliflower shapes [96].

Another preparation is using ZnO in the form of ZnO seeds, which are prepared by adding 0.02 mol/L of zinc acetate in methanol (CH_3 OH) as a solvent to the heated solution until a temperature of 50 ºC is reached while gently stirring to obtain a dissolved zinc acetate solution. Next, 0.03 mol/L of sodium hydroxide (NaOH) is added to the previous solution, and then the solution with the ZnO seeds is added, which can be formed after heating the solution at 58 °C for an hour [97].

1.9.4 Sonochemical methods

Sonochemical synthesis and the characterisation of a nano-sized zinc (II) coordination complex are precursors for the preparation of pure-phase zinc (II) oxide nanoparticles. In this study, ZnO nanoparticles of the complex compound Znic ion with a 2,9-dimethyl-1,10-phenanthroline ligand with two iodine atoms Zn(dmph)I_2] 1 were synthesised by a sonochemical approach after adding zinc acetate, KI potassium iodide and neocuproine (ligand) to methanol as a solvent. Calcination at 600 °C was then performed to decompose Zn(dmph)I_2] 1 into nanoparticles with a size of about 31 nm, and the shape was a distorted tetrahedral structure with four coordinated Zn (II) ions. Table 4 briefly illustrates the different zinc oxide synthesis methods [98].

Table 4. Synthesis methods of ZnO nanoparticles.

Methods	Size	Shape	Synthesis conditions	Reference
Direct precipitation method followed by thermal decarbonation	20.0 nm	Spherical	(1.5) M of $Zn(NO_3)_2$ $6H_2O$, (2.25) M of $(NH_4)_2CO_3$, ethanol, and deionised water Stirring for 60 min at 40 °C	[99]
Ultrasonic irradiation	L: ≈1 μm, D: ~160 nm	Hexagonal wurtzite structure, nanorod and nanowire shapes	$Zn(NO_3)_2$, deionised water, HMT (hexamethylenetetramine) Ultrasonic irradiation: 30 min at 80 °C. Drying: 2h at 60 °C.	[8]
Precipitation process	40 nm	Spherical	$ZnSO_4$, NH_4HCO_3, ethanol Drying overnight at 100 °C. 300–500 °C.	[8]
Precipitation process	40 nm	Spherical	Zn $(NO_3)_2$, NaOH Synthesis: 2 h Drying: 2 h at 100°C.	[100]
Precipitation process	D:15–25 nm, BET: 50–70 m^2/g)	Hexagonal wurtzite structure, flower-like and rod-like shapes	Micronised ZnO powder, NH_4HCO_3 Reaction: ≈ 2 h, 25 °C Drying: 80 °C Calcination: 1 h at 350 °C	[101]
Microwave techniques	D≈ 280 nm	Hexagonal wurtzite structure, nanorod and nanowire shapes	Zn $(NO_3)_2$, deionised water, HMT (hexamethylenetetramine) Microwave heating: 90 °C for 2 min Drying: 2 h at 60 °C.	[8]
Sol–gel method	83 ± 7 nm		($ZnSO_4$&H_2O) and sodium hydroxide (NaOH) Stirring, drying in oven at about 100 ºC, calcination for 2 h	[29]
Sol–gel method	Between 100 and 200 nm	Spherical	(C_2H_5OH), zinc acetate dehydrate ($C_4H_{10}O_6Zn$)	[90]

Hydrothermal methods	_	_	$Zn(CH3COO)_{2,}$ NaOH, stirring 10 min at 90 °C, adding sodium lauryl sulphate solution and deionised water up to approximately 80% of the autoclave at 120°C for 5 h	[93]
Direct precipitation method	18 nm	Spherical shape for 1:1 (Zinc acetate dihydrate: NaOH)	Zinc acetate dehydrate, NaO, distilled deionised water, stirring at ambient temperature, methanol, drying using electric oven for 5 h at 100 ºC, calcination at 250 ºC for about 3 h	[96]

1.10 Epoxy-based composites in coating

Low-molecular-weight pre-polymers with more than one epoxide group are known as epoxy resins. Parimalam et al. discovered epoxy resins in 1909. They have developed into well-known and popular polymeric materials in several sectors. The versatility of epoxy resins is a result of the oxirane ring's capacity to react with a range of substrates. Due to its powerful ability to act as a barrier and shield against corrosion, coating is one of this polymer's key applications. Once they have reacted with the curing agent during the curing reaction, they are insoluble and unbreakable thermoset polymers [102, 103].

Naturally, this product can be obtained from the reaction between two sources, epoxy resin and a hardener, which is known as a curing agent. Crosslinking polymers do not have the ability to be reshaped or remelted due to the nature of crosslinking, which consists of irreversible covalent network bonds. However, because of this, epoxy is a thermosetting polymer with a 3D crosslinking structure and a strong bond, which provides unique properties. It has been used as an attractive material in different chemical, physical and mechanical applications, such as adhesives, electronic packaging, coating and composite materials [104].

Epoxy resin, also called polyoxide, is classified as a thermosetting polymer. It has significant mechanical properties, such as a large cohesive force, good adhesive performance due to a large number of polar groups, chemical resistance, exceptional adhesion and excellent electrical insulation. Epoxy resin has great chemical and physical resistance because of its good stability and mechanical properties as a coating. Epoxy-based composites have distinct properties for their usage, such as high compressive and tensile strength, thermal stability, corrosion resistance and respectable dielectric properties.

However, epoxy resin has poor thermal properties towards electrical resistance and difficulty making thin layers due to its classification as a thermosetting polymer and its high viscosity. In addition, prior research has revealed that while the characteristics of epoxy coatings have

marginally improved, phase separation between the organic and inorganic fillers is still present in composite coatings, which remains their largest disadvantage. For the purposes of enhancing resin characteristics and preventing phase separation between epoxies and fillers, epoxy coatings have recently begun to use nanotechnology. In addition to reducing the composite material's phase separation issue, nanotechnology has extended the region where organic and inorganic materials can interact with one another [102].

The present high demand for epoxy resin for industrial, chemical and electrical applications has produced a desire to optimise and improve epoxy resin by adding inorganic nanoparticles such as ZnO into epoxies.

In addition, epoxy-based composites have the potential ability to be a distinct material for producing automobile parts, electric cables and turbine blade bushings. Recently, with further improvement in epoxy-based composites' mechanical, physical and chemical properties, the concept of using nanofillers in a matrix proves the efficiency of nanocomposites in producing multifunctional nanofillers. Many studies have found that most of the thermal, electrical, mechanical and resistance properties against corrosive agents can be reinforced by adding inorganic nanoparticles to an epoxy matrix. To study the effect of inorganic and organic nanoparticles with an epoxy matrix, it is important to understand the interfacial interaction between nanoparticles and the polymer chains to obtain a good nanocomposite. Moreover, several factors have to be taken into account to use the epoxy resin with nanoparticles, such as shape, size, type, aspect ratio and the dispersion of nanoparticles in the epoxy matrix [105, 106].

Several nanoparticles used as nanofillers, such as SiO_2, ZrO_2, carbon nanofiller and titanium oxide, have been found to improve the thermal properties of these nanoparticles as nanofillers with polymers to obtain the perfect composite. However, due to the inability of these nanoparticles to disperse, their processing difficulties are obstacles to their usage in

nanocomposites, in addition to when nanofillers have high densities, such as with carbon nanofillers.

Recently, limited research has determined the distinct role of ZnO nanoparticles as nanofillers in reinforcing the properties of epoxy nanocomposites. The varieties of sizes and shapes of ZnO nanofillers have the ability to extend their usage to cover coated composite structures [39]. Additionally, epoxy coatings have good adhesive properties, durability, toughness, formulation latitude and chemical resistance; however, due to some restrictions, such as being unsuitable for acid resistance, being brittle and having poor heat-resistance properties, they are not suitable for high-performance applications. To enhance the quality of resins, researchers have developed composite materials. Based on van der Waals force, the interfacial force between the resin and fillers increases the characteristics of the resin, such as high resistance towards chemical corrosive ions, heat resistance and adhesion properties [103].

Many studies have demonstrated that the incorporation of nanoparticles into an epoxy matrix to form nanocomposite coatings can enhance the corrosion resistance of epoxy coatings. Samad et al. showed that the effect of ZnO, SiO_2 and ZrO_2, in small quantities, as nanoparticles on epoxy coatings could enhance their corrosion resistance properties. ZrO_2 showed significant improvement compared with the other nanoparticles [107].

Surface charge growth is an important factor that strongly affects the electrical properties of some polymers, such as epoxy resin. Han et al.'s study showed the effect of adding ZnO NPs into epoxy resin. The weight percentages used were 0, 1, 3, 7 and 10. The aim of this study was to understand the effect of these percentages on cases of charge accumulating on the surface and surface potential decay (SPD). SPD calculations have been made under the effect of a corona negative charge. The study showed that the decay rate was affected by filler loading and the interfacial reaction of ZnO nanoparticles during the dispersion process [108].

SPD measurement is usually used to describe the surface charge performance for insulating material. Some of its applications include carrier mobility evaluation and conductivity blocking under suitable conditions. In general, the decay rate in the case of neat epoxy has a large value compared with epoxy nanocomposite due to the crucial role of these nanoparticles, which act as inhibitors against the dispersion of surface accumulation charges. Nanoparticles such as zinc oxide and silicon carbide can contribute to a decrease in charge accumulation through their use as fillers to prepare nonlinear resistive composites [108].

Mostafaei and Nasirpouri demonstrated the use of conducting polymers, such as poly aniline (PANI), with ZnO nanoparticles to form a PANI-ZnO nanocomposite using in situ chemical oxidative methods in epoxy coatings that are blended and utilised on carbon the steel grade ST37. This study showed that the ability of PANI-ZnO nanocomposite coatings increased corrosion resistance when compared with an epoxy-PANI coating and epoxy coating only. Epoxy zinc oxide EPZ nanocomposites could reduce the corrosion rate of steel substrates and work as corrosion inhibitors. Epoxy coated with PANI and ZnO nanorods showed degradation and delamination of the coating. This study proved that conducting a polymer-oxide nanocomposite produced a better natural barrier against corrosive agents due to the morphology of ZnO NPs with PANI, which has a flaky shape that works as a block structure for surface coatings. Moreover, the interfacial interaction between polyaniline and Zn^{2+} cations led to changing the formulation of polyaniline to form compact clusters and passive barriers on the metal/polymer [7].

This study revealed a comparison between ZnO-epoxy nanocomposites and micro composites in terms of their dielectric properties. Nanocomposites exhibit unique behaviour during filler loading and obtain a clearly decreased value of tanδ (dielectric loss measured a dielectric substantial's inherent dispersion of electromagnetic energy, such as heat, which can be parameterised using the tangent of the loss angle (δ))[109] and permittivity. This is attributed

to the interfacial interaction between zinc oxide nanoparticles and the epoxy chains around the nanoparticles. The dielectric characterisations of the polymer-ZnO nanocomposite were mostly examined at nanoparticle (filler) loadings greater than or equal to 1%. On the other hand, when filler loadings of less than 1% were used, there was an improvement in dielectric properties due to a large surface area compared to volume [105]. In another study by Dagdag et al., they stated that the capacity of the diglycidyl ether of bis phenol A - dicyandiamide DGEBA-DAA-coating zinc phosphate's pigment (DGEBA-DAA-coating ZP's) increased as the exposure time increased up to 60 days; however, after the exposure time increased to 120 days, the coating capacity decreased, which was due to the saturation of zinc phosphate's pigment structure and a decline in the hydrophilic tendency of the material. Thus, two types of corrosion were obtained, where pits and pores were formed. The pitting corrosion began and spread at the sites of the pores and pits [110].

In addition, Ibrahim et al. [111] researched the corrosion resistance of 316L stainless steel (marine grade) covered by ZnO/epoxy. The corrosion tests were obtained using measurements with a potential dynamic polarisation technique. They found that the combination of epoxy and 3% zinc oxide nanostructures enhanced corrosion protection using dispersion for zinc oxide nanoparticles.

Moreover, Saidi et al. improved the zinc oxide film on Ti6Al4V sheets in their study, stating that potential and electrochemical deposition had a significant impact on the growth process of ZnO film and affected the morphologies and orientation [112]. Furthermore, Aboorvakani et al. [113] studied the effect of zinc oxide formed via a precipitation method using zinc acetate as a zinc resource on the covered mild steel corrosion resistance of ZnO/epoxy film with normal and low pH values [113].

1.11 Nanoparticles – polymer interfacial interaction

Nanofillers such as silica nanoparticles could offer distinct features related to surface modification. Nanoparticle surface modification plays a vital role in determining the degree of compatibility between a filler and a polymer, interfacial interaction/adhesion, dispersion quality, filler loading and interphase extent, which are important factors in reinforcing the mechanical, physical and chemical properties of polymer nanocomposites [114]. Interfacial interaction is a complex phenomenon at the nanosolid level. The main reason is the numerous interaction forces at the nanoscale level [115].

It is known that adding nanoparticles into a polymer matrix produces optimisation in the characterisation and functionalities of the resultant nanocomposite. Understanding the organisation and distribution of nanoparticles, as well as the effect of interactions between two nanoparticles, could help determine self-assembly in low-density particles. Moreover, to explain the influence of paired interactions as a colloid with a polymer solution, the approach of two nanoparticles that contact each other incites the surrounding polymer chains to be driven out of the empty area among the nanoparticles. This suggestion illustrates the influence of depletion interactions in colloidal particles [116].

Qi-lin and Xin's study showed the effect of involving nanofillers in a polymer matrix on interfacial interaction and mechanical characterisation. This study exhibits the role of nanofillers in improving the properties of nanocomposites using nanofillers such as carbon nanotube (CNT), graphane (GA) and graphene (GE). The polymer matrices used poly (methyl methacrylate) (PMMA), polyethylene (PE), polyvinyl chloride (PVC) and polytetrafluoroethylene (PTFE) using molecular dynamics simulations. Using the same mass density, GE-PE and CNT-PE, the resulting nanocomposite had the highest van der Waals force interaction energy and interfacial sheer strength. By increasing the diameter of the nanofiller CNT, the influence of CNT decreased accordingly. In addition, the effect of GE chirality was

not observed in the case of a GE nanocomposite [117]. Furthermore, the presence of zinc oxide with silica nanoparticles in the coating was unaffected by 5 M of NaCl, as shown by the bright white hue, demonstrating ZnO's resistance to NaCl coating [102].

The barrier property and electrical current inertness of polymeric nanocomposite coatings are only two of their many benefits. The corrosion resistance of organic coatings can be enhanced using nanocomposite coatings. More attention has also been paid to graphene and graphene oxide [118].

Adding a thin film of silica as a cover on a ZnO surface enhances the efficiency of dispersion, which reduces the agglomeration of nanoparticles. Furthermore, the crystalline structure of ZnO is minimised by a heterogeneous azeotrope (an immiscible substance usually found in the liquid state) of the zinc produced. As a result, it can avoid a huge area of aggregation and reduce particle size [8].

Singh et al. stated that rearranging ZnO as a polycrystalline and including tiny sub-crystals in the same orientation could cause a van der Waals interaction to form the driving force that leads to aggregation [28].

A study of dynamic simulations of the grained roughness of the molecule is made to illustrate the processes of adsorption of bidisperse and monodisperse polymer chains on the surface of nanoparticles. He, L., Z. Dong, and L. Zhang's study involved the influence of the adsorption of the polymer chains on the interaction of NP/polymer chain interfaces, stiffness and chain length. The results showed the following:

- In the case of strong interfacial interaction between NPs and polymer chains, the long chains dominate interfacial zoom, while the short chains are expelled out of the region.
- For the semi-flexible chains, the NPs were warped by stiffness in a helical shape.
- Fully flexible chains represent the entire surrounding matrix.

Chain stiffness incited eclectic power for the adsorption behaviour of the interaction between NPs and the chain of polymer around. The reaction was affected by an accuracy competition between the enthalpy and entropy dynamic parameters and their contributions to energy.

The nanocomposite is defined as a combination of a polymer matrix with inclusions that have at least one dimension (i.e., length, thickness or width) in the nanometre range. The addition of nanoparticles to a polymer improves bulk material properties, such as mechanical, physical, thermal, chemical and electrical properties.

Most research studies cover how to control NP aggregation and dispersion across the polymer matrix. Theoretically, there are four types of polymer–nanomaterial organisations [119]:

1. Contact aggregation caused by depleting attraction
2. Segmental tight level of particle bridging
3. Strong stability because of thermodynamic stability
4. Telebridging, which occurs when different adsorbed layers exist with long-scale bridging

1.12 Anti-corrosion protection

In the nanotechnology field, there has been increasing interest in improving the appearance and properties of coatings, including their mechanical properties and resistance to corrosion and ultraviolet light. Over the past century, there has been a dramatic increase in the utilisation of numerous types of organic/inorganic particles to improve these properties.

However, these rapid changes are introducing problems such as poor adhesion, impact, abrasion and reduced coating flexibility. Nanotechnology is quickly becoming a key instrument in eliminating these issues due to nanoparticles' high surface areas and small sizes. This could lead to reducing some of the side effects of UV absorbers and their mechanical properties [1, 8].

A ZnO nanorod arrangement was fabricated with a thin film of titanium oxide nanoparticles used as a photoanode. Chou and Hsu investigated the effect of various high temperatures, such as 250 ºC, 350 ºC, 450 ºC and 550 ºC, on the efficiency of a ZnO nanorod layer using a solar cell. Electrochemical impedance spectroscopy (EIS) illustrates how high temperature affects the performance of the cell, especially at 550 ºC. This temperature could enhance and reinforce the interfacial interactions that optimise the growth of a ZnO nanorod collection by increasing the ability to form the crystallisation of a ZnO seed layer [97].

Aboozar et al. applied ZnO nanoparticles to polyester powder using a ball milling treatment to increase the corrosion resistance of the fabricated coating of C-steel against corrosive agents, such as H_2O and O_2 by applying an electrostatic machine. The fabricated nanocomposite polyester powder improved protection and enhanced mechanical properties. Using 0.5, 1 and 2 wt% from the synthesised ZnO-polyester nanocomposite, EIS was applied to the fabricated coating at different times for 90 days. The coated samples were immersed in 3.5% NaCl as an electrolyte containing chloride ions as corrosive agents. The study illustrated via SEM that the nanocomposite-coated samples did not contain cracked areas or defects. On the other hand, the polyester coatings without ZnO nanoparticles had several cracked areas and contained many defects in their structures. Moreover, EIS showed higher corrosion resistance for nanocomposite-fabricated coatings than for pure coatings. The EIS test results showed that applying 1 weight percentage yielded the best results for corrosion resistance, with a value of about 32,150,000 Ω cm^2, six times better than a pure coating. In addition, this study confirmed the high ability of ZnO nanoparticles to increase corrosion resistance and decrease the diffusion of NaCl as an electrolyte at 0.5%, representing a lower protection compared to 1% due to its partial coating. A concentration of 2% caused less protection against corrosion due to the agglomeration of nanoparticles [120]. Adding ZnO nanoparticles to a polymer improves resistance against scratched substrates better than a coating matrix [121].

Darvish et al. used zinc phosphate and zinc aluminium polyphosphate as anticorrosion pigments to study the performance of the interfacial interaction between nanoparticles and a polyurethane coating on cathodic behaviour. The pull-off test results clarified that at lambda 0.6, ZPA and ZP showed the most effective bonding strength, and ZPA showed the best interfacial interaction with the steel substrate. Darvish et al. imputed the precipitation of ZPA on polyurethane PU and the ability to control pH during coating [122]. As a pigment, zinc phosphate is significant because it inhibits the permeation of the electrolyte and reduces the hydrolysis process that affects the interfacial interaction in a polymer matrix.

Zinc yttria was selected and prepared as reinforcing particles to improve corrosion behaviour. Popoola et al. found that there are fine grains of zinc yttria deposit on steel surfaces that illustrate the role of the formulation of zinc yttria in improving corrosion resistance [123].

Moreover, zinc phosphate is most commonly used as a safe, non-toxic and anti-corrosive filler. The morphology of zinc phosphate, including its sheet-like shape and spherical microstructures, which have various practical uses, was found to be affected by factors, including the pH value during the synthesis process. Given the foregoing, the current study's objective is to develop an anti-corrosive coating form (DGEBA-DAA-ZP) for 15CDV6 steel that has been electrolytically treated with cadmium in a 3 wt% NaCl medium [110].

Fabricated coatings combining zinc, cobalt and TiO_2 are composited by electrodeposition. These fabricated coatings give distinctive interfacial interactions when titanium oxide reacts with the base particles. This leads to the formation of a good homogenous grain within the matrix. Atomic force microscopy results showed an increase in corrosion resistance and an improvement in micromechanical coating properties. A zinc/titanium oxide matrix limits agglomeration due to the role of the surfactant additive (GLYCINE) and using lower potential when the cathode and the particles provide strong adsorption [124]. In this research, using a composite electrode of activated carbon cloth as well as a dielectric material, such as ZnO

nanorods, was analysed for distribution. It was shown that in the case of thin coatings, the permittivity crystal was highly dielectric and was able to produce a high dielectric field. On the other hand, thick coatings were able to distribute a constant charge for centrosymmetry, decreased dielectric permittivity and provided a strong surface when a high electric field was generated [125].

For fabricated coatings that improve corrosion resistance and reinforce barrier performance, Ammar et al. illustrated the formulation of a hybrid polymeric matrix of acrylic-silicone/ZnO nanocomposite coatings. Intercalating methods using sonication were utilised to apply ZnO to the matrix. ZnO concentrations varied from 1 w% to 8% (w/w) to investigate the best loading ratio for ZnO nanoparticles. FESEM micrographs showed that the presence of ZnO prevented cracks, tunnels and phase separation. Fabricated coatings using 3% wt ZnO NPs gave the best anti-corrosion properties, as well as a high contact angle of about 95.6 degrees.

ZnO of 3% w/w exhibited the best result in achieving hydrophobic properties due to the ability of ZnO nanoparticles to increase the surface roughness, which leads to the formation of barriers from air pockets in situ separated between water molecules and the surface. As a result, a composite phase of the solid–liquid–air interface could form. Moreover, ZnO reduced the surface area that could be in contact with the water. When the loading ratio was more than 3% w/w, less efficiency was recorded in improving the coating system due to the tendency of the nanoparticles to agglomerate, thereby decreasing the surface roughness [126].

The corrosion of metallics in pipelines and ships is a significant factor threatening the economy and the sequence of inconveniences. Numerous studies have demonstrated how to reduce metallic corrosion by preventing corrosive environmental factors. There were strong aggressive solvent media types, such as water, chlorine and oxygen [118, 127]. The primary defence against metal corrosion was the use of organic coatings [118]. Due to its exceptional qualities (corrosion resistance, high adhesive properties and remarkable mechanical properties

to metal substrates), epoxy coatings were frequently used in corrosive settings [110, 128, 129]. Waterborne epoxy coatings regularly displace organic solvent-based coatings due to environmental concerns [110, 128–131]. Epoxy film has a specific feature as a barrier coating film due to its ideal resistance against corrosive solvents, great mechanical properties, high ability to adhere to metals or alloys, electrical isolating properties and dimensional stability [131]. Furthermore, these properties have paid attention to numerous applications that could be improved and optimised in recent years due to their adaptable thermosetting properties, especially as a nanocomposite coating [118].

However, aqueous epoxy coatings showed a lack of performance as a barrier to reduce the effect of the diffusion of numerous corrosive electrolytes in some environments, such as hostile environments, and had poor resistance to crack formation[129]. Furthermore, the hydrophilic groups in traditional aqueous epoxy coatings render them poor barriers. In particular, given the hostile environment, they do not provide a suitable long-term defence for the metal substrate [129, 131].

Accordingly, it was essential to add anti-corrosive nanopigments to the coating to improve its anti-corrosion performance. Numerous nanoparticles, including nano-TiO_2, nano-SiO_2, Fe_2O_3, ZrO_2, SiC and TNT, have been used in anticorrosion epoxy coatings due to the development of nanomaterials[132]. They might function as inhibitors to improve the metallic substrate surface's resistance to corrosion. These pigments were classified into three types based on the anti-corrosion mechanism – active inhibition [132, 133], sacrifice [133, 134], and containing barrier [135, 136], which were used to start coatings covering metallic substrates [118].

Nanocomposite coatings, such as epoxy nanocomposites, played a vital role in providing a superb barrier resistance and had a high-ability behaviour towards electric current. They boost the high-quality corrosion resistance of these organic coating [118].

Nanocomposite coatings provided great benefits by creating significant changes in mechanical, physical and chemical properties due to the size differences with traditional high block counterpart materials. One of these was the zinc oxide (ZnO) nanocomposite because of its multifunctional inorganic particles. Great luminous transmittance, decreased dielectric constant, chemical stability and high adoption affecting photocatalysis were examples of outstanding chemical and physical properties [137].

ZnO epoxy-based coatings have recently been largely utilised for corrosion protection for metal purposes [137, 138]. Additionally, ZnO nanoparticles could be employed as a reinforcing phase to enhance the wear-resistant and anti-slip properties of composites resulting from a high elastic modulus and strength [139–142] .

ZnO nanoparticles are harmless materials used to create ecologically friendly coatings. Additionally, it has been discovered that coatings that include this nanoparticle could significantly improve anticorrosion resistance [143, 144]. However, it is important to keep in mind that none of the advantages listed above will materialise until a complete condition of dispersion is attained. This implies that the ZnO primary substances inside the epoxy matrix must be evenly distributed and stabilized. For untreated hydrophilic ZnO particles inside a hydrophobic continuous phase, such as epoxy polymers, the latter is uncommon [139].

Some studies [145] and [102] had found that using some pigment nanocomposites, such as epoxy silicon with zinc (ESZ), and fluctuations in cross-link density in the polymer network at low temperatures may be responsible for the decline in the thermal stability of epoxy coatings. Furthermore, they showed that at a lower temperatures than the epoxy coating, epoxy silicon-zinc (ESZ) and epoxy-silicon titanium zinc (ESTZL) after exposure to 3% NaCl for 180 days were completely thermally degraded. In addition, the deterioration of the epoxy silicon (ES) and epoxy silicon titanium (EST) coatings was completed at a higher temperature than that of

the epoxy coating [145]. The fluctuations in cross-link density in the polymer network might be responsible for this phenomenon [102].

1.13 Electrochemical impedance spectroscopy

Electrochemical impedance spectroscopy (EIS), one of several electrochemical methods, plays a unique role in the electrochemical field. Traditional electrochemical methods display time-dependent measurements of currents, electrical charges or electrode potentials. EIS, on the other hand, displays signals as a function of the values of frequency when there is constant potential. Since electrochemists prefer to operate in terms of time rather than frequency, this frequently makes it difficult to comprehend a particular situation. Nevertheless, no one believed that light in optical spectroscopy was made up of sinusoidal oscillations of magnetic and electric vectors with different frequencies, phases and amplitudes. In the past, while discussing spectroscopy, the frequency range (wave number, frequency or other terminology similar to wavelength) [146] as was obtained using the Fourier transform of the optical indicator. Ordinary electrochemical techniques, such as chloride removal (CR) and cathodic protection (CP), were used to control the corrosion of a metal structure by lowering its potential with a direct cathodic current. EIS that could show how the signal could be considered a function of some frequencies at a constant value of potential instead of time or with another word, EIS was an equilibrium technique [146].

The system in the potinsiostat was perturbed with an alternating current (AC) small enough to reach approximate equilibrium. The response of this cell was also small and related only to excitation, which is called a linear response. A sinusoidal signal, such as E, was sent to the cell, following which the sinusoidal response from the cell, in this case I (current), was measured. At the end, the ratio between the signal and impedance (symbolised by Z and the unit is ohms Ω) was calculated. All these steps were repeated at different frequencies for each signal. [146]

Also, there were abundant benefits of using EIS, which could provide a lot of information for extra analysed examples. In the case of steady-state polarisation measurements, even measuring the current at constant potential or measuring the potential at constant current, the resultant slope from these curves was called polarization resistance (Rp ¼ dE/dj). Figure 20 showed the fuel cell as an example of this curve. Nevertheless, each potential point could deal with impedance, which could lead to information at different frequencies. [147]

Figure 20 and Figure 21 show how the impedance plots were complex when the imaginary values were the real Z value (Z') at different frequencies in various fuel cells. The polarization resistance (Rp) was the only value presented at the zero value of the frequency. The impedance plots and Rp could offer more information than the steady-state polarisation method in terms of complex curves that contain rich information at each point (not in one value of polarisation resistance). However, in addition to this feature, the process of finding and concluding the information that had been obtained was considered a complex problem that could be fixed using an appropriate physicochemical demonstration.

Furthermore, the EIS technique was able to show massive amounts of data and information that could be utilised for resistances, defining the kinetics of procedures, fine-tuning mechanisms and capacitances.

1.13.1 Capacitance

Electrical circuits occasionally have three passive basics: capacitors, resistors and inductors. It is important to know that the performance action of resistance is totally different from inductance and capacitance. In the case of capacitance, there was no observed constant current flow, but only an electrical charge had the ability to accumulate in the capacitance, and the charge value changed according to the applied potential during the electrical circuits.

The relation equation between voltage (V) and charges was illustrated as follows:

$$V=\frac{Q}{C} \quad (21)$$

Q presents the amount of charge accumulated in capacitors as Coulomb units.

C is the capacitance measured in the farad unit, F.

In addition, the relationship between the charge and current was demonstrated as follows:

$$Q(t)=\int_0^t i(t)dt. \quad (22)$$

1.13.2 Inductance

A coil has the ability to induce individual electromotive power, which could be opposed to all variations in the current. The inductance had a zero value for resistance in ideal conditions. The relation between the potential and the inductance is shown in the following equation:

$$V(t)=L\frac{di(t)}{dt} \quad (23)$$

L represents the inductance in the henry unit, H, which means that there is a constant flow of current over the conductance with zero resistance. Therefore, the equation that describes this system is as follows:

$$V=i(t)R+L\ \frac{di(t)}{dt} \quad (24)$$

Table 5 illustrated the element laws used in impedance measurements [147, 148].

Table 5 some essential elements in impedance measurements.

Element	Operational tools for impedance	AC impedance
R	R	R
C	$\frac{1}{sC}$	$\frac{1}{jwC}$
L	sL	jwL

1.13.3 Impedance plots

Some studies have stated that in the case of a real electrochemical system, the calculation is more complex compared with electrical circuits. This was due to the presence of considerable factors, such as electrochemical reactions, interfaces and the transport of species. However, graphical examination provided a valuable calculation, as the first data information and provided an indication of the accuracy of how the experiment had been processed [147, 148].

There are two common types of impedance plots:

- Argand diagrams or Nyquist plots. In these graphs, the imaginary value of impedance is related to the real value. Usually, -Z represents the imaginary value with a negative value in an electrochemical system. The second type of plot is called a Bode plot. First, Log |Z|, as a magnitude, represented the y-axis versus log (frequency (f)) as an x-axis. Bode plots occur when the phase angles, which are known as the shift of the angle from where the current is measured and the potential is applied (ϕ) versus the value of log f. These complex plots revealed that both imaginary and real parts were of the same length. It is important to know that these plots did not reflect all the details about frequency.

However, the Bode plots provided adequate essential details. Nyquist and Bode plots were highly recommended due to their ability to display typical detail acquisition and analysis electrochemical systems, especially when the experiments had data that needed to be compared with a suitable fit model.

1.13.4 EIS application

EIS was a measurement for plentiful applications, such as studying interfacial processes in terms of redox reaction, adsorption, kinetics of homogeneous solution when reacting with redox processes, forced mass transfer and electro adsorption, [147, 149].

Furthermore, EIS was also used in geometric structure effects: limited-volume types of electrodes, porous electrodes, resolution of how much resistance in the electrolyte, spherical, linear and the transfer of cylindrical mass. Moreover, power resources such as batteries, membranes, capacitors and fuel cells were significant subjects in EIS application. Furthermore, coatings, paints, corrosion and electrocatalytic reactions, conductive, self-accumulated monolayers, polymers, semiconductors and sensors were common applications for using EIS [149].

1.14 Electrochemical behaviour of semiconductors' electrodes in solution

At the electrode surface, excess electrons accumulated at the surface, relying on the fact that when the quantity of charged items increased, this led to shrinking in the areas that had charge in the redistribution process.

In addition, in semiconductor electrodes, the number of charges (electrons) or holes was lower than in the solution. As a result, more redistribution was created, and a specific charge space occurred on a semiconductor electrode surface at a greater distance than solutions with about 10–100 nm [150]. As a result, smaller capacitance values were produced for these semiconductor electrodes. Accordingly, there is a strong ability to form passive films on the electrode surface, which contributes to corrosion protection.

Due to the redistribution of these charge species in the valence and conduction bands, there was a possibility of the presence of potential bending at the electrode surface. It was clear that in the case of an n-type semiconductor using as an electrode in an open circuit system, the Fermi scale becomes greater than the redox potential in the solution (electrolyte) and as a result, electrons from the electrode surface migrated to the solution, leaving the electrode having a

positive charge, which was in contact with the space charge area. Upward bending was caused by the previous effect on the band boundaries [151].

When there was further exposure to the solution, more solution molecules will be located under the coating Figure 20 [152].

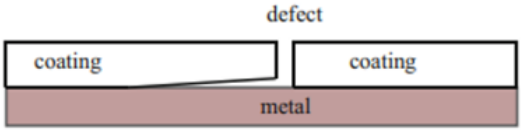

Figure 20. Presence of defects under a coating.

Figure 21 a illustrates the perfect coating in ideal conditions when it was a pure capacitor Rs in the circuit was solution resistance where coating capacitance was (Cc), although these conditions were rare due to defects and decreased cross-linking. According to that, as an example of an equivalent circuit, as shown in Figure 21 b, coating resistance in this case (Cr) was in parallel with another resistance called polarisation resistance (Rpo) and in serial with capacitance that created due to the effect of a diffuse layer (Cd).

After further exposure time to the solution, the coating could be affected by the corrosive factors that make the corrosion localized. During this process, a double-layer capacitance between the solution and the coating was generated. In this case, there will be two diffuse layers of Cd. One represented the interface between metal and solution Cd1 and one between the substrate metal and coating interface Cd2 and in this case Cd1 was greater than Cd2. In addition, when the corrosive anions penetrate the coating, this causes another kind of corrosion called faradaic corrosion and could be known as corrosion resistance (Rc) Figure 21 c. In the ongoing process of corrosion and penetration, with disbonding in the coating, the impedance could be represented as a transmission model line, which could be illustrated by a complex electric equivalent, as shown in Figure 21b. However, in the same previous case and when there was a decrease in the ohmic resistance in the area of coating, usually the Rsi value became

neglected and according to that, the electrical equivalent circuit could be drowned in a simple way, as shown in Figure 21 e [153].

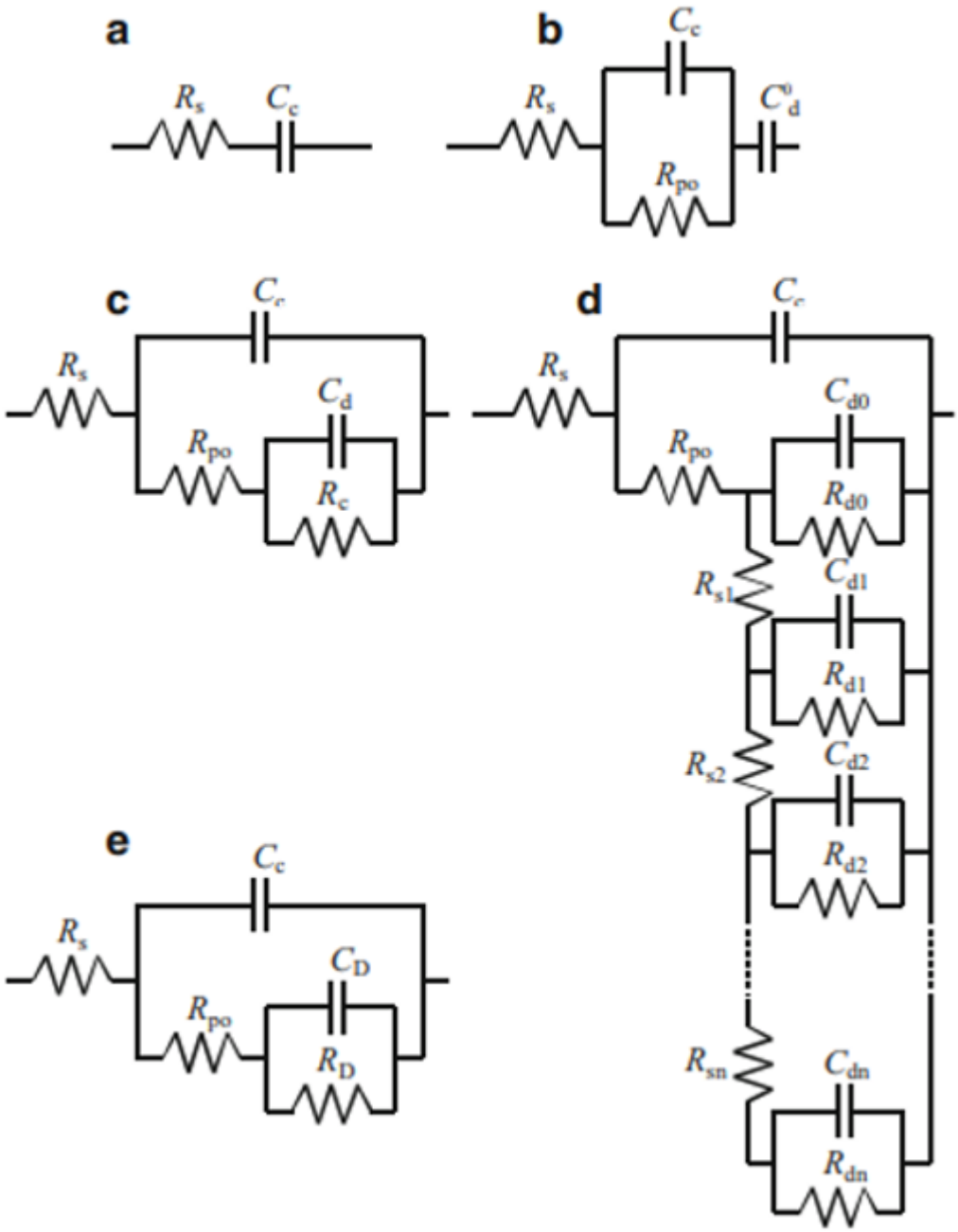

Figure 21. Electrical equivalent circuits when an organic coating was used: (a) ideal conditions for coating, (b) real coating but absence of corrosion, (c) observing coating with the presence of corrosion in holes, (d) coating in the case of disbonding, (e) coating with small Rsi value disbonding.

There were two reasons for selecting the right circuit. First, it was difficult to decide which compatible circuit represents the electrochemical cell system in the case of using a specific coating system and some circuits contain more than two circuit elements that rearrange in various paths but at the end provide the same result of impedance. Some studies have identified some advantages that could be concluded from Bode graphs that could support practical and theoretical value, such as the relationship between breakpoint frequency and the coating scattered area. At a high frequency (10 kHz), the ability to determine some material coatings, such as zinc chromate and zinc phosphate coatings, increases. In another useful way, Zuo et al. utilised the parameter phase angle to evaluate the behaviour of the multilayer coating form in the system [154].

As mentioned before, ZnO as a semiconductor metal oxide has been widely used in various applications, including several studies on ZnO and its application in the last decade. However, the focus on ZnO as a thin film and a doped film was limited [155, 156]. Some studies determined how to doped Cu p-type-ZnO and found that it was a promising material compared with other varieties of dopants, as well as highlighting only materials that had different applications [155]. In addition, Das et al. illustrated the effect of synthetic methods on the final morphology of copper oxide and ZnO nanocomposites by studying several applications [156]. Moreover, Shohany et al. mentioned the effect of using several surface morphologies of ZnO by adding seven study groups containing some metals and their effects on optical characterizations [157].

Aim of the research

Researchers have paid a lot of attention to metal oxide nanostructures that are to be used in different applications, such as those of zinc oxide ZnO, titanium oxide TiO_2 and Tin oxide SnO_2 [27, 158]. Principally, ZnO received interest due to its physical properties, such as its high electron affinity and flexibility [27]. In addition, synthesis of zinc oxide consumes less energy, is reused, costs less and is easy to store [159].

Due to the formation of several different morphologies of zinc oxide nanostructures depending on synthesis methods, different chemical and physical properties can be obtained for zinc oxide materials[27, 160]. Recent studies have focused on the effect of zero-, one-, two- and three-dimensional nanoparticles and their properties. However, this kind of study is still rare and, due to the numerous nanostructure applications, is still not covered adequately in the literature [27].

Although zinc oxide's crystalline structures have an extensive surface area [161], there are some obstacles and drawbacks during zinc oxide synthesis, such as controlling growth processes, stabilising particle size, low effectiveness and agglomeration phenomena [162]. Consequently, it is important to understand what kind of influence the surface geometry has on the solution–film interface [7, 102, 139].

Steel applications play a vital role in our daily lives, such as heavy construction (chemical and marine industries), household appliances, automotive uses and business machines. Mild steel has excellent mechanical properties that can provide corrosive environments using its resistance [163]. However, mild steel cannot offer corrosion resistance in an acidic medium [164].

Recently, the use of organic and inorganic coatings has provided greater enhancement for solutions to protect metal from corrosion [161]. Epoxies are thermoset organic polymers that

have promising applications in metal adhesion. However, epoxy has long been oversensitive to UV radiation. Moreover, the ions in an electrolyte or in water can diffuse into the epoxy barrier and penetrate defects. Accordingly, pores and corrosion can occur. The presence of a nanocomposite film in the mild steel–coating interface contributes to more cathodic protection, increases passivation behaviour, and builds a proper barrier against corrosion. Zinc oxide when used in the pores of an epoxy composite, leads to greater anticorrosion protection [165]. In addition, zinc oxide was found to form a thin layer that could react to produce hydroxide that enhances the barrier, preventing corrosive agents from developing an extensive pH range [163].

Saide et al. examined the long-term corrosion effect with a resistance film consisting of a Ti-based material substrate covered with disparate morphologies of zinc oxide using electrochemical impedance spectroscopy (EIS) [166]. Nonetheless, few studies have delved into the effect of immersion time (e.g. over 10 to 11 days) and corrosion resistance behaviour of different substrates using zinc oxide film coatings [102, 147, 167] Nevertheless, factors such as pH, particle size, smoothness and morphological dispersion are critical to investigate when trying to optimise the formulations for coating materials [168].

One method to augment the performance of anticorrosive coatings is the creation of densely structured polymer–nanocomposites. To maximise the benefits of including nanoparticles in such composites, it is important to optimise the interactions between the nanoparticles and the polymers, for which an in-depth understanding of such interactions is essential, as influenced by the nature, particularly the geometry, of nanoparticles. However, to date, there is virtually no reported study on understanding the effects of nanoparticle geometry on the nature of interactions between nanoparticles and polymers, which this work aims to study.

This research also scrutinised the effect of some parameters such as zinc sources, participation agents such as sodium hydroxide and ammonium carbonate, effect of different methods and the effect of the time by investigating the final zinc oxide morphologies to minimise these

obstacles and to understand how this study contributes to a deeper understanding of the parameters that have influenced zinc oxide synthesis.

Correspondingly, in assessing the influence of particle geometry on nanoparticle/polymer interactions, the proposed research will include studies of the roles played by various dispersion methods centred on the utilisation of ultrasonic energy in forming zinc oxide/epoxy steel composites.

Clearly, in-depth studies of physical chemical interactions at the interface of nanoparticles and polymer chains, as well as the influence of such interactions on the performance properties of the resulting anti-corrosive coatings, will form crucial parts of this research project.

Chapter 2

Experimental methods

2.1 Synthesis of zinc oxide nanoparticles

2.1.1 Materials

The materials used in the experimental studies described in this report are as follows:

- Zinc acetate dihydrate Zn $(CH_3CO_2)_2.2H_2O$ was supplied by Alfa Aesar ACS, (98.0%–101.0%) crystalline.
- Sodium hydroxide NaOH (99%) was supplied by Sigma-Aldrich.
- Deionised water as a solvent was supplied by the University of Leeds Chemistry Department.
- Methanol was supplied by the VWR Chemicals Company.
- Zinc nitrate hexahydrate (Zn $(NO_3)_2 \cdot 6H_2O$, 98%) was supplied by Alfa Aesar.
- Ammonium carbonate ($(NH_4)_2CO_3$) was supplied by Honeywell Fluka.
- Zinc oxide from MKCL7152.

2.1.1.1 Electrochemical experiments

- Sodium chloride (NaCl) by Fisher Chemical
- Epoxy and hardener from HMG Paints Ltd
- Steel panel from Q-Panel
- IviumSoft from Ivium technology for all electrochemical and corrosion purposes company from mechanical engineering University of Leeds.

IviumSoft, which includes all common electrochemical and corrosion procedures, was created with electrochemists in mind. These include electroanalysis methods (square wave

voltammetry (SWV), alternating current (AC) voltammetry, pulse builder, AC detection), sweep methods such as linear sweep voltammetry (LSV) and cyclic voltammetry (CV), transient methods – chrono potentiometry (CP), chrono amperometry (CA), corrosion methods (Tafel plot and galvanic corrosion), and impedance methods (EIS), when I = current and E = potential, controlled). When used in advance mode, this software platform has more functions, giving the expert full control over the instrument.

- PochetSTAT:

Portable potentiostat, galvanostat and EIS, pocketSTAT2 is the weight and size of a smartphone. Any Windows-powered netbook, PC or laptop can control it via a USB link.

This study aims to generate zinc oxide particles with many morphologies for use in other applications to determine the morphology with the best properties, such as chemical, physical and mechanical features. The second purpose is to find a stable morphology that can be reproduced under the same conditions that have been used every time for a specific experiment. Two chemical compounds have been used as zinc resources, $Zn(CH_3CO_2)_2$. $2H_2O$ and $Zn(NO_3)_2 \cdot 6H_2O$ and two composites used as participate agents, NaOH and $(NH_4)_2CO_3$. Three methods were used for zinc oxide synthesis – the precipitation method, the reflux method, and the hydrothermal method.

precipitation method is a famous process because of its ability to provide a huge scale of varied morphology nanoparticles as well as a useful method to implement inside the lab, low cost and easy preparation equipment [169, 170]. Figure 22 illustrates the steps that were used in the lab.

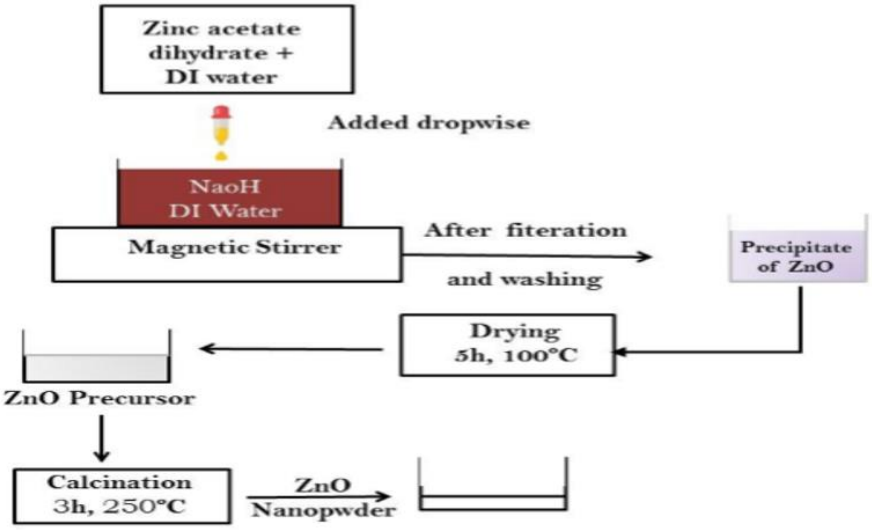

Figure 22. Steps in the precipitation method to produce zinc oxide, ZnO.

The reflux method was used due to its simplicity and low cost [171]. Figure 23 shows the steps through which the reactants were put to produce zinc oxide nanoparticles.

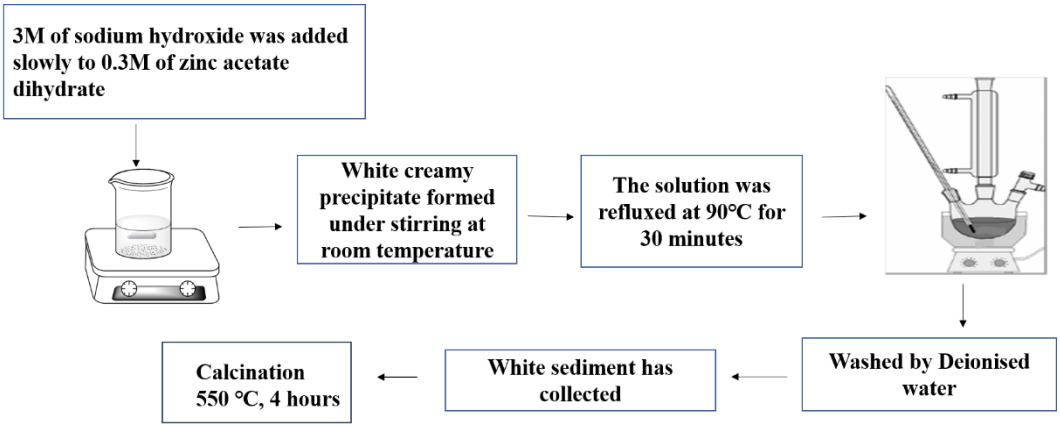

Figure 23. Steps in the reflux method for producing zinc oxide, ZnO.

In hydrothermal method, some researchers have produced zinc oxide using the hydrothermal method at different low and high temperatures (60 to 200) for 2 to 10 hours to produce nanorods and spherical shapes using more than one precipitation agent and mixed solvents [172], [94]. Our thermal method is low temperature, using one solvent to achieve the same results. Figure 24 clarifies the steps that were followed to obtain zinc oxide nanoparticles. The white

precipitate was transferred into an electric oven at 90°C for 30 minutes. Figure 24 illustrates the steps used in the hydrothermal method.

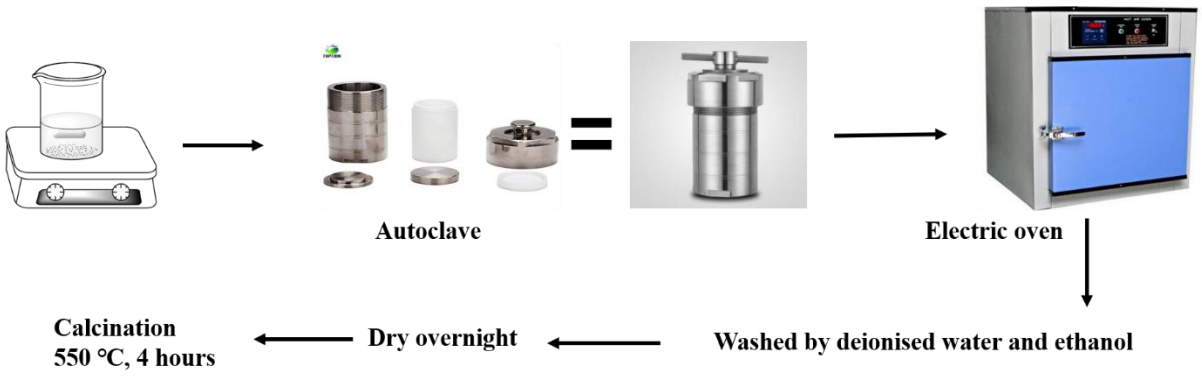

Figure 24. Steps in the hydrothermal method for producing zinc oxide, ZnO.

The experimental route was selected according to s

2.2 Synthesis of zinc oxideusing zinc acetate dihydrate Zn $(CH_3CO_2)_2.2H_2O$ and sodium hydroxide NaOH by precipitation method

In Experiment 1, zinc acetate dihydrate was calcinated at 400 °C for 12 hours. Zinc oxide was prepared using zinc acetate dihydrate (Zn $(CH_3CO_2)_2.2H_2O$) and different concentrations of sodium hydroxide NaOH by the precipitation method, where sodium hydroxide and zinc acetate dihydrate were used in deionised water as a solvent.

In Experiment 2, 0.25 M of NaOH was added slowly to 0.3 M of zinc acetate dihydrate until white creamy precipitate formed under stirring at room temperature. The solution underwent sonication for 30 minutes, then the white precipitate was washed with deionised water several times and calcinated at 550 °C for 4 hours.

In Experiments 3, 4 and 5, (0.5, 0.75 and 1) M of NaOH were added slowly to 0.3 M of zinc acetate dihydrate, respectively, using the same treatment as mentioned in Experiment 2.

Experiment 6, in this experiment, 0.3 M of zinc acetate dihydrate was added slowly to 1 M of sodium hydroxide (different addition type compared with Experiment 5) until white creamy precipitate formed under stirring at room temperature. This step consumed extra time to form the product compared with Experiment 5. Then the solution underwent sonication for 30 minutes, then the white precipitate was washed with deionised water several times and calcinated at 550 °C for 4 hours.

2.3 Synthesis of zinc oxide using zinc acetate dihydrate and sodium hydroxide NaOH by reflux method

In Experiment 7, sodium hydroxide and zinc acetate dihydrate were used in deionised water as solvents.

3 M of sodium hydroxide was added slowly to 0.3 M of zinc acetate dihydrate until white creamy precipitate formed under stirring at room temperature. The solution underwent sonication for 30 minutes, then transferred to a flask (round bottom) with three nicks on a hot plate, using a condenser (Graham) at 90 °C for 30 min. The white precipitate was washed with deionised water several times and calcinated at 550 °C for 4 hours [173]. In this experiment, the pH value was 13.

In Experiment 8, sodium hydroxide and zinc acetate dihydrate were used in deionised water as solvents.

0.3 M of zinc acetate dihydrate was added slowly to 3 M of sodium hydroxide until white creamy precipitate formed under stirring at room temperature (in this experiment only the difference compared with Experiment 7 was starting with the zinc acetate dihydrate to added to NaOH. The solution underwent sonication for 30 minutes, then transferred to a flask (round

bottom) with three nicks on a hot plate, using a condenser (Graham) at 90 °C for 30 min. The white precipitate was washed with deionised water several times and calcinated at 550°C for 4 hours. The pH was 13.

In Experiment 9, 6.58 g of sodium n-dodecyle sulphate (SDS) was added halfway through as a surfactant after adding NaOH into the acetate dehydrate solution. Importantly, a thick white foam precipitate was formed. The solution then underwent refluxing for 30 minutes at 90 °C. The solution underwent sonication for 30 minutes, then the white precipitate was washed with deionised water several times and calcinated at 550 °C for 4 hours.

2.4 Synthesis of zinc oxide using zinc acetate dihydrate and sodium hydroxide by the hydrothermal method

In Experiment 10, sodium hydroxide and zinc acetate dehydrate were dissolved in deionised water. Sodium hydroxide (3 M) was added slowly to zinc acetate dehydrate (0.3 M) until a white creamy precipitate formed under stirring at room temperature. After sonication for 30 minutes, the solution (100 ml) was then autoclaved and transferred to an electric oven at 90 °C for 30 min. The white sediment was washed several times with deionised water and ethanol and dried overnight at room temperature. The pH of the solution was 13.

2.5 Synthesis of zinc oxide using zinc nitrate hexahydrate $Zn(NO_3)_2.6H_2O$ and sodium hydroxide by precipitation method

In Experiment 11, 0.5 M of $Zn(NO_3)_2.6H_2O$ zinc nitrate was added to 1.0 M of NaOH solution, drop by drop and under constant stirring. The solution underwent sonication for 30 minutes,

then washed several times with deionised water and left to dry overnight at 60 °C and calcinated at 550 °C for 4 hours.

In Experiment 12, 1.0 M of NaOH was added to 0.5 M of Zn $(NO_3)_2$. $6H_2O$ zinc nitrate hexahydrate. The only difference from Experiment 11 was that only NaOH was added first to zinc nitrate hexahydrate.

2.6 Synthesis of zinc oxide using zinc nitrate hexahydrate and sodium hydroxide by reflux method

In Experiment 13, 0.5 M of Zn $(NO_3)_2$. $6H_2O$ zinc nitrate was added to 1.0 M of NaOH solution, drop by drop and under constant stirring. The solution remained in a sonication bath for 30 minutes, after which the white precipitate was transferred to a flask (round bottom) with three necks for the refluxing process at 90 °C for 30 minutes. Finally, the precipitate was washed with deionised water several times and left to dry overnight. The precipitate was calcinated at 550 °C for 4 hours.

In Experiment 14, NaOH was first added to investigate the effect of different addition types on zinc oxide morphology.

2.7 Synthesis of zinc oxide using zinc nitrate hexahydrate and sodium hydroxide by hydrothermal method

In Experiment 15, 1.0 M NaOH and 0.5 M Zn $(NO_3)_2 \cdot 6H_2O$ were used. Zinc nitrate was added dropwise into 50 ml of the NaOH solution under constant stirring. The solution was then autoclaved and transferred into an electric oven at 90 °C for 30 minutes after spending 30 minutes in a sonication bath. The sediment was collected by filtration and washed sequentially

with absolute ethanol and deionised water. The precipitate was dried at room temperature overnight and calcinated at 550°C for 4 hours.

2.8 Synthesis of zinc oxide using zinc nitrate hexahydrate and ammonium carbonate by precipitation method

In Experiment 16, 1 M of $(NH_4)_2CO_3$, 1 M of Zn $(NO_3)_2{\cdot}6H_2O$ were prepared using deionised water. Zinc nitrate was dropped slowly into $(NH_4)_2CO_3$ under vigorous stirring. The solution underwent sonication for 30 minutes, then collected by filtration and washed with deionised water. The precipitate was dried at 60 °C overnight and calcinated at 550 °C for 4 hours.

In Experiment 17, 1 M of $(NH_4)_2CO_3$ was added to 1 M of Zn $(NO_3)_2{\cdot}6H_2O$, and the process was the same as in Experiment 16.

2.9 Synthesis of zinc oxide using zinc nitrate hexahydrate and ammonium carbonate by reflux method

In Experiment 18, 1 M of $(NH_4)_2\,CO_3$, 1M of Zn $(NO_3)_2{\cdot}6H_2O$ were prepared using deionised water. Zinc nitrate was slowly dropped into $(NH_4)_2CO_3$ and vigorously stirred until the white sediment was obtained. The solution underwent sonication for 30 minutes, then transferred to a flask (round bottom) with three nicks on a hot plate, using a condenser (Graham) at 90 °C for 30 min. The white precipitate was washed with deionised water several times and calcinated at 250 °C for 4 hours.

In Experiment 19, the same steps were taken as in Experiment 18, except for the calcination step, which was maintained at 550 °C for 4 hours.

2.10 Synthesis of zinc oxide using zinc nitrate hexahydrate $Zn(NO_3)_2 \cdot 6H_2O$ and ammonium carbonate $(NH_4)_2CO_3$ by hydrothermal method

In Experiment 20, $(NH_4)_2CO_3$ (1 M) and Zn $(NO_3)_2$ (1 M) were prepared using deionised water. Zinc nitrate was slowly added dropwise into $(NH_4)_2CO_3$ under vigorous stirring. The solution underwent sonication for 30 minutes, then the solution (100 ml) was autoclaved and placed inside the oven at 90 °C for 30 min. The sediment was collected by filtration and washed sequentially with absolute ethanol and deionised water. The precipitate was dried at room temperature overnight and calcinated at 550 °C for 4 hours.

2.11 Effect of addition time on zinc oxide morphology using zinc nitrate hexahydrate and ammonium carbonate with reflux method

Used the same process as Experiment 19—but, before transferring the solution to the refluxing step, the tuning of the time was set at 7 stages – 5, 10, 15, 20, 30, 50 and 70 minutes for Experiments 21, 22, 23, 24, 25, 26 and 27, respectively. The solution then underwent the reflux method at 90 °C for 30 minutes. calcinated at 550 °C for 4 hours.

The current study focused on gaining more morphologies in this research to apply to other applications according to the aim of the project to find the best properties, such as chemical, physical and mechanical features. In addition, the study aimed to find a stable morphology that could be reproduced under the same conditions. Table 6 involves a brief description of all the experiments that had been done, as mentioned before.

Table 6. Brief description of methods for zinc oxide synthesis in the lab.

Experiment no.	Materials concentrations					SDS	Reaction Conditions									Calcination conditions		pH
	Zinc acetate dihydrate	zinc nitrate	Sodium hydroxide	KOH	Ammonium carbonate		Time of stirring minutes	Temperature during reaction (℃)	Time of sonication (minutes)	Time of refluxing (minutes)	Temperature of refluxing (℃)	Time of electric oven (hydrothermal)	Temperature of elctric oven	The sediment treatment	Drying step	Calcination temperature (℃)	Calcination time (hrs)	
1	solid state	0	0	0	0	0	0	21	0	0		0	0	Washed with deionised water several times	Dried at 60ºC overnight	400	12	-
2	0. 5	0	0.25		0	0	36.3	21	30	0		0	0			550	4	6
3	0. 5	0	0. 5		0	0	38	21	30	0		0	0			550	4	6.5

4	0. 5	0	0.75		0	0	36.3	21	30	0	0	0	Washed with deionised water several times.	Dried at 60ºC overnight	550	4	6.5
5	0. 5	0	1		0	0	37	21	30	0	0	0			550	4	7
6	0. 5	0	1		0	0	35.5	21	30	0	0	0			550	4	7
7	0.3 M	0	3M	0	0	0	37	21	30	30,90		0			550	4	13

8	0.3 M	0	3M	0	0	0	37	21	30	30,90		0		0	550	4	13
9	0.3 M	0	3 M	0	0	6.58 gm	38	21	30	30, 90	90 ℃	0			550	0	12
10	0.3 M		3M			0	37	21	30	0	90	30			550	4	13
11	0	0.5 M	1 M		0	0	35	20	30	0	0	0		0	550	4	7.5 5

12	0	0.5 M	1 M		0	0	35	20	30	0	0	0		0	550	4	7.5 5
13,14	0	0.5 M	1 M		0	0	35.8	20	30	30,90					550	4	7.4
15	0	0.5	1 M		0	0	36	20	30	30,90					550	4	7.4
16	0	0.5	1 M		0	0	36.3	21	30	30,90	30	90			550	4	7.5

17	0	1 M	0	0	1 M	0	37	21	30	0		0	0		0	550	4	7.64
18	0	1 M	0		1M	0	36.7	21	30	0		0	0		0	550	4	7.55
19	0	1 M	0	0	1 M	0	34	21	30	30	90 ℃	0	0		0	250	4	7.55
20	0	1 M	0	0	1M	0	35	21	30	30	90 ℃	0	0		0	550	4	7.78
21	0	1M	0	0	1M	0	5	21	30	30	90	0	0		0	550	4	8

22	0	1 M	0	0	1 M	0	10	21	30	0	90 ℃	0	0		0	550	4	8.36
23	0	1 M	0	0	1 M	0	15	21	30	0	90 ℃	0	0		0	550	4	7.59
24	0	1 M	0	0	1 M	0	20	21	30	0	90 ℃	0	0		0	550	4	7.55
25	0	1 M	0	0	1 M	0	30	21	30	0	90 ℃	0	0		0	550	4	7.34
26	0	1 M	0	0	1 M	0	50	21	30	0	90 ℃	0	0		0	550	4	7.07

27	0	1 M	0	0	1 M	0	70	21	30	0	90 ℃	0	0			0	550	4	7.28

2.12 Electrochemical method

2.12.1 Materials

- 0.06 gm of zinc oxide solid state.
- 5 ml of formic acid
- 3 mL of epoxy resin
- 1 mL of Hardener
- Steel panel (the thickness of the steel is 0.86 mm)
- The thickness of this composite after getting dry is from 3–5 µ.

To achieve zinc oxide-epoxy composite on the steel panel, we mixed 0.06 gm of zinc oxide solid state with 5 ml of formic acid to increase the dispersion of zinc oxide. The mixed solution was sonicated for one hour. An amount of 3 mL of epoxy resin was added to the sonicated solution under constant stirring for 2 h. After two hours, 1 mL of Hardener was added to the above solution and applied to the steel panel to form the film. The films were created using a K coater (RK Printcoat Instruments).

The specific K coater used was number 3, which produces a wet film deposit of 24 microns.

The film was left to dry for 24 hours before the electrochemical test. Figure 25. Zinc oxide-epoxy composite coatings on steel panel (working electrode).

The thickness of this composite after getting dry ranged from 3–5 µ.

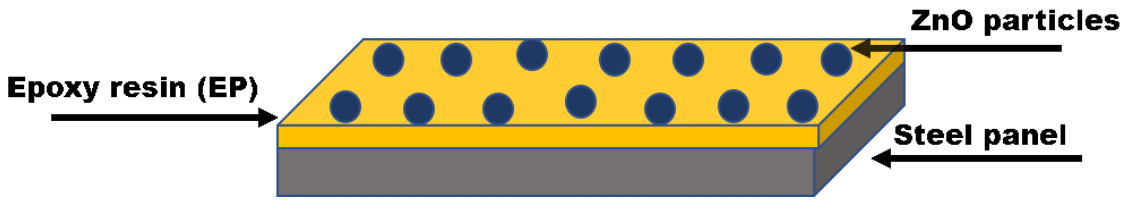

Figure 25. Zinc oxide-epoxy composite coatings on steel panel (working electrode).

2.13 Suggestion of electrochemical cell design

The suggested cell design, as shown in Figure 26, consists of three electrodes, a working electrode, WE representing the study sample, (The thickness of this composite after getting dry is from 3–5 µ on the Steel panel (the thickness of the steel is 0.86 mm), a standard Ag/AgCl cell as a reference electrode, RE and counting electrode CE such as PT. Measurements are carried out over a frequency range from 0.1 Hz to 20000 Hz, using a 10-mV amplitude sinusoidal voltage.

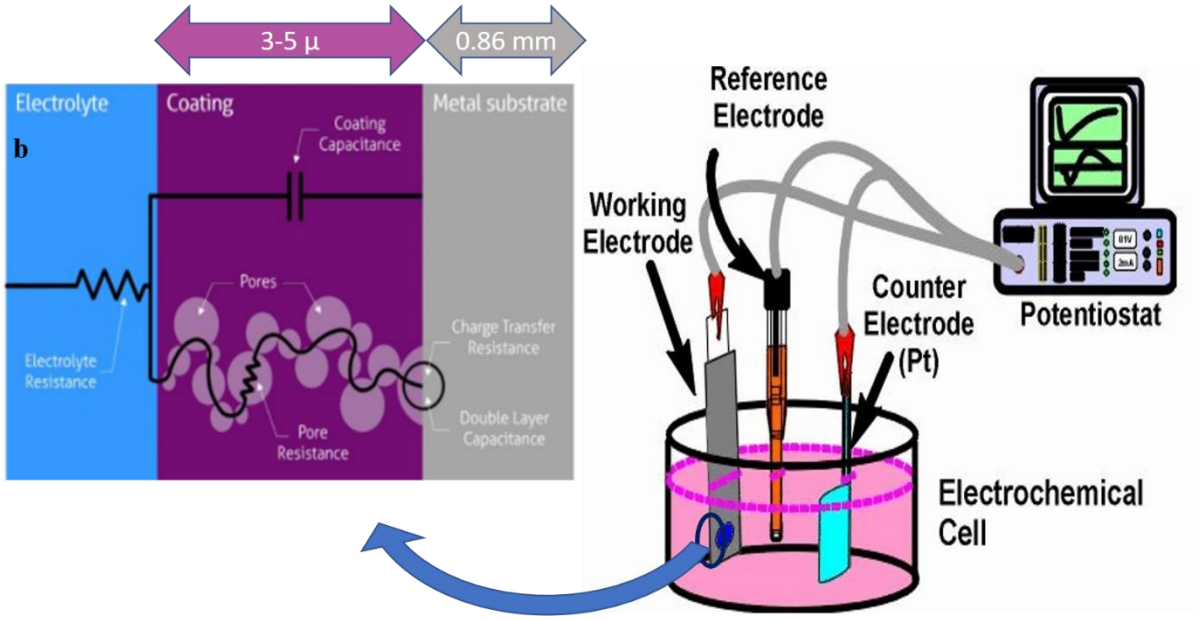

Figure 26. Suggested design for the electrochemical cell.

Figure 27clarified the electrochemical cell coating that was capable of being used in the lab to achieve the electrochemical project objectives. Three electrodes were connected with the cell in the presence of 3.5% w of NaCl solution.

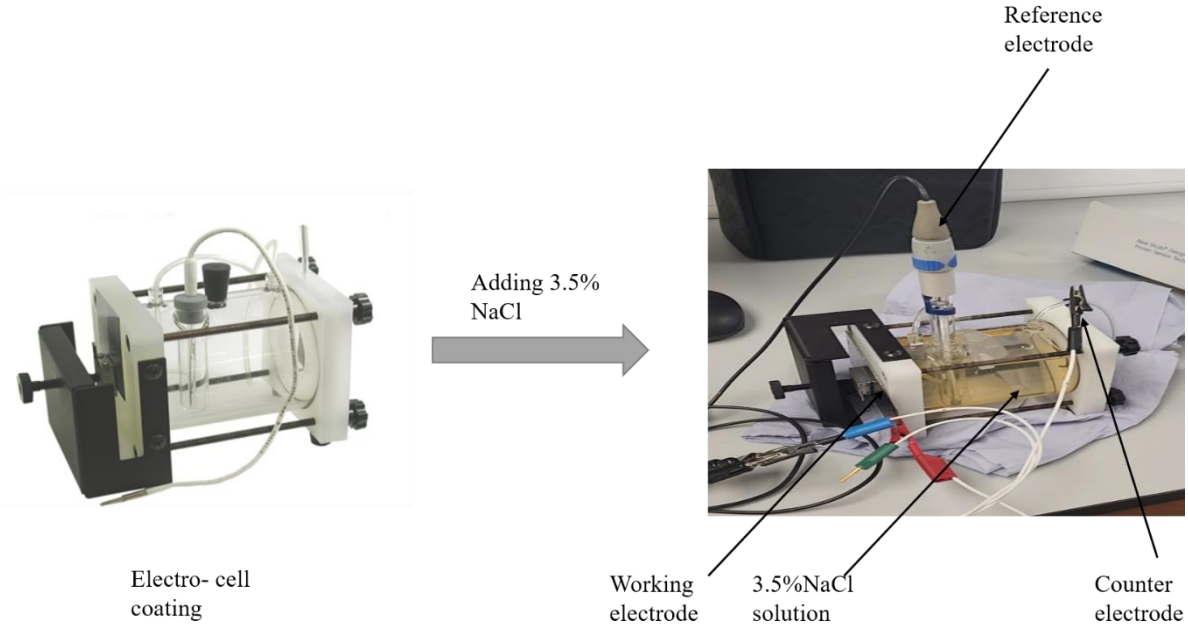

Figure 27. Applying the electrochemical cell coating in the lab.

Chapter 3

Results and discussion

3.1 Field emission scanning electron microscopy (FE-SEM) and scanning electron microscopy characterisation of ZnO NPs

The scanning electron microscopy (SEM) imaging technique involves scanning a focused electron beam over the surface of an electrically conductive sample (if not conductive, then it would require coating to achieve this via a layer of gold, gold/palladium, platinum, silver or carbon) to generate an image of the sample surface [174]. The electrons interact with the sample to produce a range of signals that can be used to obtain information regarding surface morphology and elemental composition. These signals include secondary electrons, backscattered electrons, Auger electrons (surface specific) and characteristic X-rays [175].

Dry specimens can be examined in a conventional SEM with a high vacuum or, if the specimens have a high surface area, with a low vacuum. Wet samples cannot be examined in this way and therefore require examination via variable-pressure SEM, known more commonly as environmental SEM. The most common mode of SEM operation is the production of surface images using secondary electrons, which are emitted by atoms excited in the electron beam. The second most common method of SEM operation is backscattered electron imaging.

The morphologies of the crystals were determined using field emission SEM (FE-SEM). A piece of silicon wafer supporting the crystals was mounted on an SEM stub using adhesive copper tape. All samples were coated with 4 nm infrared radiation (IR) and deposited by sputter coating. The samples were viewed with an FEI Nova 450 FE-SEM operating at 3 kV [176].

3.1.1 Zinc oxide using zinc acetate dihydrate $Zn(CH_3CO_2)_2 \cdot 2H_2O$ and sodium hydroxide NaOH by precipitation, reflux and hydrothermal method

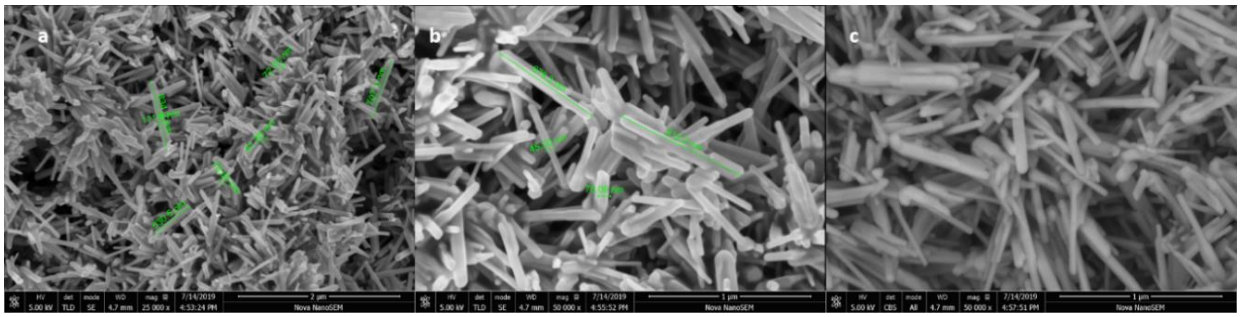

Figure 28. Zinc oxide produced from the calcination of zinc acetate dihydrate for 12 hours at

400 °C.

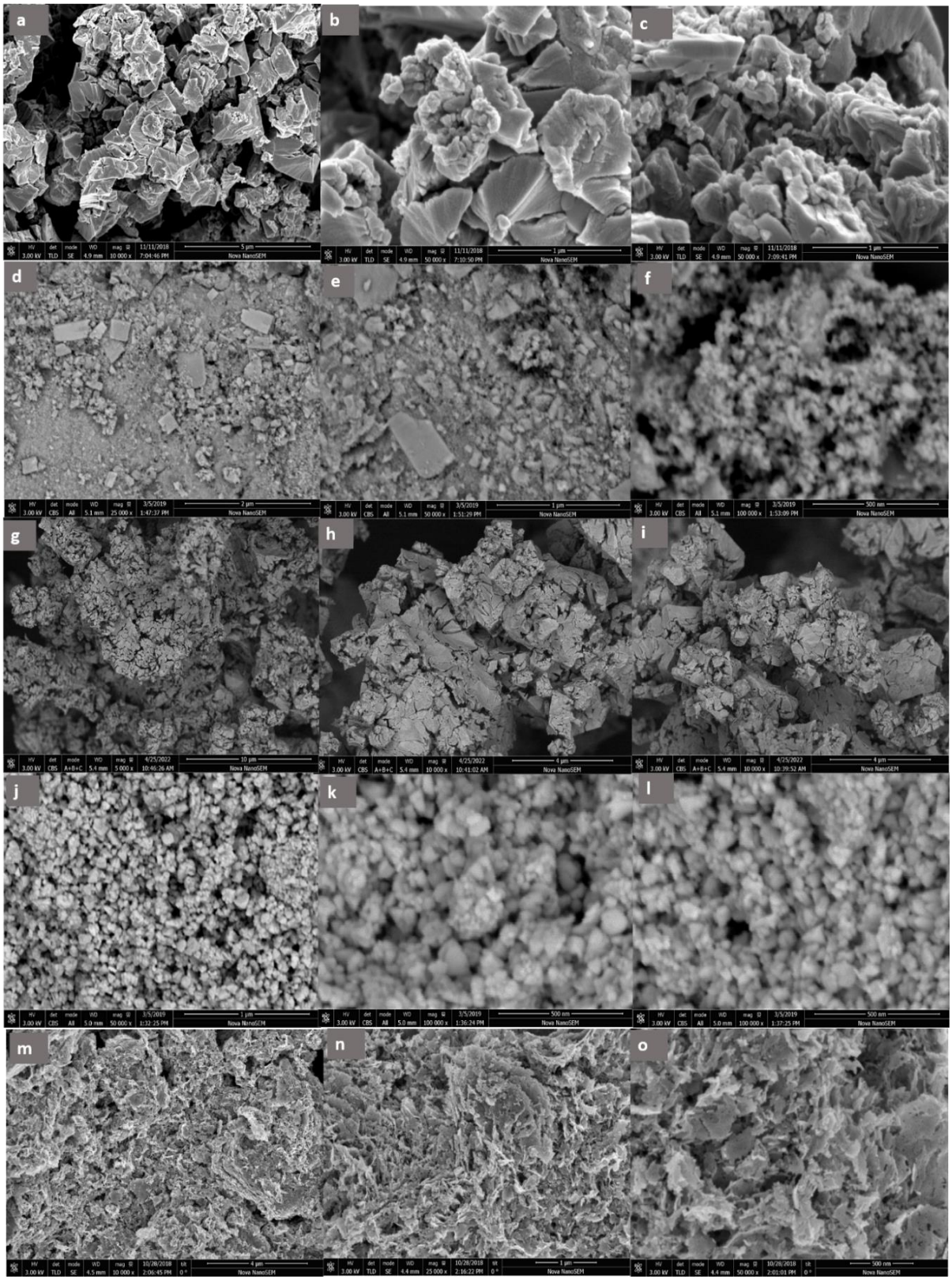

Figure 29. SEM images illustrating the effect of various NaOH concentrations on ZnO morphologies using zinc acetate dihydrate as zinc source: (a, b, c) 0.25 M of NaOH at 10,000×,

25,000× and 50,000× magnifications, respectively; (d, e, f) 0.5 M of NaOH at 25,000×, 50,000× and 100,000× magnifications, respectively; (g, h, i) 0.75 M of NaOH at 5,000×, 10,000× and 25,000×, respectively; (j, k, I) represented 1 M NaOH at 50,000×, 100,000× and 100,000× magnifications, respectively; (m, n, o) SEM of different additive types of 1 M of sodium hydroxide and zinc acetate dihydrate at 10,000×, 25,000× and 50,000× magnifications, respectively.

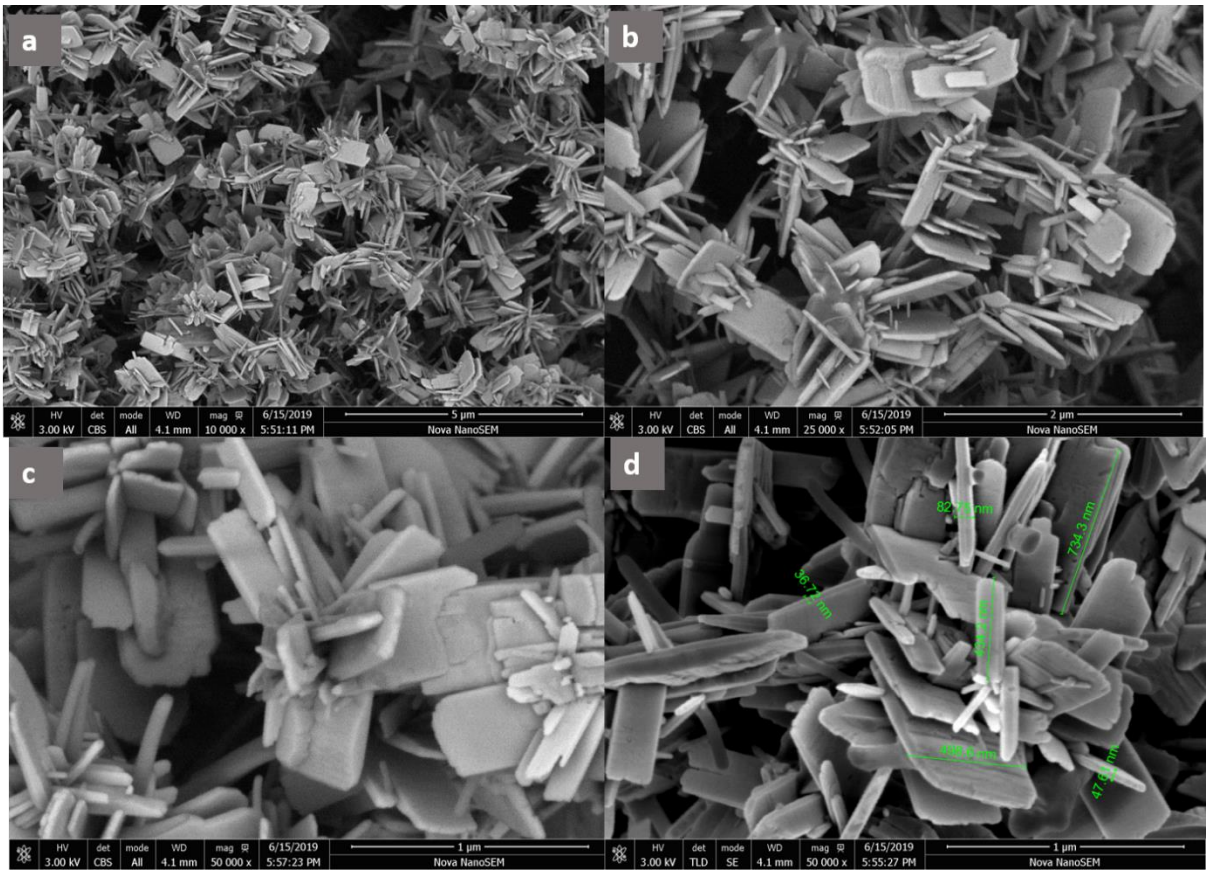

Figure 30. Zinc oxide particles prepared by reflux methods using (0.3 M zinc acetate dihydrate and 3 M of sodium hydroxide) at (a) 10,000×, (b) 25,000× and (c, d) 50,000× magnifications.

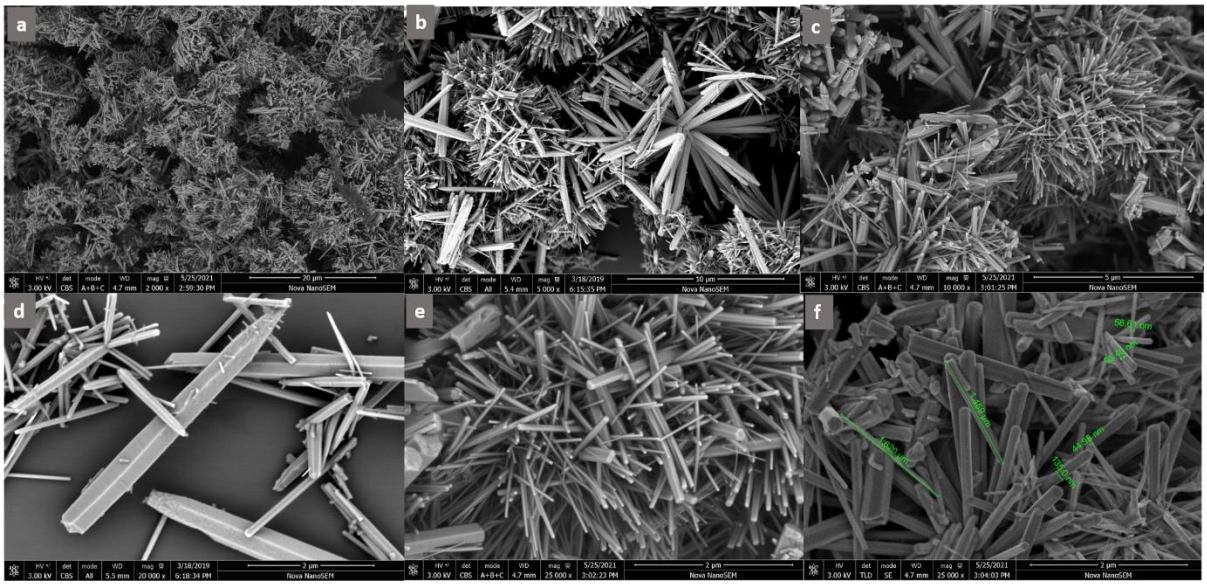

Figure 31. Zinc oxide reflux method with different additives (0.3 M zinc acetate dihydrate on 3M of sodium hydroxide). Different magnifications demonstrated flower shape particles consisting of needles at (a) 1,000×, (b) 5,000×, (c) 10,000×, (d) 20,000×, (e) 25000× and (f) 250,000× magnifications.

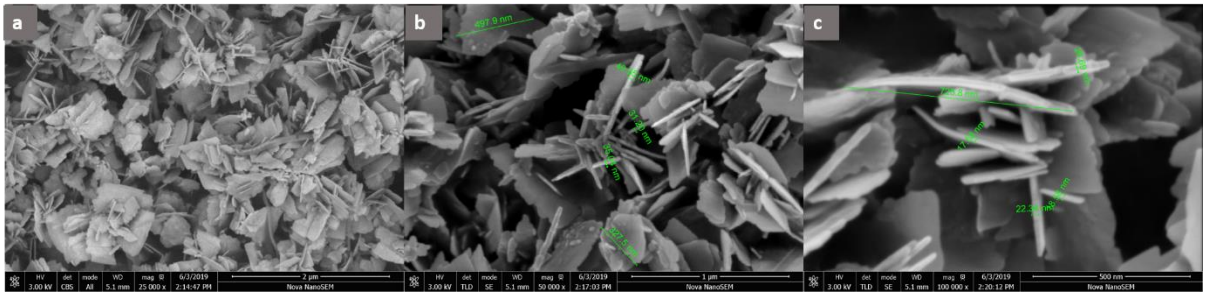

Figure 32. SEM images of zinc oxide prepared with sodium dodecyl sulphate SDS used as a surfactant in reflux method with 0.3 M of zinc acetate dihydrate and 3 M of sodium hydroxide at (a) 25,000×, (b) 50,000× and (c) 100,000× magnifications.

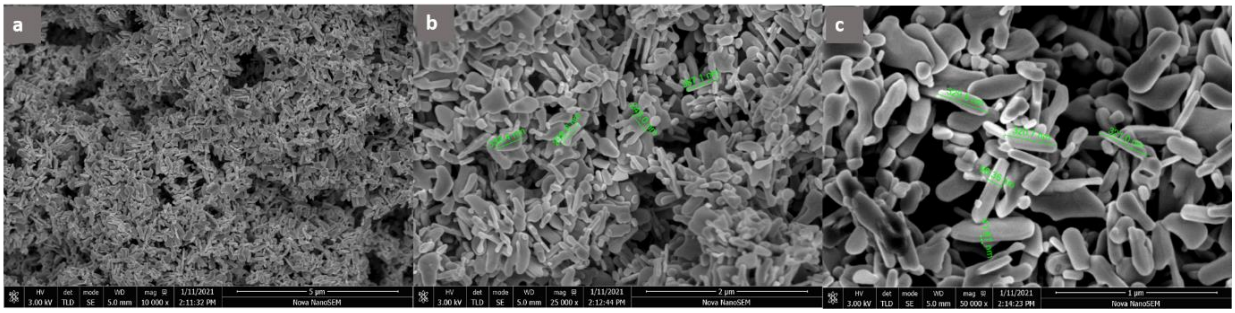

Figure 33. SEM images of zinc oxide prepared by (0.3 M of zinc acetate dihydrate with 3 M sodium hydroxide) via hydrothermal method at (a) 10,000×, (b) 25000× and (c) 50,000× magnifications.

First, the current study used zinc acetate dihydrate without a precipitation agent to study how the precipitation agent could affect the final morphology. In Experiment 1, needle-shaped particles were obtained using only zinc acetate, without using any precipitation agent (Figure 28 a−c). The needle shape had been observed, which could be a reason for the prolonged time that destroyed the flower shape system. According to Shen et al., 8 hours spent in the reaction in the is the ideal condition in this case [177].

ZnO NPs were synthesised using the direct precipitation method at ambient temperature. This method allowed several useful features, such as the large number of ZnO NPs that could be obtained with simple routes, low cost and the precursors having a high purity of zinc acetate dihydrate with sodium hydroxide.

This study revealed the effect of using various concentrations of NaOH (0.25, 05, 0.75 and 1 M) as a precipitation agent, with a constant concentration of zinc acetate dihydrate Zn $(CH_3CO_2)_2 \cdot 2H_2O$ (0.05 M), on the final morphology of ZnO NPs. This study demonstrated that the presence of NaOH played a vital role in the final morphology of zinc oxide when using zinc acetate was used as a zinc resource.

The effect of NaOH concentration as a precipitation agent on zinc oxide morphology was investigated at room temperature. The FESEM/SEM results in Figure 29 revealed that several shapes could be obtained, such as sheet, irregular clusters and cauliflower shape.

In Experiment 2, as shown in Figure 29 (a, b and c), when using 0.25 M NaOH, the zinc oxide morphology was similar to an irregular cluster with pores on the particles. Recent studies have shown that the activities and the selectivity of porous ZnO nanostructures were much better than nonporous ZnO NPs, because the porous structures could create tunnels and channels that improve durability and dispersibility, as well as decrease toxicity compared to nonporous ZnO NPs. The settlement of ZnO particles shown in these results was due to the agglomeration phenomenon as a result of the large surface area and high surface energy [178].

When the concentration was 0.5 M NaOH, sheet-shaped NPs were observed, as shown in Experiment 3, SEM Figure 29 (d, e, f) with platelet morphology and rectangle shape. The particle sizes were approximately 400–450 nm. This illustrated the effect of NaOH on the final zinc oxide morphology when using the precipitation method.

In contrast, the use of 0.75 M NaOH generated irregular and informal-shaped NPs (Experiment 4; Figure 29 (g, h and i)). This verified the effect of agglomeration in some surface areas and could have been a result of calcination-enhancing distortion in some parts.

When a concentration of 1 M NaOH was used (Experiment 5 – Figure 29 (j, k and l)), cauliflower-shaped NPs measuring 100−300 nm were observed. This result was similar to that of Moghri et al., who used a concentration ratio of 1:2 of NaOH. Moghri et al. showed a spherical shape with a size of 75 nm at the same NaOH concentration used in the current study [96]. Moreover, having a flower-shaped zinc oxide morphology (in this case, cauliflower shaped) led to obtaining a high surface-to-volume ratio in the presence of a high concentration of sodium hydroxide in the solution [179].

In Experiment 6, adding different types (add exchange) zinc acetate dihydrate on the sodium hydroxide, FESEM/SEM results, Figure 29 (m, n and o) also showed very wide particles and non-uniform morphology in some areas with different shapes (e.g., platelets), numerous pores with flaky and crust particles, and some areas with an agglomeration of particles appearing on the surface. This was consistent with the findings of Dalia et al. [180]. and Moghri et al. [96] for concentration ratios greater than 1:2 [96, 180].

In Experiment 7, zinc acetate dihydrate was used as a Zn^{2+} source, along with NaOH. Reflux was carried out at 90 °C for 30 minutes. Morphology according to SEM results. Figure 30 (a−d) showed a flower-like shape consisting of platelets with a thickness of approximately 30–80 nm in some particles that could be considered more like 2D-shaped particles, such as zinc oxide NPs.

Experiment 8 was performed under the same conditions as in Experiment 7, except zinc acetate was added to sodium hydroxide. Thus, the source of the zinc was the same, but the sequence was different from Experiment 7. The SEM images in Figure 31 (a–d) showed flower-shaped settlements, consisting of pointed nanorod petals, which were formed via combination around a single centre to form a whole 'flowery' spherical shape with lengths of 2–5 µm [181]. Barhoum et al. [39] and Wahab et al. [39, 173] reported that this could occur in only 30 min. In the case of zinc acetate dihydrate, with different concentration ratios, the permanent shape was a paired hexagonal stacking rod with an average length of 9 µm. In addition, small irregular shapes on the permanent shape were also observed, which is consistent with our results [71].

In Experiment 9, SDS was added as a surfactant in the refluxing method halfway through the time of adding NaOH to the acetate dihydrate solution. In order to avoid stacking among the particles, SDS was added as a surfactant. Figure 32 (a–d), showed a refluxing time of 30 minutes at 90 °C without calcination due to adding SDS. Importantly, a thick white foam precipitate was observed; the solution then underwent refluxing for 30 minutes at 90 °C. It was

observed that SDS served as an organiser and that the particles had a microsized flower shape consisting of a 2D sheet with a thickness of 40–20 nm and a length of 150–500 nm [182].

Furthermore, using hydrothermal methods in Experiment 10, the dominant shape was a platelet shape. In general, the morphology of these particles was irregular sheets and rods with no sharp shape and sizes ranging from 200 nm to 400 nm in length and approximately 30 nm to 90 nm in thickness. Figure 33 (a–c) represents various magnifications. The outcome from Experiment 10 had morphology results similar to those of Gusset et al. [183] in the hydrothermal method (nanoflake-shaped). In contrast to the current study that used the hydrothermal method, the use of zinc acetate in the sol–gel method resulted in a final morphology of a nanoflower shape, indicating the importance of the methods used, even when the same zinc source was used [184].

In conclusion, the nanoplate shape was dominant, even when different methods were used in the addition of sodium hydroxide to zinc acetate. This indicated that, according to the current study conditions, the major factors to control the generation of a specific shape were the precipitation agent, sodium hydroxide, particularly its concentration, and the sequence of additions had been applied during the reaction.

3.1.2 Zinc oxide using Zinc nitrate hexahydrate and sodium hydroxide by precipitation, reflux and hydrothermal method

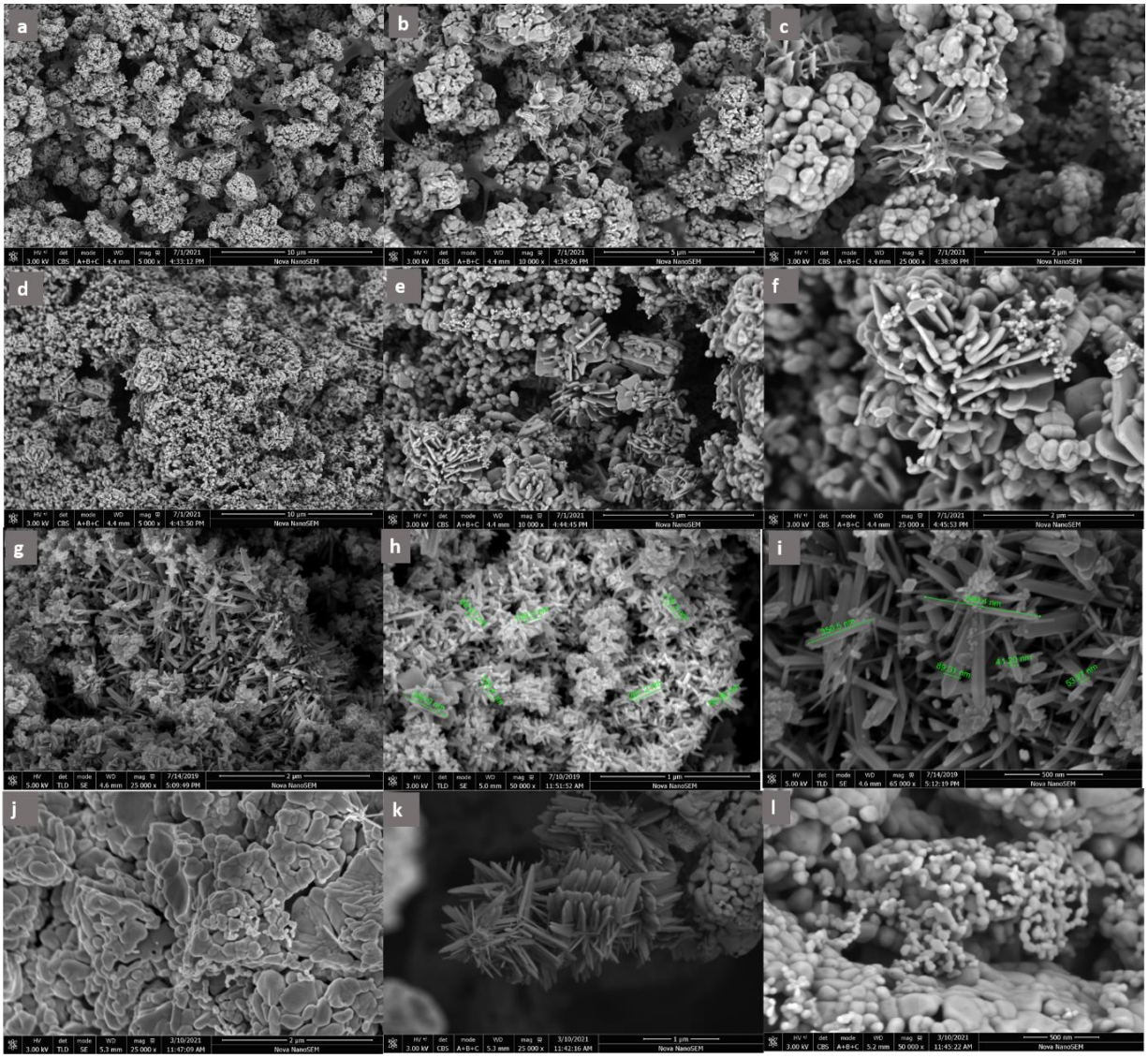

Figure 34. SEM images of ZnO NPs prepared by (0.5 M of zinc nitrate hexahydrate and 1 M of sodium hydroxide) (Experiment 11) at (a) 5,000×, (b) 10,000× and (C) 25,000× magnifications. Zinc oxide morphology by applying different addition types in precipitation method (Experiment 12) at (d) 5,000×, (e) 10,000× and (f) 250,000× magnifications. Experiment 11: Reflux method as shown in (g) 25,000×, (h) 50,000× and (i) 65,000× magnifications. Applying different additive types (added NaOH on Zn $(NO_3)_2 \cdot 6H_2O$, then added Zn $(NO_3)_2 \cdot 6H_2O$ on NaOH in the reflux method at different magnifications and (j, k, l)

zinc oxide using Zn $(NO_3)_2 \cdot 6H_2O$ and NaOH by the hydrothermal method at (j) 25000x, (k) 25,000x, (l) 50,000x magnifications (Experiment 15).

The results from Experiments 11 and 12 were represented by the SEM images of ZnO NPs when zinc nitrate hexahydrate was used. Figure 34 (a–c) demonstrate that when zinc nitrate was added to NaOH, the final morphology of the NPs was flower-shaped particles consisting of semi-pointed leaves with randomly scattered nanospheres. Figure 34 (d–f) illustrate the zinc oxide NPs when NaOH was added to zinc nitrate. The final shape was a flower-shaped settlement consisting of randomly distributed platelets and spheres. Furthermore, using refluxing methods, as shown in Figure 34 (g–i), led to a permanent flower-shaped morphology consisting of needles, which meant that the refluxing method increased the possibility of forming needles as a regular shape [185, 186], especially in alkaline mediums. This was because a hexagonal shape is the original shape of zinc oxide, as previously mentioned in Figure 28, and no other factor affected zinc oxide morphology when using zinc acetate dihydrate. When zinc nitrate was used as a zinc resource with NaOH, the possibility of forming needles increased using reflux methods compared with precipitation methods when the NaOH solution was in the vessel reaction (NaOH) in this study. This result was similar to the one using zinc acetate dihydrate with sodium hydroxide in the reflux method. The results suggested why platelets or needles are formed according to the different additives in the reflux method. The SEM images in Figure 34 (m–o) illustrate the morphology of zinc oxide when hydrothermal methods were used. In Experiment 15, zinc nitrate hexahydrate was used as a zinc resource with NaOH, as shown in SEM images pointing to the appearance of two different kinds of morphologies for ZnO NPs. Irregular flower shapes with lengths of approximately 1 μm to 2 μm were obtained. The flower-like structures consisted of needles approximately 700 nm to 1 μm in length, as shown in Figure 34 (j–l).

Kumar et al. studied the effect of nitrate and acetate ions as an anion ratio on the final morphologies of zinc oxide structures. They found that the presence of these anions could alter the final resulting structure of zinc oxide, depending on the anion ratio, the presence of sodium hydroxide, the method for zinc oxide synthesis (e.g., hydrothermal, ultrasonic) and the chemicals used, which means that these factors as internal and external factors were important during zinc oxide synthesis [187].

3.1.3 Zinc oxide using zinc nitrate hexahydrate and ammonium carbonate by precipitation method

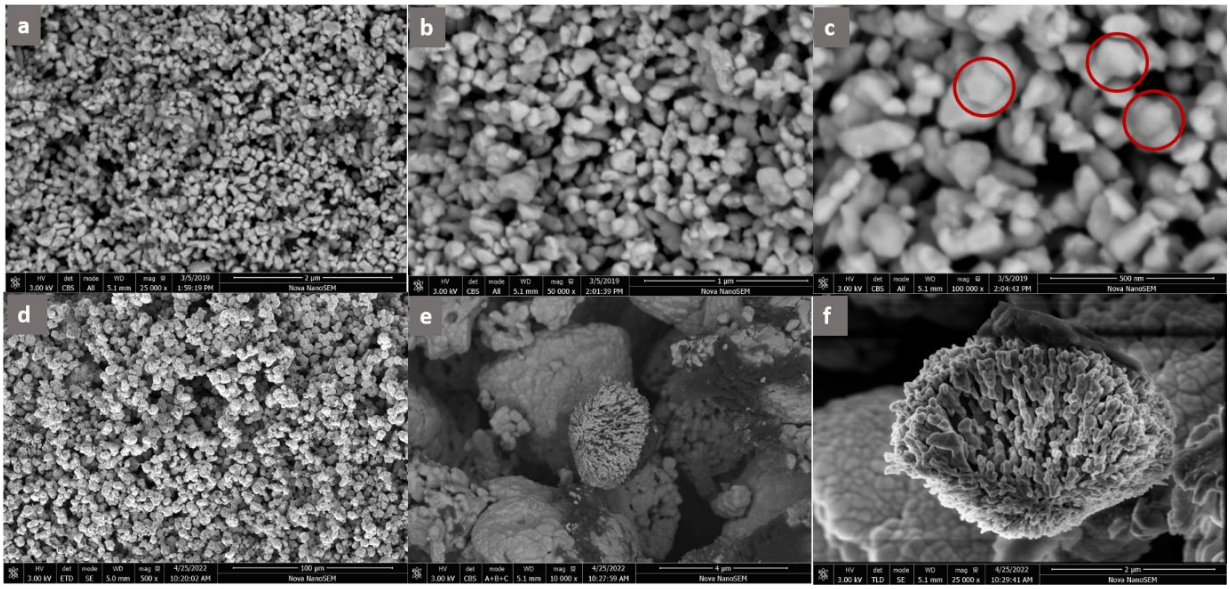

Figure 35. SEM images of ZnO NPs prepared by (1 M of zinc nitrate hexahydrate and 1 M of ammonium carbonate) at (a) 25,000×, (b) 50,000× and (c) 500,000× magnifications. Applying

different additive types at (d) 5000×, (e) 10,000× and (f) 25,000× magnifications.

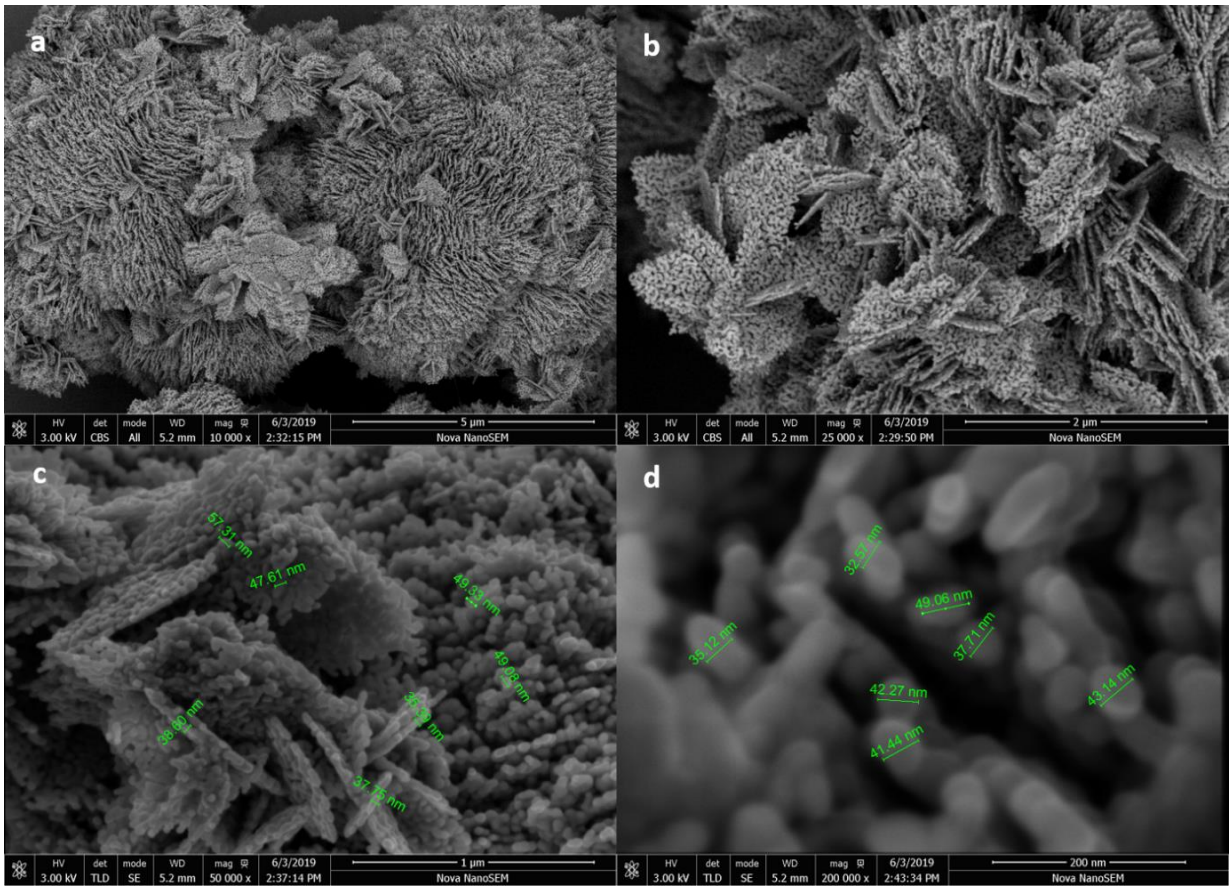

Figure 36. SEM images of zinc oxide prepared by (1 M of zinc nitrate hexahydrate and 1 M of ammonium carbonate calcinated at 250 ℃ for 4 hours at (a) 10000× (b) 25000× (c) 50000× (d) 200000× magnifications by reflux method.

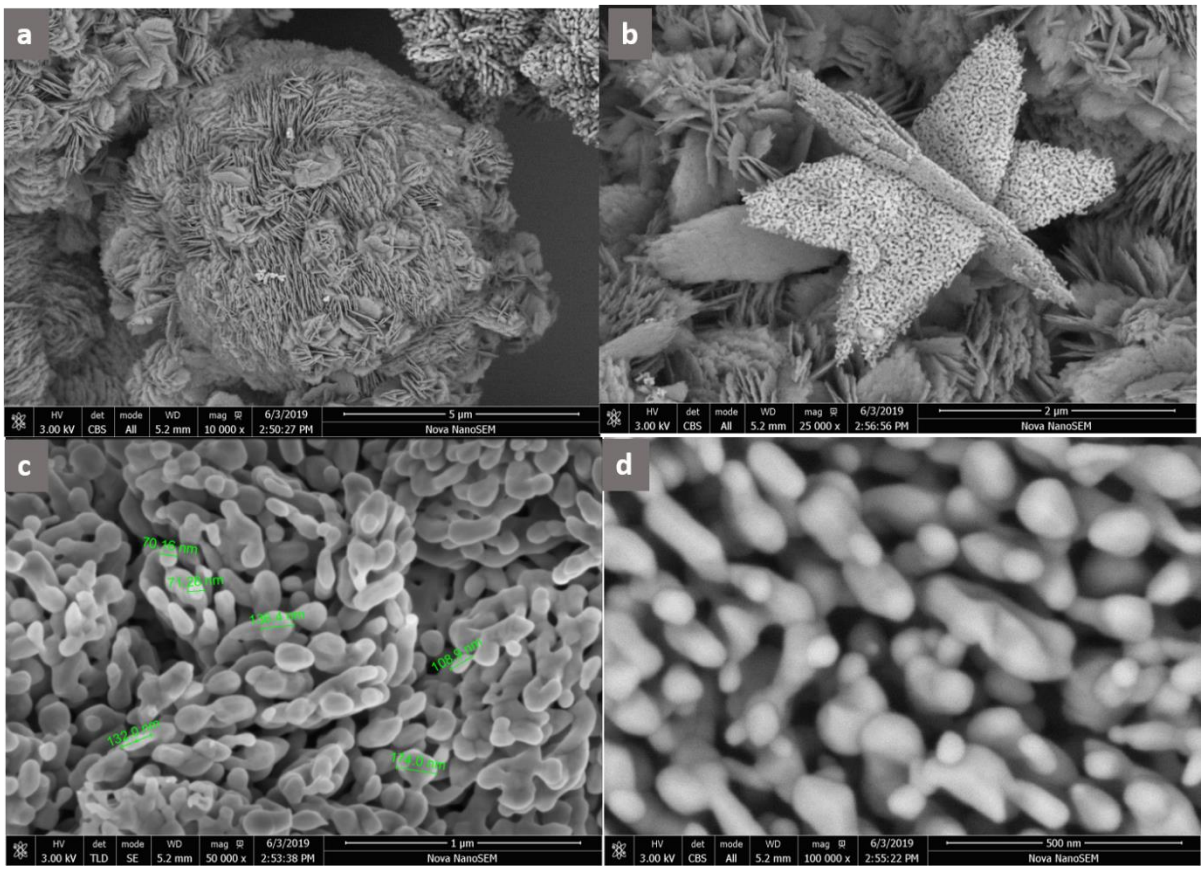

Figure 37. SEM images of zinc oxide prepared by (1 M of zinc nitrate hexahydrate and 1 M of ammonium carbonate calcinated at 550 ℃ for 4 hours) at (a) 10000× (b) 25000× (c) 50000× (d) 100000× magnifications by reflux method.

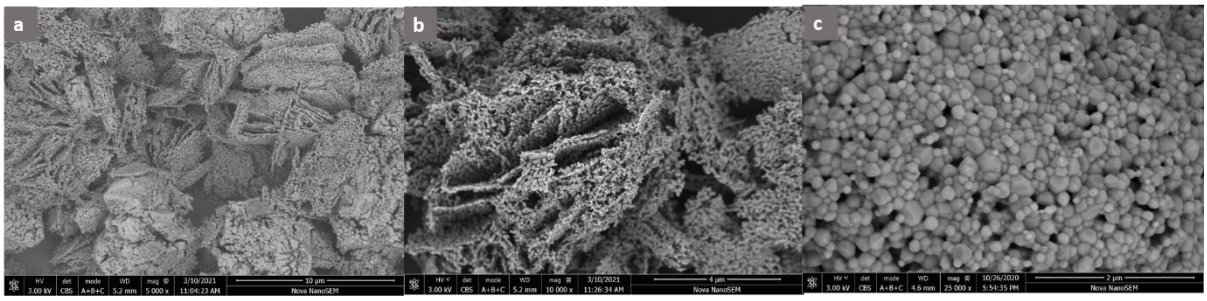

Figure 38. SEM images of zinc oxide prepared by (1 M of zinc nitrate hexahydrate and 1 M of ammonium carbonate) at (a) 5000x, (b) 10000x and (c) 25000x different magnifications by hydrothermal method.

As shown in Figure 35 (Experiments 16 and 17), two precipitation techniques were performed. In Experiment 16, zinc nitrate was added to the precipitation agent $(NH_4)_2CO_3$. Figure 35 (a–

c) showed a bifrustum-like ZnO morphology, as shown in the red circles (Figure 35 c, 100,000×). These structures were linked to one another to form a ring. The distribution, according to the SEM images, appeared to show the same arrangement for the nature of the particles (separated rings).

In Experiment 17, various additives were used and precipitation methods were performed. As shown in Figure 35 (d–f), the final morphology was irregular, with some dark points that could be due to some chemical elements hinged or trapped during the reaction. This is supported by the observation in Experiment 17, in which during the refluxing method, effervescence of releasing gas was observed when the product was transferred to the three-neck conical flask under 90 ℃ inside the conical tube. Hence, this kind of reaction was excluded in the step of the refluxing methods. In addition, this study attributed the dark spots in Figure 35 (e) to the gases released. This is supported by the refluxing method in the next discussion.

In Experiments 18 and 19, ZnO NPs were prepared from ammonium carbonate and zinc nitrate using the reflux method. After obtaining the white precipitate produced in Experiment 18, calcination was performed for 4 hours at 250 °C. In Experiment 19, after the same reflux conditions to obtain the precipitate, a 500 °C calcination temperature was used for 4 hours. As shown in Figure 36 (a–d) and Figure 37 (a–d), the new morphology, that of a flower shape, consisted of stacked platelet pores shaped in what looked like a coral shape. Recent studies have shown that the presence of porous and the activities and selectivity of porous ZnO nanostructures were much better than nonporous ZnO NPs because the porous structures could create tunnels and channels that improved durability and dispersibility and decreased toxicity compared to non-porous ZnO NPs.

This result, compared with Experiment 16, was totally different and is unreported in any published paper. Furthermore, using ammonium carbonate with zinc acetate to synthesise zinc oxide using the reflux method was a new procedure in the scientific field. Dmitry et al. (2021)

synthesised zinc oxide using ammonium carbonate as a precipitant with zinc acetate dihydrate as a zinc resource and tin (IV) chloride pentahydrate ($SnCl_2 \cdot 5H_2O$) using a precipitation method at very high temperature from 800 °C to 1300 °C [188]. Zeljković et al. (2022) used ammonium carbonate and zinc nitrate to prepare n-ion-doped zinc oxide using a mechanochemically decreased solvent-deficient method at several calcination temperatures of 300, 400, 500 and 600 °C. Platelet morphology was obtained [189]. Tanwar and Dhirendra (2021) prepared zinc oxide via the hydrothermal method at 200 °C for 10 hours in an oven and generated platelets [190].

In the current study, a simple technique was used at a low temperature to obtain a new zinc oxide morphology. As previously mentioned, zinc oxide particles with novel shapes were obtained in Experiment 16. This could be attributed to the additional step of refluxing (solution process). In this step, the solution was stirred at 90°C. Thus, the varied new conditions (refluxing, 90 °C for 30 min, increasing the temperature and continuous stirring) affected the obtained morphologies. The SEM images in Figure 36 (a–f) and Figure 37 (a–f) clearly show coral-shaped NPs in a settlement flower shape consisting of a packed sheet with pores with a specific shape that repeatedly in all zinc oxide particles. Figure 37 (d) demonstrated the morphology of these particles that looked like a butterfly. The thickness was 35–56 nm, and each sheet's length was approximately 1 to 1.5 μm, with a porous consistency as a result of the entangled rings. In Experiment 16, when the obtained morphology was a bifrustum, the shape was stacked as randomly separated rings. However, in Experiments 18 and 19, these rings appeared under an oriented attachment. This was induced by refluxing and exposure to 90 °C for 30 min, which encouraged the particles to achieve a different morphology. Crystal growth relied on the chemical composition of the surface particles, the structure of the chemical compound, and the interfacial interaction between the crystal morphology and the ambient solution. These agents may also be factors in the formation of ring and hemisphere shapes. As

previously mentioned, when doing the experiment using different sequencing of reactants, adding ammonium carbonate to zinc nitrate hexahydrate, the reaction showed an unstable solution with the sound of crackling. This could be due to the presence of some gases in the reaction, due to nitrate ions that could surround ammonium ions in the solution. In addition, zinc nitrate's nature as an endothermic compound that hence, according to Le Chatelier's principle, when the reaction is endothermic, more reactant means the reaction tends more towards the side reactions. The suggestion in this case that the end of this reaction was not complete because of the presence of nitrate ion could hinder some steps in the reaction to be continued until the end. Another suggestion was the nature of the precipitation agent. $(NH_4)_2CO_3$ was working as a base (pH 8.6) as well as during the reaction there were two steps to get carbon dioxide at the end, first to convert to ammonium bicarbonate $(NH_4)\ HCO_3$ then to CO_2 which made the process of releasing carbon dioxide hindered by the chemical properties of the reactants and the nature of the method. This could lead to that in the reflux method, the reaction until the end is only achieved by (adding ammonium carbonate to zinc nitrate (but the vice -versa it is not necessarily true). Furthermore, Figure 38 showed in some areas various hexagonal, bifrustum and spherical structures with sizes between 50 nm and 400 nm, which were never observed in refluxing or direct precipitation methods.

3.1.4 Effect of time on ZnO using ammonium carbonate and zinc nitrate hexahydrate by reflux method

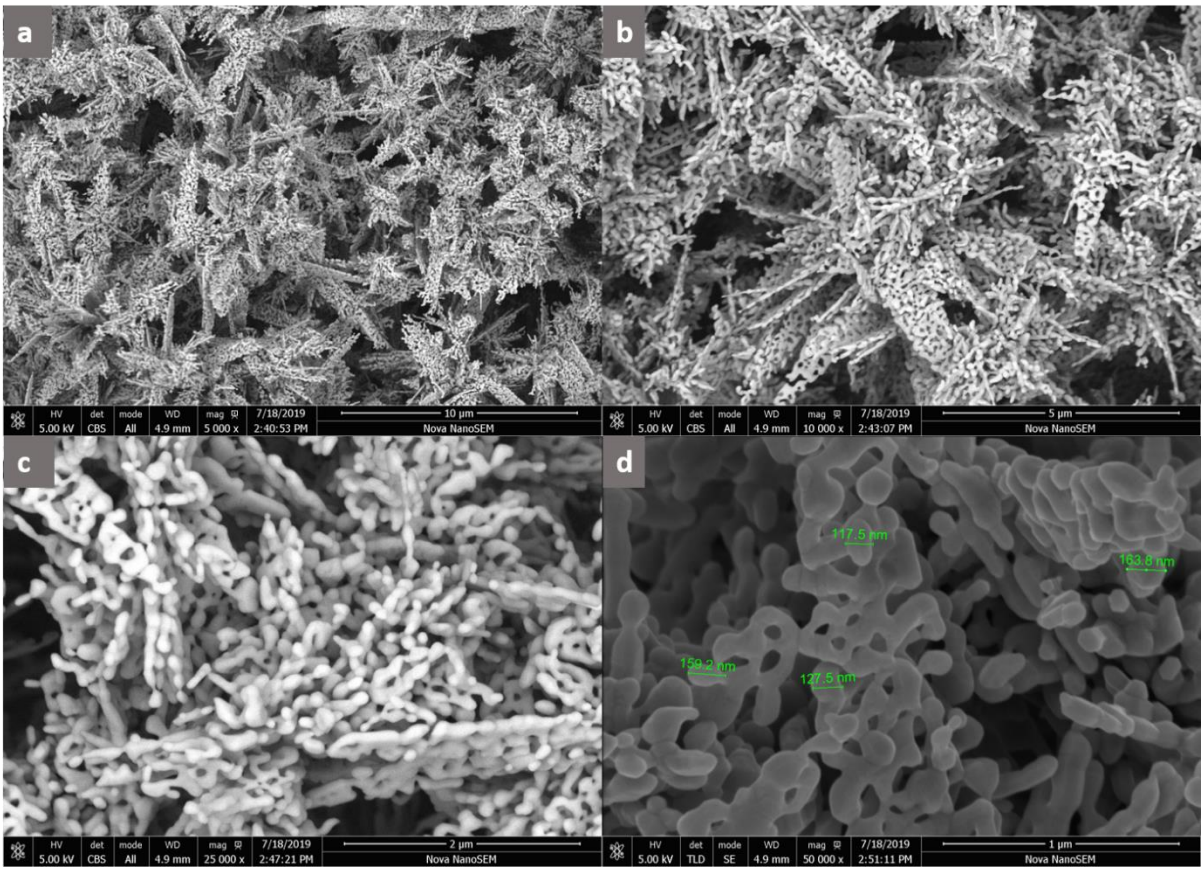

Figure 39. Effect of the reaction time, (5 minutes), on the zinc oxide particles produced in the reflux method when using 1 M of zinc nitrate hexahydrate and 1M of ammonium carbonate at (a) 5,000×, (b) 10,000×, (c) 25,000× and (d) 50,000× magnifications.

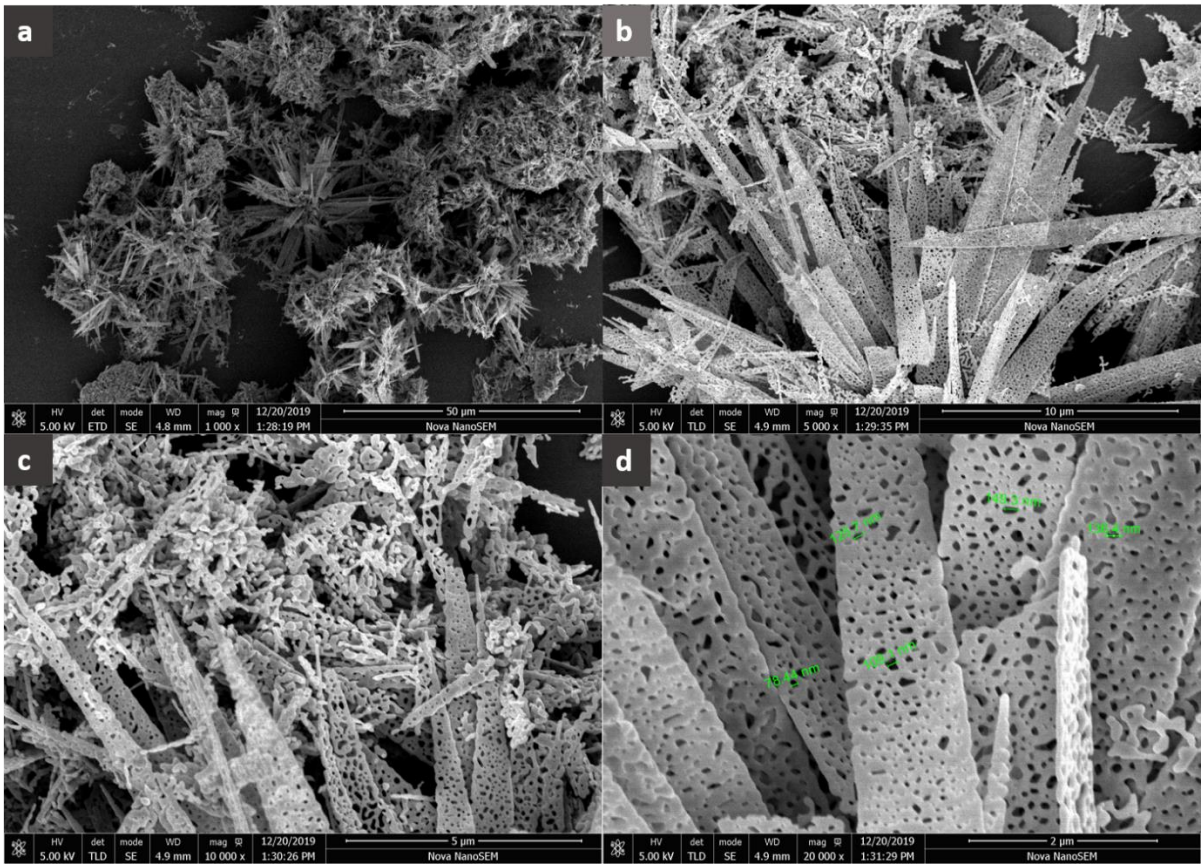

Figure 40 Effect of the reaction time (10 minutes) on zinc oxide particles in the reflux method using 1 M of zinc nitrate hexahydrate and 1 M of ammonium carbonate at (a) 1,000×, (b) 10,000×, (c) 5,000× and (d) 20,000× magnifications.

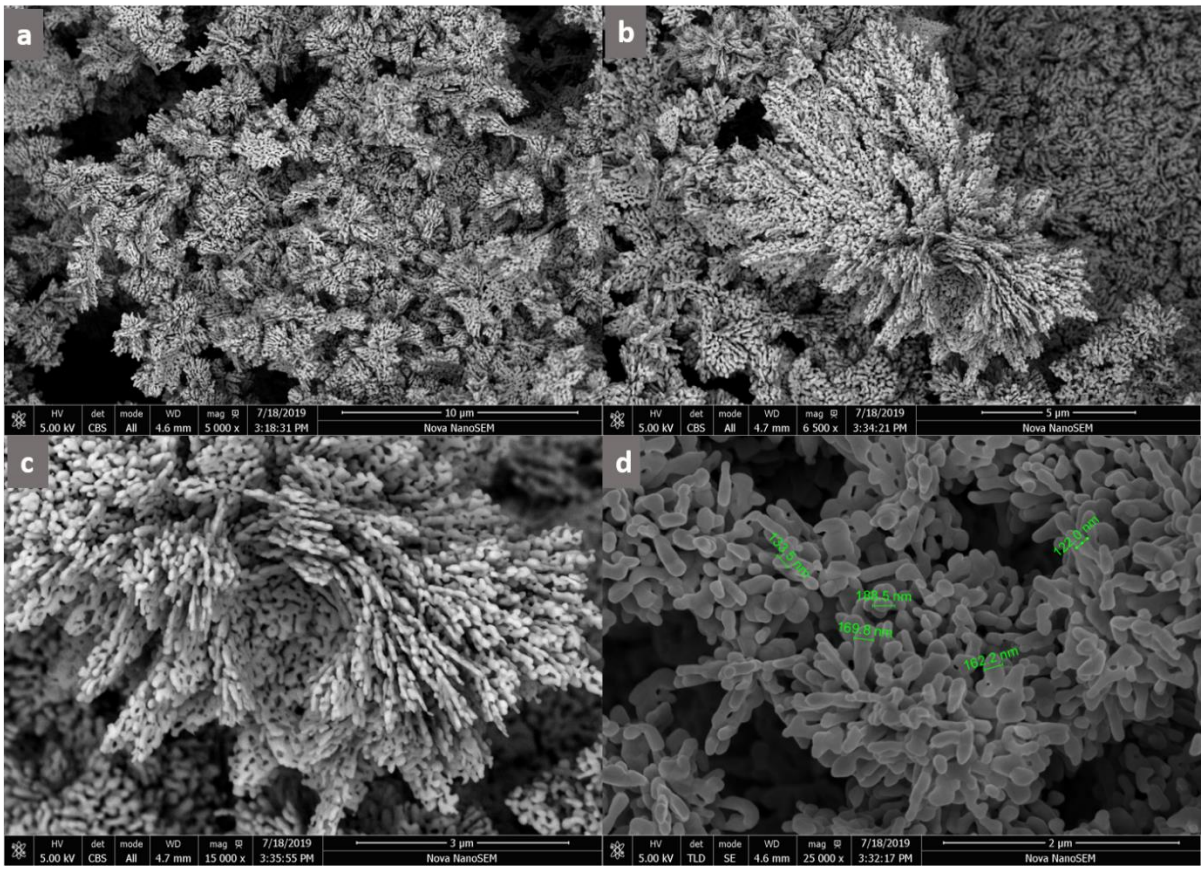

Figure 41. Effect of the reaction time (15 minutes) on zinc oxide particles in reflux method using 1 M of zinc nitrate hexahydrate and 1 M of ammonium carbonate at (a) 5,000×, (b) 6,500×, (c) 15,000× and (d) 25,000× magnifications.

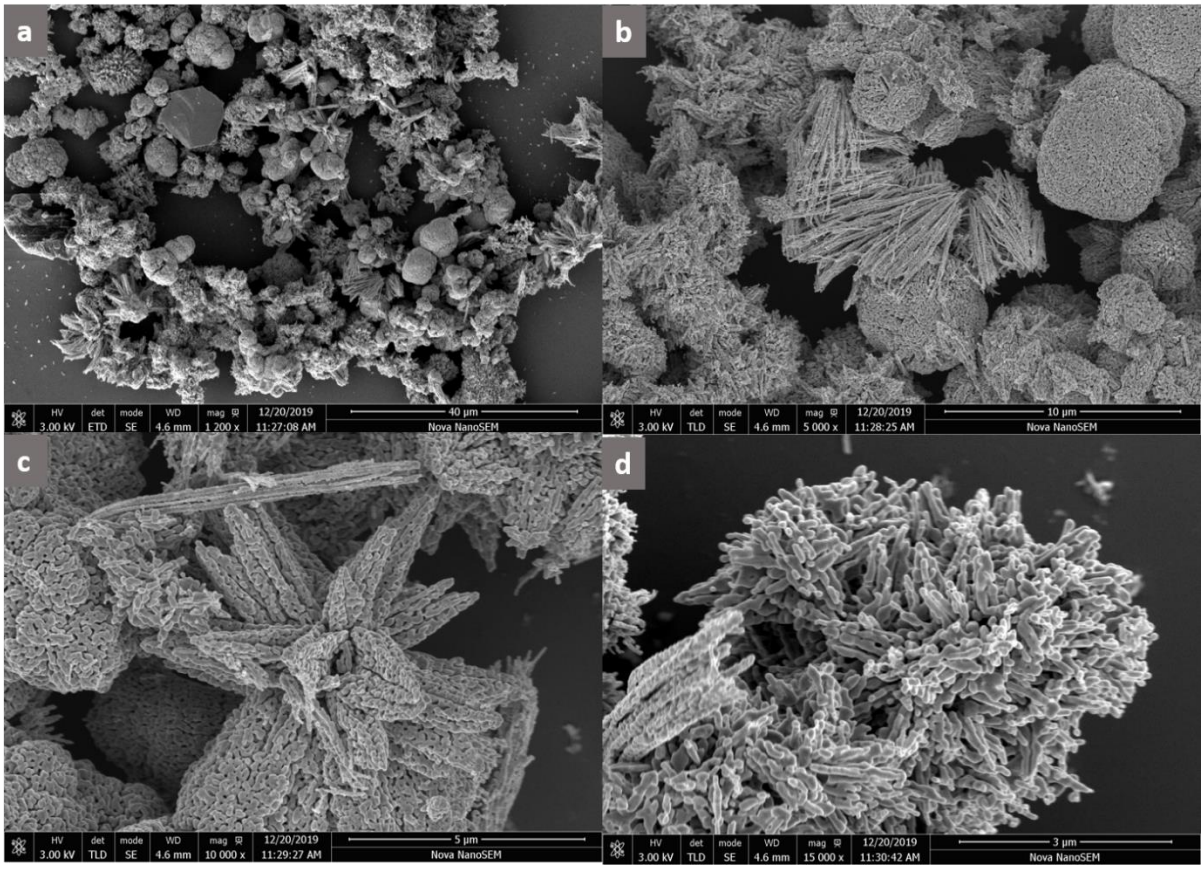

Figure 42. Effect of the reaction time (20 minutes) on zinc oxide particles in refluxing method using 1 M of zinc nitrate hexahydrate and 1 M of ammonium carbonate at (a) 1200×, (b) 5000×, (c) 10000× and (d) 15,000× magnifications.

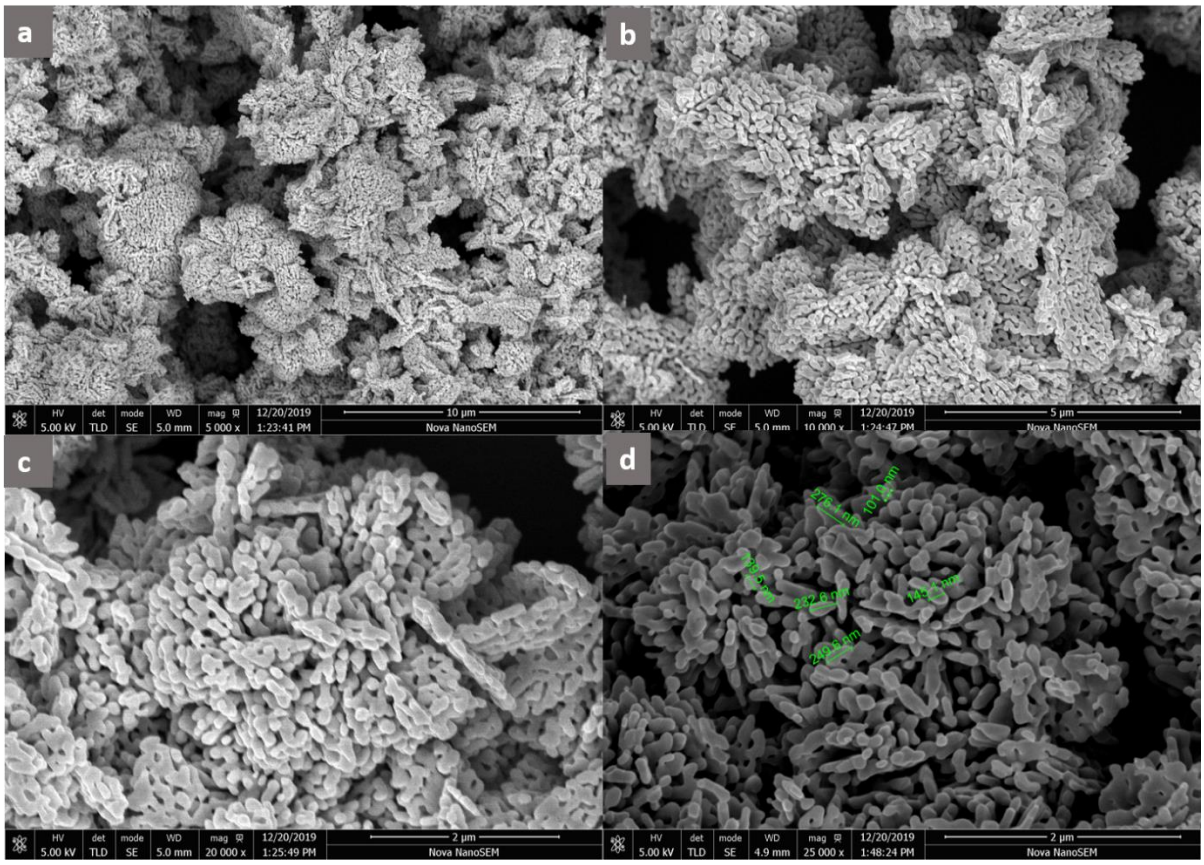

Figure 43. Effect of the reaction time (30 minutes) on zinc oxide particles in the reflux method using 1 M of zinc nitrate hexahydrate and 1 M of ammonium carbonate at (a) 5,000×, (b) 10,000×, (c) 20,000× and (d) 25,000×.

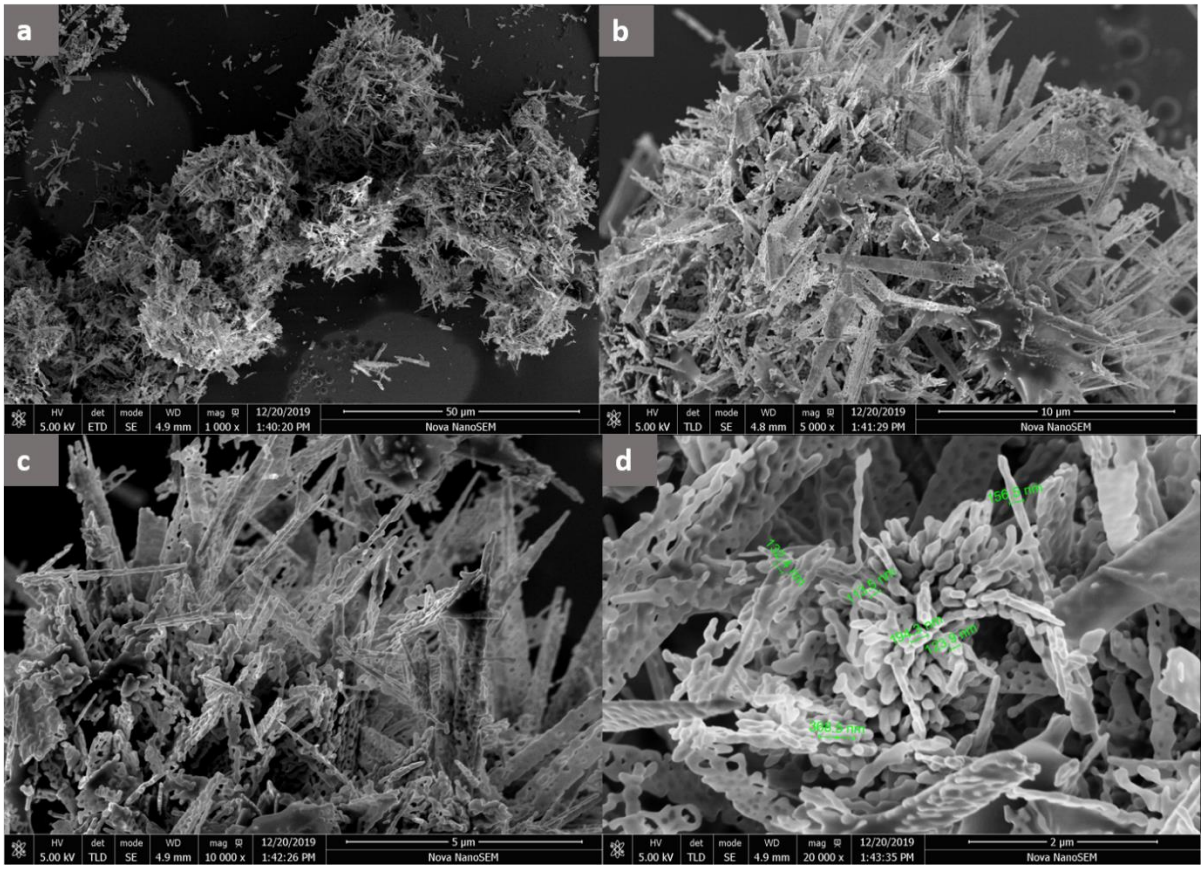

Figure 44. Effect of the reaction time (50 minutes) on zinc oxide particles in refluxing method using 1 M of zinc nitrate hexahydrate and 1 M of ammonium carbonate at (a) 1,000×, (b) 5,000×, (c) 10,000× and (d) 20,000× magnifications.

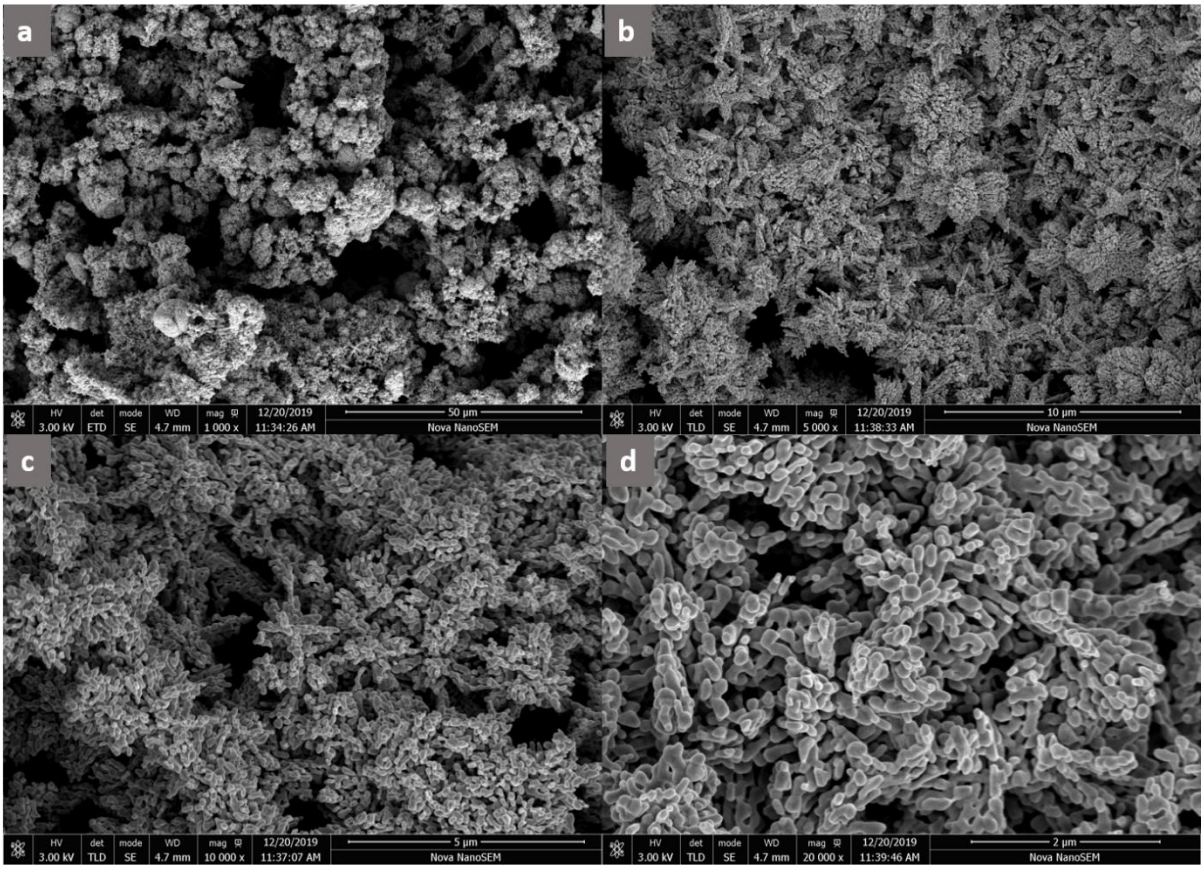

Figure 45. Effect of the reaction time (70 minutes) on zinc oxide particles in the reflux method using 1 M of zinc nitrate hexahydrate and 1 M of ammonium carbonate at (a) 1,000×, (b) 5,000×, (c) 10,000× and (d) 20,000× magnifications.

To understand the new morphology observed in Experiments 20–27, the effect of time on morphology and the growth of particles at 5, 10, 15, 20, 30, 50 and 70 minutes, for ZnO prepared from ammonium carbonate and zinc nitrate, via reflux for 30 minutes at 90 °C, followed by calcination (for 4 hours at 550 °C). The results are shown in Figure 39–44.

As shown in Figure 39 (a, b, d), at 5 minutes, the particles had tiny needle morphologies in some areas and an irregular shape in some particles. This could be a result of the short initial time (5 minutes). The particles had a thickness of 117–150 nm. Figure 40 illustrates that after 10 minutes, the morphology of the NPs was a flower consisting of needle porous sheets, which could have caused the stacked sheets to start forming during this time. At 15 minutes,

orientation and attachment to form a flower shape were observed (Figure 41). At 20 minutes, the particles had their own arrangements due to the factors that affected the growth process (Figure 42). After 30, 50 and 70 minutes, as shown in Figure 43, Figure 44 and Figure 45, respectively, the effect of oriented agglomeration was clear by increasing the time. At 50 minutes, the morphology was similar to the zinc oxide morphology at 10 minutes as a flower shape consisting of needle porous sheets as well as the zinc oxide morphology at 20 minutes but the needles at 50 minutes were sharper than the needles at 10 minutes and this could be due to the effect of the time. In addition, the flower shape consisting of needle porous sheets was the common structure morphology in this part using the reflux method. At 70 minutes, the particles start to lose their morphology due to the high time during the synthesis. In general, the zinc oxide particles prepared had spherical shapes, with sizes ranging from 3 μm to 5 μm. SEM results showed that each precipitated mass consisted of small hexagonal and bifrustum particles and spherical particles, with particle sizes ranging from 50 nm to 300 nm. Such results were similar to those of Dac *et al.*, who used the same precursors using the direct precipitation method [191].

After the previous survey of SEM results on ZnO, the study discussed the mechanism according to the final zinc oxide morphology obtained in this study.

The intrinsic crystal structure of ZnO plays a vital role in determining the final morphology of particles [56, 192]. At ambient temperature, zinc oxide nanoparticles showed some surface defects (zinc ion sites), which behaved as Lewis acids (had orbitals in its structures to accept electrons) and as Brønsted–Lowry acids that donated protons [193].

3.1.5 Suggested growth mechanism of flower shape

Even with numerous studies focusing on zinc oxide, there was a lack of an accurate understanding of the effect of some parameters during synthesis on zinc oxide structure, morphology and size [194]

ZnO had a zinc polar plane (0001) and an oxygen polar plane ($000\bar{1}$) with a nonpolar plane (1010). As a result, changing the polarities of the solvent led to changes in the characteristics of the crystal, as shown in the changes in the morphology of the ZnO crystal.

In polar solvents, the reaction tended to be stronger between the polar functional group in the solvent and the polar plane (0001), so the growth of the crystal tended to be towards the surface. In interface: solvent interactions, surface energy was known to vary according to the difference in the energy of crystal faces. Furthermore, some research revealed that solvent polarity had a significant role for example, the presence of weak polar solvent led to long rod morphology [66]. In addition, the high polarity solvents may have caused decreased growth of the ZnO crystal [195] [196]. During the process of forming ZnO particles, the polar planes (0001) had a high surface energy compared with the nonpolar planes (1010). In the presence of anions containing oxygen atoms in the solutions, the ZnO crystals tended to decrease the total surface energy by spinning the growth along the polar direction [0001] to form a rod shape (Figure 46) [186]. Khan et al. [197] showed that according to Equation (7), the presence of Zn $(OH)_2$ produced the compound $[Zn(OH)_4^{2-}]$ and ZnO due to electrostatic forces between ions. $[Zn(OH)_4^{2^-}]$ ions adsorbed on the ZnO surface led to a decrease in surface energy, which elongated along the c-axis or the [0001] directions [198]. Zn^{2+} is known to react with OH^- to form tetrahedral $Zn(OH)_4^{2-}$ complexes, which become the growth unit in the formation of zinc oxide.

Dokmai et al. suggested that the zinc oxide microprisms that remained from the zinc oxide hexagonal base could be exposing the polar planes (0001) and $(000\bar{1})$ as active polar planes together with the side non-polar face $(10\bar{1}0)$ towards the direction of growth along the c-axis. Furthermore, they suggested that the presence of some nanorods in the final morphology was considered a result of growing out of the base nuclei [193].

In this kind of solution (varying pH values of ≤ 7 or ≥ 7), the following equations were suggested:

$$Zn^{2+} + 2OH^{-} \leftrightarrow Zn(OH)_2 \quad (7)$$

$$Zn(OH)_2 + 2OH^{-} \leftrightarrow [Zn(OH)_4]^{2-} \quad (8)$$

$$[Zn(OH)_4]^{2-} \leftrightarrow (ZnO_2)^{2-} + 2H_2O \quad (9)$$

$$(ZnO_2)^{2-} + 2H_2O \leftrightarrow ZnO + 2OH^{-} \quad (10)$$

$$ZnO + OH^{-} \leftrightarrow ZnOOH^{-} \quad (11)$$

$$ZnOOH^{-} + Na^{+} \leftrightarrow ZnOOH^{-}Na^{+} \quad (12)$$

As shown in Equation (8), the complex compound $[Zn(OH)_4]^{2-}$ could be formed using another compound, such as $Zn(OH)_2$ or $[Zn(OH)_4]^{2-}$ and $Zn(OH)^{+}$. Furthermore, the type of formula that occurred depended on some parameters during the chemical reaction, such as pH and concentrations of (OH^{-}) and (Zn^{2+}) [180].

The concentrations of zinc and hydroxide ions caused the maximum degree of supersaturation to be reached, which was the initial growth step [199].

Moreover, some research has indicated that a higher pH value leads to the formation of more intermediate compounds, which increases the possibility of gaining a large crystal size [200].

However, differences in growth mechanisms, which led to different zinc oxide structures, could be affected by the speed of reactants, such as when sodium hydroxide was added to zinc acetate

during the reaction, as described by Ong et al. in the case of adding NaOH slowly (i.e. a slow addition rate), the favoured growth was in a constant direction [46]. Hence, the addition of the precursors zinc acetate and sodium hydroxide at the same concentration could lead to a rapid reaction, and the growth direction along the polar plane (0001) was preferred to form hexagonal prisms.

In the current study, it appeared that the presence of NaOH (high polarity and strong alkaline) in a reaction vessel enhanced the polarity around the ZnO formed. Furthermore, NaOH was an exothermic compound that led to more energy inside the reaction, so the system tried to decrease the high surface energy on the polar Zn^{2+} plane and then spinning along the plane (0001) caused the hexagonal shape to shift into a rod shape (Figure 46). Moreover, as the flower that had been obtained was a kind of 3D shape, this behaviour of ZnO crystals in the system evolved into needle-like ZnO and arrow-like ZnO to form packs of flower shapes [40].

Shen et al. attributed the flower shape consisting of nanorods to the molar ratio; when the OH^- /Zn^{2+} ratio was 2, this led to settlements of flower shapes consisting of sheets. However, the result was different when the molar ratio was increased to 5, which meat a higher concentration of OH^-. Hence, in this case, the needle shape was the most common initial structure for the flower shape [177]. In Figure 31 (b, c, e), there were needle and rod shapes stripped from the flower shape due to the ability of zinc oxide particles to agglomerate under a high concentration of hydroxyl functional group, as described by Shen et al. [177]. According to Le Chatelier's rule, increasing the OH^- concentration caused a reaction to accelerate ripening and growth, and the presence of nanodots and 1D nanorods [56, 57].

The current results showed that the dispersion process that came from using the stirrer for the reaction and sonication path could enhance this phenomenon, especially in the current study, where there were small needles compared with the broken microrods in Figure 31 (a). In Figure 34 (a–l), in zinc oxide formed from zinc nitrate and NaOH, tiny spherical ZnO NPs scattered

around the flower NPs were also observed. A spherical shape was a famous zinc oxide morphology when zinc nitrate was used as a zinc resource with organic solvents, such as triton, hexanol, benzene, diethyl ether, ethanol and chloroform [43]. Cheng found that using zinc acetate dihydrate as a Zn^{2+} source precursor without organic additives generated rod-shaped NPs. No spherical shape was observed. Moreover, using an organic resource without the presence of alcohol, there was no opportunity to obtain a spherical morphology [37].

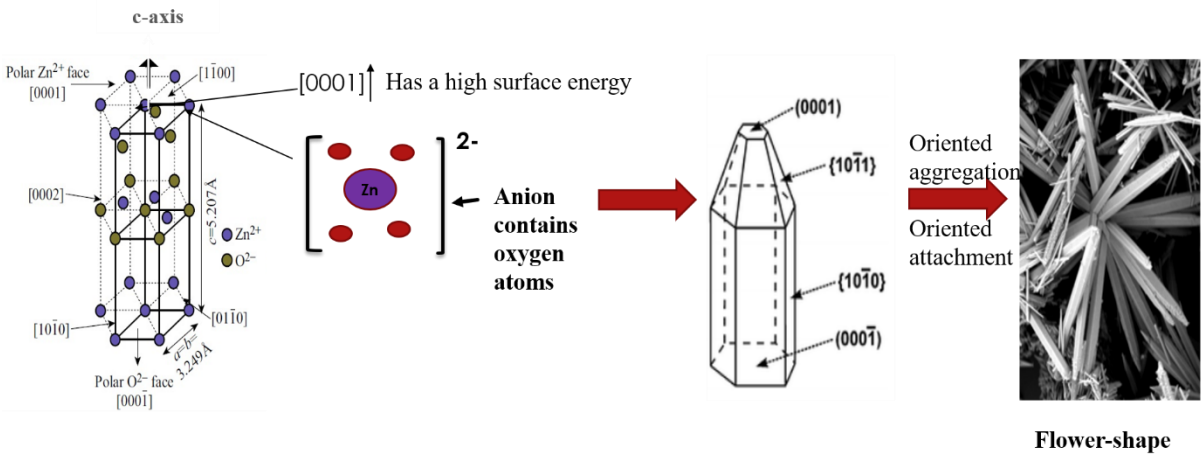

Figure 46. Mechanism of rod and flower shape formation.

According to the previous discussion, Zn^{2+} located in a tetrahedral arrangement, consisted of four oxygen anions. In hydrothermal synthesis—and according to the growth speed, along with the type of direction—the speed behaved in the pattern (0001) > (1011) > (1010). The final shape was thus affected by the growth velocity direction. Accordingly, a rod shape was the preferential morphology because of the growth process along the polar plane (0001). However, due to the rapid growth of the plane (0001), this led to accelerated disappearance—forming, as a result, a pointed shape appearing at the top of the hexagonal shape along the c-axis (Figure 47). This phenomenon subverted the assumed knowledge that 'the faster the growth rate, the quicker the disappearance of the plane [201]. As a result, in plane (1010), a hexagonal prism was the resulting shape due to low growth. Meanwhile, the (1011) facet tends to form hexagonal pyramid-like tips [39].

Zinc oxide is considered as amphoteric substances [202–204]. The second suggestion for making a nanorod was when the two faces had the same polarity. Hence, oxygen anions transferred to the surface of the lattice and formed a bridge between two unoccupied 4s− orbital with Zn terminal atoms. As a result, nanorods were obtained. Furthermore, anionic oxygen atoms migrated and combined by forming a bridge between two 4s− orbitals for Zn terminal cations through the surface. Conversely, Zn terminal atoms migrated through the surface and joined between two− orbitals of oxygen terminal atoms as a result, forming fused nanorods. However, the incorporation process of oxygen anions was the largest possibility compared with zinc anions.

Extended chain fusion could lead to a platelet shape. A platelet shape with greater width could be attributed to the rebuilding of the crystal by incorporating triangular shapes or as a result of adding the catalyst.

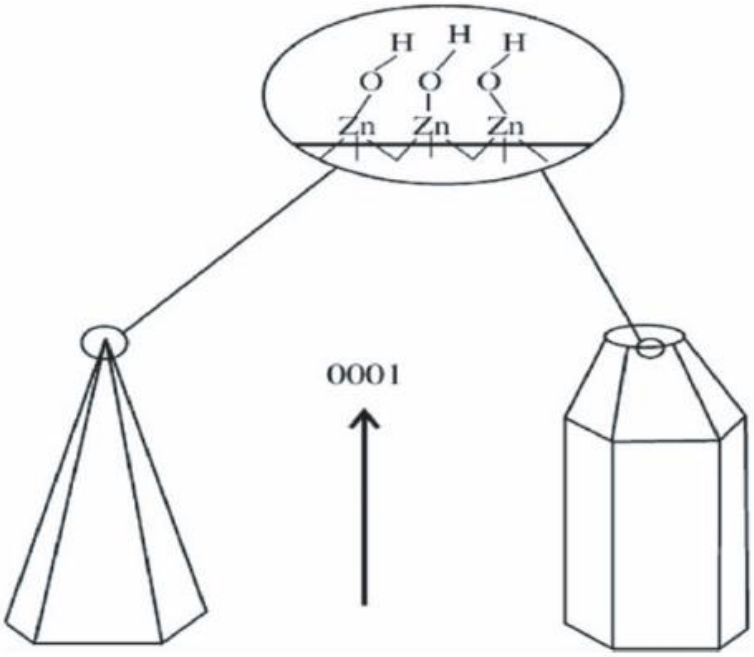

Figure 47. Growth of some well-known morphologies for plane (0001) along the c-axis [3].

3.1.6 Suggested morphology of platelet shape

Some studies attributed the platelet shape in zinc oxide to the role of some ligands that could work as hindrances and cover the polar plane. Hence, in this case, the potential would be preferable in other directions, along with $(10\bar{1}0)$ and $(2\bar{1}\bar{1}0)$ [198, 205]. In addition, Manthina and Agrios elucidated that due to the high concentration of Zn types around the ZnO crystal, the nucleation of $(10\bar{1}0)$ and (0001) planes tended to be prevented by Zn^{+} species, which led to crystal lateral growth; as a result, ZnO nanoplatelets were obtained [179]. Abdul Mohsen attributed the cracked plate to the effect of sonication [202]. In the current study, the presence of nanorods on the surface of the nanoplates could be a result of agglomeration [202].

Hence, when zinc acetate was used as a precursor (Zn source), acetate ions could replace the hydroxyl group that had been adsorbed along the [0001] direction due to its high affinity for adsorption on a zinc oxide surface. The steric effect around the zinc oxide particles inhibits growth along the (0001) plane and induces growth in the $[01\bar{1}0]$ direction. The presence of the OH^{-} functional group by adsorption at earlier stages on the polar Zn^{2+} plane (positive (0001) face) avoided acceleration in the growth rate along (0001).

In the case of zinc nitrate hexahydrate, the formation of platelet particles could be attributed to the effect of NO_3^{2-} ligands due to the presence of two negative charges and a lone pair of electrons on nitrogen, which had the ability to cover the polar planes even on (0001) or $(000\bar{1})$. Hence, the preference growth would be in other directions. Furthermore, when zinc nitrate hexahydrate was present in the reaction vessel, a high amount of these ligands received a small drop that came from sodium hydroxides at the beginning of the reaction (adding slowly in this case), supporting this suggested route. Moreover, zinc nitrate hexahydrate was also considered an endothermic compound that could be attributed to a decrease in the polar plane (0001) active energy. Hence, the possibility of making this energy more active to form hexagonal to rod-

shaped NPs decreases, which also led to platelet morphology (Figure 48). In contrast, Ong et al. showed that an excess amount of hydroxyl ions stimulated the formation of $[Zn(OH)_4]^{2-}$ to form nanosheets, which decreased surface energy to form a flower shape [46]. Moreover, in the interface solvent interactions, surface energy varied according to the difference in the energy of crystal faces. This illustrates the contribution of deionised water as a solvent to obtaining a long rod-shaped NP, as in the case of our study.

In the current study, a different morphology was observed when using the same concentrations and the new approach of this study was to know the important role of the additive type.

The ability to obtain a rod morphology at a low temperatures (less than 400 °C) was a great resource and versatility that played a vital role in microelectronic and photonic procedures [206, 207].

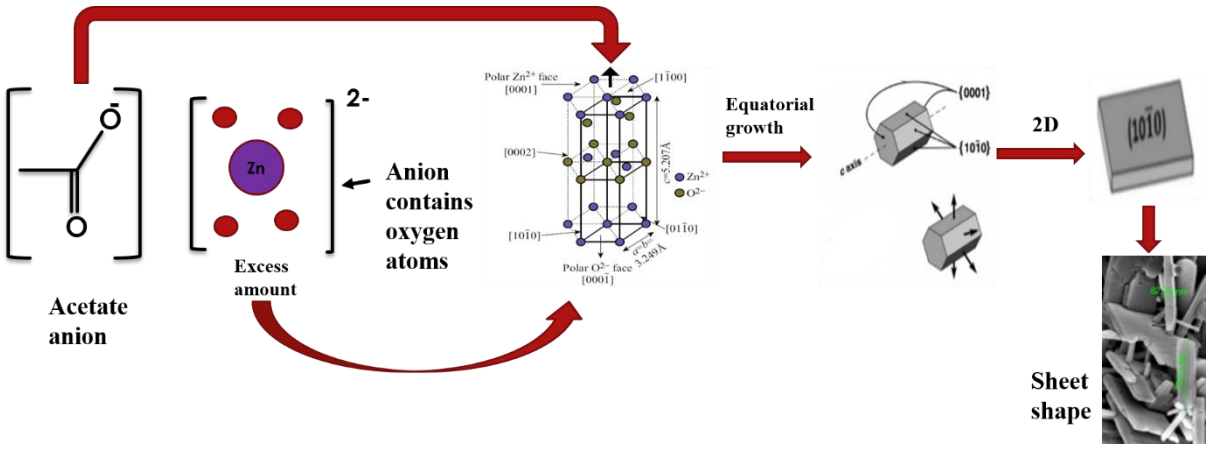

Figure 48. Mechanism of zinc oxide particles' platelet shape.

Some researchers have suggested that the reaction leading to a flowery shape could be a result of the growth process occurring in a random pattern and the effect of Van der Waal's forces [181, 208]. This process generated a very large number of polar planes. This is considered one of the most important factors in understanding face orientation and preferential growth mechanisms. In contrast, this shape could be attributed to elongated formula produced from

this kind of crystal as a result of the difference in the nature of the crystal during the growth process, in terms of polar, nonpolar and semipolar faces [209].

As shown in Figure 49, crystal growth behaved in another pattern because of the polarity of the faces. The first axial growth occurred in the {0001} planes along the x-axis. Second, tropical growth $\{10\bar{1}0\}$ faces that directed placed as a vertical on c-axes. This kind of growth affected the aspect ratio, which was related to the length and width of the crystal. This indicates that this affects the reactivity geometry according to the activities of the planes. Moreover, axial growth was faster than equatorial growth, as observed in the case of a high-speed ratio [210].

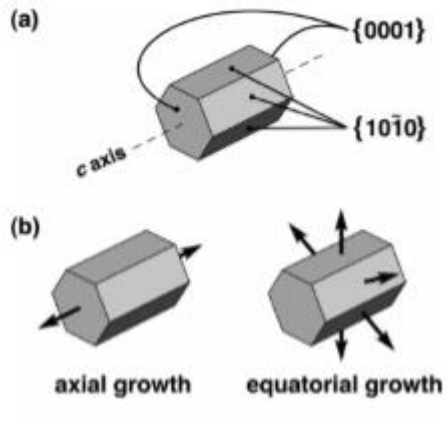

Figure 49. Differences in growth in axial and equatorial growth.

As a result, the challenges during syntheses were confined to controlling the preferred shape. The particle shape was affected by the type of precursor used [32] [38, 58, 211, 212]. In addition, increasing the molar ratio for $Zn(CH_3CO_2)_2 \cdot 2H_2O$ with sodium hydroxide NaOH to 1:2.5, 1:3—according to Boppella et al.'s study—led to a 3D trapezoid hexagonal cone-like morphology. In contrast, changing the source of the Zn precursor to $Zn(NO_3)_2$ led to interesting results. Even when gaining different morphologies, all shapes—in the case of using

$Zn(NO_3)_2$—were generally still smaller than in the case of using $Zn(CH_3CO_2)_2 \cdot 2H_2O$ [71].

The presence of a stacking morphology could be attributed to the interaction between the two (polar and nonpolar) planes during the earlier initial nucleation growth, which led to self-assembly to obtain the neutralisation of the local polar charges. In contrast, the terminal or lateral Zn^{2+} plane (0001) was more positive and vice versa: the terminal O^{2-} plane $(000\bar{1})$ was more negative. Assuming that the reactions in these polar plans were not preferable, except in the presence of the passive agent to compensate for the surface charge, such as trizma and acetate ion.

Polar faces have a strong ability to raise and present oxygen vacancies and contribute to recombination. They equilibrate the excess charge carried by bringing together and annihilating oppositely charged carriers. Terminal polar planes that were predominantly highly exposed were considered to be more active in terms of surface area.

Gaining nanorods in our results was considered a distinct feature compared with other 1D morphologies because they were easy to synthesise, and a variety of resources, such as metals, non-metals and compounds, could be used to produce nanorods [213]. In the current research, this result was obtained via refluxing and hydrothermal methods. Furthermore, the generation of flower-like-shaped zinc oxide consisting of arrow-like petals was attributed to the use of temperature over 25 °C [214] [33]. In the current study, flower-like-shaped zinc oxide particles were achieved without needing such a high temperature.

3.1.7 Zinc acetate dihydrate and sodium hydroxide using sodium dodecyl sulphate

Experiment 9 (SDS, Figure 50) worked precisely in the way the particles were able to self-assemble into a flower shape and that using SDS had a specific role in decreasing the agglomeration among particles. The synthesis of ZnO into numerous multiple-particle

symmetries was also obtained in less time using the sonication method with stirring. The degree of aggregation was thus affected by two methods:

1- Sonication [215, 216]

2- Stirring [217]

According to Boppella's results in the case of using $Zn(OAc)_2 \cdot H_2O$ with zinc nitrate concentration ratios of 1:1.5, 1:2, 1:2.5 and 1:3, the permanent shape was a hexagon, stacking rods as pairs with an average length of 9 μm [71]. There were also slight representations of some small irregular shapes on the permanent shape [78]. Clearly, adding water to the reaction had a crucial effect—in the case of single, bi or multiple superstructures—since increasing the time led to good structure properties, along with aggregation degree. Klaumünzer stated that heating at 150 °C was essential to control crystal growth and chemical reactions [36]. Comparing the two studies, it appeared that the need to increase the temperature could be overcome using the reflux method—in parallel with a temperature of less than 150 °C. Chen reported that growth in virtual direction orientation (vertical alignment) was carried out epitaxially on the polar plane (0001) on a sapphire substrate [218]. Another study stated that, in the vapour deposition method, a ZnO nanorod shape was observed to repeatedly incline at a constant angle of approximately 38°. This kind of orientational alignment is preferential, especially as an in-plane orientation [37].

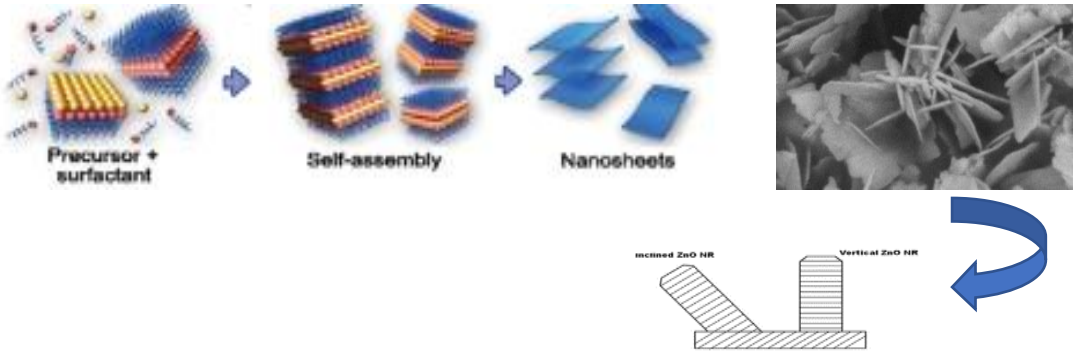

Figure 50. Effect of ion-to-ion self-assembly to form a sheet shape for ZnO in the presence of SDS.

3.1.8 Mechanism of bifrustum morphology using zinc nitrate hexahydrate and ammonium carbonate

The suggested mechanism for ZnO crystals using ammonia is described in the following equation:

$NH_3 + H_2O \leftrightarrow NH_3 \cdot H_2O \leftrightarrow NH^{4+} + HO^-$ (13)

$Zn^{2+} + NH_3 \rightarrow Zn(NH_3)_4^{2+}$ (14)

$Zn(NH_3)_4^{2+} + OH^- \rightarrow ZnO.$ (15)

Or

Another mechanism was ZnO formation, according to the following:

$Zn^{2+} + OH^- \rightarrow Zn(OH)_4^{2+},$ (16)

$Zn(OH)_4^{2+} \rightarrow ZnO.$ (17). [39, 70].

In the case of using $(NH_4)_2CO_3$, ammonium ions played a vital role in the different zinc oxide morphologies, except for the spherical shape [218].

$Zn(NO_3)_2 + (NH_4)_2CO_3 \rightarrow ZnCO_3\downarrow + 2NH_4NO_3$ (18)

$ZnCO_3 \rightarrow ZnO + CO_2\uparrow$ (19) [219].

Zinc oxide showed rigorous anisotropic growth and a high tendency to aggregate. This was due to the natural structure of the wurtzite hexagonal, which is known as a non-centrosymmetric structure. As a result, an affinity to and from the orientation attachment was demonstrated along the (0001) and $(000\bar{1})$ or (0002) polar plane orientations [71, 220]. Notably, increasing pH led to an increasing ability to obtain spherical-like shapes, especially at pH = 9 [221].

From a thermodynamic view, the possibility of interaction between an ammonium ion and a zinc ion was limited to approximately 20% to form the chemical compound $Zn(NH_3)_4^{2+}$. In Experiment 16, the particle surface exhibited a stacking ZnO bifrustum. Hence, the suggested mechanism (Figure 51) was as follows:

At the flat plane, an interface was generated. These interfaces created specific high energy for the additional extra growth of a small nanoparticle under an oriented aggregation to generate multiple structures. Oriented aggregation could involve oriented attachment, which refers to the stage of mediated particle crystal growth in which a primary crystal changes into a secondary crystal via the aggregation process [55].

As the SEM images showed, each bifrustum was stacked with the others to form a ring; this was repeatable, as observed in all particles.

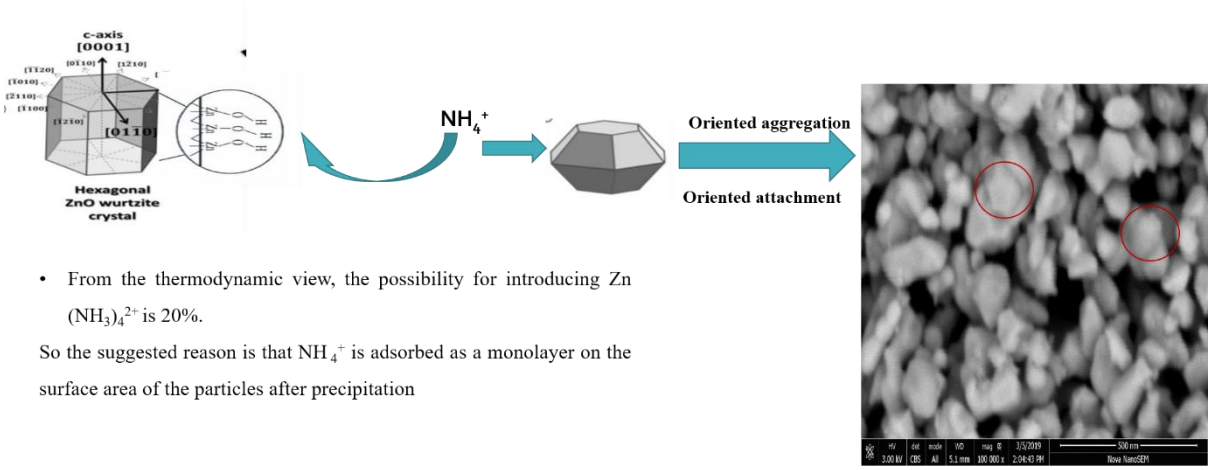

Figure 51. Suggested mechanism of zinc oxide bifrustum formation.

NH_4^+ was adsorbed as a monolayer on the surface area of the particles after precipitation due to the high-energy surface of the nanoparticles. Mohammed suggested that after ammonium ions were formed, the monolayer was connected between them by H-bounding. Hence, it looked like an uncommon rod morphology subjected to Wulff construction. The ring was that the growth of tiny units rapidly defused towards the ZnO planes. These units were placed on ZnO crystal planes. Furthermore, there was inadequate time to reposition to cover the area of the highest-energy planes. Consequently, the newly growing particles would cover $(10\bar{1}0)$ and, as a result, irregular morphologies had been obtained [57].

Experiment 19 involved refluxing for 30 minutes under the same conditions as in Experiment 18, except that the temperature of the calcination step was 550 °C for 4 hours. From the SEM magnifications, increasing the calcination temperature (with the same time of 4 hours) seemed to affect the particles and the morphology to form more aggregated groups composed of a flower shape and porous sheet consistency. Along with their tendency towards adsorption, the anions surrounding a ZnO crystal had an essential role in terms of kinetic growth, shape, size and nucleation rate [71]. Under a high pressure—which increased the stress already exerted on the particles due to refluxing and the 90 °C temperature—the zinc oxide particles were induced to grow. The presence of stacking faults was also a result of incorrectly oriented aggregation;

this could be due to the presence of defect points centred in zinc or oxygen vacancies or interfaces (interstitials), which were considered favourable positions for active defect areas [36]. If the micro/nanoparticles exhibited surface defects—for example, kinks and cracks—they may initially be attributed to conventional crystal growth type ion-by-ion attachment. Second, the presence of distorted hexagonal crystal shapes might involve surface defects, such as fracture shapes or cleavage. This could be proof that these morphologies were composed of micro/nanoparticle assemblies; in this case, the virtual aligned plane of the fracture led to the occurrence of this distorted morphology. Collision and Brownian motion made the virtual aligned towards the c-axis plan polar face (0001). The nature of the particles indicated that nanoparticle assemblies formed a spiral pattern. Moreover, crack morphology could be observed via cleavage fractures consisting of cleavage planes in a flat position (this is common in brittle materials) [54]. In the case of miniscule size—such as nanomaterials, where the size was smaller than that of atoms or ions—the direction or oriented attachment would not occur spontaneously in a flat position. Accordingly, the nanoparticles exhibited defective and incomplete alignments and an imperfect interface combination process. These processes might occur frequently, causing numerous defect regions to be observed at the interface area belonging to precursor NPs. The presence of granular features was attributed to defect-rich regions around the interface, which were exposed to a crack diffusion that underwent oriented attachment in the case of single-crystal cracks, thus revealing nanoparticles that tended to assemble. The hexagonal showed an attractive plane from crystal to another. To make ring shapes as well as aggregated particles, each particle tended to attract the other one, and due to the cracks inside the particle itself, an irregular ring shape could be formed. This phenomenon has not been previously reported, especially when using a solution process. In the step of crystal growth, oriented attachment and Ostwald ripening can be observed [222]. Crystal growth could

encourage the process of optimising the surface area, such as eliminating the grain on and around the surface and inducing reconstruction.

However, a high percentage of the defected areas at the interface occurred in the oriented attachment created on the crystal. Liu et al. asserted that the crystal growth process could be divided into two types:

1- Classical style: The addition occurred by adding a monomer to another monomer.

2- Particle attachment style [54].

Due to the suspended particles and the presence of adsorbed ions that were assembled to obtain a 2D-like plate, the stress that came from the lattice mismatches to obtain coral-shaped NPs formed an aligned arrangement, acquiring a low surface energy. In addition, electrostatic interactions occurred between nanoparticles (driving force). The suggested mechanism was that the exposed site entrance of a nanotunnel attracts ions that hold an opposite charge around it, moving from the solution to the nearest differently charged sites on the particles. Accordingly, each of the two neighbouring nanotunnels would have opposite charges. Consequently, this process produces electric dipoles under the effect of oriented attachment (dipole–dipole interactions) [54]. Boppella et al., for example, used a concentration ratio of 1:1.5 and obtained ring shapes with an average outer ambient of approximately 590–690 nm and an inner ambient of approximately 125 nm. By increasing the molar ratio to 1:2 and 1:2.5, the same ring-like shape was obtained—yet the inner length decreased to less than 1:1.5. Increasing the molar ratio leads to obtaining irregular hemispheric shapes due to agglomeration [71].

3.1.8.1 Another perspective explanation for porous morphology:

According to Mika's morphology, zinc oxide produced by simple electrochemical anodic oxidation methods was spongy with irregular porous morphology [223]. The pore size varied

between approximately 30 and 80 nm, which was consistent with the current results (see Figure 40 d). This study clarified that ZnO with nano-porous morphology could be attributed to oxygen evolution, but at the same time, this was not the main reason because there was still an undetermined mechanism for the generation of this porous zinc oxide structure inside. In the current study, porous zinc oxide could be attributed to the nature of the precipitant $(NH_4)_2CO_3$. Compared to using NaOH as a precipitant that did not produce a nano-porous morphology when using the same zinc source zinc nitrate hexahydrate, the morphology when using ammonium carbonate was very different.

As mentioned in the literature review, gas sensing was influenced, for example, by the morphology of the metal oxides. Laing et al. prepared zinc oxide with dopped with two types of NiO and obtained porous ZnO-NiO films (the layer looked like stacked structures) [224]. These structures provide a high performance by significant response in gas sensing. They found that the structure with ZnO-NiO-1 coated for 20 minutes had the perfect gas sensor efficiency, as the zinc oxide with porous structures provided a large active surface area that allowed chemical reaction and propagation of gas, resulting in higher sensor efficiency. SEM for ZnO-NiO-1 showed a similar morphology to the current results. The porous ZnO-NiO films with nanosheet structure were prepared using zinc nitrate hexahydrate (Zn $(NO_3)_2 \cdot 6H_2O$) as zinc source and urea ($(NH_2)_2CO$) as precipitant by a hydrothermal method. According to Liang etl, the reaction first produced the precipitate $Zn_4CO_3(OH)_6 \cdot H_2O$ then after treatment at 500 °C, 30 minutes, the new structure obtained was porous zinc oxide nanosheet. According to these results, the current study proposed the following equation:

$$Zn_4CO_3(OH)_6 \cdot H_2O \rightarrow 4ZnO + \uparrow CO_2 + \uparrow 4H_2O \quad (20)$$

The porous structure was formed after the release of carbon dioxide equation 15, so the porosity formed could be attributed to CO_2 release. Especially in the current results, when applied

different types of addition in the reflux method, gas was released from the flask, which attributed to the same reason as mentioned, namely the release of carbon dioxide.

3.1.9 Effect of the addition time using ammonium carbonate and zinc nitrate hexahydrate in the reflux method

Studying the effect of time on the resultant morphology—while using the same precursors—was the next step in Experiments 20–26.

Changing the addition time of zinc nitrate influenced the size and diameter of the particles. The reaction could be divided into three stages or processes:

1. Induction time: A period to allowed the building unit to form slowly, yet sufficiently to permit the reaction to start.
2. The nucleation processes
3. The growth process (disruption)

The reaction after five minutes generated no nanoparticles, with a hollow network consisting of hexagonal crystal morphology [36]. After 10 min, the particles were narrow needles in shape, which was compatible with Mohammad and Wang's study, hence, this period of time represented the nucleation process, which was known as the period of building units. Furthermore, after 10 minutes, a wide needle shape (from 850 nm to 1 μm) was evident [225]. It formed a flower shape. Each needle was porous and had a diameter of approximately 30–150 nm. Increasing the period of time from 15 minutes to 30 minutes Figure 41.Figure **41.** Effect of the reaction time (15 minutes) on zinc oxide particles in reflux method using 1 M of zinc nitrate hexahydrate and 1 M of ammonium carbonate at (a) 5,000×, (b) 6,500×, (c) 15,000× and (d) 25,000× magnifications. In Experiment 22, after 15 minutes, the particles started to change their distribution in the solution. The aggregation orientation affected the particles, leading to small settlements composed of stacking sheets. With the same ring morphology,

after 20 minutes and 30 minutes in Experiments 23 and 24, respectively, huge spherical settlements appeared that looked like pumice stones. After 30 minutes, the particles looked like coral reefs. This meant that increased time was required to overcome the adhesion inside the ring because the particles in this stage were very sensitive and—as a result—the dominant force would control the last shape The orientation aggregation was very clear during the growth progress, with an annular structure. These combinations, in some areas, emerged as hexagonal morphology, as illustrated. At 50 minutes, they exhibited a large surface area of 20.59 ± 3.619 nm. The needle shape was the dominant shape. Each needle consisted of pores, leading to an increase in the exposure area. Terminal polar planes, when predominantly exposed, were considered to be more active as mentioned before. The orientation alignment induced the growth process to first produce an amorphous ring shape—under the effect of ion-to-ion orientation due to interaction forces, high concentration and fast growth caused by pressure and temperature. Under the Ostwald ripening force and Brownian movement—and under the presence of pressure and temperature—the particles formed porous needle shapes. These consisted of a large number of thin rings that generally formed into large needles and were distributed randomly, as flower shapes were formed in some areas Figure 44. Building blocks that create elongated nanoparticles by oriented attachment also reinforce crystal growth. The presence of a weak spot between two dots illustrated the interface area that oriented attachment could affect the (0002) plane direction. However, it had not yet been confirmed that the interface between these two atoms supported a high possibility that oriented attachment was being carried out and was ongoing [36].

At 70 minutes, the particles seemed to have undergone orientation aggregation due to the high number of particles. In the presence of the high pressure and the small amount and at 90 °C temperature, the shape appeared rapidly. Hence, rapid fast growth was affected by oriented aggregation, whereas slow growth decreased defect spots. In the case of non-classical

crystallisation, this led to 2D stacking faults or defects. The growth rate might contribute to the increase of defect formation (long period of time in this case). In addition, the presence of ammonium anions in solutions with a high concentration led to the formation of a monolayer due to the high surface energy. The second reason was that the diameter of the needle after 10 minutes was greater than its diameter after 50 minutes. After 70 minutes, in this case, the effect of agglomeration appeared clearly. In addition, Shen et al. illustrated that when temperature became high (more than 180 ℃) the flower shape structure started to be deformed because excessive growth caused the particles to lose some properties, such as their original shape [177]. In the current study the reaction was subjected to long period of time with using stirrer then transfer to refluxed flask under 90°C for 30 minutes could explained the obtained morphology at 70 °C

Single or double zinc or oxygen vacancies or interfaces (interstitials) were considered a favourable position for active defect areas [36, 226]. Riyadh et al. stated that the mesostructure for ZnO obtained using a high temperature (150 °C) differed in shape from ZnO particles that were not exposed to heating (flower shape, with a needle structure at a length of 500 nm) [227].

The complex ions $Zn(NH_3)_4^{2+}$ and $Zn(OH)_4^{2-}$ were formed due to the solution mixture, so the nucleation step was carried out in a heterogeneous solution. This results in an obelisk-like single-rod structure. This morphology was due to numerous layers. It was important to know that alkalinity was important and played a vital role. For example, in the case of using zinc nitrate with sodium hydroxide pH = 10, the suggested morphology was a microrod. This was considered similar to the same result at 10 minutes. Moreover, the effect of time on the growth process, according to Baruah, was only to increase the thickness of the rod shape, compared with the length [39].

Crystal growth was directed by thermodynamic properties, such as surface energies. The desired equilibrium morphologies could be obtained from different facets according to surface energies that were subjected to Wulff construction [57]. Zinc oxide had rigorously anisotropic growth and a high tendency to aggregate. This was due to the natural structure of the wurtzite hexagonal, which was known as a non-centrosymmetric structure. As a result, there was an affinity to and from the orientation attachment, along (0001) and $(000\bar{1})$ or (0002) polar plane orientation.

Microcrystal and complex superstructures were formed, through orientation aggregation from 0D to 1D and from 1D to 3D. All the previous morphologies were under an aggregation process: dot to rod to cone to multiple cones. The best processes to control multiple cones were the stirring and sonication steps. In the initial step, ZnO nucleus particles were grown in the solution under the diffusive mechanism, which yields numerous tiny (nano) crystal particles. In the second stage, the growth process began with self-assembly under oriented attachment roles—which especially affected particles with a high surface energy. This was considered an opportunity to allow the aggregation attachment to affect the particles. This step started very early under high temperatures. Bebolla et al. suggested that obtaining a ring-like shape or

hemispherical morphology was attributed to the particles being oriented in a different way. Some researchers had illustrated the mechanism of growth of a ring shape of zinc oxide or of a hemisphere shape in terms of nucleation rate, the Ostwald ripening effect, and the favourable orientation of crystal observed in nanoparticles. In earlier steps, the primary crystals could be combined together to become a large size; at the same time, the effect of Ostwald ripening was due to a decrease in the overall energy of the surface area [44, 71].

Thus, in some cases—especially in the hydrothermal method—using sodium hydroxide and zinc precursors in the presence of organic templet agents could play a vital role in changing morphology. For example, during the synthesis of zinc oxide, increasing the temperature changed the shape of the particles formed from a rod-like to a polyhedral shape [39, 218].

At 70 minutes, the different shapes, ring and hemispherical shapes, might also be subjected to incompletely oriented attachment. The neighbouring crystal faces (planes) tended to randomly self-assemble their orientation and then, via the Ostwald ripening effect, control the morphology. The Ostwald ripening phenomenon caused these particles to reorient, redissolve, adjoin and redeposit. This was because that the internal particle region had a higher surface energy compared with the external region, thus forming a ring-like shape at the end [71].

The polar planes at the end morphology spontaneously reflected the numbers of negative ion (oxygen) defects. These defects were at a shallow level. Thus, the growth rate could contribute to the rate and type of defect formation [228].

In Experiment 27, zinc nitrate hexahydrate and ammonium carbonate by hydrothermal method, the growth rate could contribute to the type and rate of defect formation. Some studies had stated that in a hydrothermal process—using ammonium as an alkaline resource, and $Zn(NO)_3$ at 100 °C at pH <11—the surface energy of (001) was much higher than the other faces in a wurtzite hexagonal shape. Furthermore, the polarity of the solvent could affect the final morphology by affecting the growth rate. The growth process was faster in (0001), in the case

of using drops of weaker ethanol in its polarity compared with ethanol as a solvent [36, 39]. In general, in the case of using zinc salt by precipitation agents, such as $(NH_4)_2CO_3$ and NaOH, which had used in current study and according to Herrera et al, [220], the first step in the solid crystal synthesis of zinc oxide was nucleation, and the second step was the growth process. Initial growth started when zinc oxide molecules started to defuse on the surface of these nucleated particles. Next, fruitful collision and fusion between two of these particles occurred under the effect of an oriented attachment. Finally, interface particle growth occurred, subjected to Ostwald ripening. This process occurred via dissolution and diffusion inside the solution between molecules.

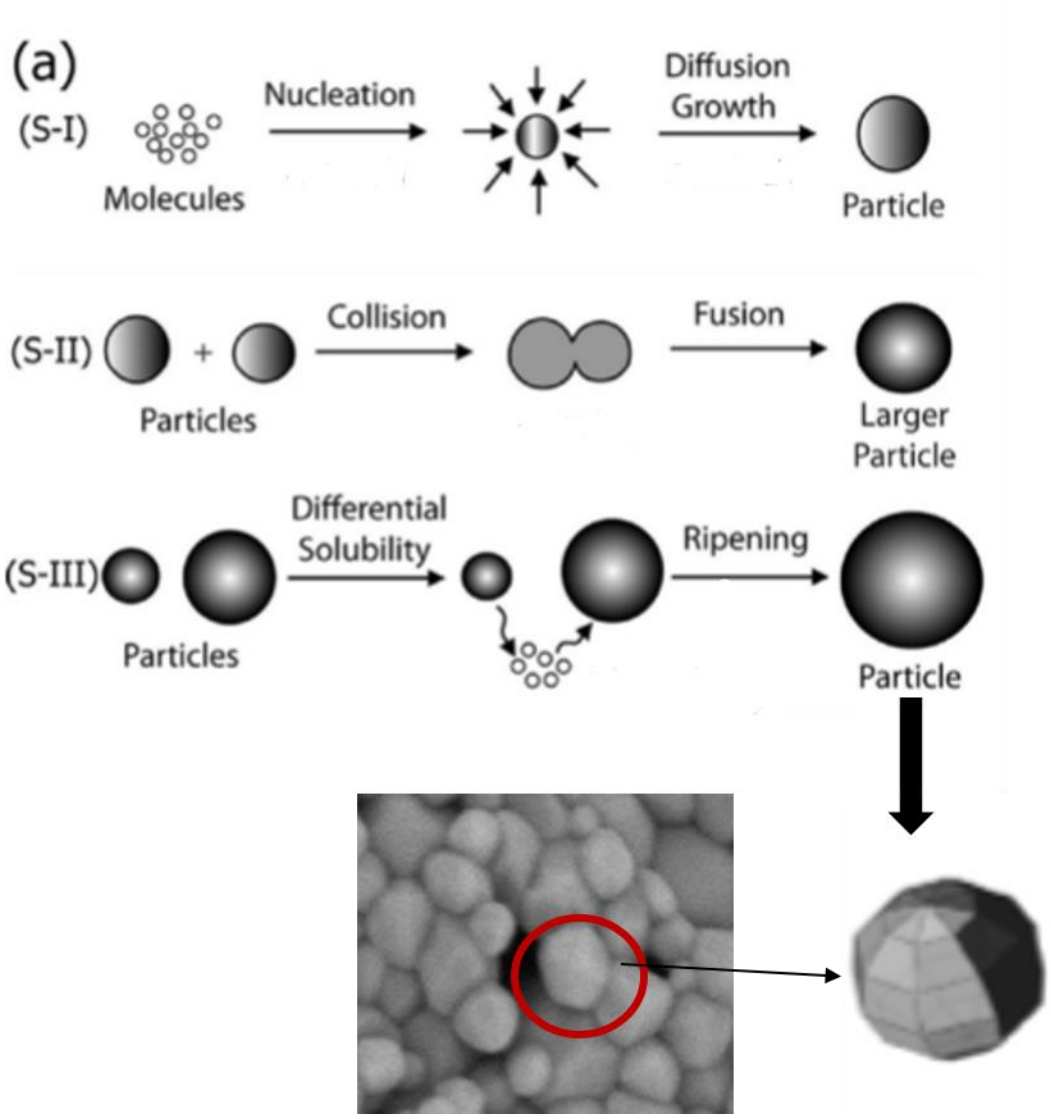

Figure 52. Mechanism of spherical nanoparticle formation (Experiment 27) [45].

Owing to the effect of the chemical structure of the surface particles on crystal growth, the structure of the chemical compound and interfacial interaction between the crystal morphology and the ambient solution could affect the formation of ring and hemisphere shapes. Along with their tendency towards adsorption, the anions surrounding a ZnO crystal had an essential role in terms of kinetic growth, shape, size and nucleation rate [71]. In addition, when the final morphology was spherical, the (100) facet usually predominated in the entire shape (Figure 52).

3.1.10 Effect of pH

Changing pH values during the reaction had a crucial role on faces; specific faces were affected by specific pH values, and the growth rate caused the formation of a specific shape.

Boppella et al. noted that this could be controlled by the pH effect. When the pH was raised from 6 to 9, the ZnO crystal was hexagonally prismatic. Hence, growth occurred simultaneously in the equatorial and axial directions. Planes $(01\bar{1}0)$ or $(10\bar{1}0)$, which were equatorial faces, grown preferentially under these pH values. They formed lateral edges, as well as grew in the c-axis direction for the plane $(000\bar{1})$, to eventually form ZnO with a hexagonal prismatic morphology.

In addition, this position encouraged symmetrically the six other equatorial planes to eventually form a hexagonal morphology. According to Buppolla et al., adding Trizma reinforced upholding the OH^- functional group; this could be affecting the growth of the nucleation process on the ZnO structure to a flower shape from a needle shape. This was attributed to the use of zinc chloride instead of $Zn(AC)_2$, and the orientation was along the polar plane (0001) direction for the nanowire [206]. At the same time, the study referred to the thickness of the nanoplate and considered the petals of the flower shape to result from the use of NaOH—depending on the fact that a strong pH value had a powerful effect on the final structure. This finding was similar to the current result [218].

As shown in Table 7, for Experiments 1–4, the pH values of the solution were between 6 and 7. The low pH led to a 2D structure and sheet shape [54]. As shown previously in Figure 29, Fardad et al. stated that at a pH of less than 10, ZnO became more stable [229, 230]. However, Alias et al. (2010) stated that the synthesis of ZnO in an acidic or neutral environment led to agglomeration [231]. Samaele et al. mentioned a hexagonal shape at pH = 8 and 10, whereas a

rod shape was the common structure obtained at pH = 12 [232]. Samaele et al. obtained results similar to those in Experiments 7, 8 and 10 (pH = 13).

The suggested morphology at pH 13, when using a basic media (NaOH) and zinc acetate as a Zn^{2+} resource, was a microrod. The previous study was consistent with current study in terms of refluxing methods. When zinc acetate was added to NaOH, a flower-shaped needle was obtained. However, further results in this study signified that, using a refluxing process with precursors, other shape(s) could be produced [182, 218]

Table 7. pH values and the obtained morphology.

Experiment	**pH**	**Morphology**
1– 4	$6 \leq pH \leq 7$	Ranging between nonuniform porous and sheet shape
5– 6	$8 \leq$ pH	Cauliflower and nonuniform shape.
7, 8	≈ 13	Flower, needle and platelet shapes
9	≈ 11	Sheet shape (see the Experiment Conditions)
10	≈ 13	Sheet shape
11– 15	$9 \leq$ pH ≤ 10	Flower shape consisted of platelet and needle shapes.
16– 27	$7.5 \leq$ pH ≤ 8.5	Bifrustum, coral and spherical shape

The effect of pH, in this aqueous solution, could affect the change in nucleation rates and contributed to increasing crystal growth. This could cause a change in the growth of the crystal planes and, in turn, led to a difference in the final morphology—due to the change in geometry. This meant that if the value of the difference between the pH at the beginning and the end was

small, the nucleation rate became very slow. As a result, the crystal becomes clearly shaped and sized. At a pH between 7 and 9, $Zn(OH)_2$ was stable and insoluble. When the pH was higher than 9, this compound dissolved $Zn(OH)_2$ started to condense in the early stages and transformed to zinc oxide at a higher temperature [225]. According to Mohammad et al., the volume of water added to the experiment as a solvent affected the size of the ZnO product. Increasing the volume of water led to larger ZnO particles.

The pH and concentrations of the precursor also had crucial roles in several morphology types, such as doughnuts, hemispheres, twin discs and collected trapezoid rings [24].

Similar rod shapes crystal had been obtained at the same pH from 9 to 10 in Experiments 11–15 [221] using zinc nitrate as a zinc resource and with the reaction carried out at 90 °C.

At a pH of 7–8.5 (i.e. neutral solution), H^+ and OH^- concentrations were equivalent; hence, pH had a minimal or negligible influence on the interfaces of ZnO crystals [233]. However, at a pH of >7, the excess amount of OH^- caused the presence of hydroxide ions around zinc ions due to strong attraction, which subsequently led to an enhanced crystallisation process and the formation of zinc oxide nanoparticles [233]. Increasing the OH^- concentration caused a reaction, according to Le Chatelier's rule, to accelerate ripening and growth, as well as the presence of nanodots and 1D nanorods [66]. pH had an important effect on zinc oxide nanoparticle synthesis; in the case of low pH, tiny crystals could be obtained in contrast to natural and alkali media under the same conditions of methods, reaction and temperature [200].

Besides precursor type, pH, temperature and time [234], morphology-directing factors [31] had a vital role in the final zinc oxide morphologies.

3.1.11 Effect of calcination

The purpose of calcination was to complete the treatment of a material by heating it at a specific temperature in a specific environment. According to Equation 1, $Zn(OH)_2$ was formed, which

had low solubility, especially type ε-$Zn(OH)_2$, Ksp = 3.5 *10^{-17} at room temperature. This compound sometimes dehydrated to form zinc oxide; however, when some oxygen molecules failed to mix with water, the reaction continued in a solid state instead of under dissolution to obtain zinc oxide [235]. In addition, the melting point of ε-Zn $(OH)_2$ was 125 ℃, and the zinc oxide was 1,974 ℃, so the selected temperature at approximately 550 ℃ was due to the purity of the yield that was obtained for each experiment.

During calcination, particles underwent fusion and continuously enlarged by coarsening. Particle coarsening occurred in a solid or liquid state to enhance the growth process for particles to develop into large crystals and to reduce the number of small particles to prioritise their continuous growth to ultimately form large particles. The reason behind the tendency of tiny particles to enlarge was that a small one was less stable and had less energy than a large one, whereas nanoparticles that were well packed or had a large crystal size were stable with adequate energy than small particles. According to these behaviours of particles, the possibility of enlarging particles at room temperature was high, which would occur in a short time under calcination. Some studies had supported the role of the calcination step [236], [230] and had shown that increasing the calcination temperature led to increasing particle size, even when different methods were used for ZnO synthesis. The calcination treatment was illustrated as follows.

The effect of the calcination process could be illustrated by two mechanisms. First, orientation attachment played a vital role in this process. Furthermore, from a thermodynamic view, a large particle was stronger than a small one. The second mechanism in this process was Ostwald ripening effect [56]. This process involved the diffusing transmission that could occur in the dispersed phase enlarge the smaller particles. At a high temperature (550 °C in our study), OR was a great influence because of its remarkable effect on the area of interfacial energy, high solubility and adequate growth rate [237]. Furthermore, oriented attachment occurred due to a

decrease in the entire system's interfacial interphase by reducing surface energy; as a result, particles tended to aggregate and enlarge. Temperature was important to achieve orientation attachment because of the energy that could provide Brownian motion. In addition, in the initial growth, when a single monocrystalline zinc oxide was formed, oriented aggregation could occur due to a high surface energy and a high surface-to-volume ratio. Orientation attachment was a physical phenomenon that could occur depending on the emergence of nanoparticles (Figure 53) [200].

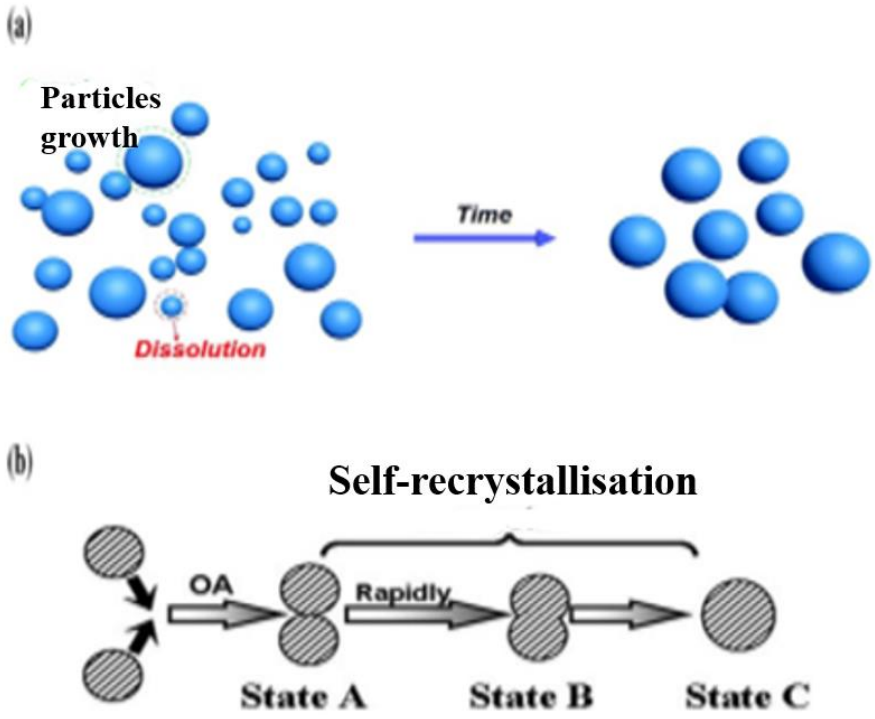

Figure 53. Scheme of ZnO particles under the effect of (a) Ostwald ripening and (b) oriented attachment [238].

3.2 Morphology of zinc oxide nanoparticles studied via X-ray diffraction analyses

X-ray diffraction analysis is a technique that could be applied to the scientific analysis of powders and single crystals. The advantages of analysis using powder diffraction included gaining an understanding of the degree to which particles had a high degree of crystallinity. In addition, this technique could be applied to analyse the nanoparticle size using Cu-Kα (1.5406 Å) as a single resource diffractometer, as well as using a detector (LynxEye) with Bragg–Brentano geometry. The Bruker D2 Phaser offered a wide scanning range, from 5° to 100° 2θ. This range is useful for many applications, including studying the inorganic and organic chemistry of compounds and engaging in material sciences research, in addition to medicinal and pharmaceutical chemistry research [239–241].

3.2.1 Effect of different concentrations of sodium hydroxide (NaOH) when using 0.03 M of zinc acetate dihydrate (Zn $(CH_3CO_2)_2.2H_2O$) in a precipitation method

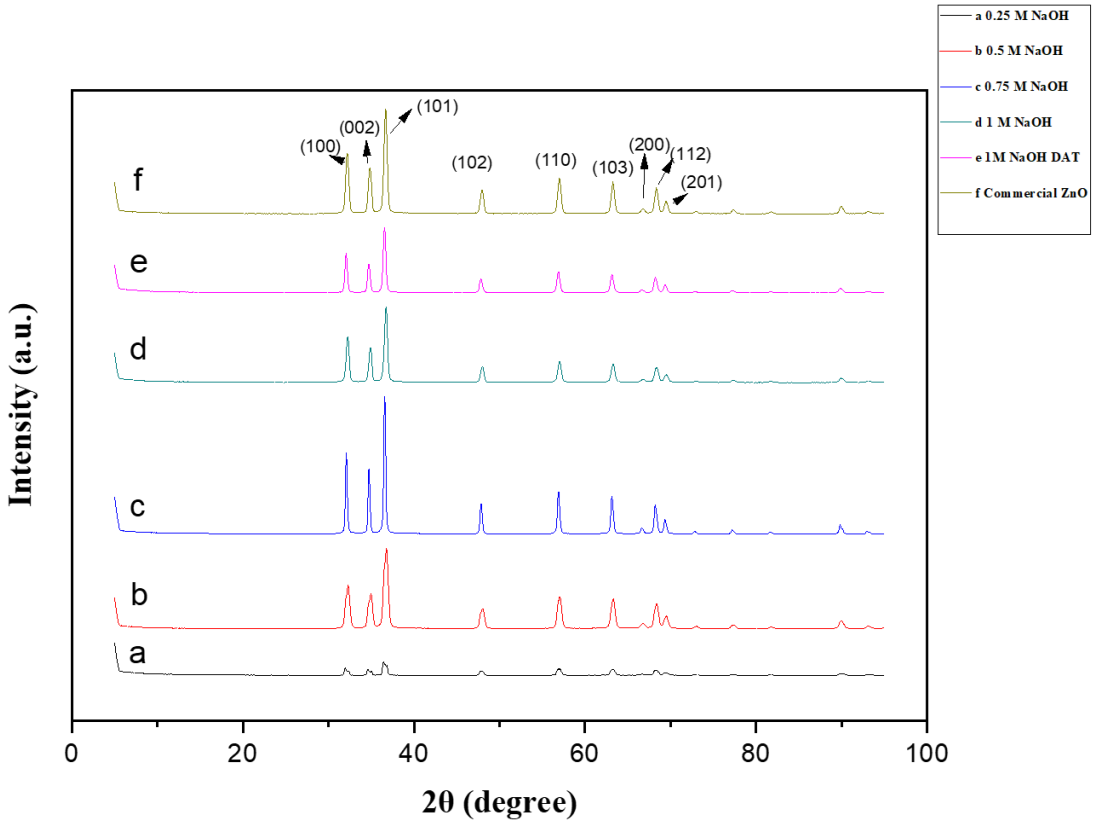

Figure 54. XRD results for zinc oxide synthesised using 0.3 M zinc acetate dihydrate with different sodium hydroxide concentrations.

As shown in Figure 54, the XRD results illustrated the effect of NaOH concentrations used in the precipitation method on the final morphology for zinc oxide Experiments 2–6 compared to a commercial zinc oxide sample. It was clear that the structures belong to pure zinc oxide. In addition, the varied intensities and strengths of peaks reflected the crystallinity in each experiment. For example, having a ‘cauliflower’ shape seemed to be the strongest option and with narrower peaks seen compared to other substances whose results were irregular and flaky.

The strongest intensity was for 002, indicating that crystal growth was better when directed towards the plane [0001] orientation along c-axis towards positive polar plane [88, 173, 226].

3.2.2 Effect of precipitation method on zinc oxide morphology

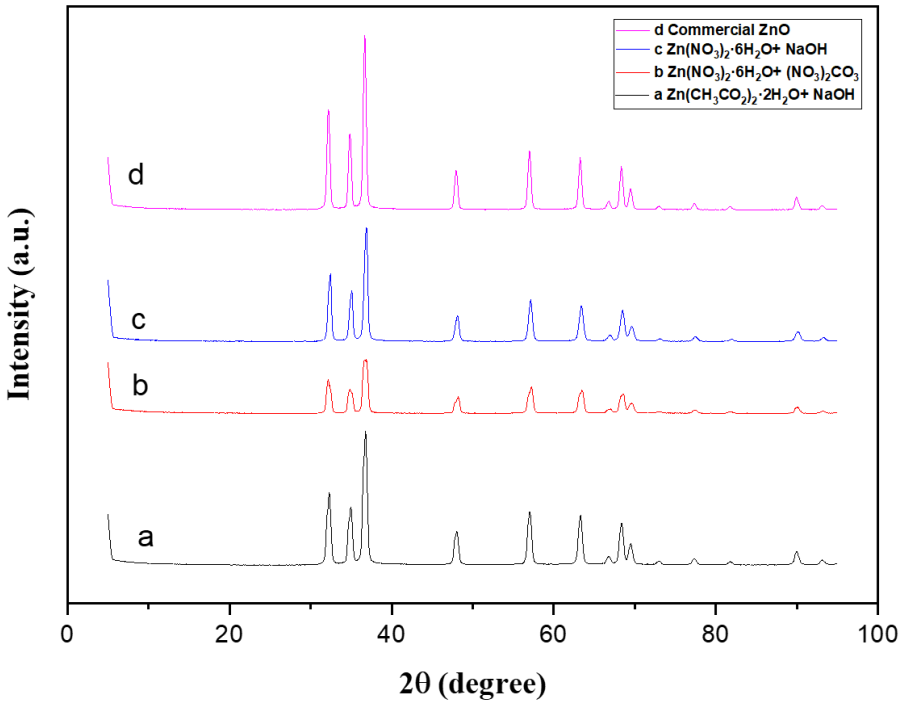

Figure 55. XRD results for zinc oxide samples, compared to a commercial ZnO, using a precipitation method.

Figure 55 showed the results for three reactions: (a) zinc acetate dihydrate with NaOH, (b) zinc nitrate hexahydrate with $(NH_4)_2CO_3$ (c) zinc nitrate hexahydrate with NaOH and (d) represented commercial ZnO. All the reactants in this study produced zinc oxide – as seen by comparing the XRD for each reaction with that for commercial zinc oxide, which gives an indication of the purity of zinc oxide produced, indicating it was (relatively) free of contaminants. Moreover, the peaks were narrower and sharper for zinc oxide when using zinc acetate dihydrate and zinc nitrate hexahydrate with NaOH than when using zinc nitrate hexahydrate with $(NH_4)_2CO_3$, which reflected the purity and high crystallinity of ZnO particles

(increasing sharpness revealed high crystallinity) [242]. This could be attributed to the last treatment of the sediment using calcination. In addition, the strongest intensity was for 002, indicating that crystal growth was better when directed towards the plane [0001] orientation [88, 173, 226]. Using zinc nitrate hexahydrate with $(NH_4)_2CO_3$ revealed lower crystallinity (weak peaks) compared to the other methods; this could be a result of the reaction conditions (such as the steps of reaction would take until the end) affecting the final zinc oxide morphology, as indicated by SEM results, such as oxygen defects and distortion in the crystals [243].

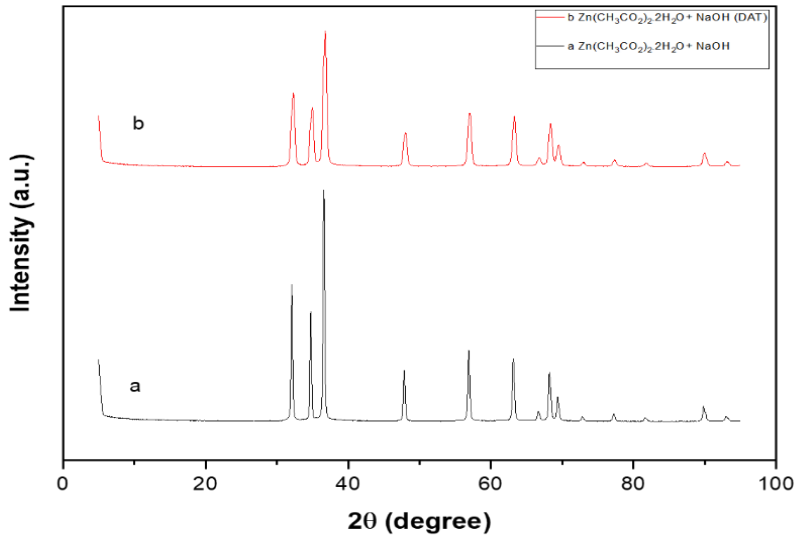

Figure 56. XRD of zinc oxide when using 0.3 zinc acetate dihydrate with 3 M of sodium hydroxide in a participation method, a) adding zinc acetate dehydrate on NaOH, b) adding NaOH on zinc acetate dihydrate (different addition type, DAT).

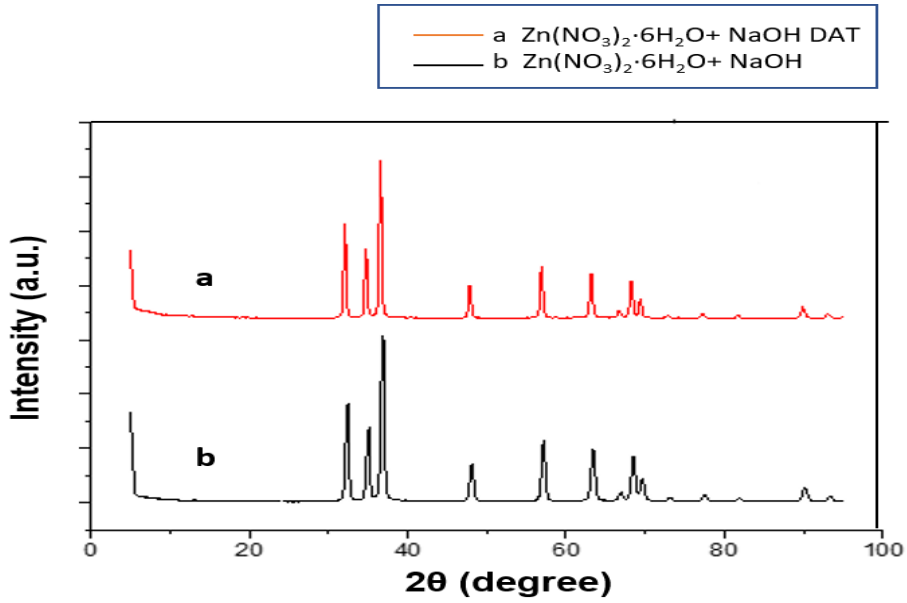

Figure 57. XRD results of zinc oxide when using 0.5 M of zinc nitrate hexahydrate with 1M of sodium hydroxide in a participation method, a) adding zinc nitrate hexahydrate on NaOH, b) adding NaOH on zinc nitrate hexahydrate (different addition type, DAT).

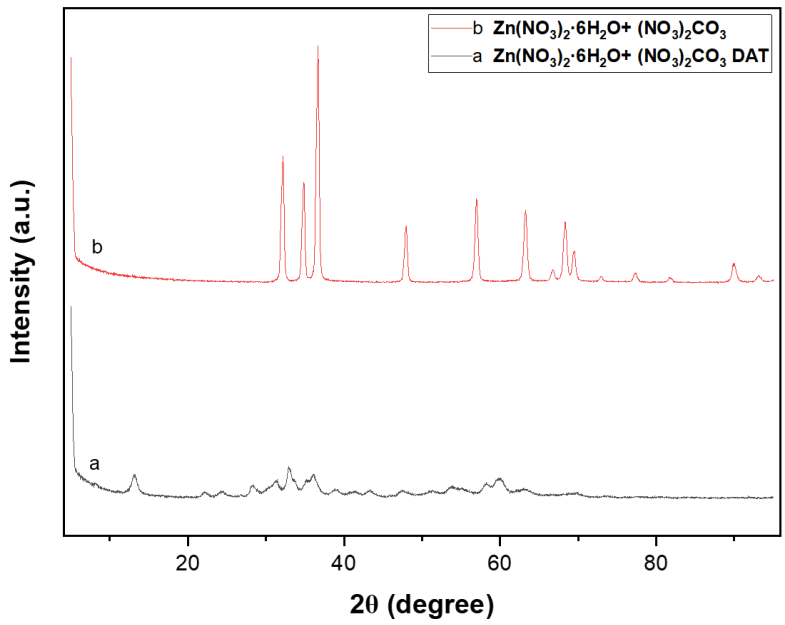

Figure 58. XRD results of zinc oxide, using 1 M of zinc nitrate hexahydrate with 1 M of ammonium carbonate as the precipitant in a participation method a) adding ammonium carbonate on zinc nitrate hexahydrate, (b adding zinc nitrate hexahydrate on ammonium carbonate (different addition type, DAT).

Figure 56–Figure 58 present the XRD results when using different addition types for the three reactions. Zinc oxide demonstrated in all cases a perfect match with commercial zinc oxide in terms of peak size and intensity. In the case of ammonium carbonate in the flask, the zinc oxide crystal lattice reflected a higher intensity [244] compared to different addition types by the 151recipitation method, potentially due to the absence of another treatment or since temperature was important for crystallinity [245].

3.2.3 Effect of the reflux method on zinc oxide crystallinity

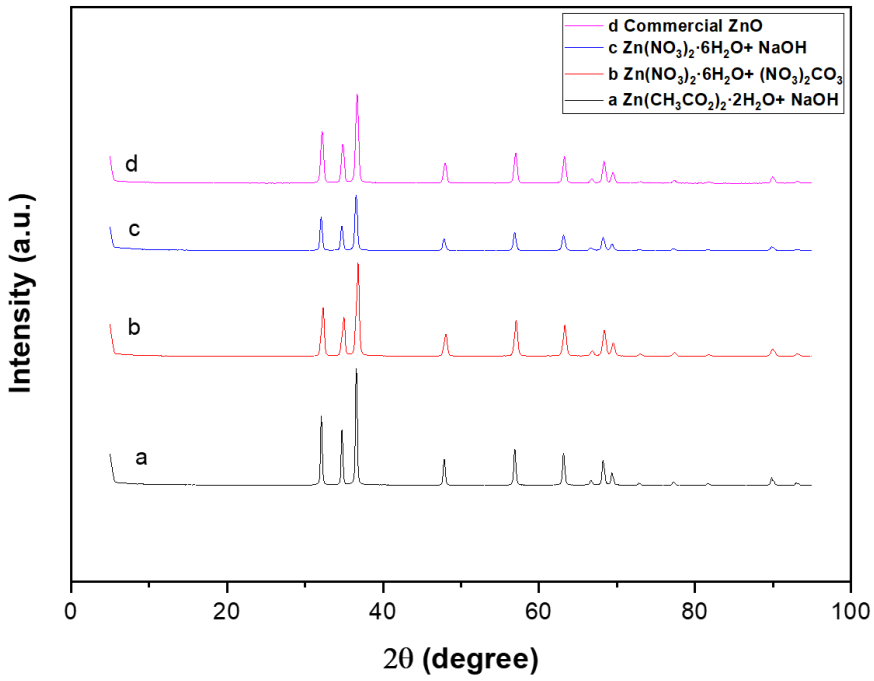

Figure 59. XRD results of zinc oxide compared to commercial ZnO when using a reflux method.

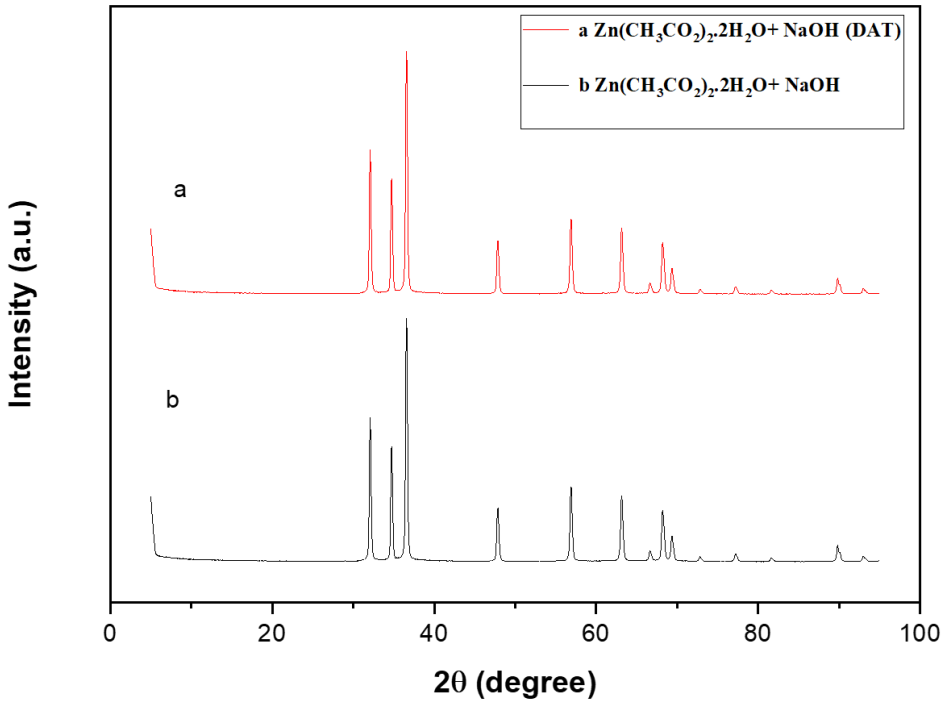

Figure 60. XRD for zinc oxide when using the reflux method with 0.3 M of zinc acetate dihydrate with 3 M of sodium hydroxide as the precipitant and with different addition types.

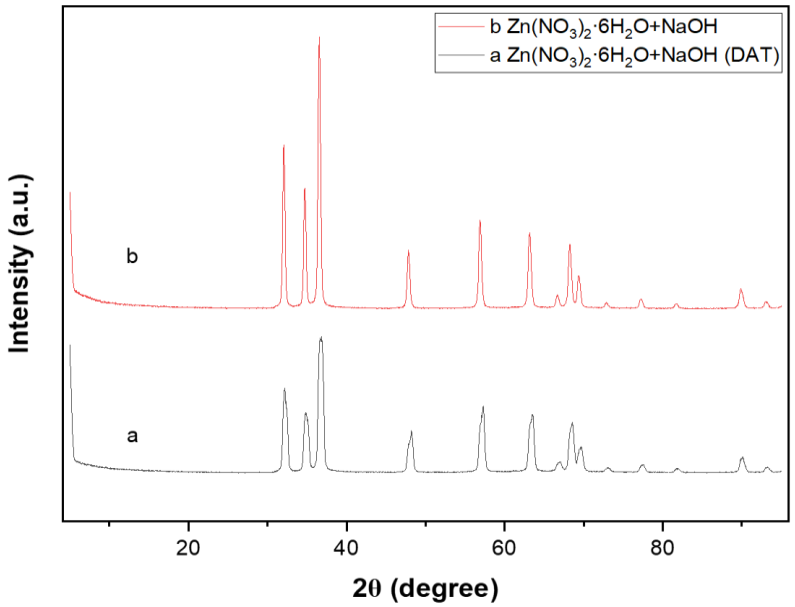

Figure 61. XRD results of zinc oxide when using a reflux method with 0.5 M of zinc nitrate hexahydrate and 1 M of sodium hydroxide as the precipitant: (a) adding zinc nitrate hexahydrate on sodium hydroxide, (b) adding NaOH on zinc nitrate hexahydrate (different addition type, DAT).

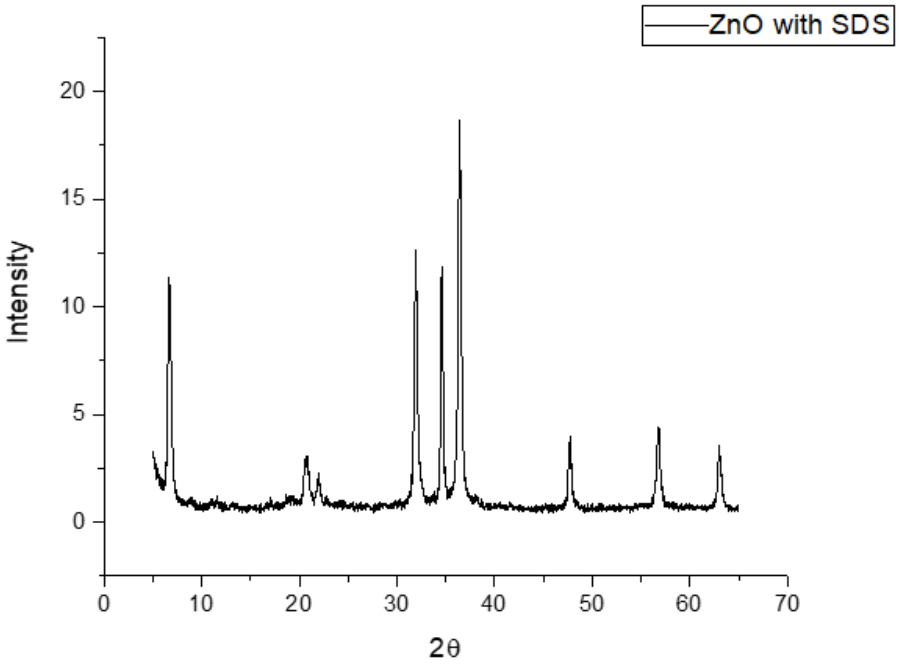

Figure 62. XRD for zinc oxide when using the reflux method with 0.3 M of zinc acetate dihydrate and 3 M of sodium hydroxide as a precipitant with sodium dodecyl sulphate (SDS).

3.2.4 The effect of different addition time in reflux method when using 1 M of ammonium carbonate $CO_3(NH_4)_2$ and 1 M of zinc nitrate hexahydrate Zn $(NO_3)_2 \cdot 6H_2O$

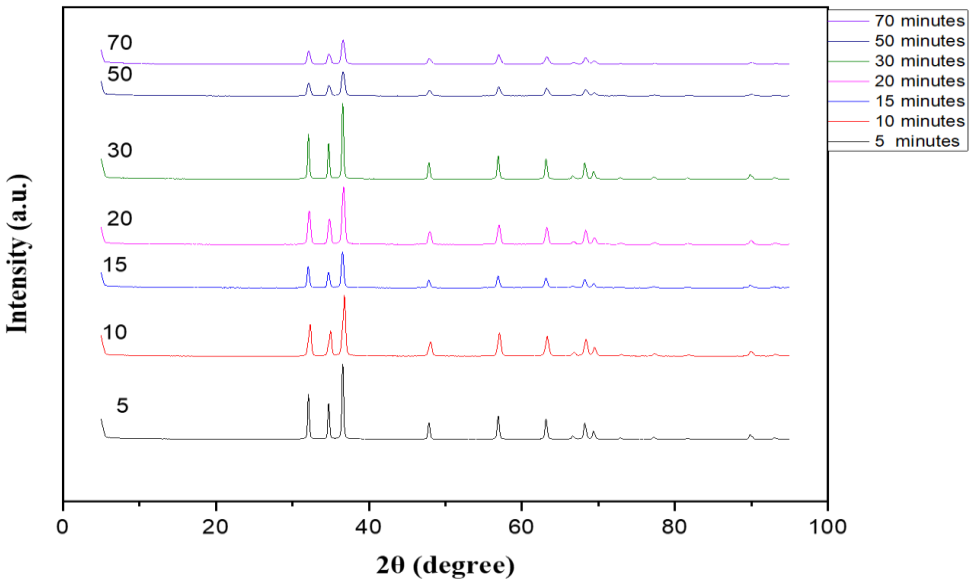

Figure 63 XRD results of zinc oxide when using1 M of zinc nitrate hexahydrate with 1 M of ammonium carbonate in a reflux method with different addition time.

Figure 59, which showed the XRD results for zinc oxide and the reflux method, again illustrated the hexagonal wurtzite morphology. As mentioned before, the sharp peaks reflected the degree of crystallinity of the ZnO particles. It appeared that the reflux method increased the ability of crystals to grow on the c-axis. The high intensity of the 002 plane means that growth towards the c-axis was the best option, as shown in Figure 59. Jung et al. illustrated that when applying an alkaline medium and using the sol–gel method, the growth of ZnO particles in the c-axis orientation was better than that in an acidic solution; this created nanorod structures in the ZnO nanoparticles [246]. In the current study, the reflux method was applied, along with a

pH value over pH 7, for zinc acetate dihydrate with NaOH, zinc nitrate hexahydrate with NaOH and zinc nitrate hexahydrate with $(NH_4)_2CO_3$.

At the same time, Figure 59, when compared with Figure 55, showed development in the crystallinity of zinc oxide using reflux with zinc nitrate hexahydrate and ammonium carbonate. Different addition types generated peaks of varying strength, which reflected the crystallinity. For example, in Figure 60, zinc acetate dihydrate had a high intensity even with the addition types in Experiments 7 and 8 due to the needle morphology obtained, especially at plane (101). Figure 61 showed sharper peaks when using the reflux method that reflected the growth to form the needle shape as a final morphology when using zinc acetate with different addition types.

When using zinc acetate and sodium hydroxide, according to the results shown in Figure 62, It could be observed that a different kind of morphology – note the peaks for 2θ values from 5 to 20 when using SDS (a lamellar structure that was thin alternating layers made up of different materials). This regularly occurred during the transformation, acting rapidly, and leaving behind a solid product [247, 248]. Nevertheless, peaks appeared at 2θ = 4 due to the residue of SDS in experiment 9 [249]. Using SDS as a surfactant (refluxed at 90 °C for 30 min), greater intensity of zinc oxide particles was achieved than in experiment 7. This was due to the role of SDS as a surfactant, serving to decrease the stacking of ZnO nanoparticles – which agglomerate due to their high surface-area-to-volume ratio [250].

In Figure 63, the XRD results (when using zinc ammonium carbonate and zinc nitrate with different periods before reflux: 5, 10, 15, 20, 30, 50 and 70 minutes) reflected the hexagonal wurtzite morphology. It was clear that 2θ values corresponded to the (101), (100) and (102) planes. The period for obtaining the strongest peaks was 5–50 minutes, which could be attributed to following the induction period at the beginning of the reaction (0–5 minutes) [36]. In addition, by 70 minutes, there might have been distortion of the zinc oxide crystal [251]. These results corroborated with the results of SEM.

3.2.5 Effect of the hydrothermal method on zinc oxide crystallinity

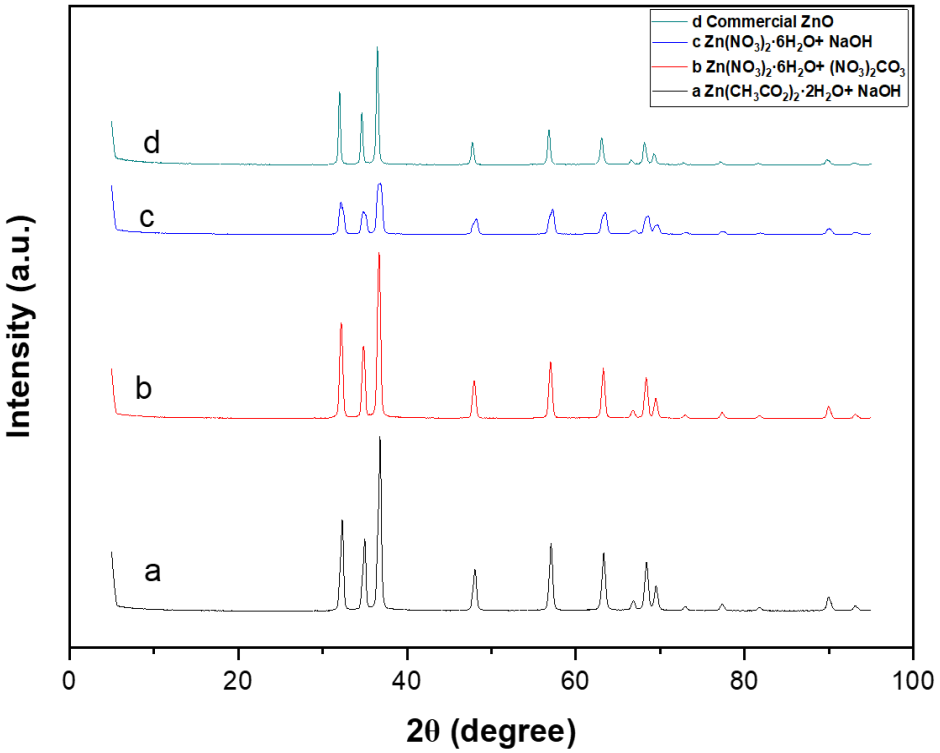

Figure 64 XRD results of zinc oxide compared to commercial ZnO when using a hydrothermal method.

Figure 64 illustrates the zinc oxide particles obtained using the hydrothermal method. All the XRD results reflect the hexagonal wurtzite phase with the space group P63mc as mentioned in (1.7 Zinc oxide crystals) [49, 225, 242]. As mentioned before, the peaks were narrow and sharp, which reflected the purity and high crystallinity of the ZnO particles. In addition, 2θ values corresponded to the (101), (100) and (102) planes [88, 252].

The intensity of zinc oxide when using zinc nitrate hexahydrate and ammonium carbonate using a hydrothermal method might be due to the nature of the resultant particles with the final morphology, in which the presence of specific organised micro-spherical settlements avoided further agglomeration and decreased the opportunity for more particles to stack [250]. In the

case of using zinc acetate dehydrate and sodium hydroxide (Experiment 10), the intensity was lower than that in Experiments 15 and 20 possibly due to irregular agglomeration, which increased the ability of particles to stack by affording them a high surface-area-to-volume ratio. This could also be due to the nature of the particles, which have two morphologies – needle and hexagonal. In addition, the increase observed in crystal size was attributed to the growth process and the types of Zn^{2+} precursors used [32].

According to equation 25 [61], the crystal sizes were 20.523, 17.194 and 26.877 nm, for Experiments 7, 13 and 27, respectively, as shown in Table 8 and Figure 65. The SEM results indicated that crystal size was slightly higher when compared with the XRD crystal size, which might be attributed to agglomeration of zinc oxide nanoparticles as a result of calcination at 550 °C for 4 hours and 90 °C for 30 minutes. In addition, the increasing crystal size observed was attributed to the growth process and the types of Zn^{2+} precursors used [49]. It could be observed when considering the properties of the chemicals used in this thesis, that the crystal size decreased when using sodium hydroxide in experiments 7 and 13. NaOH was known as a strong base and an exothermic compound. In experiment 7, zinc acetate – which was a natural compound from a thermodynamic view – was used as a zinc resource. In addition, with the use of zinc nitrate hexahydrate as an endothermic compound, reduced crystal sizes were obtained, which might be due to the nature of the chemical compound used in this research. Nevertheless, this study demonstrates the difference in size of zinc oxide crystals depends on the methods used for synthesis and other factors, not only temperature [91]. In addition, the crystallinity of zinc oxide when using ammonium carbonate as the precipitant was increased due to the effect of temperature [245].

Table 8. Crystallite sizes in experiments 7, 13 and 27 when using the hydrothermal method.

Experiment	Crystallite size (nm)
10	20.523
13	17.194
20	26.877

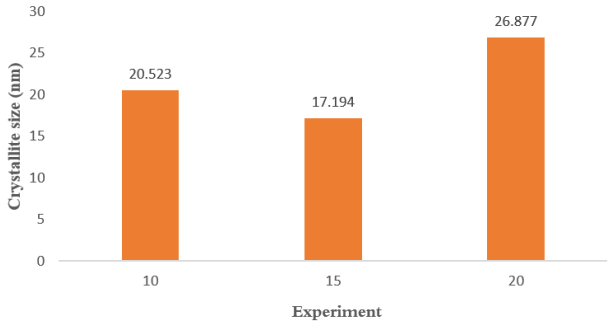

Figure 65 Zinc oxide crystallite size when using the hydrothermal method.

The sizes of the ZnO NPs were obtained in all experiments using the Debye–Scherrer equation [61]:

$$D = K\lambda / \Delta(2\theta)\cos\theta \quad (25)$$

where D is the crystal size for the ZnO structure, and K is the value of Scherrer's constant, equal to 0.9 [70, 253]. According to this equation, and based on the number of replicates and errors, when using $(NH_4)_2CO_3$ in Experiment 20, the crystallite sizes increased, on average, compared to Experiments 10 and 15. This was due to the high surface area, which made particles agglomerate. Raising the calcination temperature also increased the average ZnO particle size.

As Faure stated, agglomeration was a phenomenon that could be observed in nanoparticles or nano-powder in the gas phase or as a dried product resulting from the liquid phase [254]. Faure suggested there were two ways to reduce agglomeration. First, the particles might create a repulsive force between particles surfaces by separating the surfaces, which could be achieved by absorbing a suitable adlayer to separate the particles. The efficiency of the nanoparticles at surface interactions depended on interparticle forces in the system, such as van der Waals (Vdw), steric (polymer) and electrostatic forces (double layer), which played a vital role as interparticle forces. Dispersion force (DF) might also occur during a reaction between dipolar molecular interactions. These forces could be reduced by creating space between particles, but that was dependent on the geometry of NPs [254].

3.3 Morphology of zinc oxide nanoparticles studied via FTIR spectroscopic studies

Fourier transform infrared (FTIR) spectroscopy was considered a potentially useful technique to obtain information about the nature / purity of a solid state. An FTIR spectrometer was used to collect high-resolution data over a wide spectral range. This technique could measure intensity over a set wavelength scale for a limited time period. FTIR spectroscopy enables researchers to confirm a material's structure and identify the substance(s) it is comprised [255–257].

3.3.1 Effect of a precipitation method on zinc oxide particles studied

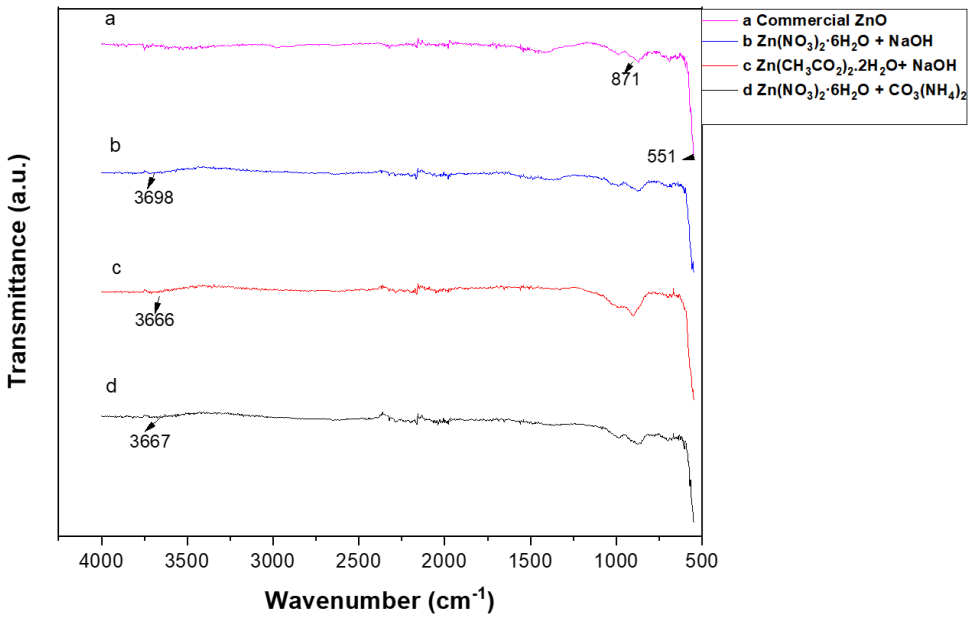

Figure 66 FT-IR spectra for zinc oxide samples, compared to commercial ZnO, when using the precipitation method.

FT-IR spectroscopy was conducted for the samples produced using the precipitation method to inspect the composition of the powder that had formed through calcination. Figure 66 presented the results of FT-IR spectroscopy for commercial zinc oxide in comparison to particles produced when using a precipitation method for three reactions: zinc acetate dihydrate with NaOH, zinc nitrate hexahydrate with NaOH and zinc nitrate hexahydrate with $(NH_4)_2CO_3$. The sharp band at 551 cm^{-1} was attributed to a Zn–O bond stretching vibration [258–261]. The band near 871 cm^{-1} was attributed to a metal oxide stretching vibration, which, in this case, belonged to ZnO. The results showed the same bands in all experiments (2 to 6). In addition, the results showed shrinking peaks when using zinc nitrate hexahydrate with NaOH.

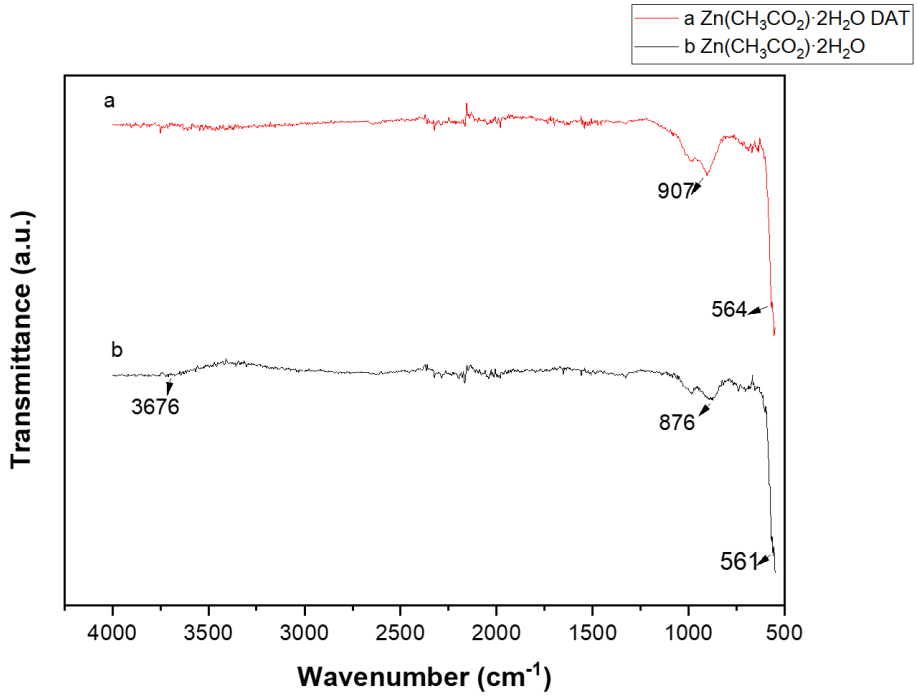

Figure 67 FT-IR spectroscopy for zinc oxide when using a) 3 M of sodium hydroxide on 0.3 zinc acetate dihydrate and b) 0.3 zinc acetate dihydrate on 2 M of sodium hydroxide (different addition types, DAT) in the precipitation method.

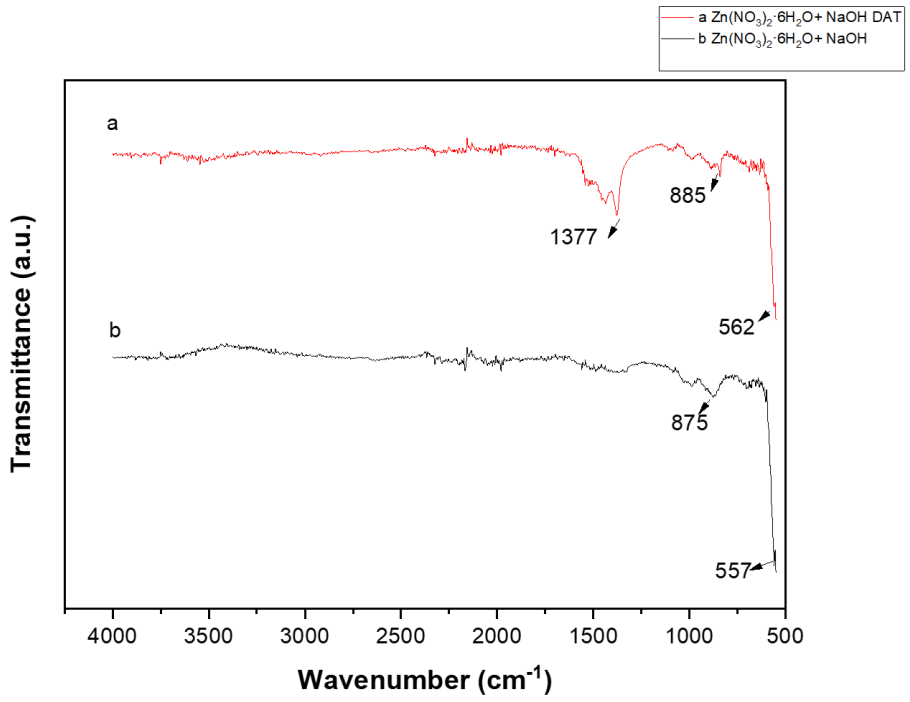

Figure 68 FT-IR spectroscopy for zinc oxide when using 1M of sodium hydroxide on 0.5 M of zinc nitrate hexahydrate and b) 0.5 M of zinc nitrate hexahydrate on 1M on NaOH in (different addition type, DAT) by precipitation method.

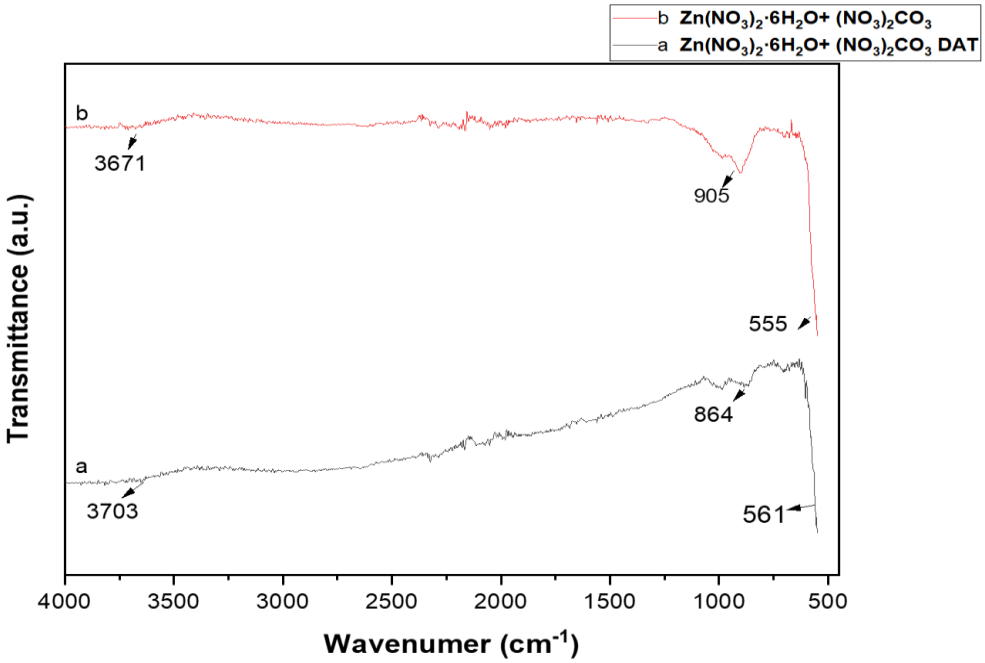

Figure 69 FT-IR spectroscopy for zinc oxide when using a) 1 M of ammonium carbonate on 1 M of zinc nitrate hexahydrate and b)1 M of zinc nitrate hexahydrate on 1M of ammonium carbonate (different addition types, DAT) by the precipitation method.

Figure 67–Figure 69 illustrated the effect of different addition types for zinc acetate with NaOH, zinc nitrate with NaOH and zinc nitrate with ammonium carbonate. When using zinc acetate dihydrate, a small peak at 687.0 cm^{-1} indicated a hexagonal morphology for zinc oxide [253], and in Figure 67, the wide peak at 1380 cm^{-1} was attributed to water molecular O–H binding [262], which indicated that changing the addition type could affected the final result by changing the characteristic properties of the product, as seen when using IR analysis. In addition, the peaks at 3265.6 cm^{-1} and 1352 cm^{-1} were attributed to water in the environment and deformation of the H–O–H bond in zinc acetate dihydrate with NaOH and zinc nitrate with ammonium carbonate [19]. Meanwhile, the band near 1000 cm^{-1} (905 – 864 cm^{-1}) was attributed to a metal oxide stretching vibration, which, in this case, belonged to ZnO [58, 197, 226]. Moreover, the wide peak at the range 3600 to 3700 cm^{-1} indicated stretching and binding,

which were associated with interlamellar or interlayer trace water molecules and the presence of a hydroxyl group [253, 261, 263].

3.3.2 Effect of reflux method on zinc oxide particles studied

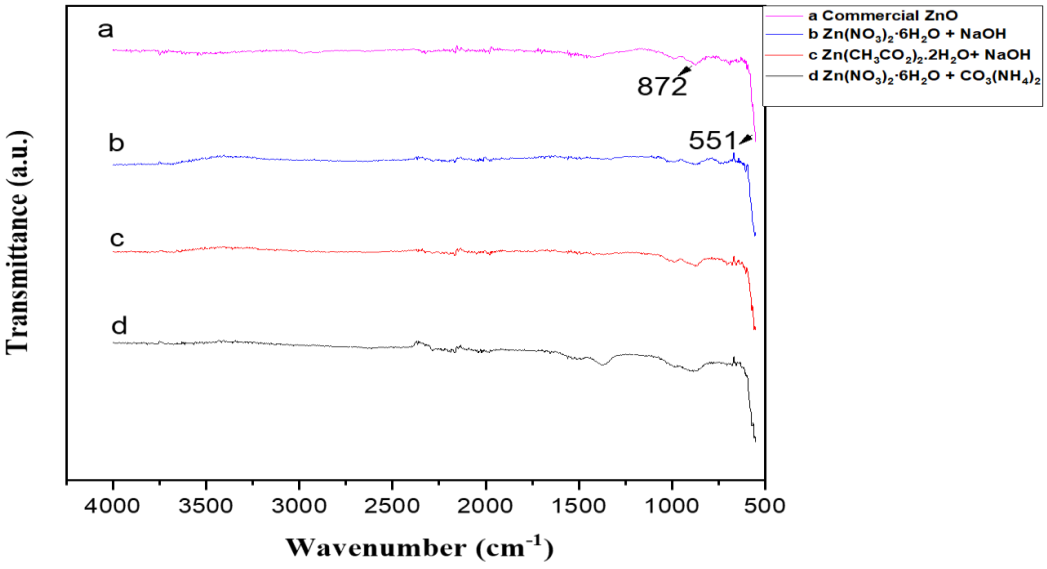

Figure 70. FT-IR spectroscopy for zinc oxide, compared to commercial ZnO, when using the reflux method.

With the reflux method (Figure 70), the reflux time was 90 minutes. Compared to the precipitation method, the reflux time had affected the IR result, and the stretching peaks in this experiment were stronger and wider. The small peak at 687 cm^{-1} indicated a hexagonal morphology for zinc oxide [253], and as mentioned before, the band at 551 cm^{-1} was the stretching vibration of the Zn−O bond [70].

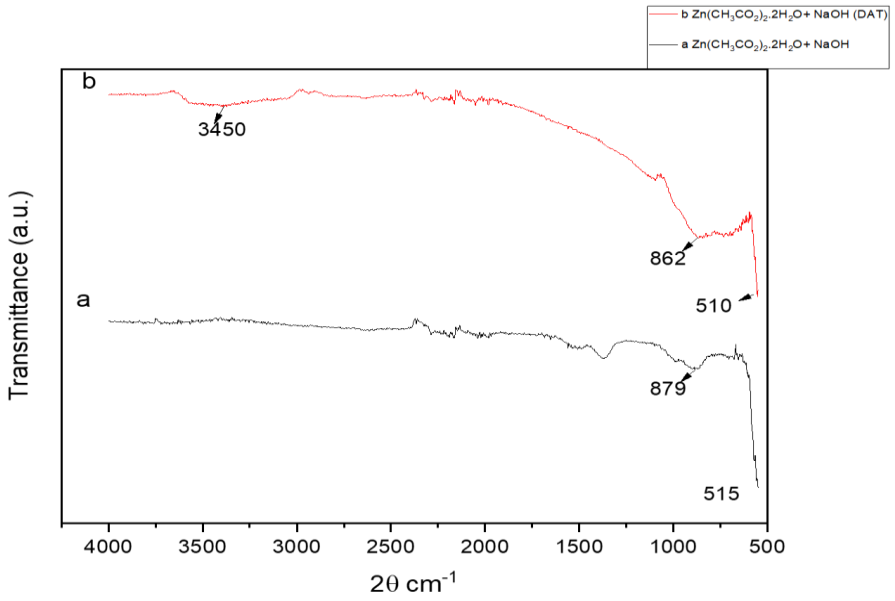

Figure 71 FT-IR spectroscopy for zinc oxide when using a) 3 M of sodium hydroxide on 0.3 zinc acetate dihydrate and b) 0.3 zinc acetate dihydrate on 3 M of sodium hydroxide (different addition type, DAT) by reflux method.

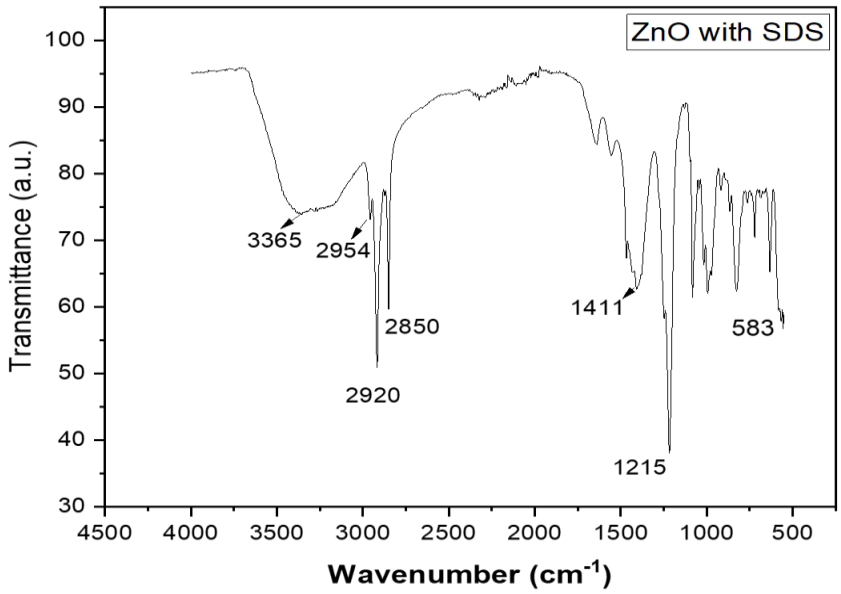

Figure 72 FT-IR spectroscopy for zinc oxide when using the reflux method with zinc acetate dihydrate with NaOH as the precipitant and when using SDS.

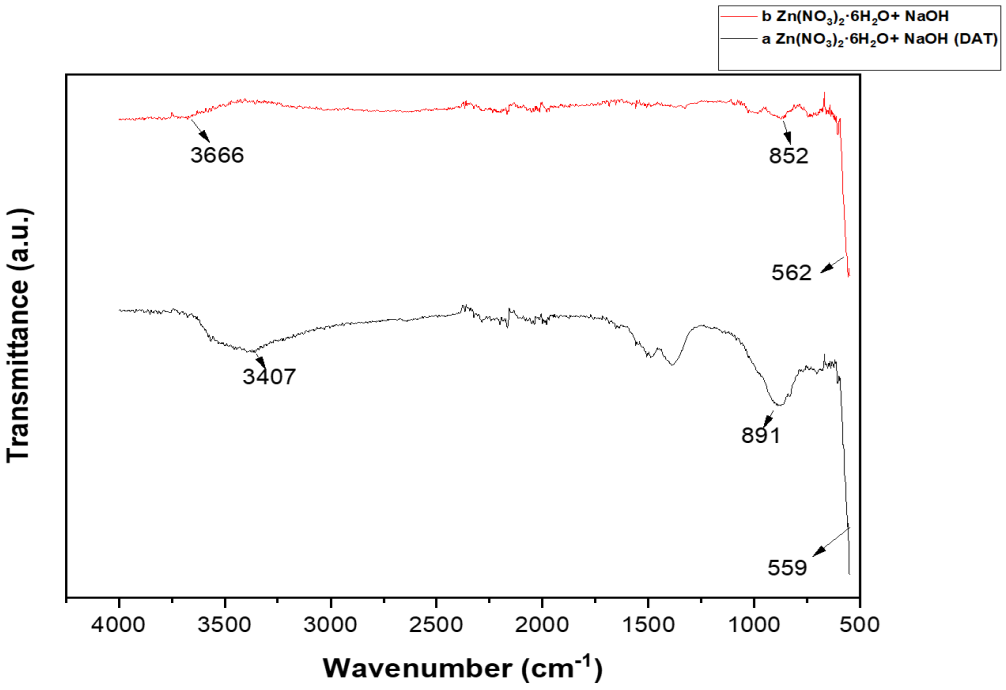

Figure 73 FT-IR spectroscopy for zinc oxide when using a) 1 M of sodium hydroxide on 0.5 M of zinc nitrate hexahydrate, b) 0.5 M of zinc nitrate hexahydrate on 1 M of sodium hydroxide (different addition type, DAT) by reflux method.

Figure 71 showed the FT-IR spectroscopy results for zinc oxide when using zinc acetate dihydrate with NaOH in the reflux method with different addition types. The peak at 687.0 cm^{-1} indicated a hexagonal morphology for zinc oxide [253]. When using different addition type, zinc oxide had a needle shape and showed a wide peak at 690 cm^{-1}, markedly different when compared to the sheet shape, which illustrated the effect of the addition type even when using the reflux method.

Figure **72** displayed two prominent vibrations at 2920 cm^{-1} and 2850 cm^{-1}, corresponded to the symmetric and antisymmetric C– H– stretching modes of the terminal –CH3 groups and a C–H bending vibration band at 1465 cm^{-1}. Moreover, using SDS affected the IR results: there were more bending and stretching at 2957, 2850 and 2918 cm^{-1}, which were attributed to the antisymmetric and symmetric stretching modes of C–H bonding. These, in turn, were related to the -CH3 (terminal group) of SDS. As previously noted, the stretching and binding at 3365

cm^{-1} were associated with interlamellar or interlayer trace water molecules and the hydroxyl group [253, 264]. The stretching beams at 1639 cm^{-1} and 1555 cm^{-1}, as well as at 1708 cm^{-1}, were associated with the O–SºO3 symmetric and asymmetric stretching vibration of the SDS sulfonate function group [264]. The adsorption band from around 1000 to 1400 cm^{-1} was also an indication of the SO^{3-} function group [264–266]. Meanwhile, the high peak at 3364 cm^{-1} and the adsorption peak at 1349 cm^{-1} indicated the presence of an (O–H) hydroxyl group due to the adsorption of water from the environment [225, 242].

In Figure 73, the FT-IR spectroscopy results demonstrated the use of the reflux method for zinc nitrate hexahydrate with NaOH under different addition types. The process was similar to when using the precipitation method, in which case zinc nitrate hexahydrate behaves the same when it was in the reaction vessel.

In experiment 9, the surfactant (SDS) and the reflux methods had been studied with zinc acetate dihydrate with NaOH as the precipitant.

3.3.3 Effect of different adding time in reflux method when using 1 M of ammonium carbonate $CO_3(NH_4)_2$ and 1 M of zinc nitrate hexahydrate Zn $(NO_3)_2 \cdot 6H_2O$

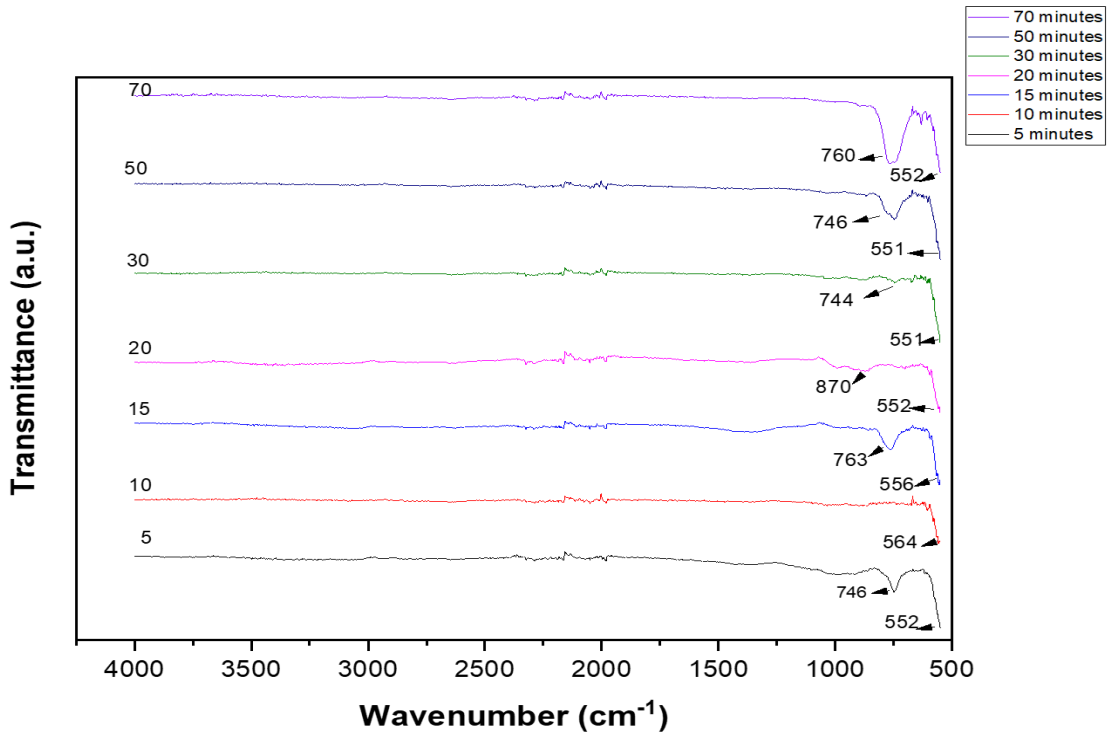

Figure 74 FT-IR spectroscopy for zinc oxide when using zinc nitrate hexahydrate and ammonium carbonate in the reflux method after different reflux times.

Figure 74 showed the effect of time on the zinc oxide morphology. It was clear that the band near 1000 cm^{-1} was due to the metal oxide stretching vibration, which, in this case, belonged to ZnO for all determination times: 5, 10, 15, 20, 30, 50 and 70 minutes. Generally, IR figures represented pure ZnO particles – especially the sharp peaks from 551 to 564 cm^{-1} [197, 261].

3.3.4 Effect of the hydrothermal method on zinc oxide particles studied

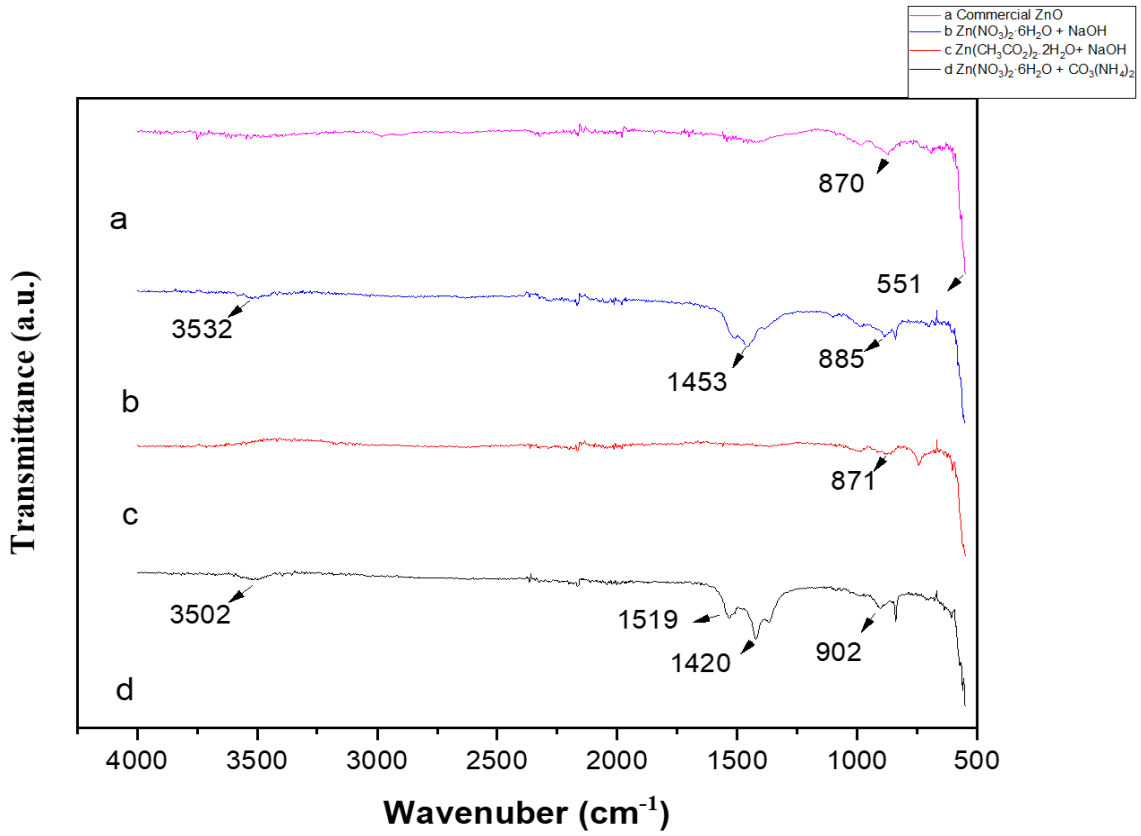

Figure 75. FT-IR spectroscopy results for zinc oxide compared to commercial ZnO when using the hydrothermal method.

Figure 75 illustrate the effect of the hydrothermal method. As mentioned earlier, the peak at 551 cm^{-1}, as well as those at 3502 to 3500 cm^{-1}, were attributed to H−O stretching vibration due to water in the environment.

It appeared that there was little difference between the three methods used based on the FT-IR results. It was notable that using zinc acetate dihydrate with NaOH, in all of the methods, gave results that were comparable with the results for commercial zinc oxide. When using the reflux

method, the results for all of the experiments were similar to those for commercial zinc oxide, even in case of the current study different times in this project.

3.4 Raman spectroscopy measurements

Raman spectroscopy could be used to determine many properties, such as chemical bonding, intermolecular bonds, crystallographic orientation, molecules in materials and population information for a phonon mode. Raman shifts measurement of a nanostructure provides information about surface defects. Zinc oxide had a (hexagonal crystal) structure with space group C^{6}_{v4}, as mentioned before (1.7 Zinc oxide crystals) [70].

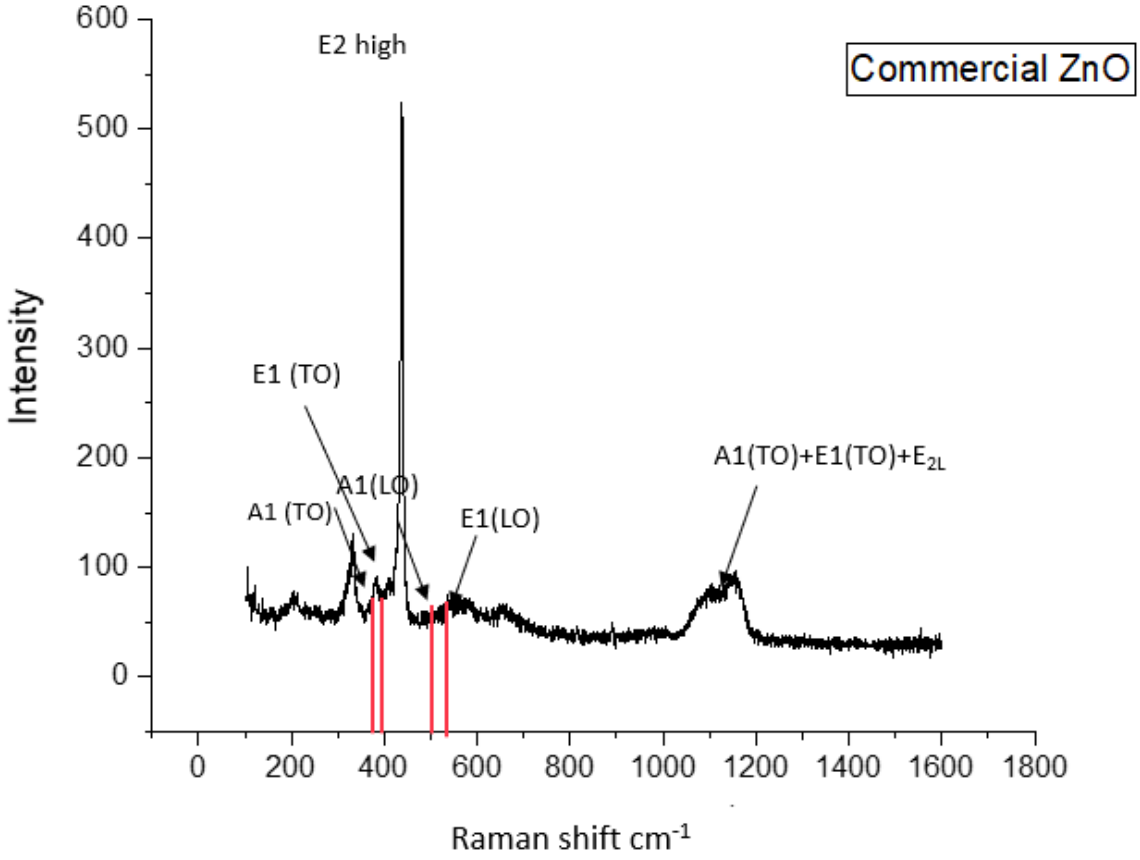

Figure 76 Raman spectrum for commercial ZnO

3.4.1 Effect of different concentrations of sodium hydroxide when using 0.05 M of zinc acetate dihydrate in precipitation method

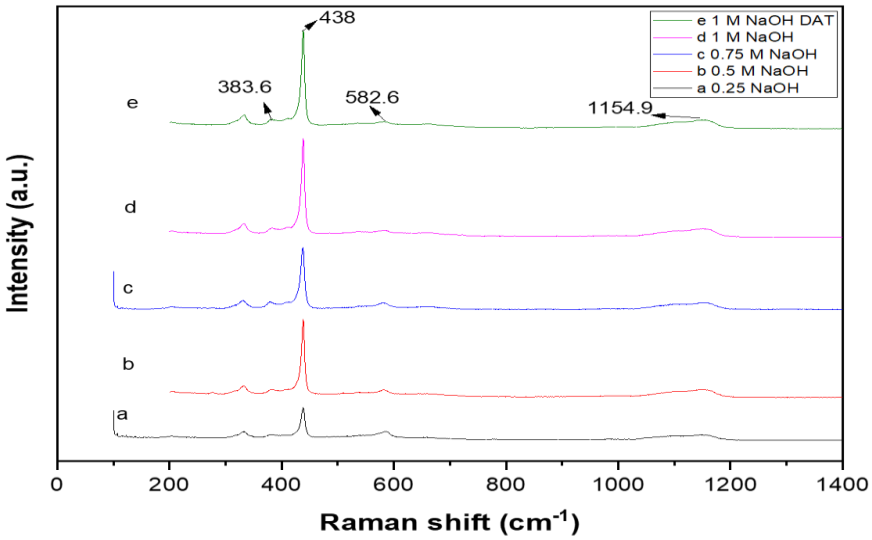

Figure 77 Raman spectra for zinc oxide using 0.05 M of zinc acetate dihydrate with different concentrations of NaOH when using the precipitation method.

3.4.2 Effect of precipitation method on zinc oxide particles studied

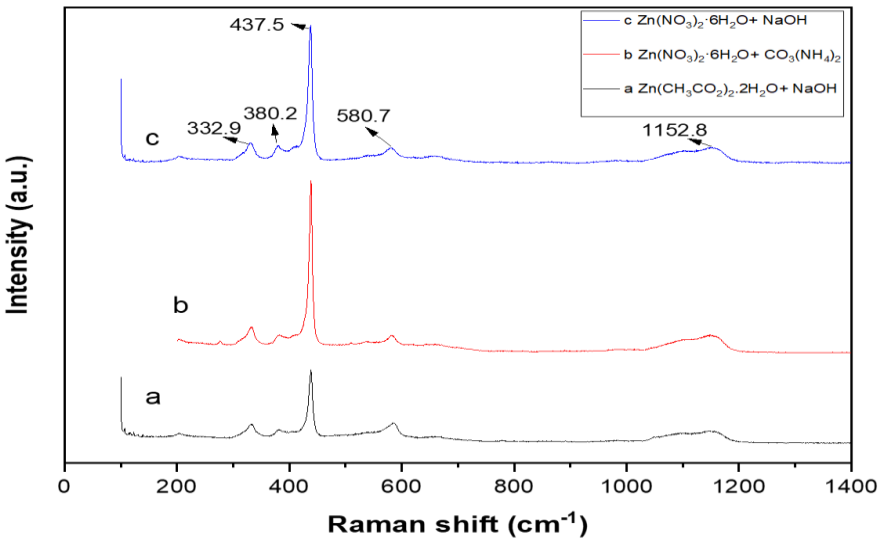

Figure 78 Raman spectra for zinc oxide when using the precipitation method.

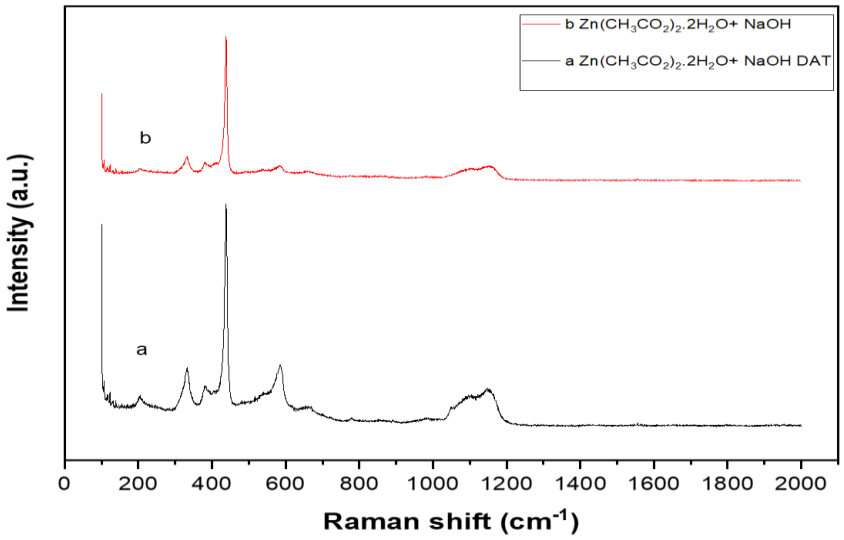

Figure 79 Raman spectra for zinc oxide when using (a 0.3 zinc acetate dihydrate on 3M of sodium hydroxide (different addition types, DAT) and b) 3M of sodium hydroxide on 3M of sodium hydroxide in the precipitation method.

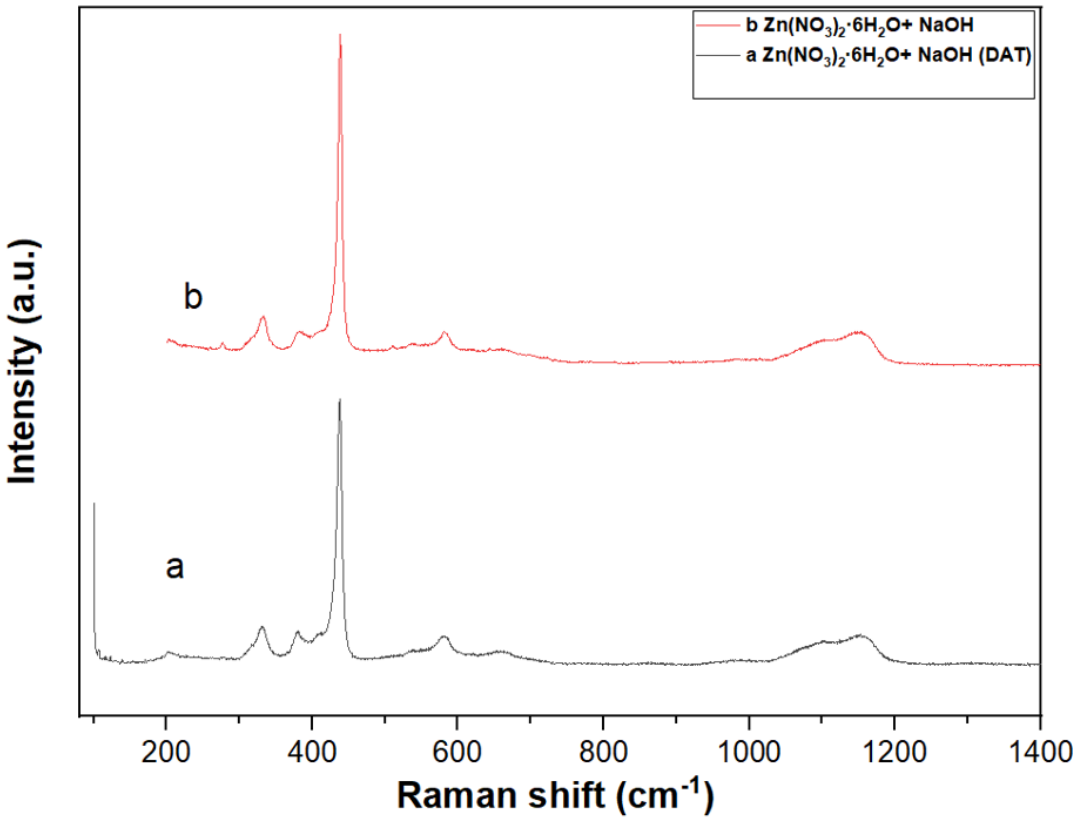

Figure 80 Raman spectra for zinc oxide when using, a) 1 M of sodium hydroxide on 0.5 M of zinc nitrate hexahydrate (different addition type, DAT) and b) 0.5 M of zinc nitrate hexahydrate on 1 M of sodium hydroxide by precipitation method.

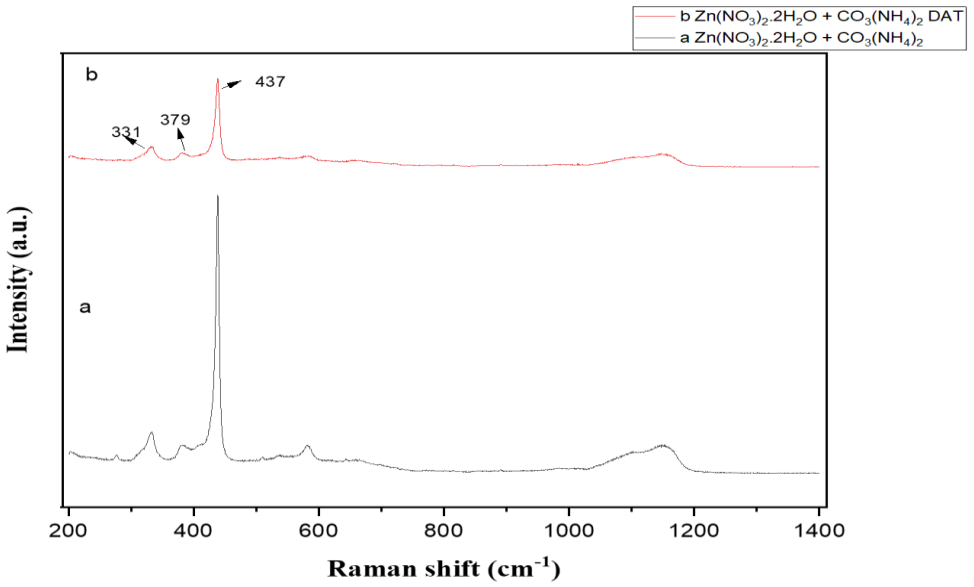

Figure 81 Raman spectra for zinc oxide when using, a) 1 M of zinc nitrate hexahydrate on 1 M of ammonium carbonate and b) 1M of ammonium carbonate on zinc nitrate hexahydrate (different addition type, DAT) by precipitation method.

3.4.3 Effect of reflux method on zinc oxide particles studied

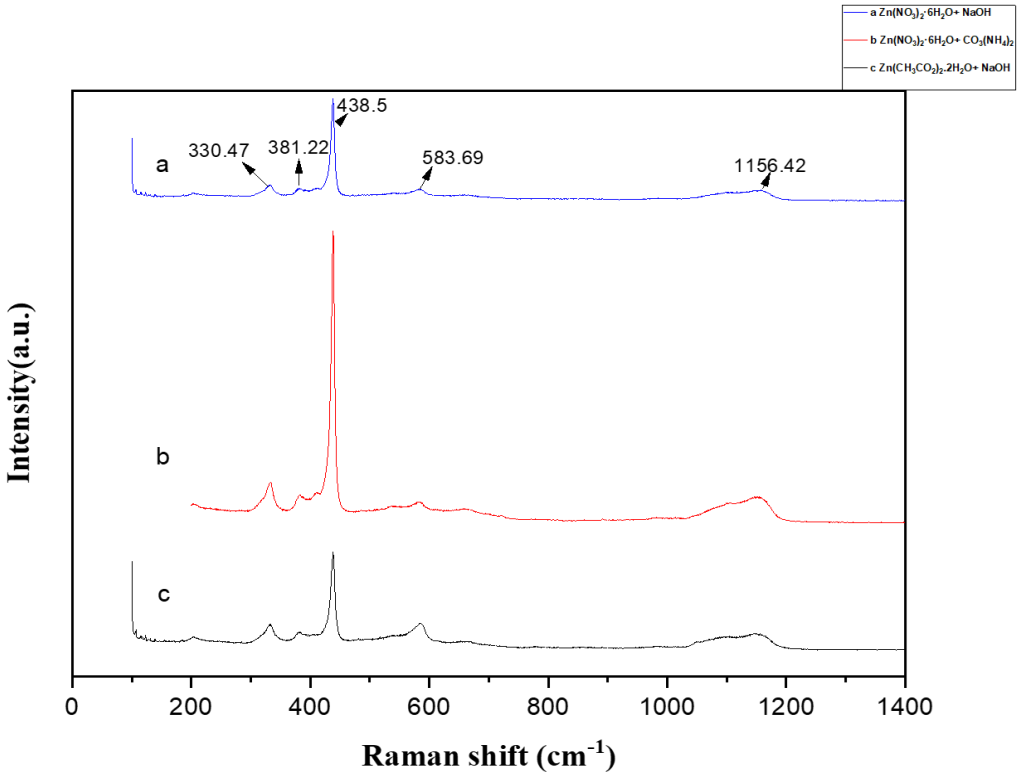

Figure 82 Raman spectra for zinc oxide in reflux method.

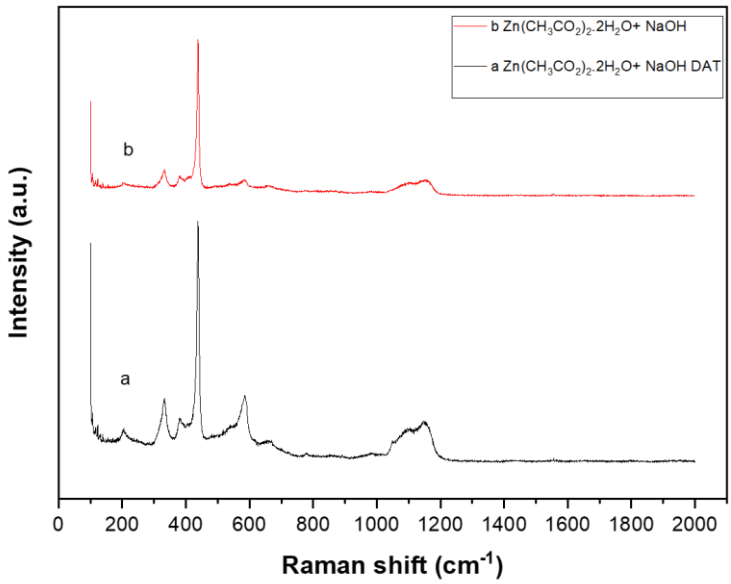

Figure 83 Raman spectra for zinc oxide when using, a) 0.3 M of zinc acetate dihydrate on 3 M of sodium hydroxide (different addition type, DAT) and b) 3 M of sodium hydroxide on 0.3 M of zinc acetate dihydrate by reflux method.

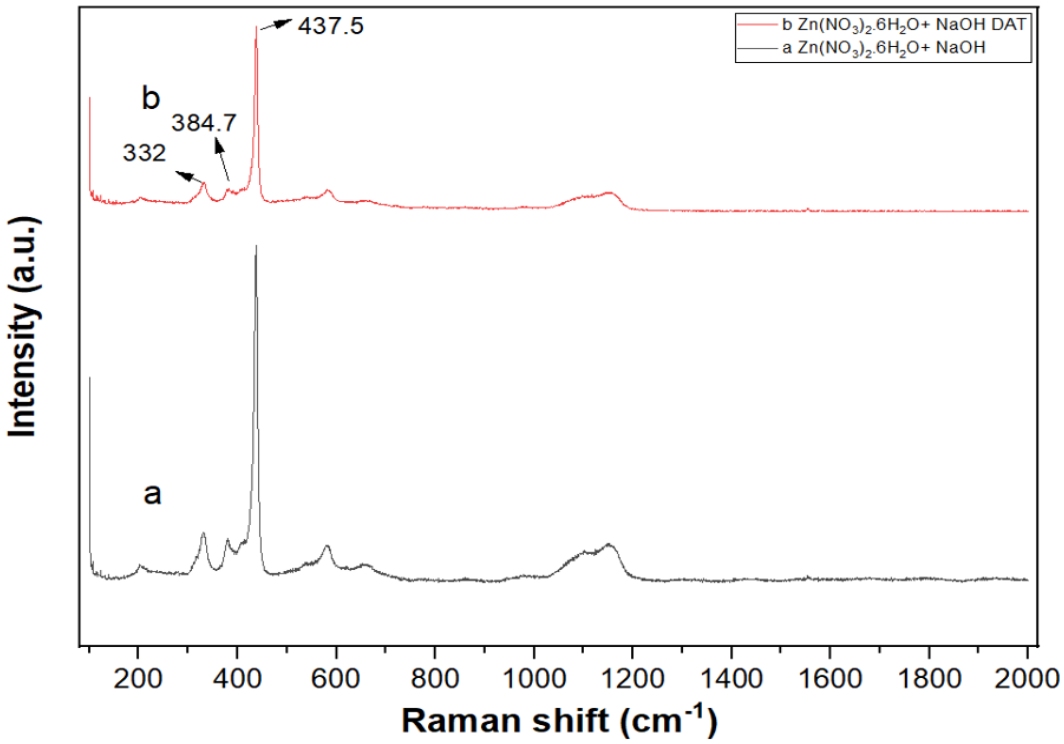

Figure 84 Raman spectrum for zinc oxide when using, (a 0.5 M of zinc nitrate hexahydrate on 1 M of sodium hydroxide and b) 1 M of sodium hydroxide on 0.5 M of zinc nitrate hexahydrate (different addition type, DAT) by the reflux method.

3.4.4 Effect of different adding time in reflux method when using 1 M of ammonium carbonate $CO_3(NH_4)_2$ and 1 M of zinc nitrate hexahydrate $Zn(NO_3)_2 \cdot 6H_2O$

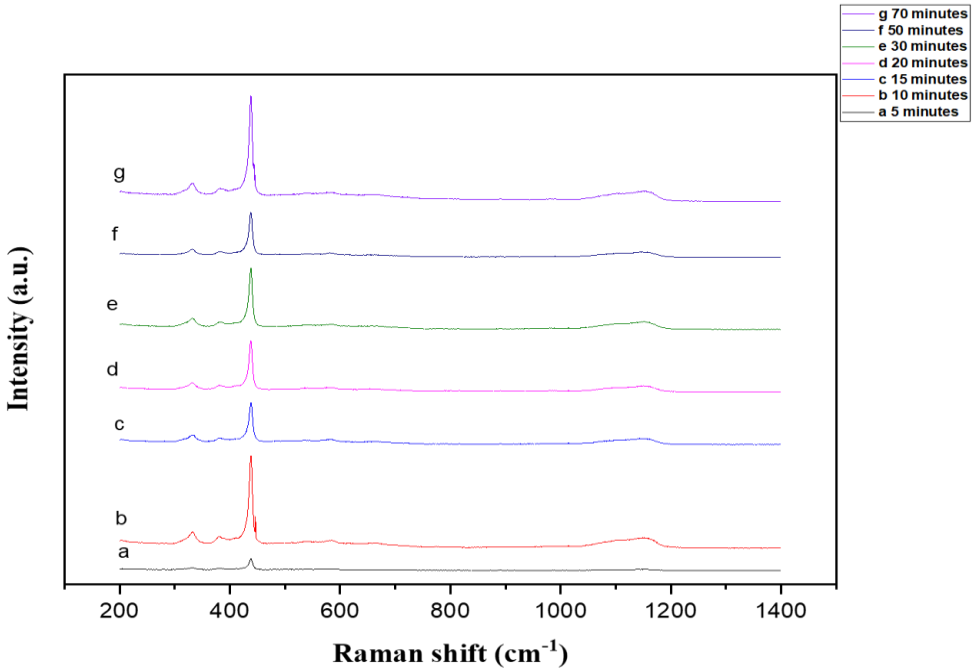

Figure 85 Raman spectra for zinc oxide when using zinc nitrate hexahydrate with ammonium carbonate when using the reflux method for different times.

3.4.5 Effect of hydrothermal method on zinc oxide particles studied

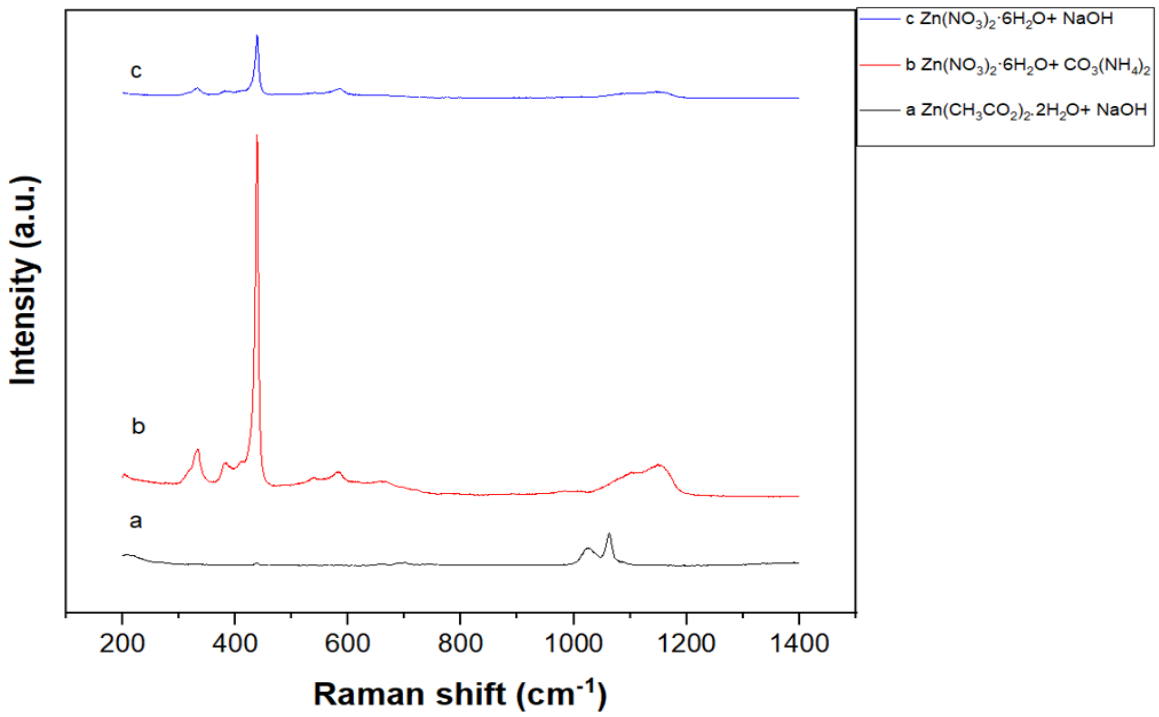

Figure 86 Raman spectra for zinc oxide when using the hydrothermal method.

All Raman peaks for zinc oxide samples occurred from 244 cm^{-1} to around 1200 cm^{-1}. All Raman peaks were related to a hexagonal wurtzite structure that had the structure phase C6v 4 (P63/mc) space group (1.7 Zinc oxide crystals) and a simple unit for a single axial crystal's structure.

In addition, a Brillouin zone centre, that formed from a reciprocal matrix or lattice, had an optical phonon, which was related directly to the first order in Raman scattering for single zinc oxide crystals [70, 267].

Figure 76 illustrated the Raman spectrum for a commercial zinc oxide, which was compatible with having a hexagonal structure. All results obtained in this study also resembled a hexagonal structure (Figure 77–Figure 86), except for some results where the methods, addition types, or

a low-density during comparisons prevented the Raman spectra from clearly peaking, such as in Figure 85 and Figure 86.

First, the point group theory known in the optical phonon modes was represented by the equation:

$$\Gamma = A1+2B1+E1+2E2 \quad (26)$$

where A1, E1 and E2 classified as the first order in a Raman-active mode [267]; A1 and E1 represent a polar mode, which could be divided into two modes: the transverse and longitudinal optical modes (TO and LO) [267]; E2 was a non-polar mode in Raman spectra consisting of low- and high-vibration phonons; B1 was modest, silent or forbidden [268]. In polar modes, the phonon mode had active Raman spectra and IR, while E2 modes only had active Raman spectra.

It was known that in Raman scattering, the density of phonons could be calculated according to matrix dynamic theory, the occurrence of light was vertical on the polar axis [0001] for Raman spectra for zinc oxide measurement, and the A1(LO) frequency does not occur.

In all figures, the peak appearing at 240 cm^{-1} was caused by interstitial defects of zinc atoms.

The vibration peaks for zinc oxide were as follows: Stokes Raman scattering, Rayleigh and anti-Stokes Raman scattering were found at 315–375 cm^{-1}, around 441 cm^{-1} and 580 cm^{-1}, respectively [267].

The peak at 333 cm^{-1} was found between the nonpolar E2-high and E2-low modes (represented as E2 (high)–E2 (low) mode), illustrated that multi-phonon scattering occurred. In addition, the peak at 375 cm^{-1} was attributed to A1(TO) due to the persistent anisotropy position in the force. The peak at 315 cm^{-1} reflected the second order in the Raman method where it referred to the nonpolar E2 mode [267]. This result was observed for all the Raman spectral measurements in our study.

The strongest, dominant and sharpest peaks were found in the range from 428 cm^{-1} to 456 cm^{-1}, which represented the high nonpolar mode, related to wurtzite zinc oxide. The high strength was linked to the strength of the crystallinity of zinc oxide. The E2-high mode and A1(LO) of all zinc oxide results were observed at 439 and 578 cm^{-1}, respectively [268]. The shift in the peak at 434 cm^{-1} could be attributed to a reduction in the crystal degree of the wurtzite order phase or distortion of the crystal morphology [243]. The Raman results in this case were compatible with the XRD results.

The peak from approximately 560 cm^{-1} to 590 cm^{-1} was usually a result of O^{2-} vacancies, which were atomic defects, or oxygen defects in the zinc oxide structure between polar mode A1 and E1 as the LO visual phonon mode. In the current results, this peak could be observed, with high density, when using the reflux method and producing a needle shape, both when using zinc acetate dihydrate with NaOH (Figure 83) and zinc nitrate hexahydrate with NaOH (Figure 84).

The mode that overlapped with A1(LO) (Figure 77–Figure 86) required that the strong peak was a result of A1(LO). The strongest peak was caused by E2 as the highest mode in the zinc oxide wurtzite crystal morphology. The high E2 phonon frequency value was attributed to compressive stress. In turn, the low value in the E2 phonon mode was a result of tensile stress. This stress was basically generated due to a mismatch that occurred in the lattice, for example, thermal enlargement factors of the metal oxide nanoparticles or distortion in the crystal structure.

The low-value mode had been observed in Figure 84 when using zinc nitrate hexahydrate with NaOH in the reflux method. Different methods illustrated the effect of changing the addition type on the final zinc oxide morphology when using the same zinc resource and precipitation agent. The current study showed the same phenomena when using the reflux method at different times after 5 minutes, as mentioned before, as a result of a growth process that began after the induction time for the reaction. Moreover, the peak at 583 cm^{-1}, as shown in Figure

86 when using zinc acetate dihydrate with NaOH in the hydrothermal method, could be a result of the irregular morphology of zinc oxide. This peak was weak, which could be attributed to polar mode longitudinal optical A1 and E1. E1 frequencies were related to unoccupied oxygen sites, the presence of complex defects and zinc interstitial space in the crystal [268, 269].

The peak at 1095–1200 cm^{-1} reflected the A1(TO) mode due to defects in the crystal such as interstitial zinc, oxygen vacancies and other complexes [270]. In addition, the presence of the broad peak in the range of 1050–1200 cm^{-1}, which could be represented by A1(TO) + E2(TO) + E2L [268], was a distinctive property of (II–VI) semiconductors as well as a sign of multi-phonon processes in Raman spectra [243].

3.5 Electrochemical method

In this part of the current study, the corrosion resistance of the blank substrate (steel panel), epoxy-only coated steel, and ZnO-epoxy nanocomposite coating was investigated. Each substrate was separately placed in a 3.5% NaCl solution for different times (typically 8, 9 and 10 days) before being measured.

For the electrochemical experiments, the three-electrode cell, as the most common for the typical type of electrochemical measurement setup, was employed. In this kind of three-electrode configuration, the interfacial potential was controlled precisely [148]. The working electrode was the investigated sample (5.08 cm * 10.16 cm), the counter electrode was made of Pt, and the reference electrode was a saturated calomel electrode. The frequency range for the EIS measurements was 20 kHz–0.01 Hz. All these were at an AC signal amplitude of 10 mV = 0.01 V at the open-circuit potential (OCP) [110, 137].

Corrosion studies of the protective properties of blank steel, pure epoxy, ZnO 1 epoxy and ZnO 2 epoxy composites coated with steel panel as working electrodes were investigated at ambient temperature in an aerated solution. Table 9 (show the samples that have been used in this chapter.

Table 9. Samples used in electrochemical corrosion test

Number of samples	Name	Sample type
1	Blank steel	Only steel panel
2	Epoxy steel	Epoxy with steel panel
3	ZnO–epoxy composite 1	Zinc oxide (rod morphology) with epoxy steel coating

4	ZnO–epoxy composite 2	Zinc oxide (novel morphology) with epoxy steel coating

A positive OCP value indicated that more corrosion protection had been obtained due to inducing the diffusion penetration into solution /coating interface [164].

It was worth noting that the adhesion of the protective coating represents an integral function for corrosion inhibition due to the accumulation process of steel ions and anions that attacked the films inside the vacancies in the coating and steel panel interface, which could affect the kinetics of these anions in the corrosion process.

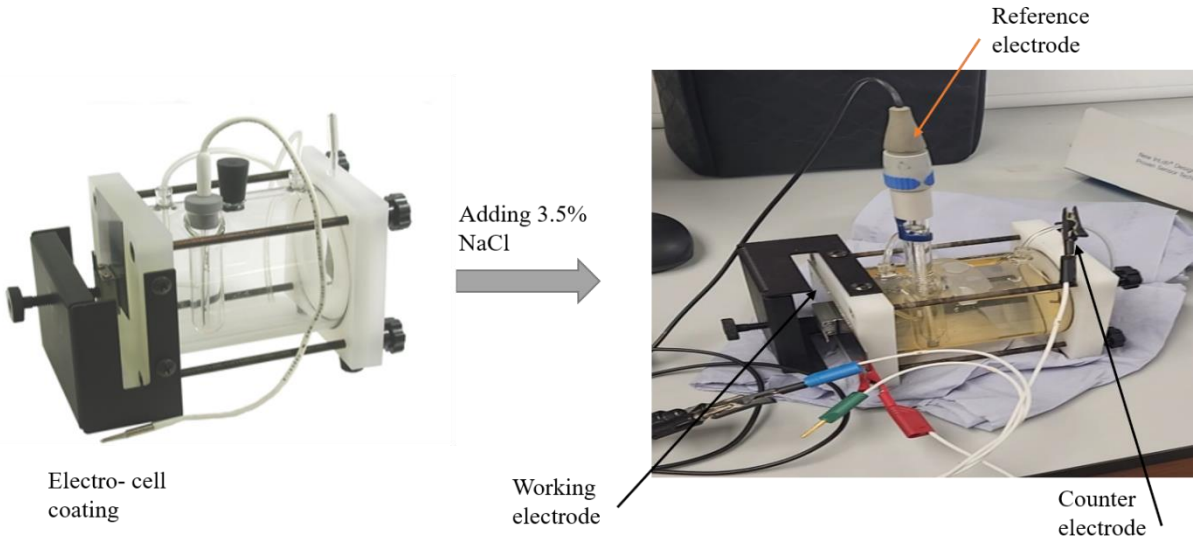

Figure 87 The electrochemical coating cell contained three electrodes.

Figure 88 Blank steel, Epoxy/steel coating and ZnO/epoxy steel coating after exposure to 3.5% NaCl solution for 10 days.

Figure 87 showed the electrochemical coating cell that was used in this project. The working electrode was fitting to the cell, as Figure 87 illustrated electro-cell coating that have been used for corrosion study.

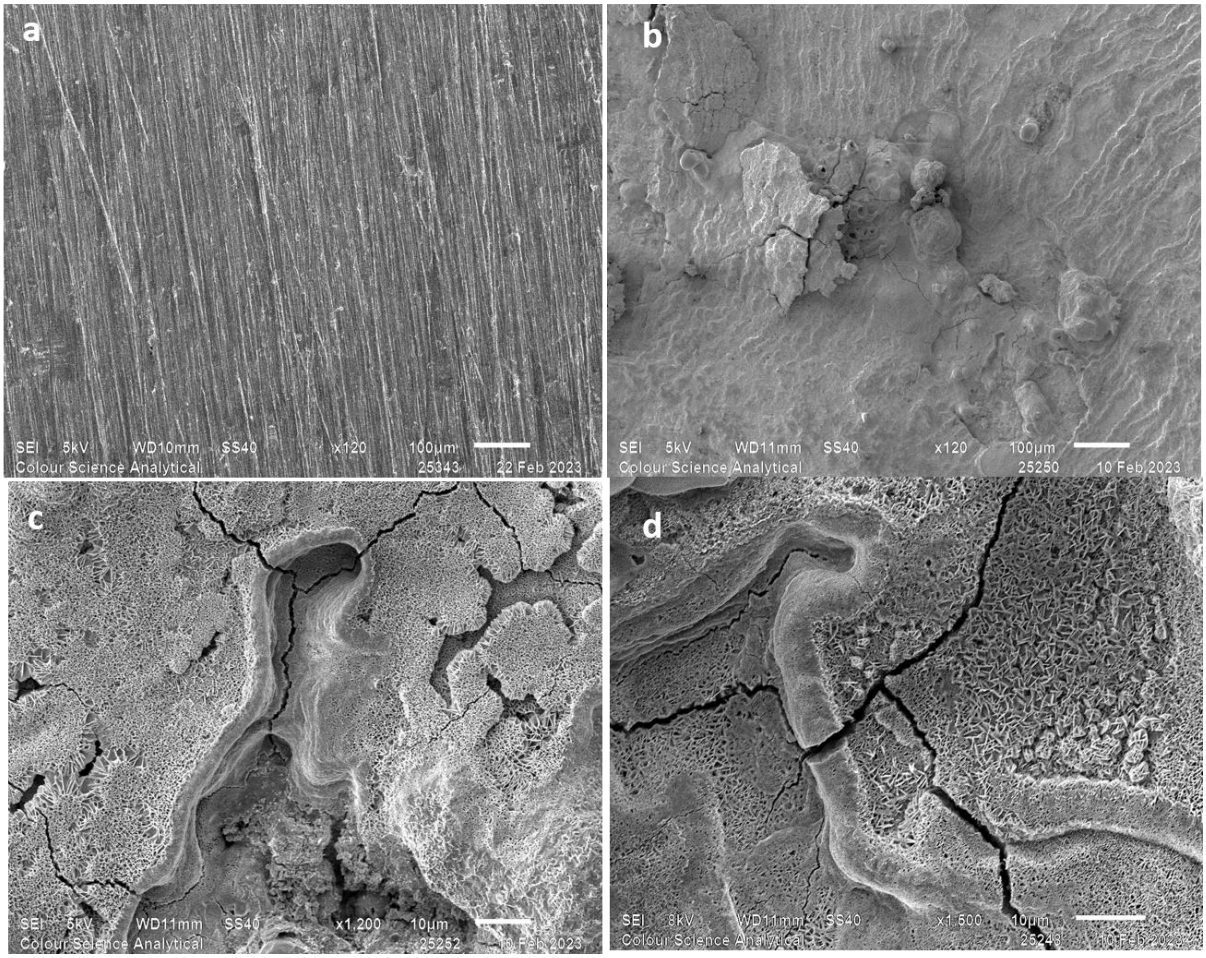

Figure 89 SEM images of blank steel surface a) before at 120 x magnification and blank steel after exposure to NaCl solution after 10 days at different magnifications b) 120 x, c) 1200 x, and d) 1500 x magnification.

Figure 88 showed the effect of the sample's exposure to 3.5% NaCl after 10 days for blank panel steel, epoxy coated steel and ZnO-epoxy composite coating steel. Figure 87 illustrates the degree of damage in surfaces due to the corrosive agents that had the highest impact on the blank steel then the epoxy steel coated and the low damage in ZnO- epoxy composite steel coating.

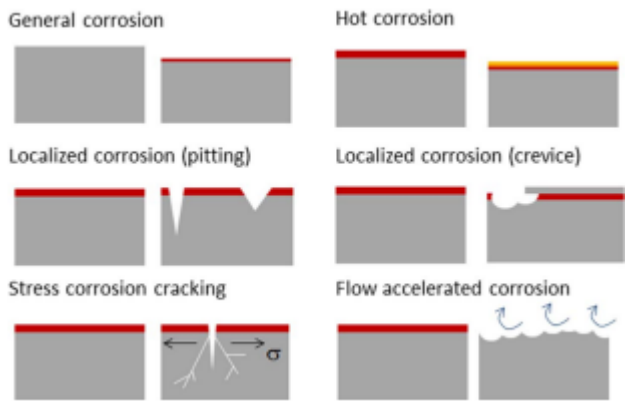

Figure 90 corrosion types in metals and alloys [271]**.**

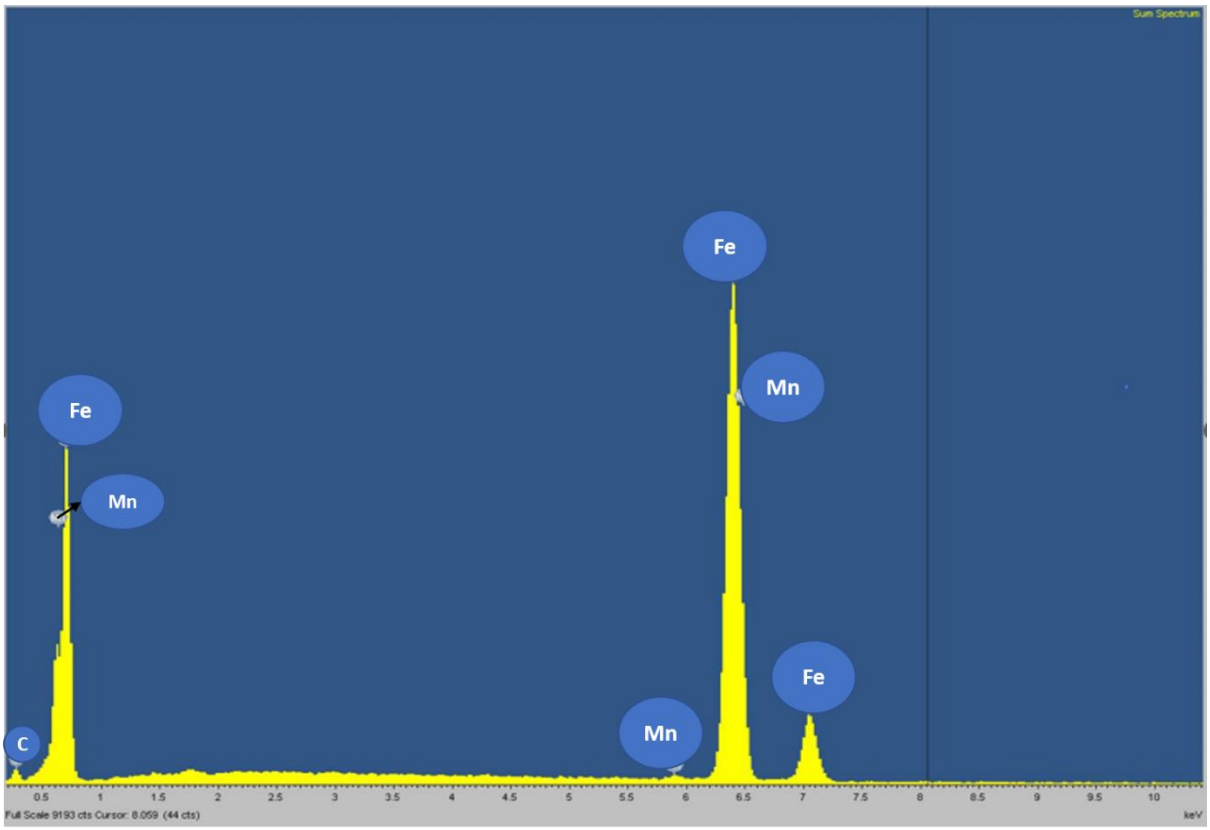

Figure 91 EDX data for blank steel before exposure to NaCl solution for 10 days.

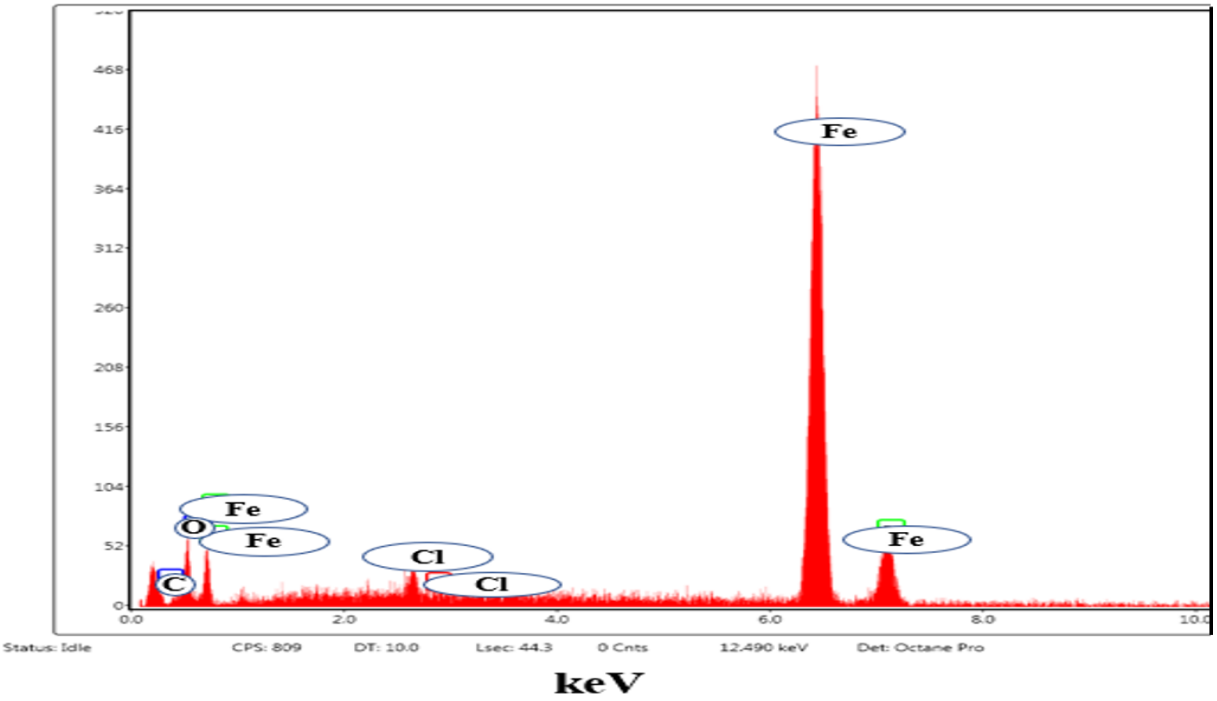

Figure 92 EDX result for blank steel after exposure to NaCl solution for 10 days.

Figure 89 showed SEM results surface for blank steel a) before exposure to electrolyte solution and b, c and d blank steel after exposure to NaCl solution after 10 days at different magnifications. It appeared that there were observed potential (PTC), localised corrosion pitting and crevice and stress crack (SCC) types. These results were similar to Zhou et al.'s results [272]. Corrosion, thermodynamically known as a degradation process, occurred in materials such as alloys and metals in various forms, such as high temperature corrosion, potential corrosion, localised corrosion and mechanically supported corrosion and Figure 90 clarified the common types of corrosion usually recognized in metal and alloys [271].

In Figure 91, it appeared that the most common components for the blank steel before exposure to NaCl were C, O, Mn and Fe. After exposure to the electrolyte, it appeared that stress corrosion cracking as well as pitting and crevice, as localised corrosion affected the blank steel panel the most and that this reflected the effect of chloride ions and oxygen on the steel, as

Figure 92 shows the corrosive ions as a component of the steel surface after 10 days of immersion time.

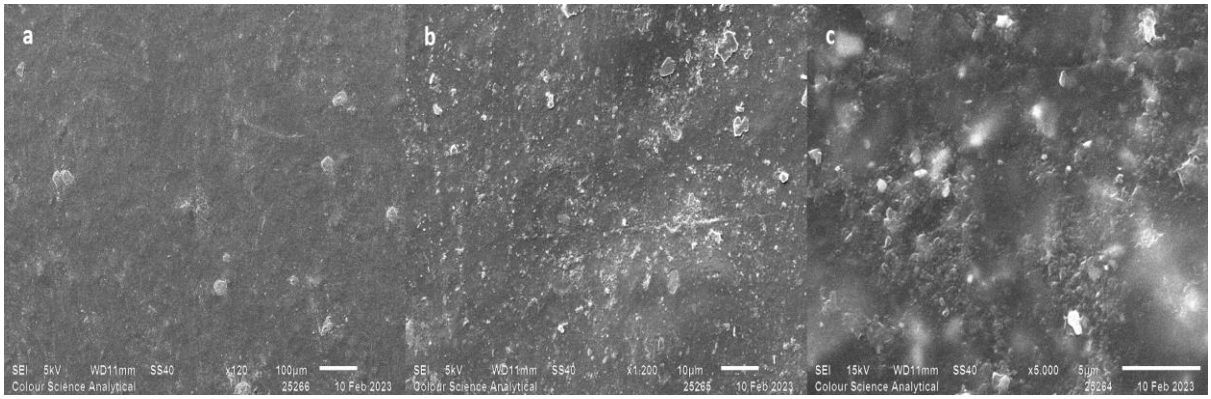

Figure 93 SEM images of epoxy-steel surface before exposure to NaCl solution a) 120 x, b) 1200 x and c) 1500 x magnification.

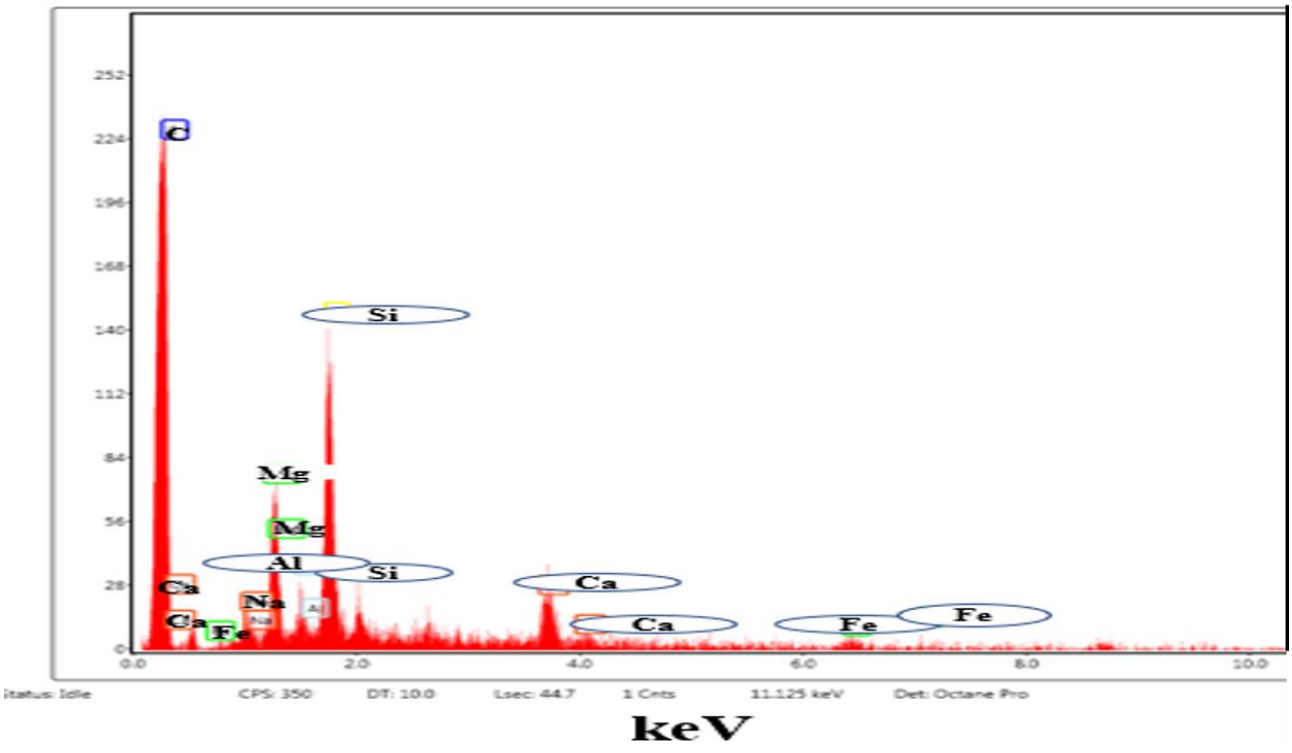

Figure 94 EDX data for epoxy steel before the corrosion test.

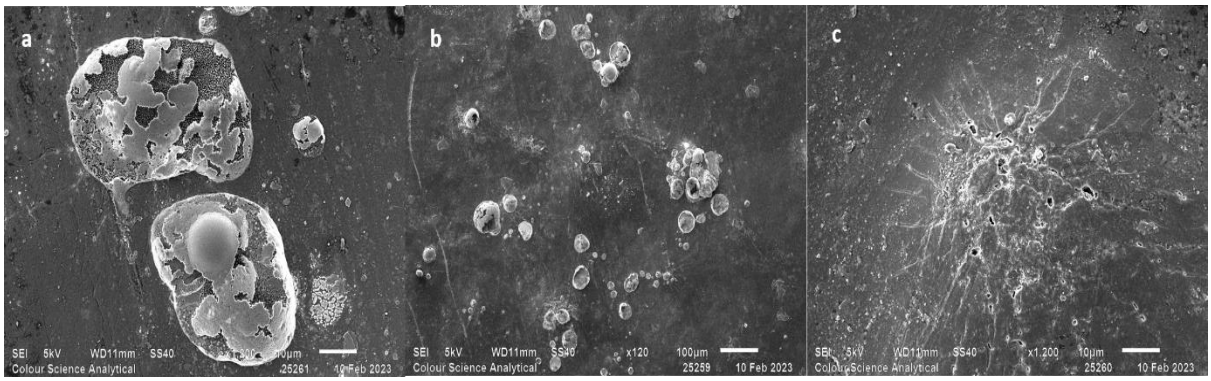

Figure 95 SEM images of epoxy-steel surface after exposure to NaCl solution at 10 days immersion time at a) 500 x, b) 1000 x, c) 5000 x magnification.

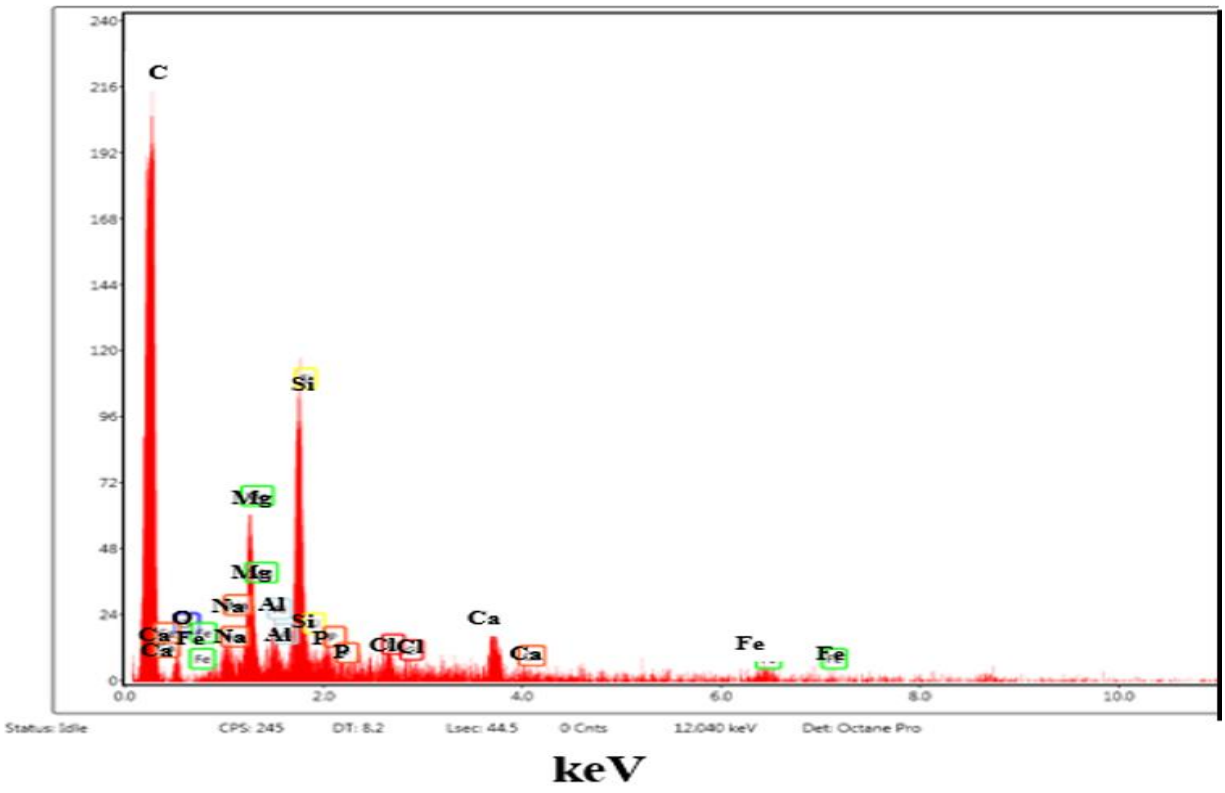

Figure 96. EDX data for epoxy steel after exposure to NaCl solution for 10 days.

Figure 93 shows the SEM results for epoxy steel coating before exposure to the electrolyte. Adding the epoxy coating made the surface smoother with the main components Figure 94 being C, O, Mn, Fe, Mg, Si and Ca, from EDX results. After 10 days of immersion time, it

appeared from Figure 95, which shows SEM results, that there was localised corrosion in some areas and pitting corrosion. This could be attributed to the decline in thermal stability in epoxy steel coating, which was demonstrated by SEM analysis [273]. It is clear from the EDX results in Figure 96 that the appearance of Cl^- ions as a new element reflected the damage that occurred at the surface of epoxy steel coating after 10 immersion days and the presence of corrosive ions on the surface Cl^- and O^{2-} after the immersion time, which meant that the corrosive ions had the ability to penetrate the two interfaces, solutions/epoxy and the solution with the steel interface.

The degradation in the epoxy steel coating was still less than the result in blank steel, which revealed the effect of adding epoxy on enhancing the properties of corrosion resistance towards electrolyte solution.

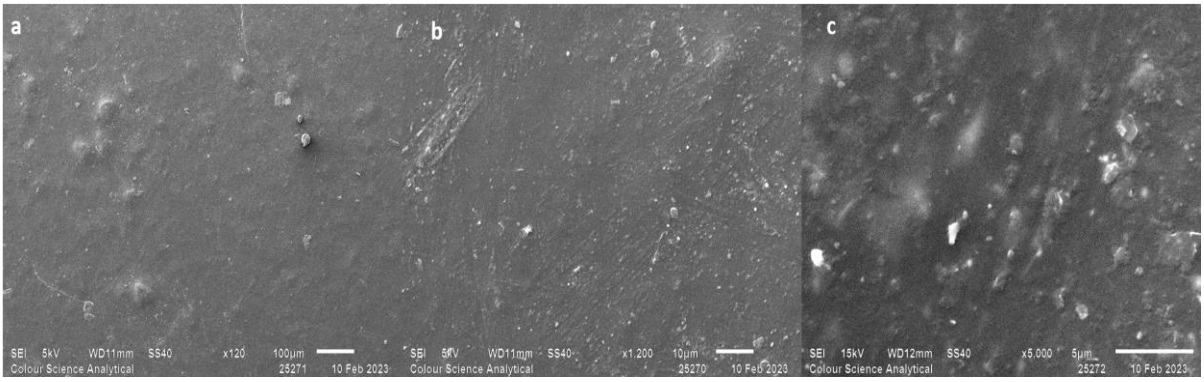

Figure 97 SEM images of the ZnO-epoxy steel 1 surface before exposure to NaCl solution a) 120 x, b) 1200 x and c) 1500 x magnification.

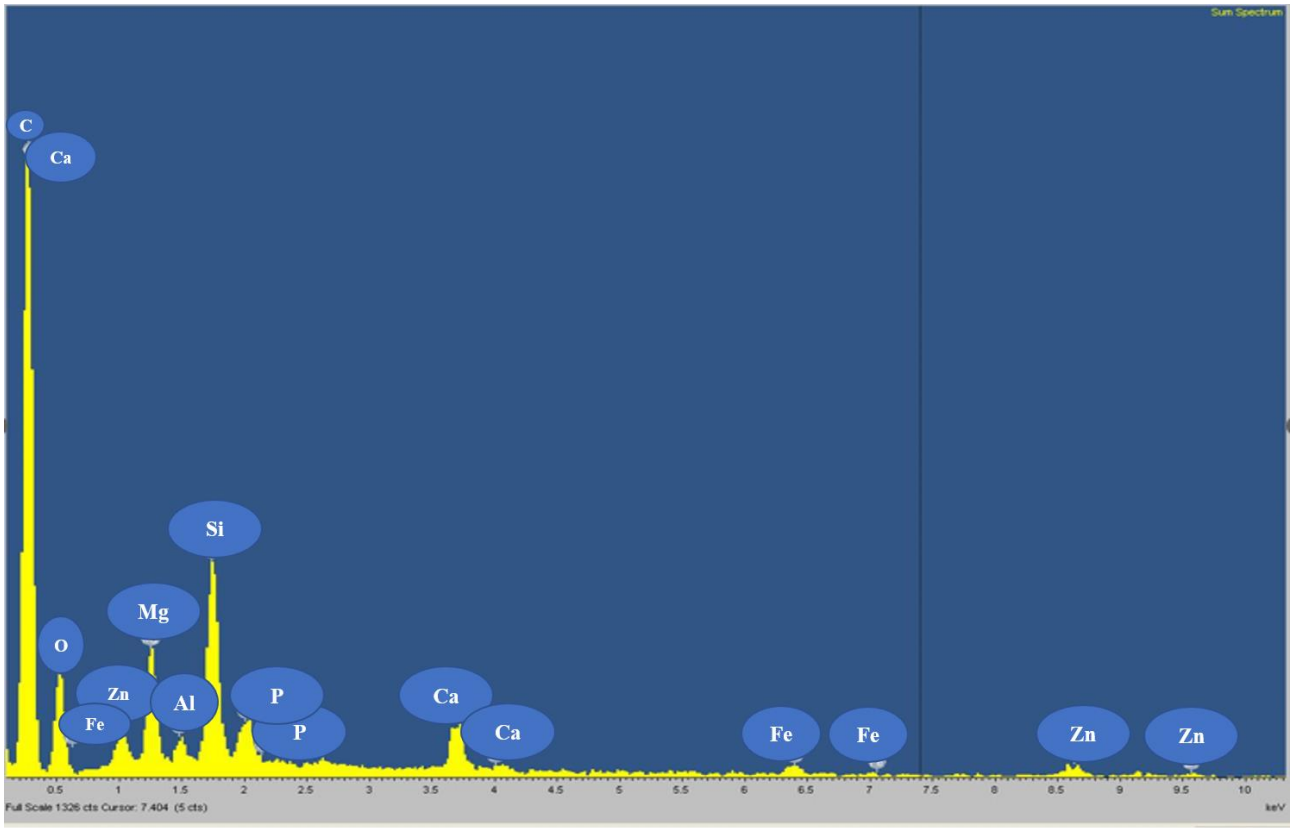

keV

Figure 98 EDX data for ZnO-epoxy steel 1 before exposure to NaCl solution for 10 days.

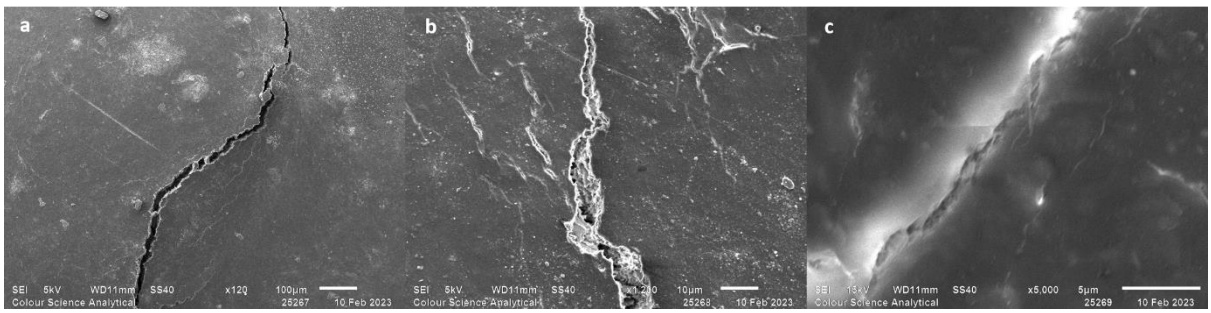

Figure 99 SEM images of ZnO-epoxy steel 1 surface after exposure to NaCl solution a) 120 x, b) 1200 x and c) 1500 x at different magnifications.

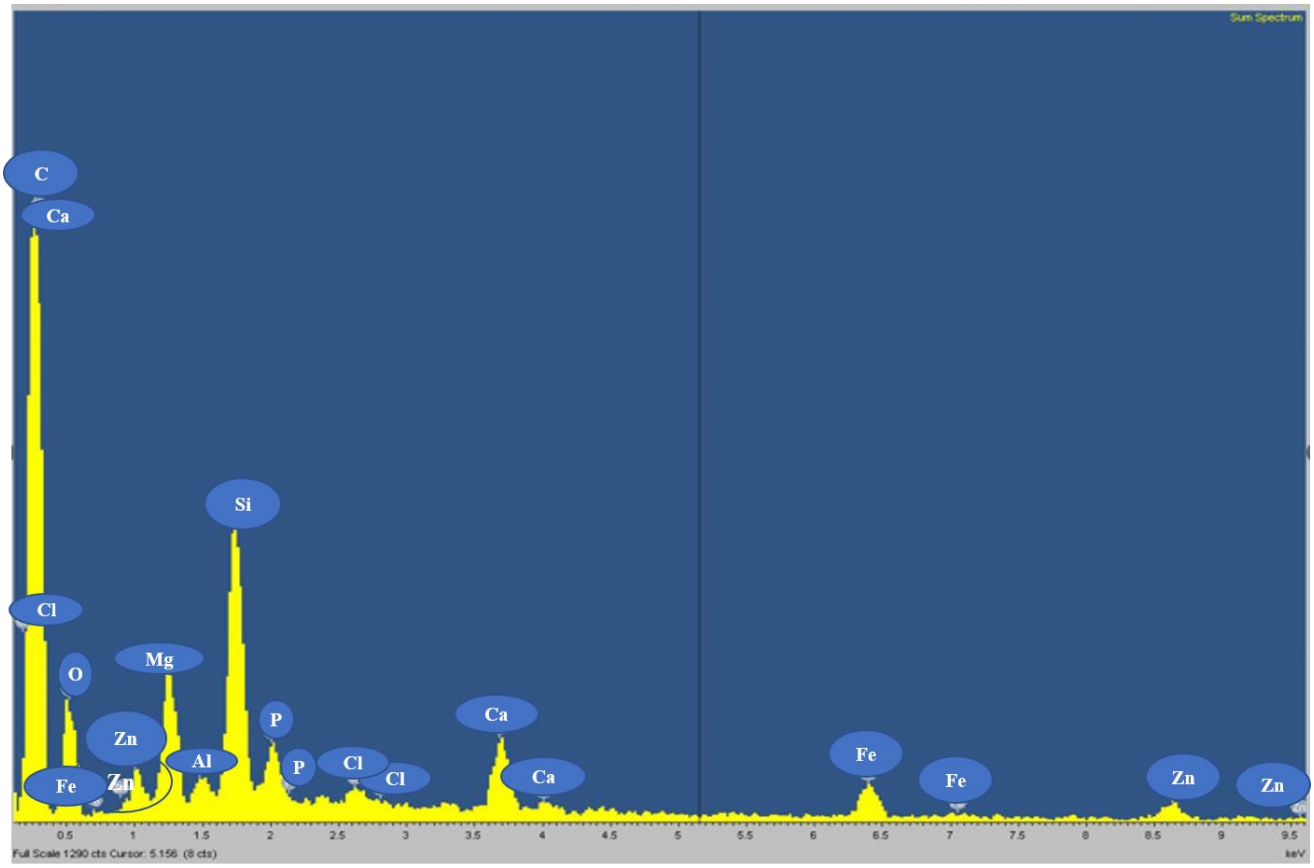

Figure 100. EDX data of ZnO-epoxy steel 1 coated result after exposure to NaCl solution for 10 days.

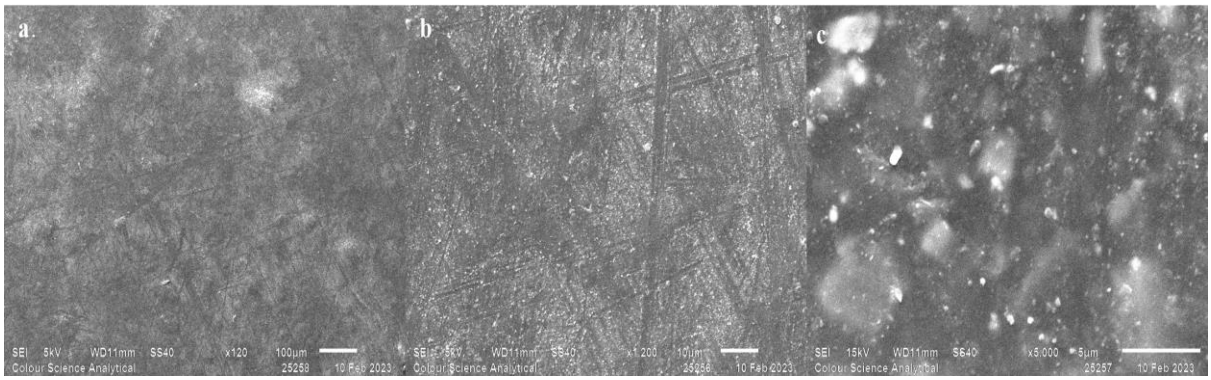

Figure 101. SEM images of ZnO-epoxy steel 2 surfaces before exposure to NaCl solution a) 120 x, b) 1200 x and c) 1500 x at different magnifications.

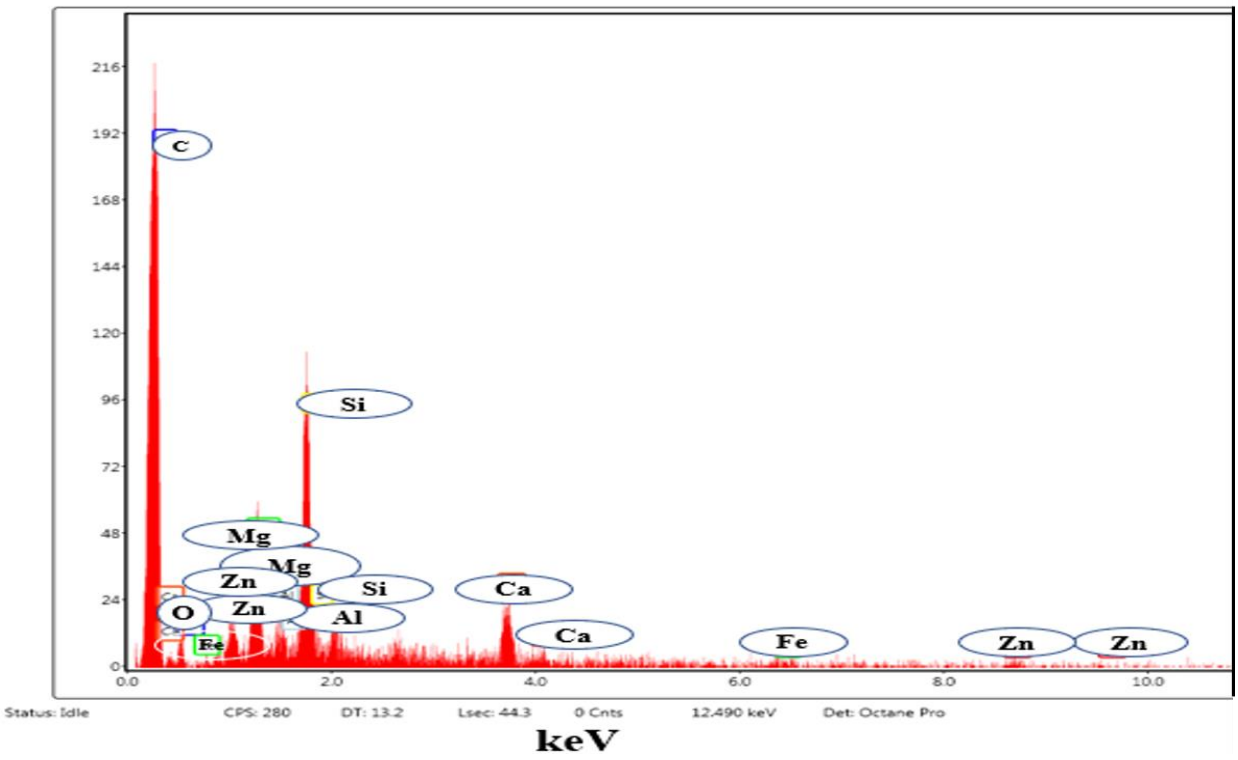

Figure 102. EDX data for ZnO-epoxy steel 2 before exposure to NaCl solution for 10 days.

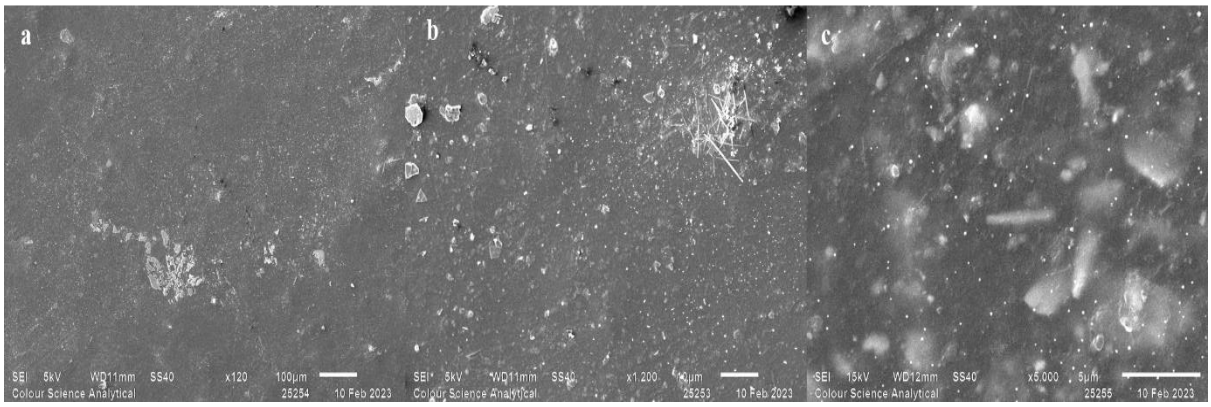

Figure 103. SEM images ZnO-epoxy steel 2 surface before exposure to NaCl solution a) 120 x, b) 1200 x and c) 1500 x at different magnifications.

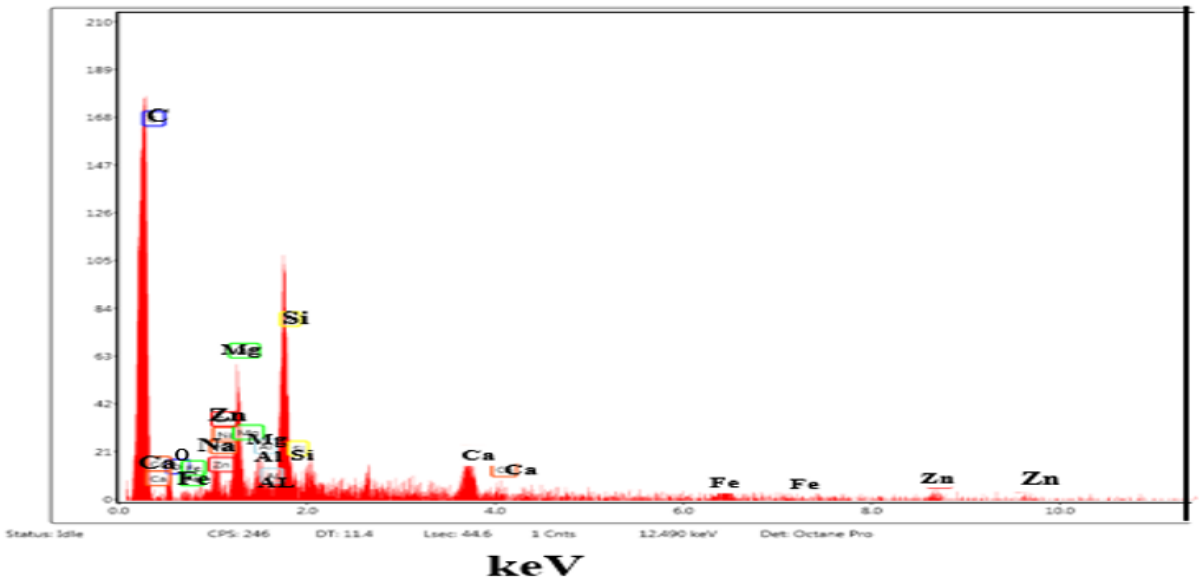

Figure 104. EDX data for ZnO-epoxy steel 2 after exposure to NaCl solution for 10 days.

Table 10. EDX analysis data (Weight %) for corrosion samples tested before and after exposure to NaCl solution for 10 days.

Sample reference	C	O	Mn	Fe	Mg	Al	Si	P	Ca	Zn	Cl
Blank Steel before	3.72	22.81	0.44	73.02	-	-	-	-	-	-	-
Blank steel after	1.36	3.90	-	93.54	-	-	-	-	-	-	1.90
Epoxy-steel before	83.25	4.49	-	0.87	2.98	-	5.26	-	2.14	-	-
Epoxy- steel after	76.51	7.02	-	1.31	2.97	0.68	6.38	1.13	2.14	-	0.59

ZnO- epoxy steel 1 before	50.07	40.56	-	0.60	2.06	0.32	2.95	0.73	1.10	1.61	-
ZnO- epoxy steel 1 after	37.33	49.94	-	5.18	1.51	0.23	2.67	0.59	1.00	1.09	0.45
ZnO-epoxy steel 2 before	82.29	4.97	-	0.67	2.97	0.62	5.09	-	2.36	1.03	-
ZnO-epoxy steel 2 after	83.93	4.86		0.55	2.80	0.59	4.94		0.93	1.07	

In Figure **97** it observed in the ZnO-epoxy steel 1 with a rod-shape coating surface before exposure to the electrolyte at different magnification a) 120 x, b) 1200 x and c) 1500 x with the chemical components shown in the EDX graph in Figure 98. Figure 98 illustrated there was ZnO on the surface in addition with epoxy steel components and the results showed no percentage of chloride ions on the surface before. In Figure 99, some areas were affected by corrosion factors after exposure to the electrolyte. As mentioned before, potential corrosion and localised corrosion, such as crevice as well as the trace of pitting corrosion, but in general these cracks seem to be less than the same factors in the case of using epoxy-steel coated and blank steel according to Figure 100. EDX data of ZnO-epoxy steel 1 coated result after exposure to NaCl solution for 10 days. In addition, Table 10. EDX analysis data (Weight %) for corrosion samples tested before and after exposure to NaCl solution for 10 days. This meant that adding pigments such as ZnO in the current study increased the resistance against corrosive agents due to the ability of the composite to reduce at the penetration of the corrosive agent to arrive at the interface between solution/composite by producing a self-cleaning when added to epoxy coating because of the ability to zinc oxide to sliding the corrosive ions in the solution droplets [274]. Furthermore, Other studies showed that zinc oxide could enhance the

mechanical properties of epoxy. Figure 101. SEM images of ZnO-epoxy steel 2 surfaces before exposure to NaCl solution a) 120 x, b) 1200 x and c) 1500 x at different magnifications. Figure 103 shows the SEM results for ZnO-epoxy steel 2 with a novel shape after exposure to electrolytes. Moreover, Figure 102 and Figure 104 show that there was an absence of chloride ions. The SEM results illustrate that no clear corrosion appeared on the surface. As shown in Figure 104. EDX data for ZnO-epoxy steel 2 after exposure to NaCl solution for 10 days. EDX confirmed the SEM results. According to Table 10, there was no amount of chloride ions on the surface after ten days, which could be attributed to its low quantity in the interface composite /steel metal. The corrosive ions, such as chloride in this current study, could not reach the interface layer.

3.5.1 Impedance spectroscopy measurements

The samples were investigated after 8, 9 and 10 days of immersion time and the results were as follows:

3.5.1.1 Nyquist plots

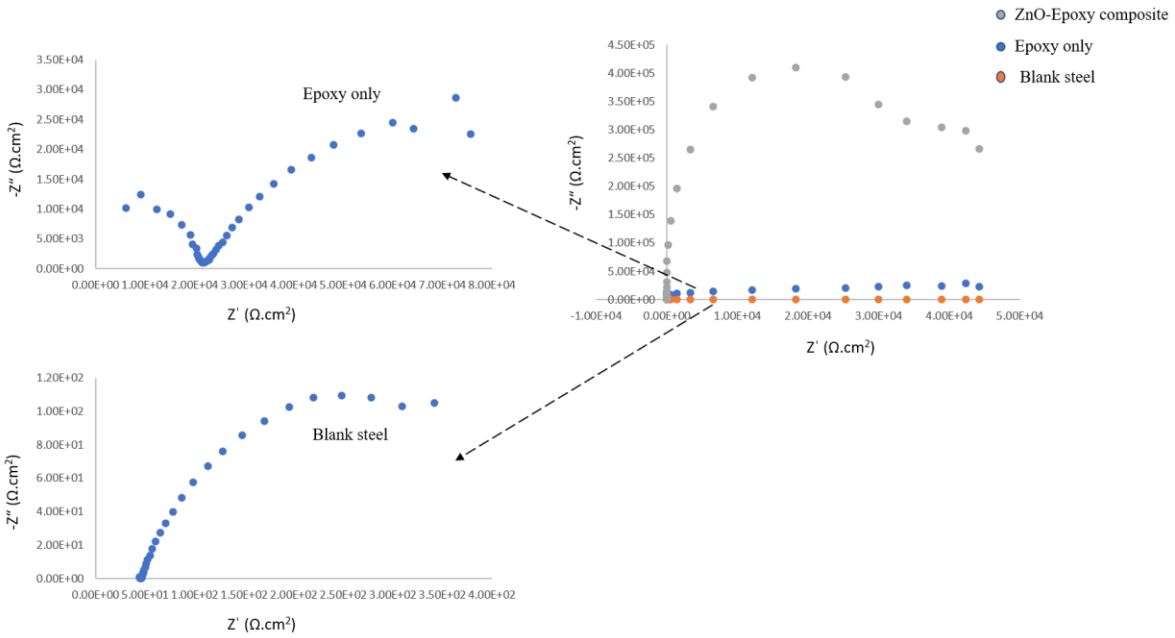

Figure 105. Nyquist plots for all samples after 8 days.

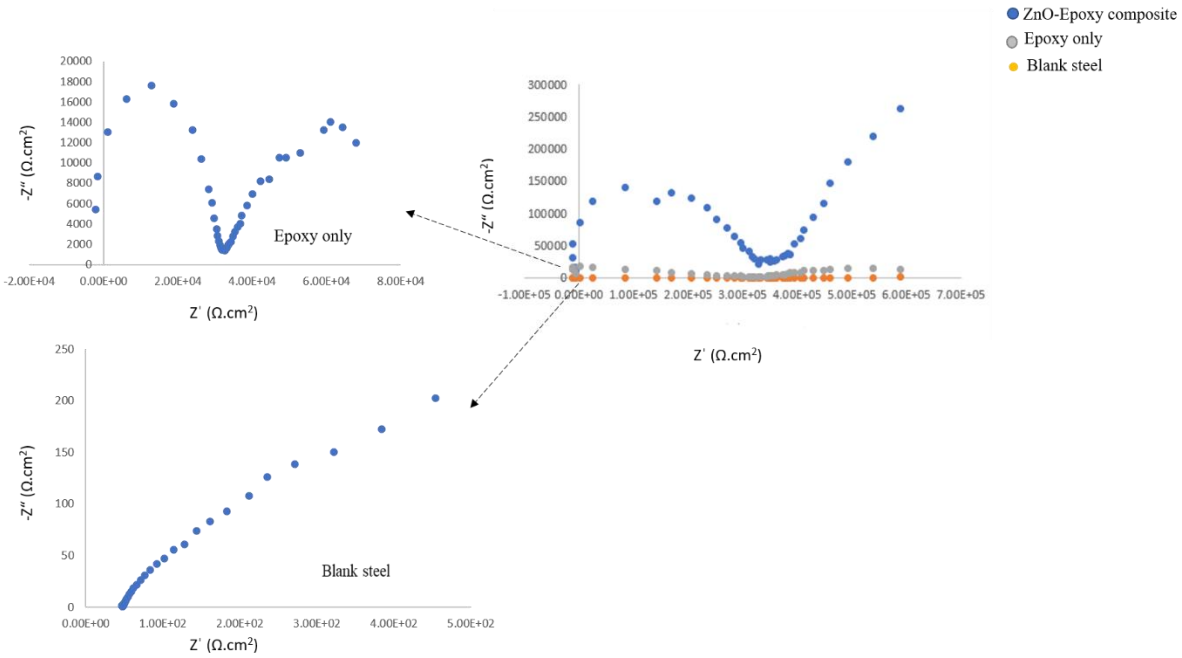

Figure 106. Nyquist plots for all samples after 9 days.

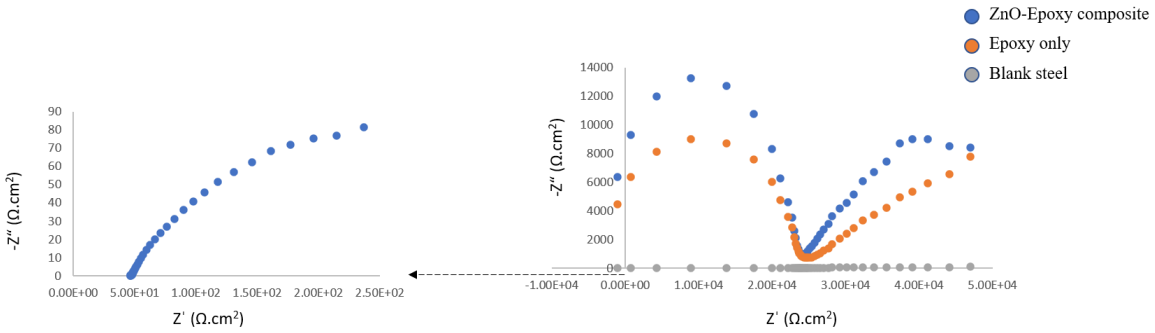

Figure 107. Nyquist plots for all samples after 10 days.

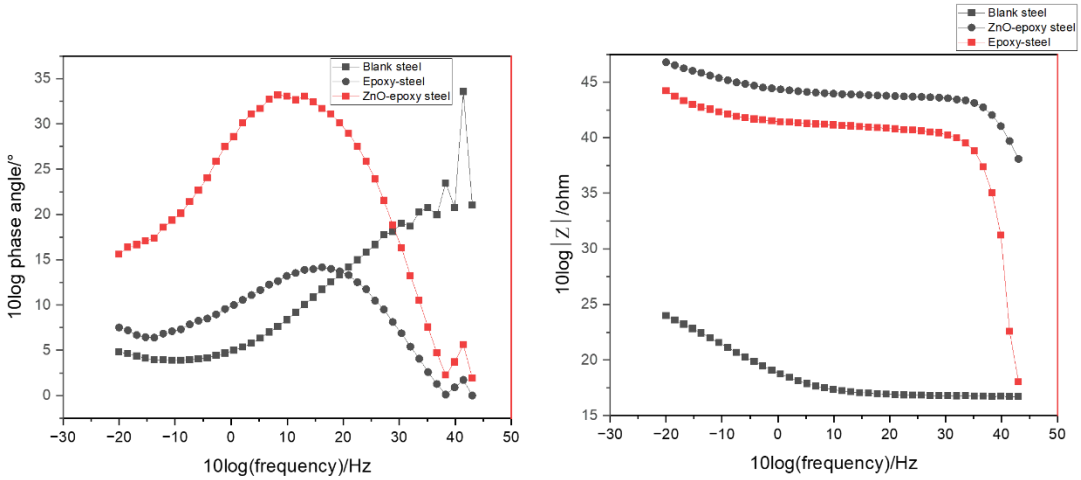

Figure 108. Bode plots with |Z| modules and phase angle for all samples in 3.5% NaCl solution after 10 days of immersion.

The Nyquist plots showed the behaviour of three samples after 8 days of immersion time. There were two-time constant semicircles for ZnO-epoxy steel film and epoxy steel coated due to the penetration of corrosive agents in the interface between the solution and the surface barrier that had pores or defect points, which then continued to be in between the interface of the steel and film coating. It was observed that in the case of using blank steel, there was only one semicircle due to the interface reaction between the exposed steel surfaces. This behaviour was observed in Figure 106 and Figure 107 after 9 and 10 days, respectively.

In general, we can conclude the following:

1/ when uncoated, one semicircle was observed, which explains the reaction between the electrode and the solution interface.

2/ in the case of a steel panel coated with a ZnO-epoxy composite, the semicircle was obtained, and it was attributed to the reaction occurring at the interface between the coating and the solution. [164]

Also, the impedance measurements illustrated essential points as follows:

- Low frequency could reflect how stable the coating was during the immersion time.

The epoxy-based coating formed a barrier that prevented the corrosive anions from permeating under the film, making the coating work with high resistance.

In addition, the impedance measurement at low frequency was optimised in the case of ZnO-epoxy coated film compared with epoxy steel only.

The presence of ZnO contributed to greater interfacial contact between ZnO and epoxy according to surface functionalities, as illustrated from Figure 105, Figure 106 and Figure 107.

The big semicircle was shown on the Nyquist plots for ZnO-epoxy steel corrosion in 3.5% NaCl. This may be related to the barrier coating composite showing on all different days. According to this, covering composite surfaces prevents corrosive species such as chloride ions, water and other environmental contaminants from contacting the surface of metal substrates [275, 276].

Perfect dispersion of ZnO in the epoxy, which leads to a long convoluted corridor for corrosive molecules to arrive and remain stable on the surface.

The ZnO epoxy shape showed the highest maximum phase angle, and the impedance had an obvious behaviour by changing from a low to a high value of the frequency region.

In general, it was clear that the ZnO-epoxy steel 1 rod-shaped sample had greater resistance to charge transfer compared with epoxy only and blank steel. Moreover, ZnO- epoxy showed a greater high resistance which confirmed the optimisation in barrier properties [277–281].

3.5.1.2 Bode plots

It was known from the following equation that

$|Z| = \sqrt{(Z`)^2 + (Z")^2}$. (27)

And

$\varphi = Arg\ (Z) = \text{atan}\ (\frac{Z"}{Z`})$. (28)

The relationship between the obtained frequencies from the potentiostat and the phase angle is illustrated in Figure 108.

It was clear from Bode plots that the relationship between frequency and Z module and phase angle phase, in case of adding ZnO as a pigment in epoxy coating, contributed to enhancing the efficiency of the ZnO-epoxy steel coating compared with epoxy-steel coated and blank steel.

ZnO-epoxy steel coating 2, which contained ZnO coral shape with pores, spent 10 days in 3.5% NaCl without any current due to the highest ability to resist compared with ZnO-epoxy steel coating 1 (zinc oxide had rod shape). The resistance against corrosive agents was as follows:

ZnO-epoxy steel 2 > ZnO-epoxy steel 1 > epoxy steel > blank steel.

as shown previously, it could be concluded that the ZnO-epoxy steel coating offers a superb physical barrier that prevents the passage of corrosive species [282, 283].

After 10 days, the Bode plot indicated a greater effect of barrier resistance in the coating in the ZnO-epoxy steel coating than in the epoxy steel coating compared with blank steel [135].

As mentioned before, from the Bode results with the impedance module and with the phase angle reflected, variable states for the corrosion reaction occurred at the electrode. A steel panel coated with ZnO-epoxy 2 could show the suggested equivalent circuit, as shown in Figure 109: resistance by the solution (Rs), impedance that had occurred by capacitance of ZnO-epoxy coating (Cc), coating resistance (Rc), the effect of resistance caused by charge transfer (Rct) and the impedance generated by double-layer capacitance (Cdl) [138].

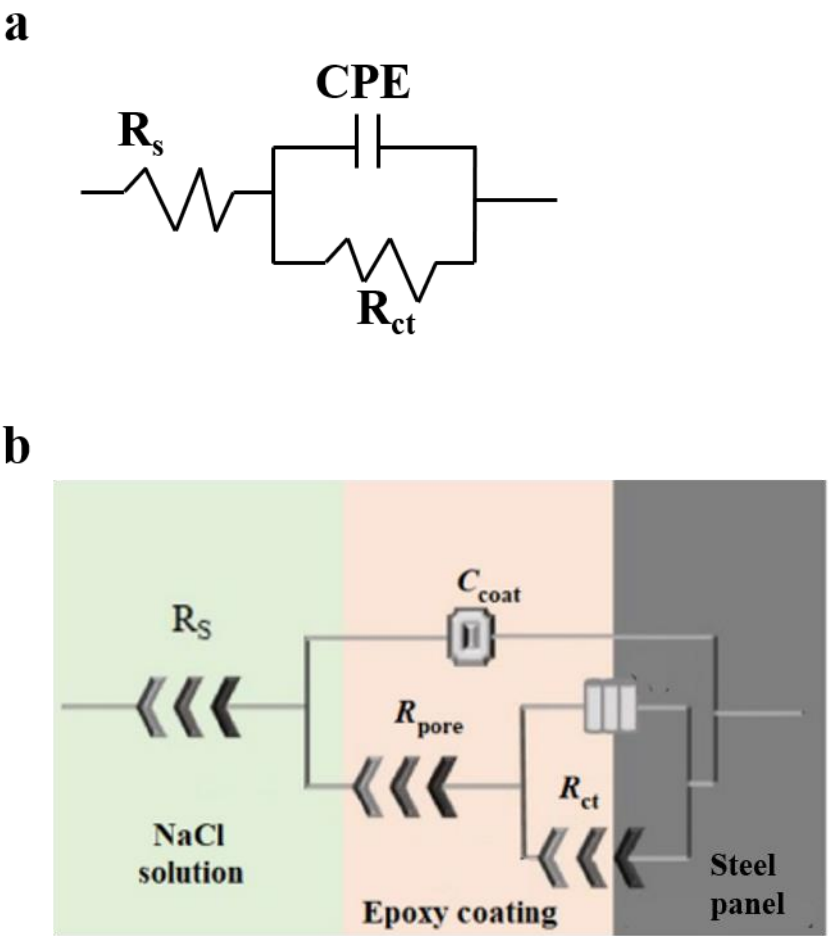

Figure 109. Equivalent electrochemical circuit model a) for blank steel, b) for ZnO-epoxy steel 1 and epoxy steel coating [128].

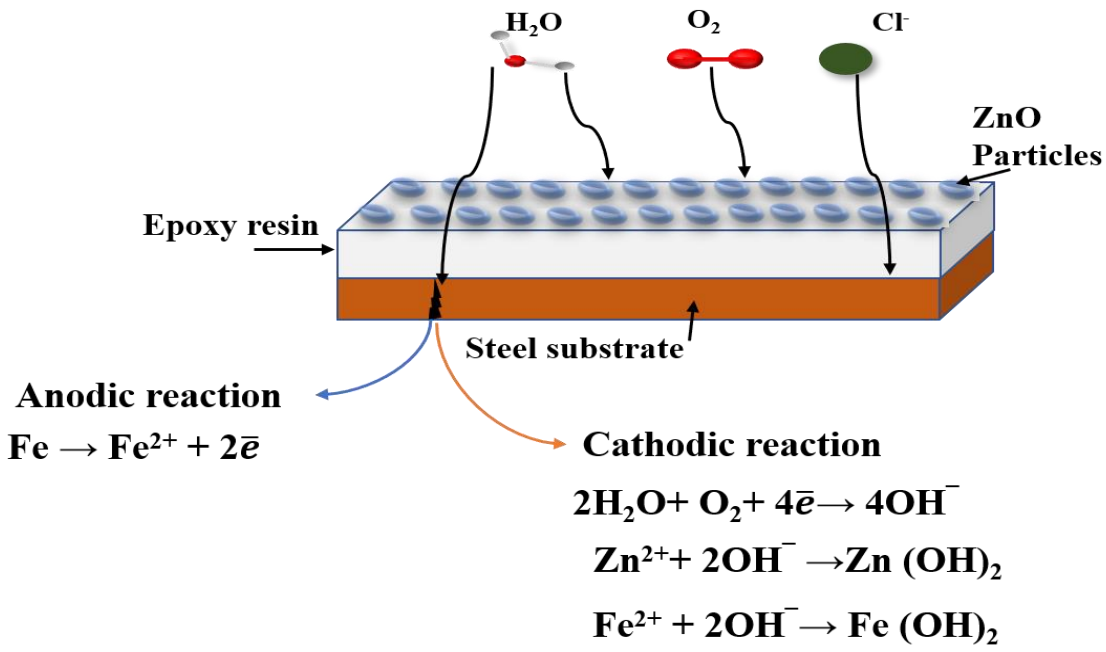

Figure 110. ZnO-epoxy steel coating mechanism.

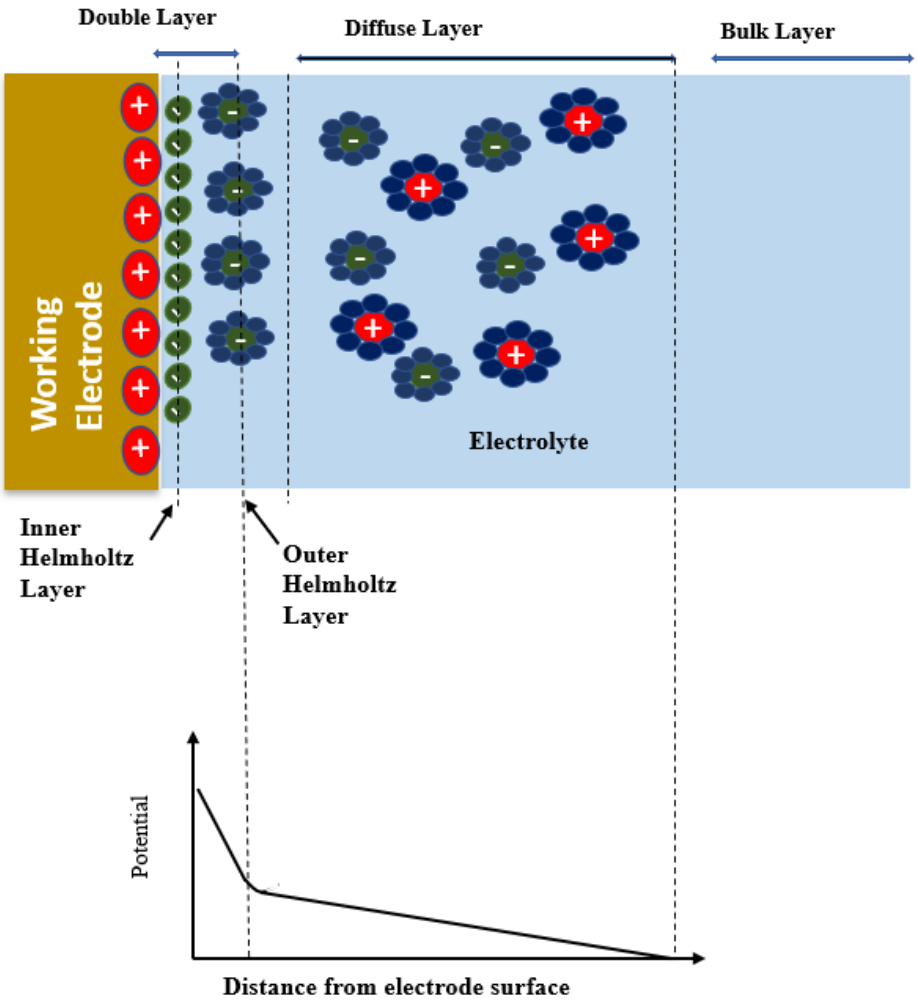

Figure 111. Electrochemical double-layer diagram with an illustration of the potential distribution that occurs at the interface of the working electrode and the electrolyte solution.

3.5.2 Mechanism of the corrosion process

The chloride ion could react with iron ions to increase the anodic route, and there would be a reduced reaction on the cathodic side, represented by the following reactions:

$O_2+2H_2O + 4\bar{e} \rightarrow 4OH^-$ (cathodic reaction) (21).

$Zn^{2+}+ 2OH^- \rightarrow Zn(OH)_2$ (22) [284] .

The reactions in the presence of oxygen molecules on the surface were as follows:

$Fe + O_2 + 4H^+ \rightarrow 2Fe^{2+} + 2H_2O$ (23)

$4Fe^{2+}_{aq} + O_{2g} + (2 + 4x)\ H_2O \rightarrow Fe_2O_3 \cdot xH_2O + 4H^{+}_{aq}$ (24)

In contrast, the anodic reaction could be as follows:

$Fe \rightarrow Fe^{3+} + 3\bar{e}$ (anodic reaction) (25) [137].

According to the above reactions, the Fe_2O_3 (ferric oxide) rust is formed through a series of reactions due to the oxidation step. The presence of a coating in some samples provided protection against corrosion where it should work, for example, avoiding the diffusion process of H_2O and O_2 through the surface of metal film and preventing chemical metal oxidation Figure 110. [285]

It is known that in the case of the presence of nanocomposite materials when corrosion takes place,

- A high surface energy creates (caused by the nanostructure) a hydrophobic and irregular surface that forms above the surface coating.
- There will be adjacent particles observed that have an interconnection structure to decrease the high surface energy.
- This structure had tough adhesion between the layers of the composite coating interface.

For all the above reasons, the steel panel composite film had the ability to generate a sufficient impediment to decrease the corrosive ions in the electrolyte, which had been observed as a defensive line against corrosive factors [285–288].

Lower solution absorption was observed for epoxy steel and blank steel, which meant that the presence of ZnO with a rod shape was attributed to a decrease in the penetration of corrosive agents through the film, as well as the continued diffusion process inside the film.

Some studies have stated that adding ZnO (n-type semiconductor) to the epoxy to make a nanocomposite could lead to a decrease in the ability for water dissemination from the surface of the nanocomposite. Therefore, the nano-size of the materials, especially in organic source

coatings, inhibited the penetration of corrosive ions and enhanced the building of a massive block effect by avoiding the potential possibility of forming corrosive electrolyte iron dissemination routes. This information, as mentioned, all concluded that size and morphology had a vital impact on the quality of the corrosion coating. When there were tiny nanoscale sizes, there were greater building block features in the film [7].

Furthermore, when ZnO nanoparticles were added to solid epoxy matrix-based nanocomposites, the curing process of activation energy decreased, according to research by Karasinski et al. [289]. This phenomenon increases the network's crosslinking density by enabling the reaction to last for a longer time [139].

ZnO nanoparticles could be affected by cross-linking density in a relationship with Tg, according to Ramezanzadeh et al. Additionally, they discovered that the ZnO nanoparticles' presence impacted the epoxy coating's curing behaviour and increased its toughness properties [102, 290].

Ultimately, the ZnO rod shape with the nature of the epoxy network structure was attributed to avoiding water penetration, which therefore reduced the degradation and swelling of the coating film.

However, the coating's tightness and compactness were reduced as a result of the creation of cracks, pores and pits when exposed to harsh environments like marine solutions and salt chambers. The polymer matrix was supplemented with a few inorganic species, known as inorganic pigment, to cover these surface flaws. In addition to this, it has been well documented that occasionally corrosion products like Fe_2O_3 and Fe_3O_4 also form a passive coating on the metallic surface and act as physical barriers [291].

As shown in Figure 110, in natural solutions and solutions at pH 8, zinc oxide occurs in a stable form [292]. Zinc atoms have been used in coatings for cathode protection by exploiting zinc as a sacrificial element and forming stable passive layers on surface coatings [292].

The morphology of a zinc oxide rod has many polar planes {0001}, and oxygen vacancies are the preferred positions for anion attacks. Water molecules from the solution are adsorbed onto the zinc oxide polar faces, as are chloride anions [293]. The stability of the polar faces in zinc oxide crystals can be enhanced by the adsorption of surrounding anions, such as OH^-, and in the presence of oxygen atoms [292, 294], which enables the ability to reform triangular structures that then form stable coverings [295].

For nonpolar planes, an important point to consider is that studies are lacking regarding the actual stability of the nonpolar planes of zinc oxide crystals, such as $(10\bar{1}0)$. Dworschak et al. used atomic force microscopy (AFM) to show that the surfaces of zinc oxide nonpolar faces dissolved due to the restructuring of the zinc oxide crystal, which tended to form a polar surface [292, 296]. Other analyses located defect points and considered the presence of oxygen atom vacancies as stabilising topographies for polar plane surfaces [297]. The oxygen vacancies could also lead to large interfaces and compactness of packed charges [298, 299].

In a rod shape, the wurtzite structure has packed layers that end with terminal O atoms and Zn atoms on the opposite side. This generates two dipole-terminated atoms across the zinc oxide crystal that increase a steady state for the zinc oxide (0001) face reconstructor [292]. The terminal zinc ions (Zn^{2+}) in zinc oxide crystals occur in polar planes and have the ability to adsorb anions around the crystal [293]. In this case, more anions can be adsorbed onto the polar face (0001), which can ultimately offer tunnels that allow aggressive anions to continue to penetrate the interfaces between the solution/Zn epoxy, the zinc oxide epoxy composite and the steel substrate.

One suggestion for improving the resistance of the zinc oxide rod shape has been to cover the polar plane of the zinc oxide rod structure with OH^- molecules, as this could produce various molecules, such as $Zn(OH)_2$, that could serve as passive layers. These reactions would increase according to the surface area of the zinc oxide structure [292]. Conversely, the nature of the particles would affect their ability to agglomerate, which could be another reason why corrosive species are able to attack the film [137].

In the case of zinc oxide, its novel shape, with its distinctive porous structure, was visualised using scanning electron microscopy (SEM). Porosity creates a high surface area and produces observable stability while also providing reproducibility [298]. The high resistance could be attributed to the ability of a porous shape to increase the effective surface area. Then, due to the presence of oxygen defect vacancies, this could lead to spots that have more resistive behaviour [298, 299] against corrosive agents (e.g. chloride and OH^-).

The novel shape of zinc oxide creates a porous morphology of stacked sheets, which offers a greater surface area compared with zinc oxide rod morphology and provides a greater adsorption of molecules from the solution. The duration of protection would also be longer due to the release of zinc from zinc oxide under a potential that could allow a cathode reaction with OH- anions to form $Zn(OH)_2$, which would then function as a passive barrier to protect the film. This suggestion is compatible with the EDX results.

Porosity structures that offer a high surface area have received particular attention in recent decades in some fields, such as solar cells [300], photocatalysis [301], gas sensing [302] and biomedical applications [303]. Therefore, the suggestion to exploit the novel morphology of zinc oxide could achieve some new coating effects that are not attainable when using rod-shaped zinc oxide as an epoxy composite.

Adding ZnO to epoxy on metal enhanced the corrosion resistance of the coated metal. This was observed and was known by two essential mechanisms:

1/ nanoparticles enhanced the two process the protection mechanisms that influence decreasing the process of the corrosion and building the barriers. This could be achievable by ZnO particles that dissolve in the solution then the inhibitive items could be released such as the current results Zn^{2+} that could be positioned at the interface between coating and metal (steel panel) then reacted with anions that released from cathodic side such as hydroxyl anions and chloride anions to form a protection layer that could precipitate the cathodic side and avoid the penetration of corrosive agents. These processes enhanced the protection and corrosion resistance of the coating metal [163].

2/In case of nanoparticle size, due to the ratio of small size to a high surface area, nanoparticles such as ZnO had the ability to generate strong bonds when adding epoxy to the coating film. In this case, the possibility of destroying the coating was decreased by the diffusion of corrosive agents in the electrolytes, such as chloride and hydroxyl ions [163].

As shown in Figure 111, when the potential was applied to the system, the energy in the entire electrochemical cell system changed. The current that started to flow measured the reaction rate. All the reactants in the electrochemical cell transported towards the working electrode surface from the bulk solution and the current started to flow. According to this, the products started to be transported to the bulk solution when the reaction took place.

Therefore, in this case, the diffusion process took place by the movement of molecules towards the area that had a low concentration of charge species. In addition, there was a higher possibility of migration of anions and cations (charged species) under the effect of the applied electric field. Moreover, convention was a process that involved the transportation of the species by applying hydrodynamic transport.

In general, this kind of morphology reduced the ability of diffusion and penetration routes of solution ions, which successfully improved the performance of the film against corrosive factors. Also, it was observed that after 10 days of immersion when ZnO-epoxy steel 2 was

used, a novel shape impedance signal was not recorded, which meant that even with the use of the same pigments (ZnO) but different morphology, the effect of coating was more efficient than the coating with ZnO-epoxy steel 1 when ZnO had a rod shape. The observed results demonstrated that the presence of porous and flowery shapes consisting of these pore plate shapes played a significant role in increasing the resistance coating regarding corrosive agents.

At the end, this section showed how the changing morphology of zinc oxide affects the coating of steel panels, which clarified one of the current study objectives.

Chapter 4
Conclusion

- Asymmetric zinc oxide (ZnO) crystals have a hexagonal wurtzite structure. The method of ZnO synthesis significantly impacts crystal morphology, and different ZnO structures emerged due to various factors during the synthesis process, from the type of reactants until the calcination step.
- The concentration of sodium hydroxide as a precipitation agent significantly influenced the morphology of ZnO when zinc acetate dihydrate (Zn $(CH_3CO_2)_2 \cdot 2H_2O$) was used as a zinc source.
- In general, flower-shaped crystals developed when zinc oxide was precipitated from 0.05 M of zinc acetate dihydrate using 1M of sodium hydroxide; flower-shaped crystals also formed with 3 M of sodium hydroxide and 0.3 M of zinc acetate dihydrate.
- The flower-shaped crystals consisted of platelet shapes when 3 M of sodium hydroxide was added to 0.3 M of zinc acetate dihydrate in reflux method. Flower shapes with needles and rods were obtained when 0.3 M of zinc acetate dihydrate was added to sodium hydroxide in the reflux method. This led to the conclusion that the order in which the chemicals were added impacted the final morphology of ZnO.
- The three different methods (precipitation, reflux and hydrothermal) processes resulted in different zinc oxide morphologies. When ammonium carbonate was used as a precipitation agent and zinc nitrate hexahydrate as a zinc source, ZnO had a ring morphology. However, this combination led to an irregular bifrustum shape by the precipitation method, a flower shape with pores in a platelet shape was observed by the reflux method, and a spherical shape was formed by the hydrothermal method.

- In the case of using sodium hydroxide and zinc acetate dihydrate, the reflux method showed clear morphologies results for zinc oxide such as (platelet and rod shape) compared with precipitation (irregular shape) and hydrothermal methods (platelet and irregular shape).
- A novel shape was obtained using the reflux method with ammonium carbonate as the precipitation agent and zinc nitrate hexahydrate as the zinc source. This morphology was not previously observed by other researchers using this simple route (reflux method at 90°C for 30 minutes).
- In the present study, using different zinc sources with the same precipitation agent (NaOH) resulted in different ZnO morphologies. This indicates that the anions in the zinc resource affected the mechanism, causing different morphologies to result from a single method. For example, using the hydrothermal method to obtain ZnO from zinc acetate using sodium hydroxide resulted in irregular crystal shapes, while using zinc nitrate hexahydrate and sodium hydroxide led to flower-like needle shapes using the same method.
- The use of different precipitation agents with the same zinc source also impacted ZnO morphology. With the reflux method, zinc nitrate hexahydrate and sodium hydroxide generated flower-like needle-shaped ZnO crystals, whereas ammonium carbonate led to flower-like crystals with pores in a sheet shape, similar to a coral shape.
- Adding the materials in different addition types also impacted the results, even when the same precipitant and zinc resource were used, as mentioned in close two.
- Using SDS as a surfactant enhanced the attachment orientation of the ZnO platelets and decreased the agglomeration of ZnO particles.
- The time of addition also impacted the ZnO geometry. Adding the precipitation agent, $(NH_4)_2CO_3$, to the zinc resource, zinc nitrate hexahydrate, at 5, 10, 15, 20, 30, 50 and 70 minutes using the reflux method. The final morphology started to appear after five minutes.

After 50 minutes, the ZnO morphology was distorted, as observed in the SEM results. This indicates that ZnO morphology was significantly influenced by the duration of ZnO synthesis.

- The common morphology during the study of the effect of time addition was the flower shape consisting of needle porosity sheets.
- The XRD, IR and Raman results complement the SEM results, indicating that all the studied factors impact the final ZnO morphology.
- The electrochemical results of a corrosion test (conducted with aqueous sodium chloride) indicated the following trend in the relative resistance of the ZnO against corrosion:

  steel 2 coated with ZnO-epoxy > steel 1 coated with ZnO-epoxy > steel coated with epoxy > plain steel.
- Impedance was measured using Nyquiest plots and Bode plots for 8, 9 and 10 days of immersion time.
- The morphology of different ZnO crystals with the same chemical composition impacted the coating compound's resistance against corrosive ions, such as Cl^- and OH^-. This enhanced resistance suggests that more research on the impact of ZnO crystal morphology is needed.

Future work

- ZnO is non-centrosymmetric in its well-known wurtzite hexagonal structure. Accordingly, it exhibits precise anisotropic growth—as well as a strong ability towards aggregation under several factors in a specifically oriented manner [12]. All previous reasons led to the suggestion that studying additional factors could affect the zinc oxide morphologies, such as the temperature, surfactants, different zinc sources, precipitation agents such as KOH, using co-solvents such as ethanol using different methods such as microwave method or sol–gel method.
- Add additional treatments or alternative treatments that could lead to controlling zinc oxide morphology. Adding more analysis for zinc oxide powder, such as small-angle x-ray scattering (SAXS) analysis, which is a typical international standard that can deal with tiny particle sizes ranging from 1 to 100 nm. SAXS should be performed to determine the average particle diameter and surface area and has the ability to measure the particle size distribution [304]. This established technique could potentially help to provide more understanding of the particle's behaviour and the effect of the size on the particles, especially in terms of the agglomeration phenomena and self-assembly for the particles for more understanding of the nano-particle morphologies.
- Different morphologies of zinc oxide with epoxy led to essential results in the current study, which meant the geometry of the particles had a vital role in the application in terms of studying the effect of coating resistance on corrosion test.
- Upon on electrochemical study in the current study, applying zinc oxide nanocomposite in many applications such as coating, optical and several fields to investigate the effect of different morphologies that could lead to greater understanding of nanoparticles, at least in this type of study (zinc oxide nanoparticles).

List of abbreviation

(ABAB)	A chemical structure that relied on changing the planes of the O^{2-} and Zn^{2+} ions.
(AFM)	Atomic force microscopy (AFM)
(AL_2O_3)	alumina
(APTES)	Amino-propyltriethoxysilan
(B_4C)	Boron carbide
(BCE)	Before Common Era
(CA)	Contact angle
(Cc)	Capacitance coating
(Cd)	Capacitance of a diffuse layer
(Cdl)	Double-layer capacitance
(CNT)	Carbon nanotube
(CP)	Cathodic protection, electrochemical test
(CR)	Chloride removal
(Cr)	Coating resistance
(CZs)	Nanoplatelets/nanorods
(DAT)	Different addition type
(DFT)	Density functional theory
DGEBA-DAA-coating ZP's	Epoxy risen with zinc phosphate

(EIS)	Electrochemical impedance spectroscopy
(EP)	Epoxy -based composites
EPZ	Epoxy zinc oxide
(ES)	Epoxy silicon
(EST)	Epoxy silicon titanium
(ESTZL)	Epoxy-silicon titanium zinc after exposure
(GA)	Graphane
(GE).	Graphene
(HCP)	Hexagonal close-packed
(HMTA)	hexamethylenetetramine
(NNI)	The National Nanotechnology Initiative
(NPs)	Nanoparticles
(NWS)	ZnO nanowires
(PANI)	Poly aniline
(PE)	Polyethylene
(PMMA),	Polymethyl methacrylate
(PTFE)	Polytetrafluoroethylene
(PZs)	Nanoplatelets
PU	Polyurethane
(PVDC)	Polyvinylidene chloride
(Rc)	Corrosion resistance

(Rp)	Polarisation resistance
(Rs)	Solution resistance
(SDS)	Sodium dodecyl sulphate
(SEM)	Scanning electron microscopy
(SFE)	Stacking fault energy
(SiC)	Silicon carbide
(SiO_2)	Silica
(SPD)	Surface potential decay
(SZs)	Nanospheres
(TEM)	Transmission electron microscopy
(TiO_2)	Titania
(UV)	Ultra violet rays
(V)	Voltage
(VTES).	Vinyl triethoxysilan
(WO_2)	Tungsten dioxide
XRD	X-Ray diffration
(ZC-PAC)	Zinc chloride polyacrylic acid salt
(ZC-EtH)	Zinc chloride ethanol
(ZC-PVP)	Zinc chloride polyvinyl pyrrolidone
(ZC-Trit)	Zinc chloride Triton X-100
(Z-EtH)	Ethanol

(Zn(dmph)I_2] 1)	Znic ion with a 2,9-dimethyl-1,10-Phenanthroline ligand with two Iodine atoms
(ZnO)	Zinc Oxide
(ZP)	Zinc phosphate
(ZPA)	Zinc aluminum poly phosphate
(Z-PVP)	Zinc Oxide with Poly vinyl pyrolidone
(C^4_{6V} or P63ms group)	A space group, the basis of piezoelectricity in some semiconductors, such as zinc oxide
(f_1)	Phillip's ionicity as a function of the c/a ratio
(ϕ)	Phase angle

Appendix A

Producing zinc oxide by zinc acetate dihydrate $Zn(CH_3CO_2)_2 \cdot 2H_2O$ and different concentrations of sodium hydroxide NaOH

In these experiments, 0.05 M of zinc acetate dihydrate with four concentrations of NaOH – 1, 0.75, 0.2 and 0.1 M – for Experiments 1, 2, 3 and 4, respectively, using the precipitation method. The sediments underwent two tests before and after calcination. The calcination process was conducted at 250°C for 3 hours. In this study, zinc acetate dihydrate and sodium hydroxide were each dissolved in deionised water to form a liquid media of a specific concentration. The zinc acetate dihydrate solution was slowly added dropwise in all experiments to the sodium hydroxide solution under vigorous stirring at room temperature to form a transparent white solution. The precipitate was collected by filtration and rinsed three times with deionised water using vigorous stirring for 1 hour after washing. Fourth, the washed precipitates were dried in an electric oven at 60°C overnight. Finally, the calcination process was completed at 250 °C for 3 hours. In Experiment 4, the calcination process was subjected to more calcination time at 250°C for 3, 5, 7 and 10 hours ZnO powder (Figure 112).

Figure 112. ZnO after calcination.

A1 Keyence VHX-2000 digital microscope analysis

One of the methods that used zinc oxide characterisation was a Keyence VHX-2000 digital microscope with a magnification capability of 500x–2500x.

All the white sediments were ground using marble for 30 minutes for each experiment and then subjected to a Keyence microscope. The results are shown as follows:

Zinc acetate dehydrate and sodium hydroxide at different concentrations. As shown in Figure 116 to Figure 116, when the concentrations were 1, 0.75, 0.2 and 0.1, the ZnO particles seemed to decrease in size, especially after calcination at 250 ℃ for 3 hours. However, when increasing the time of calcination for the NaOH concentration 0.1 M at 250 ℃ for 3, 5, 7 and10 (Figure 116 to 8), the ZnO particles appeared to be large size and agglomerated particles.

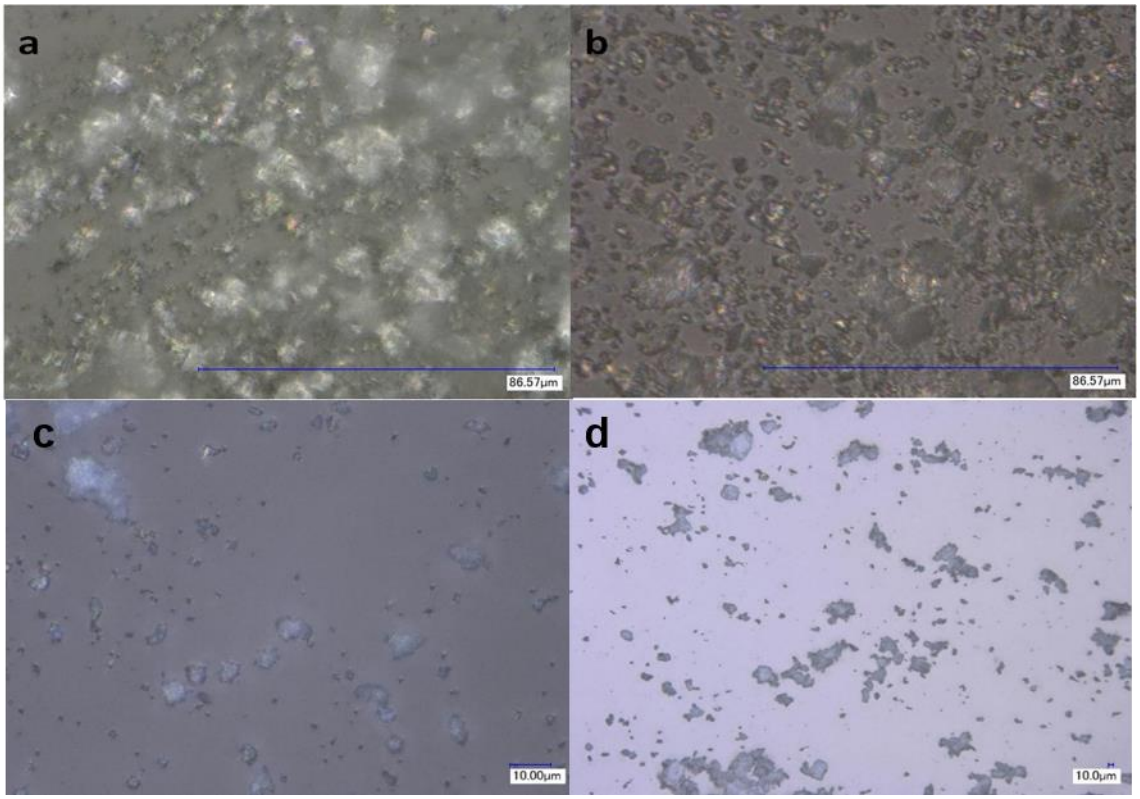

Figure 113. Zinc acetate dihydrate Zn $(CH_3CO_2)_2 \cdot 2H_2O$ with 1 M of sodium hydroxide NaOH (a and b) before and (c and d) after calcination at 250 ℃ for 3h.

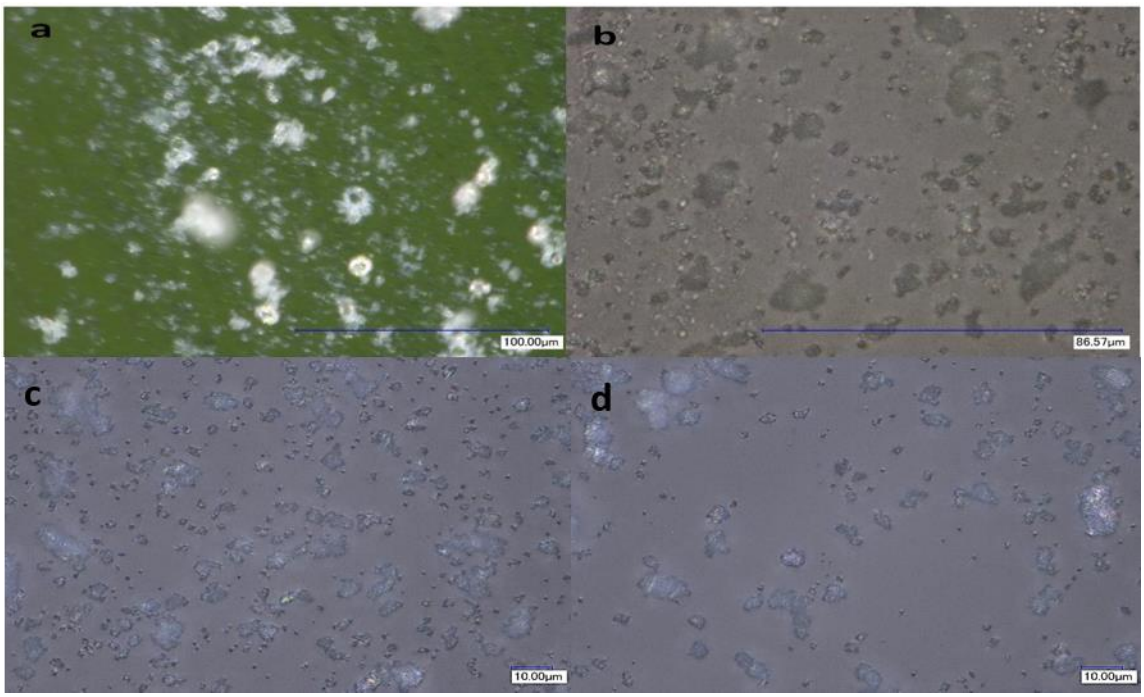

Figure 114. Zinc acetate dihydrate Zn $(CH_3CO_2)_2 \cdot 2H_2O$ with 0.75 M of sodium hydroxide NaOH (a and b) before and (c and d) after calcination at 250 °C for 3 hours.

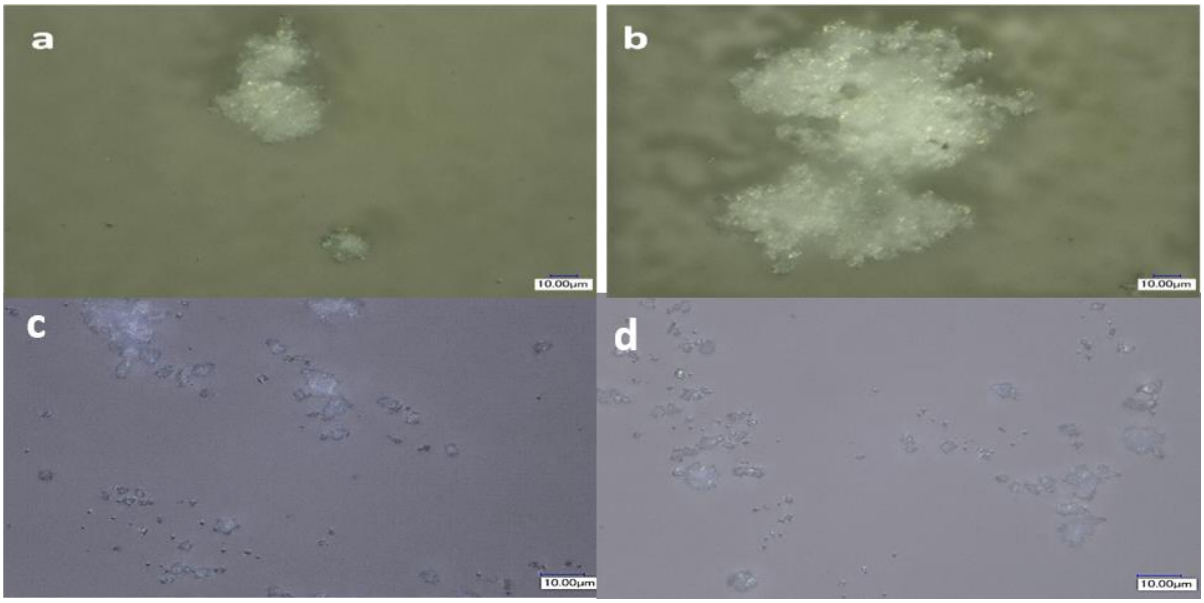

Figure 115. Zinc acetate dihydrate Zn $(CH_3CO_2)_2 \cdot 2H_2O$ with 0.2 M of sodium hydroxide NaOH (a and b) before and (c and d) after calcination at 250 °C for 3 hours.

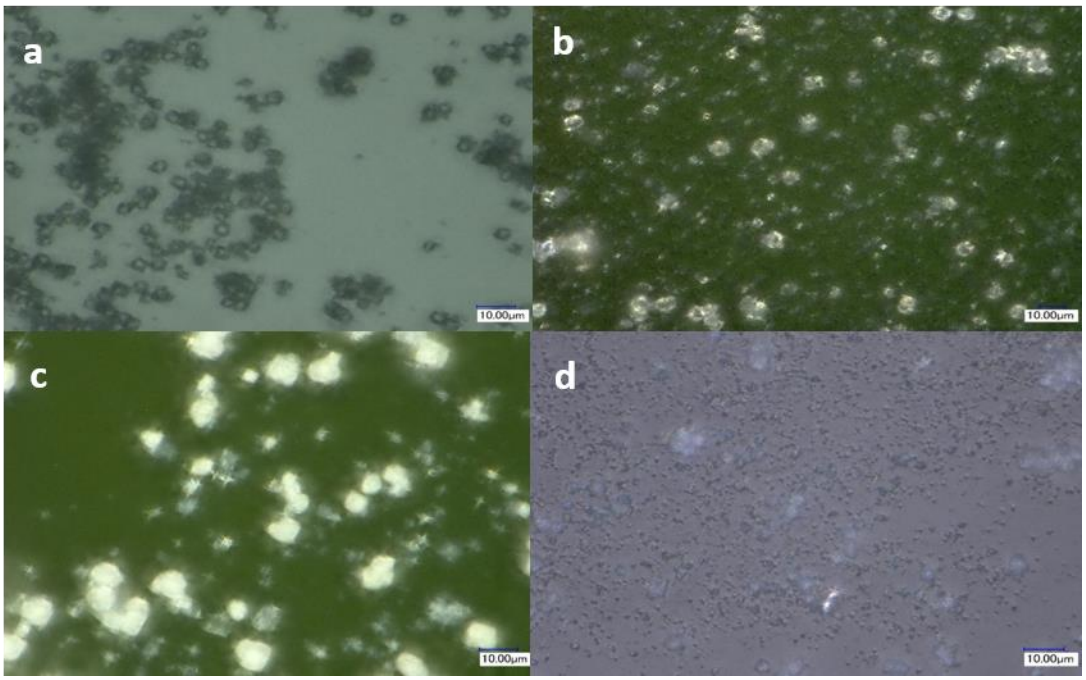

Figure 116. Zinc acetate dihydrate Zn $(CH_3CO_2)_2 \cdot 2H_2O$ with 0.1 M of sodium hydroxide NaOH (a and b) before and (c and d) after calcination at 250 °C for 3 hours.

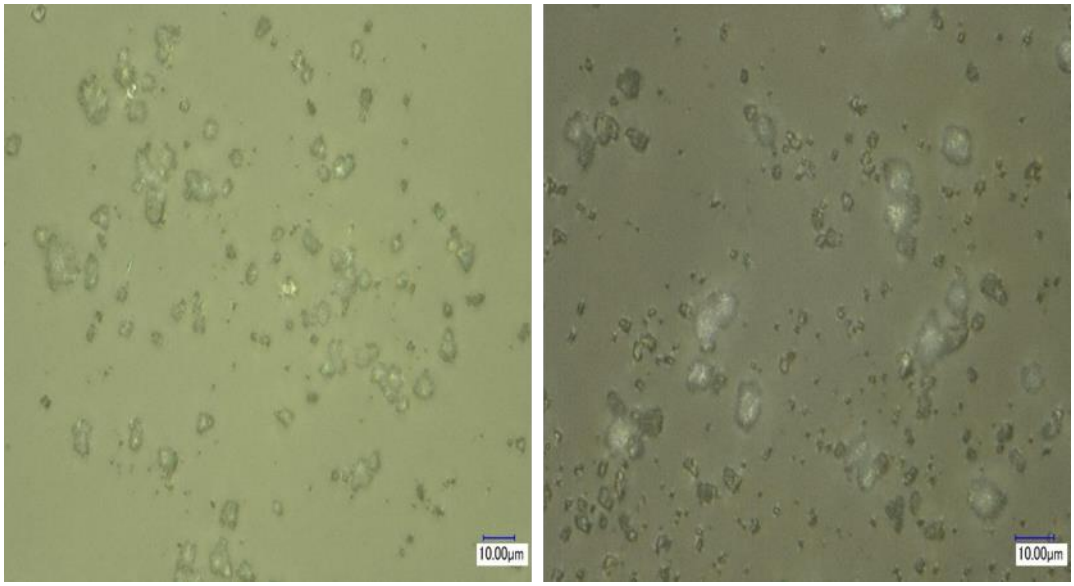

Figure 117 zinc acetate dihydrate Zn $(CH_3CO_2)_2 \cdot 2H_2O$ with 0.1 M of sodium hydroxide NaOH after calcination at 250 °C for 5 hours

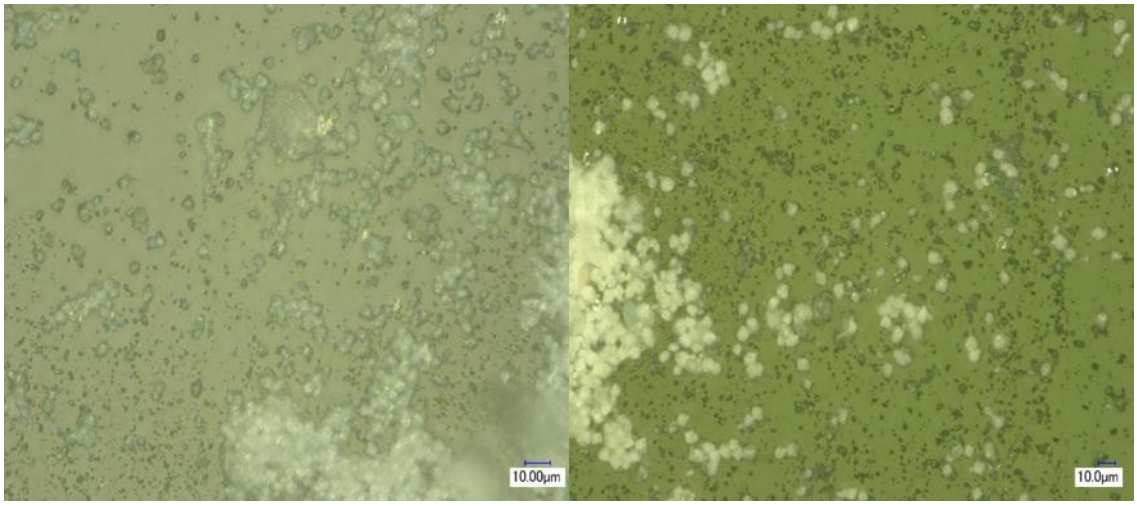

Figure 118. zinc acetate dihydrate Zn $(CH_3CO_2)_2 \cdot 2H_2O$ with 0.1 M of sodium hydroxide NaOH after calcination at 250 °C for 7 hours

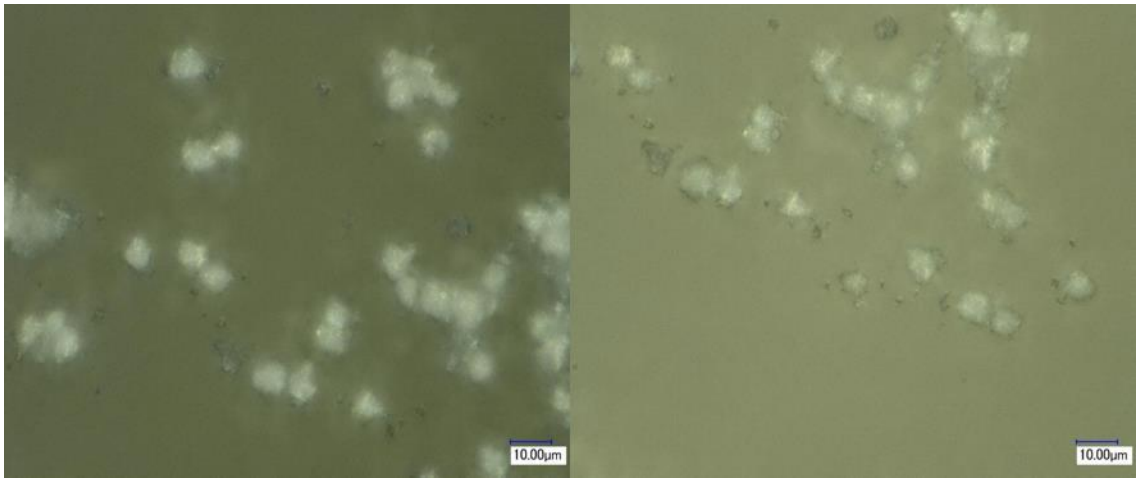

Figure 119 zinc acetate dihydrate Zn $(CH_3CO_2)_2 \cdot 2H_2O$ with 0.1 M of sodium hydroxide NaOH after calcination at 250 °C for 10 hours

Appendix B

Preparing zinc oxide by zinc acetate dihydrate Zn (CH3CO2)2·2H2O sodium hydroxide NaOH after 7 days

In this experiment, 0.88 gm of zinc acetate dehydrate Zn $(CH_3CO_2)_2 \cdot 2H_2O$ was used in 200 ml of ethanol as a solvent. In Experiment 8, 1 gm of NaOH was used. In Experiment 9, 2 gm of NaOH, and in Experiment 10, 3 gm of NaOH was used.

All the above concentrations were dissolved in 200 ml of ethanol for three experiments, each of which had been treated twice. NaOH was added to zinc acetate dehydrate under stirring for two hours at room temperature. The cloudy formed solution was placed and kept in dark for seven days at ambient temperature. After one week, the white sediment was collected using centrifugation at 4000 rpm for 20 min. Deionised water and ethanol were used to wash it several times [66]. Figure 120, illustrated the process of producing ZnO particles using zinc acetate and NaOH with ethanol as a solvent. Figure 121 showed centrifuge machine that was used.

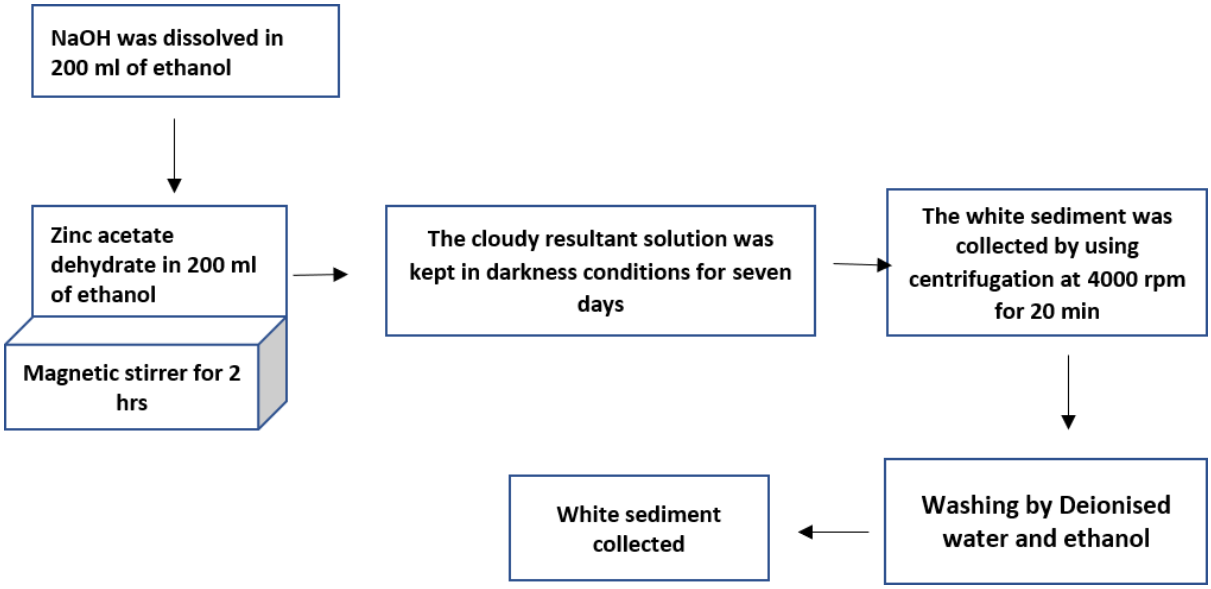

Figure 120 illustration scheme of the process of ZnO particles using zinc acetate and NaOH when ethanol is the solvent.

Figure 121. Centrifuge machine.

Keyence microscope and SEM for had used for Experiments 8, 9 and 10.Figure 122 shows seemingly tiny particles in KM. Figure 123, Figure 124 and Figure 125 clarify SEM results which shown irregular and non-uniform shapes in all NaOH concentrations as well. It had observed holes over the crystal. In addition, SEM images indicated the real morphology and size. Moreover, an increased amount of NaOH seemed to be not affected in this kind of experiment.

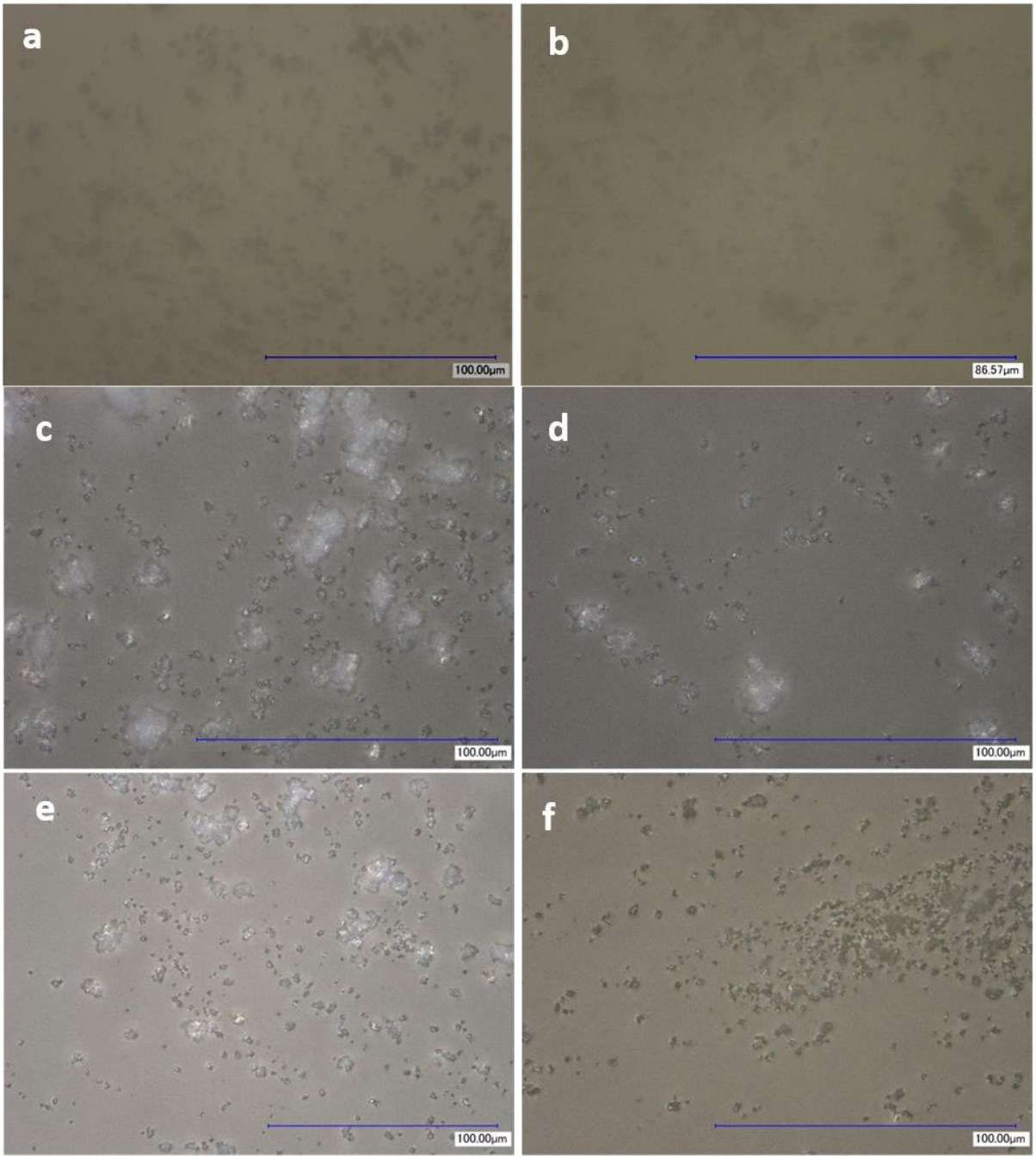

Figure 122. Keyence microscope illustrated zinc acetate dihydrate Zn $(CH_3CO_2)_2 \cdot 2H_2O$ with (a, b) 1 gm, (c, d) 2 gm and (e, f) 4 gm of sodium hydroxide NaOH with after 7 days.

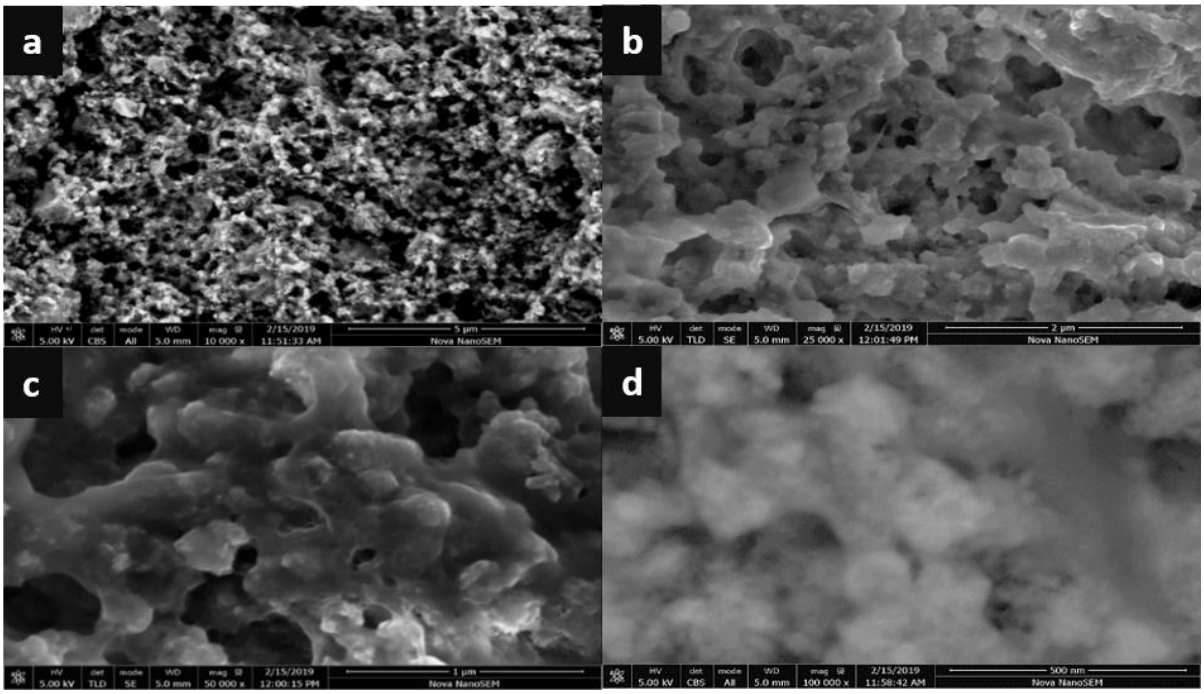

Figure 123. SEM results for zinc acetate dihydrate Zn $(CH_3CO_2)_2 \cdot 2H_2O$ with 1gm of NaOH, reaction took place in the in darkness for 7 days at room temperature at different magnification, a) 10000x, b) 25000x, c) 50000x, d) 100000x.

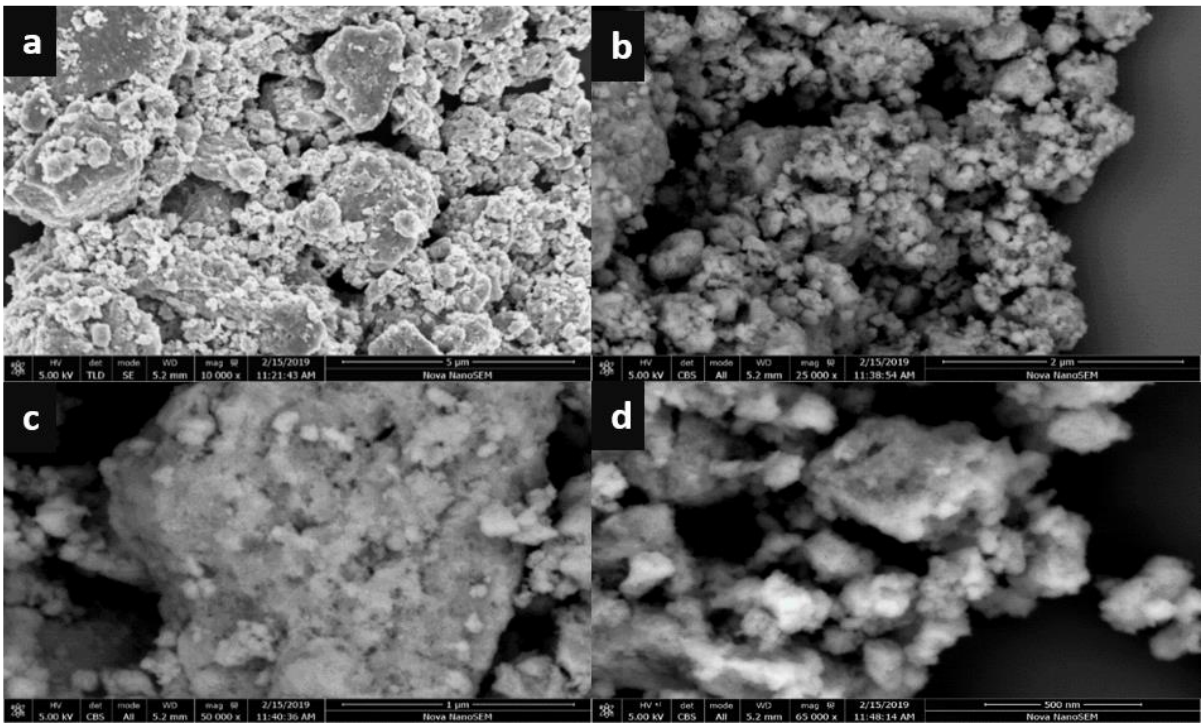

Figure 124. SEM results for zinc acetate dihydrate Zn $(CH_3CO_2)_2 \cdot 2H_2O$ with 2gm of NaOH, reaction took place in the in darkness for 7 days at room temperature at different magnification, a) 10000x, b) 25000x, c) 50000x, d) 65000x.

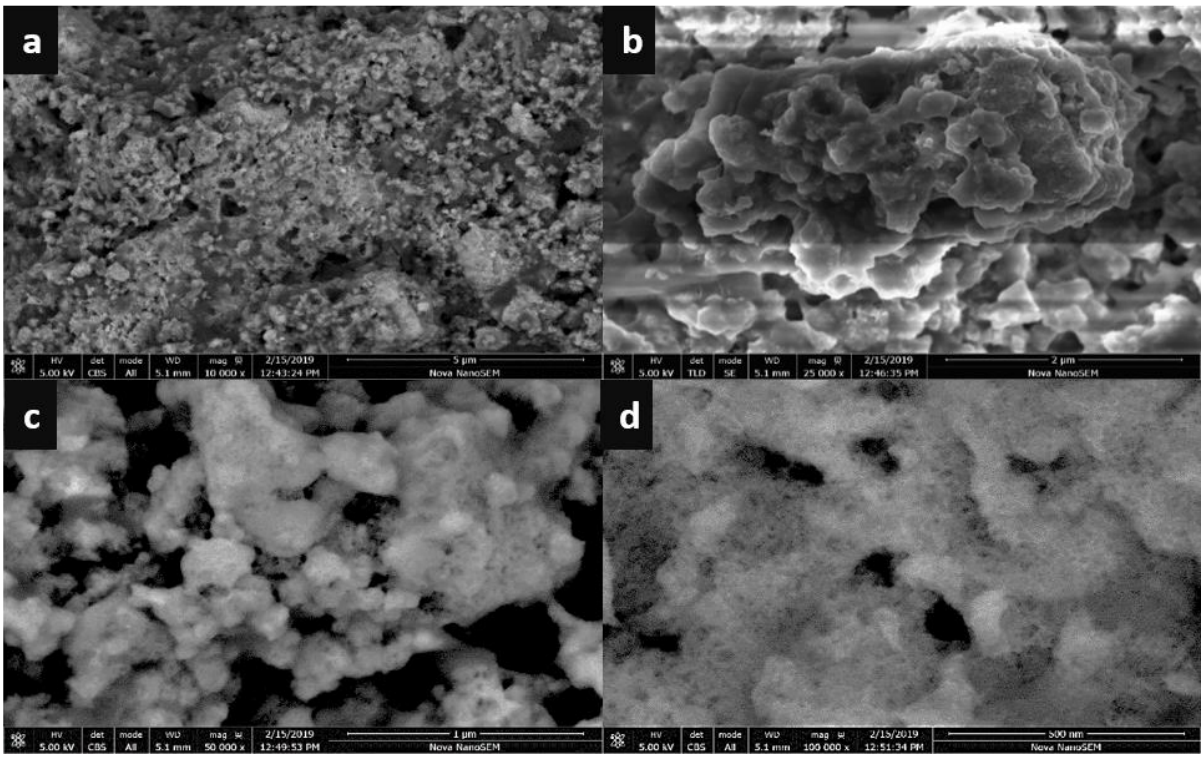

Figure 125. SEM results for zinc acetate dihydrate Zn $(CH_3CO_2)_2 \cdot 2H_2O$ with 4gm of NaOH, reaction took place in the in darkness for 7 days at room temperature at different magnification, a) 10000x, b) 25000x, c) 50000x, d) 100000x.

Appendix C

Preparing zinc oxide using zinc nitrate hexahydrate $Zn(NO_3)_2 \cdot 6H_2O$ and potassium hydroxide KOH

In Experiment 11, 0.4 mole/L of KOH was added dropwise onto zinc nitrate ($Zn(NO_3)_2 \cdot 6H_2O$) under vigorous stirring at ambient temperature. This process continued until white sediment was formed. The precipitate was separated using a centrifuge at 4500 rpm for 25 minutes. The white precipitate was washed three times with deionised water and ethanol, respectively and calcinated at 500 °C for 4 hours [219]. Figure 126 reveals the KM results for the agglomeration of the particles in most parts of the sample, so this experiment was excluded.

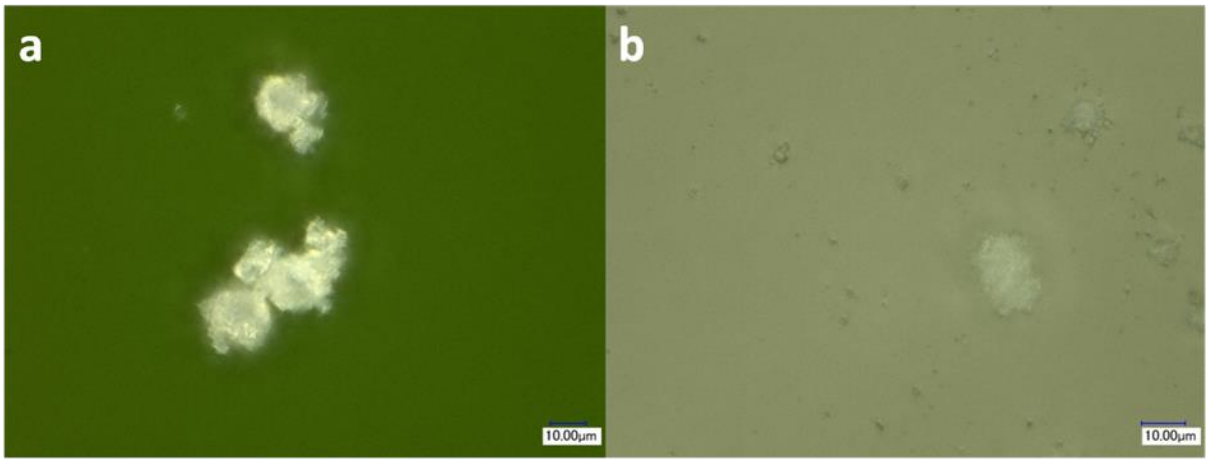

Figure 126. KM for ZnO by zinc oxide using zinc nitrate hexahydrate $Zn(NO_3)_2 \cdot 6H_2O$ and potassium hydroxide KOH.

Appendix D

Preparing zinc oxide using zinc nitrate hexahydrate $Zn(NO_3)_2 \cdot 6H_2O$ and ammonium carbonate $(NH_4)_2CO_3$

A total of 1.0 M of $(NH_4)_2CO_3$ and the same concentration of Zn $(NO_3)_2$ were prepared using deionised water. The sediment was collected by filtration and washed with absolute ethanol and deionised water, respectively. The precipitate was dried at 60 ^oC overnight and calcinated at 550 ^oC for 4 hours. Figure 16 shows the particles that looked like spherical shapes supported in this study, as mentioned in Experiment 11.

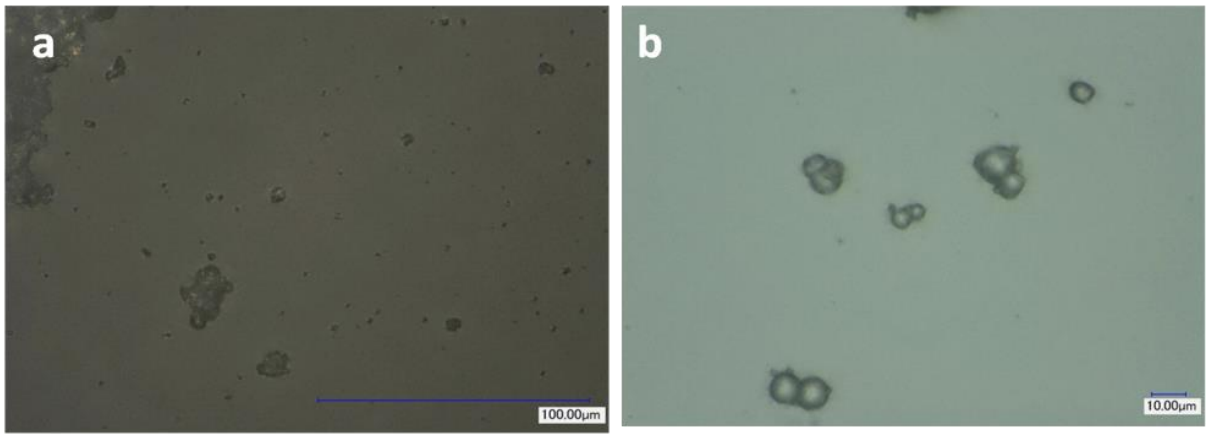

Figure 127. KM results for ZnO particles using zinc nitrate hexahydrate $Zn(NO_3)_2 \cdot 6H_2O$ and ammonium carbonate $(NH_4)_2CO_3$.

Appendix E

Preparing zinc oxide using ammonium carbonate $(NH_4)_2CO_3$ and zinc nitrate hexahydrate $Zn(NO_3)_2 \cdot 6H_2O$ (adding different type)

1 M of $(NH_4)_2CO_3$, 1M of $Zn(NO_3)_2 \cdot 6H_2O$ were prepared using deionised water. $(NH_4)_2CO_3$ was slowly dropped into zinc nitrate under vigorous stirring. The solution was transferred to a flask (round bottom) with three nicks on a hot plate using a condenser (Graham). This step can't be completed and the reason could be due to the speed of releasing gases being so very high and notable that the refluxing step didn't take place.

Appendix F

Preparing zinc oxide using zinc acetate dihydrate Zn $(CH_3CO_2)_2 \cdot 2H_2O$ sodium hydroxide NaOH using reflux method

Figure 128 shows KM results for the reflux method, as mentioned for Experiment 7 in the current study. It was clear that tiny particles made this experiment subjected to more characterizations and details. In addition, Figure 129 clarifies the zinc oxide morphology after being ground for Experiment 7 in the current study.

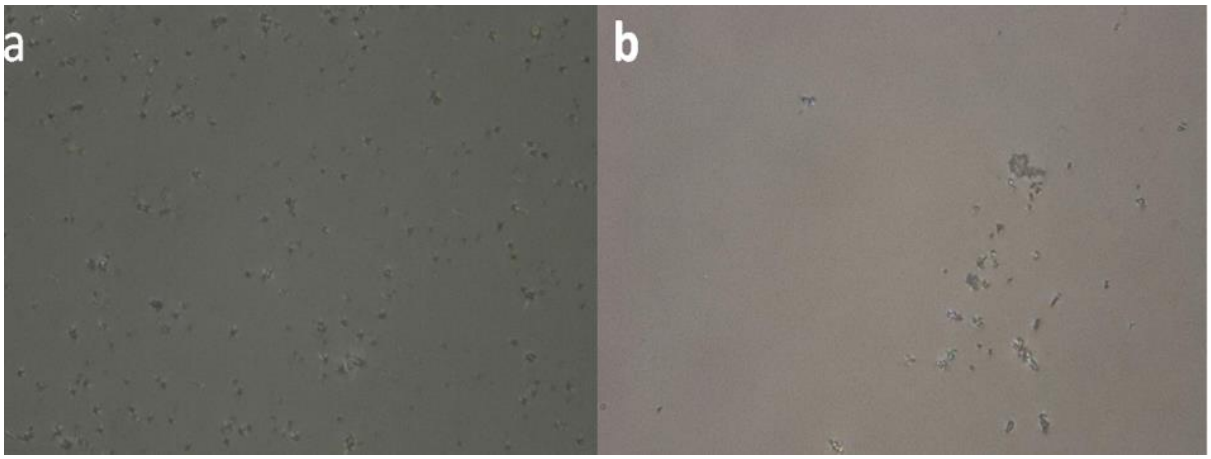

Figure 128. KM results for ZnO particles by solution process at low temperature of zinc acetate dihydrate Zn $(CH_3CO_2)_2 \cdot 2H_2O$ with sodium hydroxide NaOH.

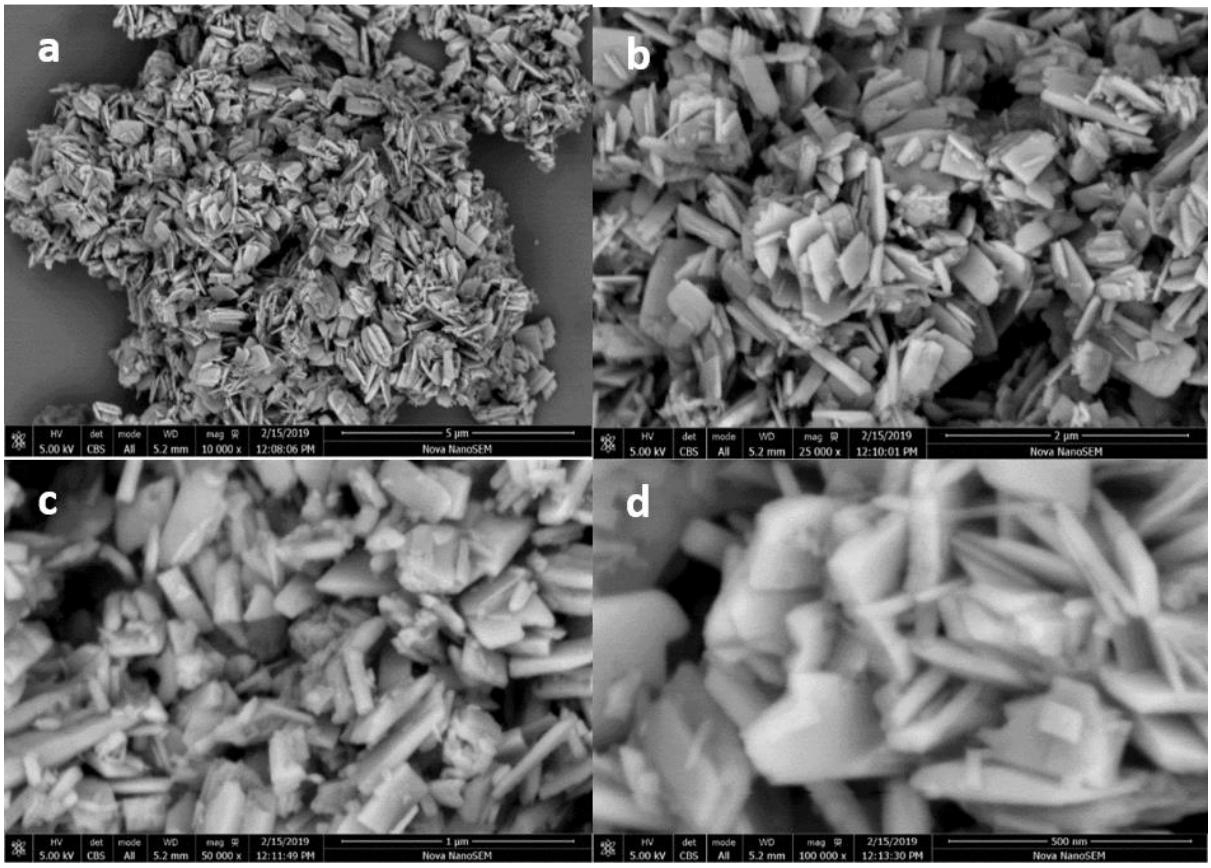

Figure 129. SEM results for ZnO particles by solution process at low temperature of zinc acetate dihydrate Zn $(CH_3CO_2)_2 \cdot 2H_2O$ with sodium hydroxide NaOH after grinded a) 10000x, b) 250000x, c) 50000 and d) 100000x.

Appendix G

Preparing zinc oxide using Zinc acetate dihydrate Zn $(CH_3CO_2)_2 \cdot 2H_2O$ sodium hydroxide NaOH, by reflux method using polyvinyl pyrrolidone PVP

PVP was added as a surfactant halfway through after adding NaOH into the acetate dihydrate solution. Importantly, a thick white foam precipitate was formed. The solution then underwent refluxing for 30 minutes at 90°C.

As shown in Figure 130, SDS worked more precisely than PVP—especially in the way the particles were able to self-assemble into a flower shape—and it has a specific role in decreasing the agglomeration among particles. Zinc oxide morphology in this part showed a flake shape more than a platelet shape, which could indicate that adding PVP could play a significant role in zinc oxide synthesis.

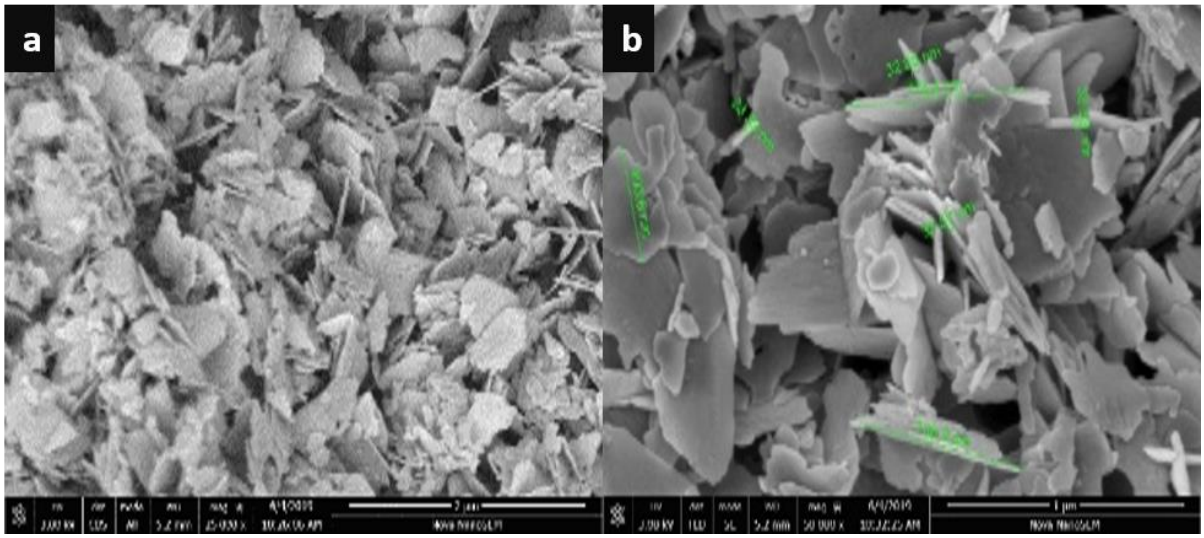

Figure 130. Zinc acetate dihydrate Zn $(CH_3CO_2)_2 \cdot 2H_2O$ with sodium hydroxide NaOH adding PVP by reflux method at different magnification, a) 25000x and d) 50000x.

References

1. Samira Bagheri, I.S.A., Amin Termeh Yousefi, Sharifah Bee Abd Hamid, *Nanocomposites in Electrochemical Sensors.*

. 1st edition ed. 2016, London.
2. Sridhar, A., et al., *Food preservation techniques and nanotechnology for increased shelf life of fruits, vegetables, beverages and spices: a review.* Environ Chem Lett, 2021. **19**(2): p. 1715-1735.
3. Wojnarowicz, J., T. Chudoba, and W. Lojkowski, *A Review of Microwave Synthesis of Zinc Oxide Nanomaterials: Reactants, Process Parameters and Morphoslogies.* Nanomaterials (Basel), 2020. **10**(6).
4. Ikumapayi, O.M., et al., *Microfabrication and nanotechnology in manufacturing system – An overview.* Materials Today: Proceedings, 2021. **44**: p. 1154-1162.
5. Rangayasami, A., et al., *Influence of nanotechnology to combat against COVID-19 for global health emergency: A review.* Sens Int, 2021. **2**: p. 100079.
6. Nguyen, T.H.A., et al., *Novel biogenic silver and gold nanoparticles for multifunctional applications: Green synthesis, catalytic and antibacterial activity, and colorimetric detection of Fe(III) ions.* Chemosphere, 2022. **287**(Pt 3): p. 132271.
7. Mostafaei, A. and F. Nasirpouri, *Epoxy/polyaniline–ZnO nanorods hybrid nanocomposite coatings: Synthesis, characterization and corrosion protection performance of conducting paints.* Progress in Organic Coatings, 2014. **77**(1): p. 146-159.
8. Kolodziejczak-Radzimska, A. and T. Jesionowski, *Zinc Oxide-From Synthesis to Application: A Review.* Materials (Basel), 2014. **7**(4): p. 2833-2881.
9. Samyn, P., et al., *Review: nanoparticles and nanostructured materials in papermaking.* Journal of Materials Science, 2017. **53**(1): p. 146-184.
10. Johnston, R.L., *Metal Nanoparticles and Nanoalloys*, in *Metal Nanoparticles and Nanoalloys*. 2012. p. 1-42.
11. Goh, P.S. and A.F. Ismail, *Review: is interplay between nanomaterial and membrane technology the way forward for desalination?* Journal of Chemical Technology & Biotechnology, 2015. **90**(6): p. 971-980.
12. Lin, Z.-T., et al., *Molecularly Imprinted Polymer-Based Biosensors: For the Early, Rapid Detection of Pathogens, Biomarkers, and Toxins in Clinical, Environmental, or Food Samples.* IEEE Nanotechnology Magazine, 2018. **12**(1): p. 6-13.
13. William D. Callister, J., David G. Rethwisch, *Fundamentals of Materials Science and Engineering: An Integrated Approach*. 2020
14. Turan, M.E., Y. Sun, and Y. Akgul, *Mechanical, tribological and corrosion properties of fullerene reinforced magnesium matrix composites fabricated by semi powder metallurgy.* Journal of Alloys and Compounds, 2018. **740**: p. 1149-1158.
15. Rondags, A., et al., *Fullerene C60 with cytoprotective and cytotoxic potential: prospects as a novel treatment agent in Dermatology?* Exp Dermatol, 2017. **26**(3): p. 220-224.
16. Robertson, C.G. and N.J. Hardman, *Nature of Carbon Black Reinforcement of Rubber: Perspective on the Original Polymer Nanocomposite.* Polymers (Basel), 2021. **13**(4).
17. Rajendran, S.P. and K. Sengodan, *Synthesis and Characterization of Zinc Oxide and Iron Oxide Nanoparticles Using Sesbania grandiflora Leaf Extract as Reducing Agent.* Journal of Nanoscience, 2017. **2017**: p. 1-7.
18. Kimura, M., *Emerging applications using metal-oxide semiconductor thin-film devices.* Japanese Journal of Applied Physics, 2019. **58**(9).
19. Liu, Y. and X. Chen, *Black Titanium Dioxide for Photocatalysis*, in *Semiconductors for Photocatalysis*. 2017. p. 393-428.
20. Kumar, S.G. and K.S.R.K. Rao, *Comparison of modification strategies towards enhanced charge carrier separation and photocatalytic degradation activity of metal oxide semiconductors (TiO 2 , WO 3 and ZnO).* Applied Surface Science, 2017. **391**: p. 124-148.
21. Phothisarattana, D. and N. Harnkarnsujarit, *Migration, aggregations and thermal degradation behaviors of TiO2 and ZnO incorporated PBAT/TPS nanocomposite blown films.* Food Packaging and Shelf Life, 2022. **33**.

22. Bharti, et al., *A review on the capability of zinc oxide and iron oxides nanomaterials, as a water decontaminating agent: adsorption and photocatalysis.* Applied Water Science, 2022. **12**(3).
23. Moezzi, A., A.M. McDonagh, and M.B. Cortie, *Zinc oxide particles: Synthesis, properties and applications.* Chemical Engineering Journal, 2012. **185-186**: p. 1-22.
24. Mishra, P.K., et al., *Zinc oxide nanoparticles: a promising nanomaterial for biomedical applications.* Drug Discov Today, 2017. **22**(12): p. 1825-1834.
25. Jiang, J., J. Pi, and J. Cai, *The Advancing of Zinc Oxide Nanoparticles for Biomedical Applications.* Bioinorg Chem Appl, 2018. **2018**: p. 1062562.
26. Firdaus, C.M., et al., *Characterization of ZnO and ZnO: TiO2 Thin Films Prepared by Sol-Gel Spray-Spin Coating Technique.* Procedia Engineering, 2012. **41**: p. 1367-1373.
27. Manabeng, M., et al., *A Review of the Impact of Zinc Oxide Nanostructure Morphology on Perovskite Solar Cell Performance.* Processes, 2022. **10**(9).
28. Singh, B., et al., *Understanding the adsorption behavior of surface active molecules on ZnO nanostructures by experimental and first-principles calculations.* Phys Chem Chem Phys, 2015. **17**(45): p. 30450-60.
29. Prasad, T., et al., *Morphological dissimilarities of ZnO nanoparticles and its effect on thermo-physical behavior of epoxy composites.* Polymer Composites, 2018. **39**(1): p. 135-145.
30. Agbo, P.E., P. A. Nwofe and E. U. Ahworehe *MORPHOLOGICAL AND OPTICAL PROPERTIES OF POLYMER CAPPED ZnO NANOPARTICLES.* Digest Journal of Nanomaterials and Biostructures, 2017. **12**(3): p. 653-658.
31. Fricke, M., et al., *Miniemulsion-Based Process for Controlling the Size and Shape of Zinc Oxide Nanoparticles.* Industrial & Engineering Chemistry Research, 2015. **54**(42): p. 10293-10300.
32. Farhat, O.F., et al., *Morphological and structural characterization of single-crystal ZnO nanorod arrays on flexible and non-flexible substrates.* Beilstein J Nanotechnol, 2015. **6**: p. 720-5.
33. AKE, P., *Tutorial on crystallography and how the hexagonal crystal is almost always different.* University of Strathclyde, 2017: p. 29.
34. Marc De Graef, M.E.M., *Structure of materials; An introduction to crystallography, diffraction and symmetry*. 2012, Cambridge University Press.
35. M. De Graef, M.E.M., *Structure of materials; An introduction to crystallography, diffraction and symmetry. .* Cambridge University Press, 2012.
36. Klaumünzer, M., et al., *ZnO superstructures via oriented aggregation initiated in a block copolymer melt.* CrystEngComm, 2014. **16**(8): p. 1502-1513.
37. Chen, B., et al., *Three-dimensional structure analysis and percolation properties of a barrier marine coating.* Sci Rep, 2013. **3**: p. 1177.
38. Nadzim, U.K.H.M., et al., *Effects of different zinc oxide morphologies on photocatalytic desulfurization of thiophene.* Journal of Alloys and Compounds, 2022. **913**.
39. Barhoum, A., et al., *Synthesis, growth mechanism, and photocatalytic activity of Zinc oxide nanostructures: porous microparticles versus nonporous nanoparticles.* Journal of Materials Science, 2016. **52**(5): p. 2746-2762.
40. Malakooti, M.H., H.S. Hwang, and H.A. Sodano, *Morphology-controlled ZnO nanowire arrays for tailored hybrid composites with high damping.* ACS Appl Mater Interfaces, 2015. **7**(1): p. 332-9.
41. Pushpanathan, K., et al., *Influence of Reaction Temperature on Crystal Structure and Band Gap of ZnO Nanoparticles.* Materials and Manufacturing Processes, 2012. **27**(12): p. 1334-1342.
42. Guillemin, S., et al., *Formation Mechanisms of ZnO Nanowires: The Crucial Role of Crystal Orientation and Polarity.* The Journal of Physical Chemistry C, 2013. **117**(40): p. 20738-20745.
43. Ali, A., A.-R. Phull, and M. Zia, *Elemental zinc to zinc nanoparticles: is ZnO NPs crucial for life? Synthesis, toxicological, and environmental concerns.* Nanotechnology Reviews, 2018. **7**(5): p. 413-441.
44. Mohammad Vaseem, A.U., Yoon-Bong Hahn, *ZnO Nanoparticles: Growth,*

Properties, and Applications. Metal Oxide Nanostructures and Their Applications

2010. **5**: p. 1-36.
45. Layek, A., et al., *A Generalized Three-Stage Mechanism of ZnO Nanoparticle Formation in Homogeneous Liquid Medium.* The Journal of Physical Chemistry C, 2012. **116**(46): p. 24757-24769.

46. Ong, C.B., L.Y. Ng, and A.W. Mohammad, *A review of ZnO nanoparticles as solar photocatalysts: Synthesis, mechanisms and applications.* Renewable and Sustainable Energy Reviews, 2018. **81**: p. 536-551.
47. Sirelkhatim, A., et al., *Review on Zinc Oxide Nanoparticles: Antibacterial Activity and Toxicity Mechanism.* Nanomicro Lett, 2015. **7**(3): p. 219-242.
48. Wu, W.-Y., C.-C. Yeh, and J.-M. Ting, *Effects of Seed Layer Characteristics on the Synthesis of ZnO Nanowires.* Journal of the American Ceramic Society, 2009. **92**(11): p. 2718-2723.
49. Hua, G., et al., *Fabrication of ZnO nanowire arrays by cycle growth in surfactantless aqueous solution and their applications on dye-sensitized solar cells.* Materials Letters, 2008. **62**(25): p. 4109-4111.
50. Lee, J.-H., et al., *Density-controlled growth and field emission property of aligned ZnO nanorod arrays.* Applied Physics A, 2009. **97**(2): p. 403-408.
51. Meskine, H. and P.A. Mulheran, *Simulation of reconstructions of the polar ZnO(0001)surfaces.* Physical Review B, 2011. **84**(16).
52. Baruah, S. and J. Dutta, *Hydrothermal growth of ZnO nanostructures.* Sci Technol Adv Mater, 2009. **10**(1): p. 013001.
53. Gupta, A., et al., *Nanoemulsions: formation, properties and applications.* Soft Matter, 2016. **12**(11): p. 2826-41.
54. Liu, Y., et al., *Oriented Attachment Revisited: Does a Chemical Reaction Occur?* Matter, 2019. **1**(3): p. 690-704.
55. Penn, R.L. and J.A. Soltis, *Characterizing crystal growth by oriented aggregation.* CrystEngComm, 2014. **16**(8).
56. Cao, D., et al., *Preparation of ZnO Nanoparticles with High Dispersibility Based on Oriented Attachment (OA) Process.* Nanoscale Res Lett, 2019. **14**(1): p. 210.
57. Qi, K., et al., *Morphology-controllable ZnO rings: Ionic liquid-assisted hydrothermal synthesis, growth mechanism and photoluminescence properties.* CrystEngComm, 2013. **15**(34).
58. Dhar, V. and A. Provino, *Ferromagnetism in the orthorhombic PrPd and SmPd.* Journal of Alloys and Compounds, 2018. **762**: p. 254-259.
59. Bazzi, L., et al., *Ultrasound and microwave assisted-synthesis of ZIF-8 from zinc oxide for the adsorption of phosphate.* Results in Engineering, 2022. **13**: p. 100378.
60. Gherbi, B., et al., *Effect of pH Value on the Bandgap Energy and Particles Size for Biosynthesis of ZnO Nanoparticles: Efficiency for Photocatalytic Adsorption of Methyl Orange.* Sustainability, 2022. **14**(18): p. 11300.
61. Dar, R.A., et al., *Performance of graphene-zinc oxide nanocomposite coated-glassy carbon electrode in the sensitive determination of para-nitrophenol.* Scientific reports, 2022. **12**(1): p. 1-14.
62. Pankaew, A., N. Traiphol, and R. Traiphol, *Synthesis of color-responsive polydiacetylene assemblies and polydiacetylene/zinc (II) ion/zinc oxide nanocomposites in water, toluene and mixed solvents: Toward large-scale production.* Colloids and Surfaces A: Physicochemical and Engineering Aspects, 2021. **617**: p. 126431.
63. Hessien, M., *Recent progress in zinc oxide nanomaterials and nanocomposites: From synthesis to applications.* Ceramics International, 2022. **48**(16): p. 22609-22628.
64. Abdullah, F., N.A. Bakar, and M.A. Bakar, *Current advancements on the fabrication, modification, and industrial application of zinc oxide as photocatalyst in the removal of organic and inorganic contaminants in aquatic systems.* Journal of hazardous materials, 2022. **424**: p. 127416.
65. Devi, K.N., et al., *Nickel doped zinc oxide with improved photocatalytic activity for Malachite Green Dye degradation and parameters affecting the degradation.* Journal of Materials Science: Materials in Electronics, 2021. **32**(7): p. 8733-8745.
66. Cao, H.L., et al., *Shape- and size-controlled synthesis of nanometre ZnO from a simple solution route at room temperature.* Nanotechnology, 2006. **17**(15): p. 3632-3636.
67. Saqib, S., et al., *Catalytic potential of endophytes facilitates synthesis of biometallic zinc oxide nanoparticles for agricultural application.* BioMetals, 2022. **35**(5): p. 967-985.
68. Alluhaibi, A.A. and R.K. Sendi. *Effect of Plasticisers and Zinc Oxide Nanoparticle Concentration on the Properties of Polyethylene Thin Films*. in *IOP Conference Series: Materials Science and Engineering*. 2022. IOP Publishing.
69. Al-Kordy, H.M., S.A. Sabry, and M.E. Mabrouk, *Statistical optimization of experimental parameters for extracellular synthesis of zinc oxide nanoparticles by a novel haloalaliphilic Alkalibacillus sp. W7.* Scientific reports, 2021. **11**(1): p. 1-14.

70. Samanta, P.K. and A.K. Bandyopadhyay, *Chemical growth of hexagonal zinc oxide nanorods and their optical properties.* Applied Nanoscience, 2011. **2**(2): p. 111-117.
71. Boppella, R., et al., *Facile Synthesis of Face Oriented ZnO Crystals: Tunable Polar Facets and Shape Induced Enhanced Photocatalytic Performance.* The Journal of Physical Chemistry C, 2013. **117**(9): p. 4597-4605.
72. Myrovali, E., et al., *Long-range ordering effects in magnetic nanoparticles.* ACS Applied Materials & Interfaces, 2021. **13**(18): p. 21602-21612.
73. Tancredi, P., et al., *Size and doping effects on the improvement of the low-temperature magnetic properties of magnetically aligned cobalt ferrite nanoparticles.* Journal of Alloys and Compounds, 2022. **894**: p. 162432.
74. Ahmed, D., *Detection of Superparamagnetic Iron Oxide Nanoparticles in Fluid Flow for Molecular Communication Applications: Analysis, Simulation, Experimentation and Design Guidelines*. 2022, FAU University Press.
75. Wang, Y., et al., *Biomineralization inspired crystal growth for biomimetic materials preparation.* Journal of Crystal Growth, 2023. **603**.
76. Tabrizi Hafez Moghaddas, S.M., et al., *Green synthesis of hexagonal-shaped zinc oxide nanosheets using mucilage from flaxseed for removal of methylene blue from aqueous solution.* Journal of Molecular Liquids, 2019. **296**.
77. Özgür, Ü., V. Avrutin, and H. Morkoç, *Zinc oxide materials and devices grown by molecular beam Epitaxy*, in *Molecular Beam Epitaxy*. 2018, Elsevier. p. 343-375.
78. Ashrafi, A. and C. Jagadish, *Erratum: "Review of zincblende ZnO: Stability of metastable ZnO phases" [J. Appl. Phys. 102, 071101 (2007)].* Journal of Applied Physics, 2020. **127**(4).
79. Ashrafi, A., *Recent progress in Cadmium Oxide thin films* 2015.
80. Rocha, L., et al., *Novel ozone gas sensor based on ZnO nanostructures grown by the microwave-assisted hydrothermal route.* Ceramics international, 2016. **42**(3): p. 4539-4545.
81. Yuan, Y., et al., *Temperature Dependence of Structural and Optical Properties of ZnO Nanoparticles Formed by Simple Precipitation Method.* MATEC Web of Conferences, 2016. **43**.
82. Jawaid, M., et al., *Microwave-assisted Synthesis of Hierarchical ZnO Nanostructures and Their Photocatalytic Properties.* MATEC Web of Conferences, 2016. **67**.
83. Li, X., et al., *Gas sensing properties of flower-like ZnO prepared by a microwave-assisted technique.* RSC Advances, 2014. **4**(88): p. 47319-47324.
84. Zhang, Z., et al., *Shape-controlled synthesis of zinc oxide: a simple method for the preparation of metal oxide nanocrystals in non-aqueous medium.* Chemistry, 2007. **13**(2): p. 632-8.
85. Šarić, A., et al., *Solvothermal synthesis of zinc oxide microspheres.* Journal of Alloys and Compounds, 2015. **652**: p. 91-99.
86. Ludi, B. and M. Niederberger, *Zinc oxide nanoparticles: chemical mechanisms and classical and non-classical crystallization.* Dalton Trans, 2013. **42**(35): p. 12554-68.
87. Amin, G., et al., *Influence of pH, Precursor Concentration, Growth Time, and Temperature on the Morphology of ZnO Nanostructures Grown by the Hydrothermal Method.* Journal of Nanomaterials, 2011. **2011**: p. 1-9.
88. Kumar, S.S., et al., *Synthesis, characterization and optical properties of zinc oxide nanoparticles.* International Nano Letters, 2013. **3**(1): p. 1-6.
89. Beig, B., et al., *Development and testing of zinc sulfate and zinc oxide nanoparticle-coated urea fertilizer to improve N and Zn use efficiency.* Front Plant Sci, 2022. **13**: p. 1058219.
90. Arya, S., P.K. Lehana, and S.B. Rana, *Synthesis of Zinc Oxide Nanoparticles and Their Morphological, Optical, and Electrical Characterizations.* Journal of Electronic Materials, 2017. **46**(7): p. 4604-4611.
91. El-Naggar, M.E., et al., *Surface modification of SiO2 coated ZnO nanoparticles for multifunctional cotton fabrics.* J Colloid Interface Sci, 2017. **498**: p. 413-422.
92. Davar, F., et al., *Green Synthesis of ZnO Nanoparticles and Its Application in the Degradation of Some Dyes.* Journal of the American Ceramic Society, 2015. **98**(6): p. 1739-1746.
93. Isawi, H., et al., *Surface nanostructuring of thin film composite membranes via grafting polymerization and incorporation of ZnO nanoparticles.* Applied Surface Science, 2016. **385**: p. 268-281.
94. Edalati, K., et al., *Low-temperature hydrothermal synthesis of ZnO nanorods: Effects of zinc salt concentration, various solvents and alkaline mineralizers.* Materials Research Bulletin, 2016. **74**: p. 374-379.
95. Dien, N.D., *Preparation of various morphologies of ZnO nanostructure through wet chemical methods.* Adv. Mater. Sci, 2019. **4**: p. 1-5.

96. Moghri Moazzen, M.A., S.M. Borghei, and F. Taleshi, *Change in the morphology of ZnO nanoparticles upon changing the reactant concentration.* Applied Nanoscience, 2012. **3**(4): p. 295-302.
97. Chou, H.-T. and H.-C. Hsu, *The effect of annealing temperatures to prepare ZnO seeds layer on ZnO nanorods array/TiO 2 nanoparticles photoanode.* Solid-State Electronics, 2016. **116**: p. 15-21.
98. Ranjbar, M., et al., *Sonochemical synthesis and characterization of nano-sized zinc(II) coordination complex as a precursor for the preparation of pure-phase zinc(II) oxide nanoparticles.* Nanochemistry Research, 2017. **2**(1): p. 120-131.
99. Mahmoodi, A., et al., *A hybrid dye-clay nano-pigment: Synthesis, characterization and application in organic coatings.* Dyes and Pigments, 2017. **147**: p. 234-240.
100. Lanje, A.S., et al., *Low temperature dielectric studies of zinc oxide (ZnO) nanoparticles prepared by precipitation method.* Advanced Powder Technology, 2013. **24**(1): p. 331-335.
101. Khoshhesab, Z.M., M. Sarfaraz, and Z. Houshyar, *Influences of Urea on Preparation of Zinc Oxide Nanostructures Through Chemical Precipitation in Ammonium Hydrogencarbonate Solution.* Synthesis and Reactivity in Inorganic, Metal-Organic, and Nano-Metal Chemistry, 2012. **42**(10): p. 1363-1368.
102. Parimalam, M., M.R. Islam, and R.M. Yunus, *Effects of nanosilica, zinc oxide, titatinum oxide on the performance of epoxy hybrid nanocoating in presence of rubber latex.* Polymer Testing, 2018. **70**: p. 197-207.
103. Jin, F.-L., X. Li, and S.-J. Park, *Synthesis and application of epoxy resins: A review.* Journal of Industrial and Engineering Chemistry, 2015. **29**: p. 1-11.
104. Shokuhfar, A. and B. Arab, *The effect of cross linking density on the mechanical properties and structure of the epoxy polymers: molecular dynamics simulation.* J Mol Model, 2013. **19**(9): p. 3719-31.
105. Khan, R., et al., *Facile synthesis of epoxy nanocomposite coatings using inorganic nanoparticles for enhanced thermo-mechanical properties: a comparative study.* Journal of Coatings Technology and Research, 2015. **13**(1): p. 159-169.
106. Chen, P., et al., *Effective reinforcement of amino-functionalized molybdenum disulfide on epoxy-based composites via strengthened interfacial interaction.* Journal of Materials Science, 2018. **53**(11): p. 8221-8231.
107. Alam, M.A., et al., *Anti-corrosive performance of epoxy coatings containing various nano-particles for splash zone applications.* Korean Journal of Chemical Engineering, 2017. **34**(8): p. 2301-2310.
108. Han, Y., et al. *Effect of ZnO nanoparticles on the surface potential decay of epoxy nanocomposites*. in *Electrical Insulating Materials (ISEIM), 2017 International Symposium on*. 2017. IEEE.
109. Huifei Jin, I.-A.T., Jiayang Wu, Armando Rodrigo Mor, Johan Smit. *The_effect_of_frequency_on_the_dielectric_strength_of_epoxy_resin_and_epoxy_resin_based_nanocomposites*. in *Conference Proceedings of ISEIM*. 2017.
110. Dagdag, O., et al., *Development and Anti-corrosion Performance of Polymeric Epoxy Resin and their Zinc Phosphate Composite on 15CDV6 Steel in 3wt% NaCl: Experimental and Computational Studies.* Journal of Bio- and Tribo-Corrosion, 2020. **6**(4).
111. Ibrahim, N.F., et al., *Corrosion Inhibition Properties of Epoxy-Zinc Oxide Nanocomposite Coating on Stainless Steel 316L.* Solid State Phenomena, 2020. **307**: p. 285-290.
112. Saidi, R., et al., *Electrochemical aspects of zinc oxide electrodeposition on Ti6Al4V alloy.* Surface and Coatings Technology, 2020. **402**.
113. Aboorvakani, R., S.J. Kennady Vethanathan, and K.U. Madhu, *Influence of Zn concentration on zinc oxide nanoparticles and their anti-corrosion property.* Journal of Alloys and Compounds, 2020. **834**.
114. Singha, S. and T. Jana, *Structure and properties of polybenzimidazole/silica nanocomposite electrolyte membrane: influence of organic/inorganic interface.* ACS Appl Mater Interfaces, 2014. **6**(23): p. 21286-96.
115. Harikrishnan, A.R., et al., *Particle and surfactant interactions effected polar and dispersive components of interfacial energy in nanocolloids.* Journal of Applied Physics, 2017. **122**(5).
116. Lian, Z., et al., *Solvent determines nature of effective interactions between nanoparticles in polymer brushes.* J Phys Chem B, 2015. **119**(10): p. 4099-108.
117. Qi-lin, X. and T. Xin, *Effect of polymer matrix and nanofiller on non-bonding interfacial properties of nanocomposites.* Journal of Polymer Research, 2016. **24**(1).
118. Jia, S., et al., *Anticorrosion performance of Zn-Al-Gr/waterborne epoxy composite coatings on mild steel.* Materials Research Express, 2019. **6**(9).
119. He, L., Z. Dong, and L. Zhang, *Selective adsorption behavior of polymer at the polymer-nanoparticle interface.* Journal of Polymer Science Part B: Polymer Physics, 2016. **54**(18): p. 1829-1837.

120. Golgoon, A., Aliofkhazraei, M., Toorani, M., Moradi, M., Rouhaghdam, A., & Asgari, M., *Corrosion behavior of ZnO-polyester nanocomposite powder coating. .* Anti-Corrosion Methods and Materials, 2017. **4**(64): p. 380-388.
121. Fajzulin, I., X. Zhu, and M. Möller, *Nanoparticulate inorganic UV absorbers: a review.* Journal of Coatings Technology and Research, 2015. **12**(4): p. 617-632.
122. Darvish, A., R. Naderi, and M.M. Attar, *The impact of pigment volume concentration on the protective performance of polyurethane coating with second generation of phosphate based anticorrosion pigment.* Progress in Organic Coatings, 2014. **77**(11): p. 1768-1773.
123. Popoola, A.P.I., V.S. Aigbodion, and O.S.I. Fayomi, *Anti-corrosion coating of mild steel using ternary Zn-ZnO-Y2O3 electro-depositon.* Surface and Coatings Technology, 2016. **306**: p. 448-454.
124. Fayomi, O.S.I. and A.P.I. Popoola, *Anti-corrosion properties and structural characteristics of fabricated ternary coatings.* Surface Engineering and Applied Electrochemistry, 2015. **51**(1): p. 76-84.
125. Laxman, K., et al., *Effect of a semiconductor dielectric coating on the salt adsorption capacity of a porous electrode in a capacitive deionization cell.* Electrochimica Acta, 2015. **166**: p. 329-337.
126. Ammar, S., et al., *Formulation and characterization of hybrid polymeric/ZnO nanocomposite coatings with remarkable anti-corrosion and hydrophobic characteristics.* Journal of Coatings Technology and Research, 2016. **13**(5): p. 921-930.
127. Chen, W., et al., *Investigation on anti-wear and corrosion-resistance behavior of steel-steel friction pair enhanced by ionic liquid additives under conductive conditions.* Tribology International, 2023. **177**: p. 108002.
128. Amiri, M., et al., *Development and anti-corrosion performance of hyperbranched polyglycerol-decorated Fe3O4@ SiO2 on mild steel in 1.0 M HCl.* Journal of Molecular Liquids, 2020. **314**: p. 113597.
129. Dagdag, O., et al., *Fabrication on designing of a macromolecular epoxy resin as anti-corrosive coating material for electrocatalytically deposited cadmium on 15CDV6 steel in 3% NaCl solution.* Journal of Materials Research and Technology, 2020. **9**(3): p. 5549-5563.
130. Xiong, H., et al., *Effect of organically modified sepiolite as inorganic nanofiller on the anti-corrosion resistance of epoxy coating.* Materials Letters, 2020. **260**: p. 126941.
131. Richards, C., H. McMurray, and G. Williams, *Smart-release inhibition of corrosion driven organic coating failure on zinc by cationic benzotriazole based pigments.* Corrosion Science, 2019. **154**: p. 101-110.
132. Izadi, M., T. Shahrabi, and B. Ramezanzadeh, *Synthesis and characterization of an advanced layer-by-layer assembled Fe3O4/polyaniline nanoreservoir filled with Nettle extract as a green corrosion protective system.* Journal of industrial and engineering chemistry, 2018. **57**: p. 263-274.
133. Jalili, M., M. Rostami, and B. Ramezanzadeh, *An investigation of the electrochemical action of the epoxy zinc-rich coatings containing surface modified aluminum nanoparticle.* Applied Surface Science, 2015. **328**: p. 95-108.
134. Ramezanzadeh, B., et al., *Effects of highly crystalline and conductive polyaniline/graphene oxide composites on the corrosion protection performance of a zinc-rich epoxy coating.* Chemical Engineering Journal, 2017. **320**: p. 363-375.
135. Ramezanzadeh, B., et al., *Enhancement of barrier and corrosion protection performance of an epoxy coating through wet transfer of amino functionalized graphene oxide.* Corrosion Science, 2016. **103**: p. 283-304.
136. Sari, M.G., M. Shamshiri, and B. Ramezanzadeh, *Fabricating an epoxy composite coating with enhanced corrosion resistance through impregnation of functionalized graphene oxide-co-montmorillonite Nanoplatelet.* Corrosion Science, 2017. **129**: p. 38-53.
137. Hsissou, R., *Review on epoxy polymers and its composites as a potential anticorrosive coatings for carbon steel in 3.5% NaCl solution: Computational approaches.* Journal of Molecular Liquids, 2021. **336**.
138. Xu, Y., et al., *Anticorrosive behavior of epoxy coating modified with hydrophobic nano-silica on phosphatized carbon steel.* Progress in Organic Coatings, 2021. **151**.
139. Sari, M.G., et al., *Epoxy/starch-modified nano-zinc oxide transparent nanocomposite coatings: A showcase of superior curing behavior.* Progress in Organic Coatings, 2018. **115**: p. 143-150.
140. Puglia, D., et al., *Cure kinetics of epoxy/MWCNTs nanocomposites: isothermal calorimetric and rheological analyses.* Progress in Organic Coatings, 2017. **108**: p. 75-83.

141. Kang, J.W., et al., *Resistance and wear resistance control in zno substrates for electrostatic discharge-safe ceramics through variation of sintering temperature and additives.* Nanoscience and Nanotechnology Letters, 2017. **9**(1): p. 85-88.
142. Yang, C., et al., *Anti-icing properties of superhydrophobic ZnO/PDMS composite coating.* Applied Physics A, 2016. **122**(1): p. 1-10.
143. Mahidashti, Z., T. Shahrabi, and B. Ramezanzadeh, *The role of post-treatment of an ecofriendly cerium nanostructure Conversion coating by green corrosion inhibitor on the adhesion and corrosion protection properties of the epoxy coating.* Progress in Organic Coatings, 2018. **114**: p. 19-32.
144. Ramezanzadeh, B., M. Rostami, and S. Niroumandrad, *Enhancement of the physical/mechanical properties of an epoxy composite by addition of aluminum nanoparticles through modification with cerium oxides and functionalization by SiO2-NH2 thin films.* Progress in Organic Coatings, 2017. **112**: p. 244-253.
145. Parameswaranpillai, J., et al., *Investigation of cure reaction, rheology, volume shrinkage and thermomechanical properties of nano-TiO2 filled epoxy/DDS composites.* Journal of Polymers, 2013. **2013**.
146. Dimitris I. Pantelis, T.E.T., *Corrosion of weldments*, in *Electrochemical technique used to control corrosion of a metal structure by lowering*

its potential by means of a direct cathodic current.

, W.P.S.i. Energy, Editor. 2017.
147. Gopi, D., et al., *Electrodeposition of a porous strontium-substituted hydroxyapatite/zinc oxide duplex layer on AZ91 magnesium alloy for orthopedic applications.* J Mater Chem B, 2014. **2**(34): p. 5531-5540.
148. Holmes, J., *Electrochemistry E-Learning Courses - via Teams.* 2022.
149. Padha, B., et al., *Electrochemical Impedance Spectroscopy (EIS) Performance Analysis and Challenges in Fuel Cell Applications.* Journal of Electrochemical Science and Technology, 2022. **13**(2): p. 167-176.
150. Rajeshwar, K., *Encyclopedia of electrochemistry.* American Cancer Society, 2007.
151. Orazem, M.E. and B. Tribollet, *Electrochemical impedance spectroscopy.* New Jersey, 2008. **1**: p. 383-389.
152. Holmes, J. *Electrochemistry Practical Electrochemistry Workshop*. 2022. Metrohm UK, Runcorn
153. Kendig, M.W., S. Jeanjaquet, and J. Lumsden, *Electrochemical impedance of coated metal undergoing loss of adhesion.* ASTM SPECIAL TECHNICAL PUBLICATION, 1993. **1188**: p. 407-407.
154. Xu, A., et al., *The Evaluation of Coating Performance by Analyzing the*

Intersection of Bode Plots. Int. J. Electrochem. Sci. , 2014. **9**: p. 5116 - 5125.
155. Fan, J.C., et al., *p-Type ZnO materials: Theory, growth, properties and devices.* Progress in Materials Science, 2013. **58**(6): p. 874-985.
156. Das, S. and V.C. Srivastava, *An overview of the synthesis of CuO-ZnO nanocomposite for environmental and other applications.* Nanotechnology Reviews, 2018. **7**(3): p. 267-282.
157. Benrezgua, E., et al., *Synthesis and properties of copper doped zinc oxide thin films by sol-gel, spin coating and dipping: A characterization review.* Journal of Molecular Structure, 2022. **1267**.
158. Schutt, K., et al., *Overcoming Zinc Oxide Interface Instability with a Methylammonium-Free Perovskite for High-Performance Solar Cells.* Advanced Functional Materials, 2019. **29**(47).
159. Cai, Q., et al., *Insight into Biological Effects of Zinc Oxide Nanoflowers on Bacteria: Why Morphology Matters.* ACS Appl Mater Interfaces, 2016. **8**(16): p. 10109-20.
160. Pinkas, A., et al., *Morphology effect on zinc oxide quantum photoinitiators for radical polymerization.* Nanoscale, 2021. **13**(15): p. 7152-7160.
161. Castro-Mayorga, J.L., et al., *The impact of zinc oxide particle morphology as an antimicrobial and when incorporated in poly(3-hydroxybutyrate-co-3-hydroxyvalerate) films for food packaging and food contact surfaces applications.* Food and Bioproducts Processing, 2017. **101**: p. 32-44.
162. Shankar, S. and J.-W. Rhim, *Effect of Zn salts and hydrolyzing agents on the morphology and antibacterial activity of zinc oxide nanoparticles.* Environmental Chemistry Letters, 2018. **17**(2): p. 1105-1109.

163. Raj, X.J., *Application of EIS and SECM Studies for Investigation of Anticorrosion Properties of Epoxy Coatings Containing Zinc Oxide Nanoparticles on Mild Steel in 3.5% NaCl Solution.* Journal of Materials Engineering and Performance, 2017. **26**(7): p. 3245-3253.
164. Kherfi, A., et al., *Improvement of the protective properties of the nanocomposite polypyrrole-Zinc oxide coating on mild steel by adding the dispersant sodium hexametaphosphate.* Synthetic Metals, 2021. **277**.
165. Xu, X., et al., *Hydrothermal In-Situ Synthesis and Anti-Corrosion Performance of Zinc Oxide Hydroxyapatite Nanocomposite Anti-Corrosive Pigment.* Coatings, 2022. **12**(4).
166. Saidi, R., et al., *The effect of zinc oxide coating morphology on corrosion performance of Ti-6Al-4 V alloys.* Journal of Alloys and Compounds, 2021. **883**.
167. Trino, L.D., et al., *Zinc oxide surface functionalization and related effects on corrosion resistance of titanium implants.* Ceramics International, 2018. **44**(4): p. 4000-4008.
168. Rohani, R., et al., *Green Approaches, Potentials, and Applications of Zinc Oxide Nanoparticles in Surface Coatings and Films.* Bioinorg Chem Appl, 2022. **2022**: p. 3077747.
169. Saleem, S., et al., *Modification in structural, optical, morphological, and electrical properties of zinc oxide (ZnO) nanoparticles (NPs) by metal (Ni, Co) dopants for electronic device applications.* Arabian Journal of Chemistry, 2022. **15**(1).
170. Rezaei, A., E. Katoueizadeh, and S.M. Zebarjad, *Investigation of the parameters affecting the morphology of zinc oxide (ZnO) nanoparticles synthesized by precipitation method.* Materials Today Chemistry, 2022. **26**.
171. Muchtar, A.R., et al., *Preparation of Graphene–Zinc Oxide Nanostructure Composite for Carbon Monoxide Gas Sensing.* Journal of Electronic Materials, 2018. **47**(7): p. 3647-3656.
172. Hadia, N.M., S. Garcia-Granda, and J.R. Garcia, *Effect of the temperature on structural and optical properties of zinc oxide nanoparticles.* J Nanosci Nanotechnol, 2014. **14**(7): p. 5443-8.
173. Wahab, R., et al., *Low temperature solution synthesis and characterization of ZnO nano-flowers.* Materials Research Bulletin, 2007. **42**(9): p. 1640-1648.
174. Lee, M., *X-Ray diffraction for materials research: from fundamentals to applications*. 2017: CRC Press.
175. Mathieu, H.J., *Auger electron spectroscopy.* Surface Analysis the Principal Techniques, 2009: p. 9-46.
176. Zhu, Y., *Engineering silver nanomaterials: From transparent*

conductors to resistive switching devices, in *School of Materials Science & Engineering*

Faculty of Science. 2019, THE UNIVERSITY OF NEW

SOUTH WALES. p. 87.
177. Shen, X., et al., *Synthesis and photocatalytic performance of ZnO with flower-like structure from zinc oxide ore.* Journal of Materials Science & Technology, 2020. **51**: p. 1-7.
178. Das, R., et al., *Effect of growth temperature on the optical properties of ZnO nanostructures grown by simple hydrothermal method.* RSC Advances, 2015. **5**(74): p. 60365-60372.
179. Manthina, V. and A.G. Agrios, *Single-pot ZnO nanostructure synthesis by chemical bath deposition and their applications.* Nano-Structures & Nano-Objects, 2016. **7**: p. 1-11.
180. Dalia Ahmed Mohammed Osman, M.A.M., *Synthesis and Characterization of Zinc Oxide Nanoparticles using Zinc Acetate Dihydrate and Sodium Hydroxide. .* Nanoscience and Nanoengineering, 2015. **1**(4): p. 4.
181. Sahu, V., et al., *Zinc oxide nanoring embedded lacey graphene nanoribbons in symmetric/asymmetric electrochemical capacitive energy storage.* Nanoscale, 2015. **7**(48): p. 20642-51.
182. Bhoge, Y.E., et al., *Synthesis and anticorrosive performance evaluation of zinc vanadate pigment.* Vacuum, 2017. **145**: p. 290-294.
183. M. Gusatti, G.S.B., et al., *EFFECT OF DIFFERENT PRECURSORS IN THE CHEMICAL SYNTHESIS OF ZnO.* 19º Congresso Brasileiro de Engenharia e Ciência dos Materiais, 2010. **21**.
184. J. Mayekar1, V.D., S. Radha3, *ROLE OF SALT PRECURSOR IN THE SYNTHESIS OF ZINC OXIDE NANOPARTICLES* International Journal of Research in Engineering and Technology e, 2014. **3**(3).
185. Kwoka, M., et al., *Flower-like ZnO Nanostructures Local Surface Morphology and Chemistry.* Nanomaterials (Basel), 2022. **12**(15).
186. Raj, V.J., et al., *Application of zinc oxide nanoflowers in environmental and biomedical science.* BBA Advances, 2022. **2**.

187. Kumar, N., et al., *Morphogenesis of ZnO nanostructures: role of acetate (COOH−) and nitrate (NO3−) ligand donors from zinc salt precursors in synthesis and morphology dependent photocatalytic properties.* RSC Advances, 2015. **5**(48): p. 38801-38809.
188. Dmitry A. Antonov, V.V.A. and a.M.A.T. , *Application of the Method of Coprecipitation ofCoprecipitation of*

Salts to Obtain Zinc Orthostannate, in *MATEC Web of Conferences*. 2021.
189. Zeljković, S., et al., *Mechanochemically induced synthesis of N-ion doped ZnO: solar photocatalytic degradation of methylene blue.* Green Chemistry Letters and Reviews, 2022. **15**(4): p. 869-880.
190. Tanwar, S. and D. Mathur, *Hydrothermal synthesis and characterization of zinc oxide nanoplates.* Materials Today: Proceedings, 2021. **47**: p. 4647-4651.
191. Dac Dien, N., *Preparation of various morphologies of ZnO nanostructure through wet chemical methods.* Advanced Material Science, 2019. **4**(1).
192. Penn, R.L. and J.A. Soltis, *Characterizing crystal growth by oriented aggregation.* CrystEngComm, 2014. **16**(8): p. 1409.
193. Dokmai, V., et al., *Effects of catalyst surfaces on adsorption revealed by atomic force microscope force spectroscopy: photocatalytic degradation of diuron over zinc oxide.* Phys Chem Chem Phys, 2020. **22**(26): p. 15035-15047.
194. Raha, S. and M. Ahmaruzzaman, *ZnO nanostructured materials and their potential applications: progress, challenges and perspectives.* Nanoscale Adv, 2022. **4**(8): p. 1868-1925.
195. Liu, J., et al., *Synthesis of high crystallinity ZnO nanowire array on polymer substrate and flexible fiber-based sensor.* ACS Appl Mater Interfaces, 2011. **3**(11): p. 4197-200.
196. Lokesh, K., et al., *Effective Ammonia Detection Using n-ZnO/p-NiO Heterostructured Nanofibers.* IEEE Sensors Journal, 2016. **16**(8): p. 2477-2483.
197. Khan, M.F., et al., *Flower-shaped ZnO nanoparticles synthesized by a novel approach at near-room temperatures with antibacterial and antifungal properties.* Int J Nanomedicine, 2014. **9**: p. 853-64.
198. Han, L., et al., *Effects of morphology on the thermoelectric properties of Al-doped ZnO.* RSC Advances, 2014. **4**(24).
199. Dalia Ahmed Mohammed Osman, M.A.M., *SynthesisandCharacterizationofZincOxideNanoparticlesusingZincAcetateDihydrateandSodiumHydroxide.* Journal of Nanoscience and Nanoengineering

2015. **1**(4): p. 4.
200. Shaba, E.Y., et al., *A critical review of synthesis parameters affecting the properties of zinc oxide nanoparticle and its application in wastewater treatment.* Applied Water Science, 2021. **11**(2).
201. Panda, N., B. Acharya, and P. Nayak, *Sonochemical synthesis of nitrogen doped ZnO nanorods: effect of anions on growth and optical properties.* Journal of Materials Science: Materials in Electronics, 2013. **24**: p. 4043-4049.
202. Abdelmohsen, A.H., et al., *Morphology Transition Engineering of ZnO Nanorods to Nanoplatelets Grafted Mo(8)O(23)-MoO(2) by Polyoxometalates: Mechanism and Possible Applicability to other Oxides.* Sci Rep, 2017. **7**(1): p. 5946.
203. El-Belely, E.F., et al., *Green synthesis of zinc oxide nanoparticles (ZnO-NPs) using Arthrospira platensis (Class: Cyanophyceae) and evaluation of their biomedical activities.* Nanomaterials, 2021. **11**(1): p. 95.
204. Anju, S., S. Yesodharan, and E. Yesodharan, *Zinc oxide mediated sonophotocatalytic degradation of phenol in water.* Chemical Engineering Journal, 2012. **189**: p. 84-93.
205. Leung, D.P.a.K.T., *Vertical Growth of TwoDimensional Zinc Oxide Nanostructures on ITOCoated Glass.* J. Phys. Chem. , 2008. **112**.
206. Misra, S. and H. Wang, *Review on the growth, properties and applications of self-assembled oxide-metal vertically aligned nanocomposite thin films-current and future perspectives.* Mater Horiz, 2021. **8**(3): p. 869-884.
207. Khan, W., et al., *Induced Photonic Response of ZnO Nanorods Grown on Oxygen Plasma-Treated Seed Crystallites.* Nanomaterials (Basel), 2018. **8**(6).
208. Panahandeh, N., et al., *Effect of incorporation of zinc oxide nanoparticles on mechanical properties of conventional glass ionomer cements.* Journal of conservative dentistry: JCD, 2018. **21**(2): p. 130.
209. Davis, K., et al., *Band gap engineered zinc oxide nanostructures via a sol–gel synthesis of solvent driven shape-controlled crystal growth.* RSC advances, 2019. **9**(26): p. 14638-14648.

210. Simon P. Garcia, a.S.S., *Controlling the Morphology of Zinc Oxide Nanorods Crystallized.* Chem. Mater, 2007. **19**.
211. Kaenphakdee, S., et al., *Zinc Oxide Synthesis from Extreme Ratios of Zinc Acetate and Zinc Nitrate: Synergistic Morphology.* Materials, 2022. **15**(2): p. 570.
212. Limón-Rocha, I., et al., *Effect of the Precursor on the Synthesis of ZnO and Its Photocatalytic Activity.* Inorganics, 2022. **10**(2).
213. Meenakshi, G. and A. Sivasamy, *Synthesis and characterization of zinc oxide nanorods and its photocatalytic activities towards degradation of 2,4-D.* Ecotoxicol Environ Saf, 2017. **135**: p. 243-251.
214. Meenakshi, G. and A. Sivasamy, *Synthesis and characterization of zinc oxide nanorods and its photocatalytic activities towards degradation of 2, 4-D.* Ecotoxicology and environmental safety, 2017. **135**: p. 243-251.
215. Hutin, A. and M.S. Carvalho, *Effect of contamination from direct sonication on characterization of nanofluid stability.* Powder Technology, 2022. **399**: p. 117157.
216. Barbosa, R., et al., *Improving the swelling, mechanical, and electrical properties in natural rubber latex/carbon nanotubes nanocomposites: Effect of the sonication method.* Journal of Applied Polymer Science, 2022. **139**(23): p. 52325.
217. Cai, Q., et al., *Effect of zinc oxide nanoparticles on physical properties of carboxymethyl cellulose/poly (ethylene oxide) matrix.* Physica B: Condensed Matter, 2022. **633**: p. 413771.
218. Chen, H., et al., *Hydrothermally Grown ZnO Micro/Nanotube Arrays and Their Properties.* Nanoscale Res Lett, 2009. **5**(3): p. 570-5.
219. Raoufi, D., *Synthesis and microstructural properties of ZnO nanoparticles prepared by precipitation method.* Renewable Energy, 2013. **50**: p. 932-937.
220. Herrera-Rivera, R., M.d.l.L. Olvera, and A. Maldonado, *Synthesis of ZnO Nanopowders by the Homogeneous Precipitation Method: Use of Taguchi's Method for Analyzing the Effect of Different Variables.* Journal of Nanomaterials, 2017. **2017**: p. 1-9.
221. Ogbomida, E.T., et al., *Accumulation patterns and risk assessment of metals and metalloid in muscle and offal of free-range chickens, cattle and goat in Benin City, Nigeria.* Ecotoxicol Environ Saf, 2018. **151**: p. 98-108.
222. Hormozi-Nezhad, M.R., M. Jalali-Heravi, and F. Kafrashi, *Detecting intermediate particles in the growth of colloidal zinc oxide nanoparticles in different chemical routes using MCR-ALS.* Journal of Chemometrics, 2013. **27**(10): p. 353-358.
223. Mika, K., et al., *Electrochemical synthesis and characterization of dark nanoporous zinc oxide films.* Electrochimica Acta, 2019. **305**: p. 349-359.
224. Liang, Y.C., Y.C. Chang, and W.C. Zhao, *Design and Synthesis of Novel 2D Porous Zinc Oxide-Nickel Oxide Composite Nanosheets for Detecting Ethanol Vapor.* Nanomaterials (Basel), 2020. **10**(10).
225. Muhammed, L.W.a.M., *Synthesis of zinc oxide nanoparticles withconttrolled morphology.* Materials Chemistry Division, Royal Institute of Technology, 1999.
226. Riyadh M. Alwan, Q.A.K., Kassim M. Sahan, Rawaa A. Ali, and N.A.K. Roaa J. Mahdi, Alwan N. Jassim, *Synthesis of Zinc Oxide Nanoparticles via SolGel.* Nanoscience and Nanotechnology, 2015. **5**(1): p. 1-6.
227. Chang, J., et al., *Self-assembled 3D ZnO porous structures with exposed reactive 0001 facets and their enhanced gas sensitivity.* Sensors (Basel), 2013. **13**(7): p. 8445-60.
228. Kumar, S.G. and K.K. Rao, *Zinc oxide based photocatalysis: tailoring surface-bulk structure and related interfacial charge carrier dynamics for better environmental applications.* Rsc Advances, 2015. **5**(5): p. 3306-3351.
229. Fardad S, M.R., Manteghi A, Amini MM. *Synthesis, size and colloidal stability of ZnO nanoparticles in ionic solutions.* . in *Nanotechnology*. 2007.
230. Ashraf, R., et al., *Effect of Calcination on Properties of ZnO Nanoparticles.* Materials Today: Proceedings, 2015. **2**(10): p. 5468-5472.
231. Alias, S., A. Ismail, and A. Mohamad, *Effect of pH on ZnO nanoparticle properties synthesized by sol–gel centrifugation.* Journal of Alloys and Compounds, 2010. **499**(2): p. 231-237.
232. by, E.o.p.o.t.m.a.o.p.o.m.Z.p. and S.v.a.p. method, *Effect of pH on the morphology and optical properties of modified ZnO particles by SDS via a precipitation method.* Powder Technology, 2010. **203**(2): p. 243-247.
233. Mohammed Gazzali, P.M., S. Rajan, and G. Chandrasekaran, *Transformation from conducting ferromagnetic to insulating diamagnetic in vanadium doped ZnO nanoparticles.* Journal of Materials Science: Materials in Electronics, 2017. **29**(1): p. 823-836.

234. Wozniak, A., et al., *ZnO@Gd2O3 core/shell nanoparticles for biomedical applications: Physicochemical, in vitro and in vivo characterization.* Mater Sci Eng C Mater Biol Appl, 2017. **80**: p. 603-615.
235. Wang, J., P. Ma, and L. Xiang, *Effects of NaOH on formation of ZnO nanorods from ε-Zn(OH)2.* Materials Letters, 2015. **141**: p. 118-121.
236. Parra, M.R. and F.Z. Haque, *Aqueous chemical route synthesis and the effect of calcination temperature on the structural and optical properties of ZnO nanoparticles.* Journal of Materials Research and Technology, 2014. **3**(4): p. 363-369.
237. van Westen, T. and R.D. Groot, *Effect of Temperature Cycling on Ostwald Ripening.* Cryst Growth Des, 2018. **18**(9): p. 4952-4962.
238. Kang, K.-K., B. Lee, and C.-S. Lee, *Recent progress in the synthesis of inorganic particulate materials using microfluidics.* Journal of the Taiwan Institute of Chemical Engineers, 2019. **98**: p. 2-19.
239. Bunaciu, A.A., E.G. UdriŞTioiu, and H.Y. Aboul-Enein, *X-ray diffraction: instrumentation and applications.* Critical reviews in analytical chemistry, 2015. **45**(4): p. 289-299.
240. Fakhari, S., M. Jamzad, and H. Kabiri Fard, *Green synthesis of zinc oxide nanoparticles: a comparison.* Green chemistry letters and reviews, 2019. **12**(1): p. 19-24.
241. ALMASHNOWI, M. and A. YAHEA, *Mechanisms of Nanoparticle Synthesis for the Production of Well-Defined Models of Heterogeneous Catalysts*. 2022, Durham University.
242. Ahmadpour, G., et al., *Effect of substrate surface treatment on the hydrothermal synthesis of zinc oxide nanostructures.* Ceramics International, 2022. **48**(2): p. 2323-2329.
243. Ahmed, M.A.M., et al., *Effect of Sm doping ZnO nanorods on structural optical and electrical properties of Schottky diodes prepared by chemical bath deposition.* Materials Science in Semiconductor Processing, 2018. **79**: p. 53-60.
244. Gan, X.Z.a.F., *The Synthesis of Nano-Crystalline Metal Oxides by Solution Method*

2ed, ed. S. Neralla. 2012. 212.
245. Laurenti, M., et al., *Lead-free piezoelectrics: V(3+) to V(5+) ion conversion promoting the performances of V-doped Zinc Oxide.* Sci Rep, 2017. **7**: p. 41957.
246. Jung, H.J., et al., *Various shaped-ZnO nanocrystals via low temperature synthetic methods: Surfactant and pH dependence.* Solid State Sciences, 2013. **21**: p. 26-31.
247. Arsha Kusumam TV, P.T., Divya T, Nikhila MP, Anju M, Anas K, et al, *Morphology controlled synthesis and photocatalytic activity of zinc oxide nanostructures.* 2016. **42**(3): p. 3769-75.
248. W, c., *Lamellar_structure*, in *Lamellar_structure*, T.F. Encyclopedia, Editor. 2013. p. 1.
249. Yan, Z.B., R; Chrisey, DB *Self-assembly of zinc hydroxide/dodecyl sulfate nanolayers into complex three-dimensional nanostructures by laser ablation in liquid* Chemical Physics Letters, 2010. **497** (4-6): p. 205-207
250. Ramimoghadam, D., M.Z. Hussein, and Y.H. Taufiq-Yap, *The effect of sodium dodecyl sulfate (SDS)*

and cetyltrimethylammonium bromide (CTAB) on the Properties of ZnO synthesized by hydrothermal

method. Int J Mol Sci, 2012. **13**(10): p. 13275.
251. Lo, S.-S., et al., *Raman scattering and band-gap variations of Al-doped ZnO nanoparticles synthesized by a chemical colloid process.* Journal of Physics D: Applied Physics, 2009. **42**(9).
252. Md. Shah Alam, M.Z.H., *A Simple Hydrothermal Protocol for the Synthesis of Zinc Oxide.* JnUJSic, 2021. **7**: p. 75-80.
253. Muhammad, W., et al., *Optical, morphological and biological analysis of zinc oxide nanoparticles (ZnO NPs) using Papaver somniferum L.* RSC Adv, 2019. **9**(51): p. 29541-29548.
254. Faure, B., et al., *Dispersion and surface functionalization of oxide nanoparticles for transparent photocatalytic and UV-protecting coatings and sunscreens.* Sci Technol Adv Mater, 2013. **14**(2): p. 023001.
255. Drozdowska, K., et al., *Combined chemoresistive and in situ FTIR spectroscopy study of nanoporous NiO films for light-activated nitrogen dioxide and acetone gas sensing.* Sensors and Actuators B: Chemical, 2022. **353**: p. 131125.
256. Dazzi, A., et al., *AFM–IR: combining atomic force microscopy and infrared spectroscopy for nanoscale chemical characterization.* Applied spectroscopy, 2012. **66**(12): p. 1365-1384.
257. Abb, M., et al., *Surface-enhanced infrared spectroscopy using metal oxide plasmonic antenna arrays.* Nano letters, 2014. **14**(1): p. 346-352.

258. Bulcha, B., et al., *Synthesis of Zinc Oxide Nanoparticles by Hydrothermal Methods and Spectroscopic Investigation of Ultraviolet Radiation Protective Properties.* Journal of Nanomaterials, 2021. **2021**: p. 1-10.
259. Rafique, M., et al., *Hydrothermal synthesis of an efficient and visible light responsive pure and strontium doped zinc oxide nano-hexagonal photocatalysts for photodegradation of Rhodamine B dye.* Applied Nanoscience, 2021. **11**(3): p. 1045-1056.
260. Zahra, S., et al., *Synthesis of nanosize zinc oxide through aqueous sol-gel route in polyol medium.* BMC Chem, 2022. **16**(1): p. 104.
261. Halanayake, K.D., N.K. Kalutharage, and J.W. Hewage, *Microencapsulation of biosynthesized zinc oxide nanoparticles (ZnO-NPs) using Plumeria leaf extract and kinetic studies in the release of ZnO-NPs from microcapsules.* SN Applied Sciences, 2021. **3**(1).
262. SUNTAKO, R., *Effect of zinc oxide nanoparticles synthesized by a precipitation method.* Indian Academy of Sciences, 2015. **38**(4): p. 1033–1038.
263. S, G., et al., *Synthesis and Characterizations of Zinc Oxide Nanoparticles for Antibacterial Applications.* Journal of Nanomedicine & Nanotechnology, 2017. **s8**.
264. Babakhani, S., et al., *Optical and Thermal Properties of Zn/Al-Layered Double Hydroxide Nanocomposite Intercalated with Sodium Dodecyl Sulfate.* Journal of Spectroscopy, 2014. **2014**: p. 1-10.
265. Koczkur, K.M., et al., *Polyvinylpyrrolidone (PVP) in nanoparticle synthesis.* Dalton Trans, 2015. **44**(41): p. 17883-905.
266. Sundaram Sanjay, S., R. S. Yadav, and A. C. Pandey, *Synthesis Of Lamellar Porous Photocatalytic Nano ZnO With The Help Of anionic Surfactant.* Advanced Materials Letters, 2013. **4**(5): p. 378-384.
267. Terrones, H., et al., *New first order Raman-active modes in few layered transition metal dichalcogenides.* Sci Rep, 2014. **4**: p. 4215.
268. Song, Y., et al., *Raman Spectra and Microstructure of Zinc Oxide irradiated with Swift Heavy Ion.* Crystals, 2019. **9**(8).
269. Li, P., et al., *Investigation of the Charge-Transfer Between Ga-Doped ZnO Nanoparticles and Molecules Using Surface-Enhanced Raman Scattering: Doping Induced Band-Gap Shrinkage.* Front Chem, 2019. **7**: p. 144.
270. Konan, F.K., et al., *X-ray Diffraction, XPS, and Raman Spectroscopy of Coated ZnO:Al (1—7 at%) Nanoparticles.* e-Journal of Surface Science and Nanotechnology, 2019. **17**(0): p. 163-168.
271. Walczak, M., et al., *Materials corrosion for thermal energy storage systems in concentrated solar power plants.* Renewable and Sustainable Energy Reviews, 2018. **86**: p. 22-44.
272. Zhou, H., et al., *Experimental study on erosion-corrosion behavior of liquid–solid swirling flow in pipeline.* Materials & Design, 2022. **214**.
273. Dagdag, O., et al., *Anticorrosive property of heterocyclic based epoxy resins on carbon steel corrosion in acidic medium: Electrochemical, surface morphology, DFT and Monte Carlo simulation studies.* Journal of Molecular Liquids, 2019. **287**: p. 110977.
274. Abdus Samad, U., et al., *Effect of Incorporated ZnO Nanoparticles on the Corrosion Performance of SiO(2) Nanoparticle-Based Mechanically Robust Epoxy Coatings.* Materials (Basel), 2020. **13**(17).
275. Chen, B., et al., *A novel and green method to synthesize a epoxidized biomass eucommia gum as the nanofiller in the epoxy composite coating with excellent anticorrosive performance.* Chemical Engineering Journal, 2020. **379**.
276. Shahrabi, T., B. Ramezanzadeh, and G. Bahlakeh, *Development of a high-performance corrosion protective functional nano-film based on poly acrylic acid-neodymium nitrate on mild steel surface.* Journal of the Taiwan Institute of Chemical Engineers, 2019. **96**: p. 610-626.
277. Krishnan, A., et al., *Unfolding the anticorrosive characteristics of TiO2–WO3 mixed oxide reinforced polyaniline composite coated mild steel in alkaline environment.* Polymer Composites, 2019. **40**(6): p. 2400-2409.
278. Al-Gamal, A.G., et al., *Comparative impact of doping nano-conducting polymer with carbon and carbon oxide composites in alkyd binder as anti-corrosive coatings.* Composite Interfaces, 2018. **25**(11): p. 959-980.
279. Pourhashem, S., et al., *Exploring corrosion protection properties of solvent based epoxy-graphene oxide nanocomposite coatings on mild steel.* Corrosion Science, 2017. **115**: p. 78-92.
280. Ghasemi-Kahrizsangi, A., et al., *Corrosion behavior of modified nano carbon black/epoxy coating in accelerated conditions.* Applied surface science, 2015. **331**: p. 115-126.

281. Sivakumarb, S., P.K. Selvaraja, and S. Selvaraj, *Water Soluble CdO-PANI Composite as Corrosion Resistive Delegate in Acidic Abode for Mild Steel.* 2022.
282. Zhu, Q., et al., *Epoxy coating with in-situ synthesis of polypyrrole functionalized graphene oxide for enhanced anticorrosive performance.* Progress in Organic Coatings, 2020. **140**: p. 105488.
283. Bhaskaran, Y., et al., *To evaluate an ionic liquid for anticorrosive impact on iron–carbon steel: synthesis, computational and experimental mechanism.* Chemical Papers, 2020. **75**(2): p. 789-803.
284. Dagdag, O., et al., *Anticorrosive Formulation Based of the Epoxy Resin–Polyaminoamide Containing Zinc Phosphate Inhibitive Pigment Applied on Sulfo-Tartaric Anodized AA 7075-T6 in NaCl Medium.* Journal of Bio- and Tribo-Corrosion, 2019. **5**(1).
285. Ibrahim, M., et al., *Enhanced Corrosion Protection of Epoxy/ZnO-NiO Nanocomposite Coatings on Steel.* Coatings, 2020. **10**(8).
286. Bandil, K., et al., *Microstructural, mechanical and corrosion behaviour of Al–Si alloy reinforced with SiC metal matrix composite.* Journal of Composite Materials, 2019. **53**(28-30): p. 4215-4223.
287. Feng, L. and P. Yuan, *Corrosion protection mechanism of aluminum triphosphate modified by organic acids as a rust converter.* Progress in Organic Coatings, 2020. **140**: p. 105508.
288. Gobara, M., et al., *Corrosion protection mechanism of Ce 4+/organic inhibitor for AA2024 in 3.5% NaCl.* RSC advances, 2020. **10**(4): p. 2227-2240.
289. Karasinski, E., et al., *Nanostructured coating based on epoxy/metal oxides: Kinetic curing and mechanical properties.* Thermochimica Acta, 2013. **569**: p. 167-176.
290. Ramezanzadeh, B., M. Attar, and M. Farzam, *Effect of ZnO nanoparticles on the thermal and mechanical properties of epoxy-based nanocomposite.* Journal of thermal analysis and calorimetry, 2011. **103**(2): p. 731-739.
291. Lu, H., et al., *Synthesis of graphene oxide-based sulfonated oligoanilines coatings for synergistically enhanced corrosion protection in 3.5% NaCl solution.* ACS applied materials & interfaces, 2017. **9**(4): p. 4034-4043.
292. Dworschak, D., C. Brunnhofer, and M. Valtiner, *Photocorrosion of ZnO Single Crystals during Electrochemical Water Splitting.* ACS Appl Mater Interfaces, 2020. **12**(46): p. 51530-51536.
293. Chen, W., et al., *Exposed facet dependent stability of ZnO micro/nano crystals as a photocatalyst.* Applied Surface Science, 2019. **470**: p. 807-816.
294. Valtiner, M., et al., *In Situ Study of the Polar ZnO (0001)− Zn Surface in Alkaline Electrolytes.* The Journal of Physical Chemistry C, 2010. **114**(36): p. 15440-15447.
295. Dulub, O., U. Diebold, and G. Kresse, *Novel stabilization mechanism on polar surfaces: ZnO (0001)-Zn.* Physical review letters, 2003. **90**(1): p. 016102.
296. Nicholas, N.J., W. Ducker, and G.V. Franks, *Differential etching of ZnO native planes under basic conditions.* Langmuir, 2012. **28**(13): p. 5633-41.
297. D'Amico, N.R., G. Cantele, and D. Ninno, *First-principles calculations of clean and defected ZnO surfaces.* The Journal of Physical Chemistry C, 2012. **116**(40): p. 21391-21400.
298. Roy, S., et al., *Morphological and electrical study of porous TiO2 films with various concentrations of Pluronic F-127 additive.* Journal of Porous Materials, 2020. **28**(1): p. 231-238.
299. Henrist, C., et al., *Hierarchical porous TiO2 thin films by soft and dual templating: a quantitative approach of specific surface and porosity.* Thin Solid Films, 2013. **539**: p. 188-193.
300. Ramos, F.J., et al., *Perovskite solar cells based on nanocolumnar plasma-deposited ZnO thin films.* ChemPhysChem, 2014. **15**(6): p. 1148-1153.
301. Simon, Q., et al., *Vertically oriented CuO/ZnO nanorod arrays: from plasma-assisted synthesis to photocatalytic H 2 production.* Journal of Materials Chemistry, 2012. **22**(23): p. 11739-11747.
302. Sanchez-Valencia, J.R.n., et al., *Oxygen optical sensing in gas and liquids with nanostructured ZnO thin films based on exciton emission detection.* The Journal of Physical Chemistry C, 2014. **118**(18): p. 9852-9859.
303. Laurenti, M. and V. Cauda, *Porous Zinc Oxide Thin Films: Synthesis Approaches and Applications.* Coatings, 2018. **8**(2).
304. Michael Krumrey, R.G.-D., Christian Gollwitzer, and S. Langner, *Size Determination of Nanoparticles with Small-angle X-ray Scattering.* PTB-Mitteilungen, 2014. **124**(3/4).